MOLECULAR MECHANISMS OF HOMOLOG-INDEPENDENT DNA REPAIR DURING *C. ELEGANS* MEIOSIS

by
ERIK PAUL TORAASON

A DISSERTATION
Presented to the Department of Biology
and the Division of Graduate Studies of the University of Oregon
in partial fulfillment of the requirements
for the degree of
Doctor of Philosophy
June 2022

DISSERTATION APPROVAL PAGE

Student: Erik Paul Toraason

Title: Molecular Mechanisms of Homolog-Independent DNA Repair During *C. elegans* Meiosis

This dissertation has been accepted and approved in partial fulfillment of the requirements for the Doctor of Philosophy degree in the Department of Biology by:

Nadia Singh	Chairperson
Diana E. Libuda	Advisor
Bruce Bowerman	Core Member
Kryn Stankunas	Core Member
Ken Prehoda	Institutional Representative

And

Krista Chronister	Vice Provost for Graduate Studies

Original approval signatures are on file with the University of Oregon Division of Graduate Studies.

Degree awarded June 2022.

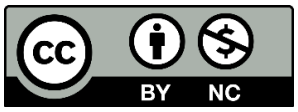

DISSERTATION ABSTRACT

Erik Paul Toraason

Doctor of Philosophy

Department of Biology

June 2022

Title: Molecular Mechanisms of Homolog-Independent DNA Repair During *C. elegans* Meiosis

Meiosis is the specialized cell division by which most sexually reproducing organisms generate haploid gametes such as sperm and eggs. Meiotic cells of diploid organisms contain four copies of the genome: two homologous chromosomes as well as identical replicates of each homolog called sister chromatids. Although DNA damage threatens genomic stability, meiotic cells intentionally induce DNA double-strand breaks (DSBs) across the genome. Most studies of meiotic DSB repair have focused on how a limited subset of DSBs are resolved with the homologous chromosome as crossovers, which are required for accurate meiotic chromosome segregation. The remaining DSBs that are not repaired with the homologous chromosome have been long hypothesized in metazoans to be repaired using the sister chromatid. The perfect identity shared by sister chromatids, however, has precluded testing of this model by sequencing approaches.

To directly detect the long-hypothesized homolog-independent recombination events during metazoan meiosis, I developed an 'intersister/intrachromatid repair assay' (ICR assay) in the nematode *Caenorhabditis elegans* which enables the direct detection of homolog-independent crossover and noncrossover recombination during meiosis. Using the ICR assay, I demonstrate that the sister chromatid or same DNA molecule can indeed be engaged to repair DSBs as crossovers or noncrossovers, and that intersister/intrachromatid repair is the sole recombination pathway utilized in late meiotic prophase I. Additionally, using the ICR assay in conjunction with cytological and functional DSB repair assays, I show that the highly conserved structural maintenance of chromosomes 5/6 complex (SMC-5/6) and tumor suppressor BRCA1 (BRC-1) restrict intersister crossover recombination and error-prone repair during meiotic prophase I.

Finally, I investigated how meiotic DNA repair is impacted during germline aging. Utilizing a computational image analysis pipeline I developed, I find that sperm depletion causes reduced DSB induction, while processes associated with germline aging contribute to DNA

repair defects in aged germlines. Moreover, I identify the ubiquitin ligase-like protein UEV-2 as a putative regulator of DNA repair defects during aging. Taken together, my thesis work illuminates mechanisms regulating metazoan intersister/intrachromatid meiotic recombination and defines pathways balancing efficiency and accuracy of DNA repair in the immortal germline.

This dissertation contains previously published and co-authored material.

CURRICULUM VITAE

NAME OF AUTHOR: Erik P. Toraason

GRADUATE AND UNDERGRADUATE SCHOOLS ATTENDED

University of Oregon, Eugene OR
University of Wisconsin Madison, Madison WI

DEGREES AWARDED:

Doctor of Philosophy, Biology, 2022, University of Oregon
Bachelor of Science, Genetics, with certificates in German and Studio Art, 2016, University of Wisconsin Madison

AREAS OF SPECIAL INTEREST:

Biology of Aging
Genetics
DNA Repair

PROFESSIONAL EXPERIENCE

Undergraduate Research Assistant, Dr. Michael Gould Lab, McArdle Laboratory for Cancer Research, 2014-2016

Undergraduate Research Assistant, Dr. William Dove Lab, McArdle Laboratory for Cancer Research, 2013-2014

GRANTS, AWARDS, AND HONORS

2021 – University of Oregon Raymond-Stevens Fellowship
2021 – Oral Session Chair, European Students and Postdocs Meiosis Workshop
2020 – University of Oregon von Hippel Outstanding Senior Graduate Student Award
2020 – University of Oregon Donald E. Wimber Fund Award
2019 – University of Oregon Knight Campus Undergraduate Scholars Program Clark Honors College Mentor
2018 – NSF Graduate Research Fellowship Honorable Mention
2017-2020 – NIH NIGMS T32 Genetics Training Grant (T32GM007413)
2017 – University of Oregon Adamson Family Outstanding First Year Graduate Student Award
2016-2018 – ARCS® Anderson Scholar Award

PUBLICATIONS:

TORAASON, E., Almanzar, A., Salagean, A., Ofer, R., Libuda, D.E. BRCA1/BRC-1 and SMC-5/6 regulate DNA repair pathway engagement during *C. elegans* meiosis. *In preparation.*

TORAASON, E.*, Adler, V.L.*, Libuda, D.E. Aging and sperm signals alter DNA damage induction and repair in the *C. elegans* germline. *In preparation*.
* indicates Co-first Authorship

TORAASON, E., Horacek, A., Glover, M.G., Libuda, D.E. Detection of homolog-independent meiotic DNA repair events in C. elegans with the intersister/intrachromatid repair assay. STAR Protocols 2021. DOI: 10.1016/j.xpro.2021.100801

TORAASON, E., Horacek, A., Clark, C., Glover, M.L., Adler, V.L., Premkumar, T., Salagean, A., Cole, F. Libuda, D.E. Meiotic DNA break repair can utilize homolog-independent chromatid templates in C. elegans. Current Biology 2021. DOI: 10.1016/j.cub.2021.03.008

TORAASON, E., Adler, V.L., Kurhanewicz, N.A., DiNardo, A., Saunders, A.M., Cahoon, C.K., Libuda, D.E. Automated and customizable quantitative image analysis of whole Caenorhabditis elegans germlines. Genetics 2021. DOI: 10.1093/genetics/iyab010 (featured article in March 2021 issue of Genetics)

Pleiman, J.K., Irving, A.A., Chen, X. TORAASON, E., Clipson, L., Dove, W.F., Wang, Z., Deming, D.A., Newton, M.A. The conserved protective cyclic AMP-phosphodiesterase function PDE4B is expressed in the adenoma and adjacent normal colonic epithelium of mammals and silenced in colorectal cancer. PLoS Genetics 2018. DOI: 10.1371/journal.pgen.1007611.

ACKNOWLEDGEMENTS

The work presented in this thesis would not have been possible without the guidance and support of mentors both at the University of Oregon and beyond. Diana Libuda is the best graduate mentor I could ask for and has pushed me to grow both intellectually and professionally as a scientist. Her dedication to excellent science and building a lab environment which is both challenging and supportive has forever shaped the way I will think about and pursue research. The support and kindness of the amazing members of the Libuda lab, including Cori Cahoon, Nicole Kurhanewicz, and Alice Naftaly, have been vital in completing this work. Francesca Cole's expertise and contributions to my thesis research have been invaluable, and I cannot overstate how much I appreciate her support. I thank my committee, Nadia Singh, Jeff McKnight, Bruce Bowerman, Ken Prehoda, and Kryn Stankunas, for their assistance and feedback in shaping my project. I also thank the members of the Center for Genome Function for their thoughtful feedback, and Peter Ralph for encouraging my interest in coding and statistics. The Genetics Training Program has also provided excellent training and given me the opportunity to build my scientific network for the next steps in my career.

I additionally thank the members of the ARCS® organization, in particular my sponsors Jamie and Mike Anderson. Their support, both financial and personal, has been pivotal in building my career. I also owe much of my success to the brilliant and talented undergraduate scientists who I had the privilege to work with.

I finally thank the friends, family, and cats in my life. I would not be here today without you.

To my siblings, Inger and Claire.

TABLE OF CONTENTS

LIST OF FIGURES.

CHAPTER I

INTRODUCTION

The somatic tissues of organisms are subject to environmental challenges and, in many systems, aging processes which can contribute to their eventual demise over time. In contrast, the germline is “immortal”, enabling the creation of new generations largely untouched by the somatic decline of their parents (Smelick and Ahmed 2005). Thus, reproduction is fundamental to the continuation of life itself. In sexually reproducing organisms, progeny are produced via the fusing of reproductive cells (gametes). The ploidy of the parental genome must be halved to generate haploid gametes so that progeny inherit the correct complement of chromosomes. Gametes in most organisms are created via the specialized cell division called ‘meiosis’. In diploids, each meiotic nucleus begins prophase I with four copies of the genome – two homologous chromosomes inherited from that organism’s parents and an identical replicate of each homolog called a sister chromatid (Figure 1.1). As mutations incurred in the gamete genome may cause defects in resultant progeny, the integrity of DNA sequences must be preserved during meiosis.

Meiotic prophase I is composed of 5 phases – leptotene, zygotene, pachytene, diplotene, and diakinesis (Figure 1.1) (Reviewed in (Garcia-Muse and Boulton 2007)). Specific cytological events must occur in each of these steps for successive meiotic stages to be successful. During leptotene and zygotene, the meiotic chromatin condenses and homologous chromosomes align and pair (Figure 1.1). A proteinaceous superstructure called the ‘synaptonemal complex’ (SC) then assembles between paired homologous chromosomes (Figure 1.1). These processes occur concurrently with the formation of double-strand DNA breaks (DSBs) by the highly conserved topoisomerase-like protein Spo11 (Keeney *et al.* 1997; Dernburg *et al.* 1998). Meiotic DSBs are primarily repaired by recombination and preferentially utilize the homologous chromosome as a repair template (Figure 1.1, Figure 1.2).

During pachytene, a limited subset of DSBs which have engaged the homologous chromosome are designated to be resolved as crossovers. Crossovers physically exchange DNA sequence between homologs and create a tether that links homologs together (Figure 1.1). The majority of DSBs are not repaired as crossovers and must therefore be resolved by other DNA repair

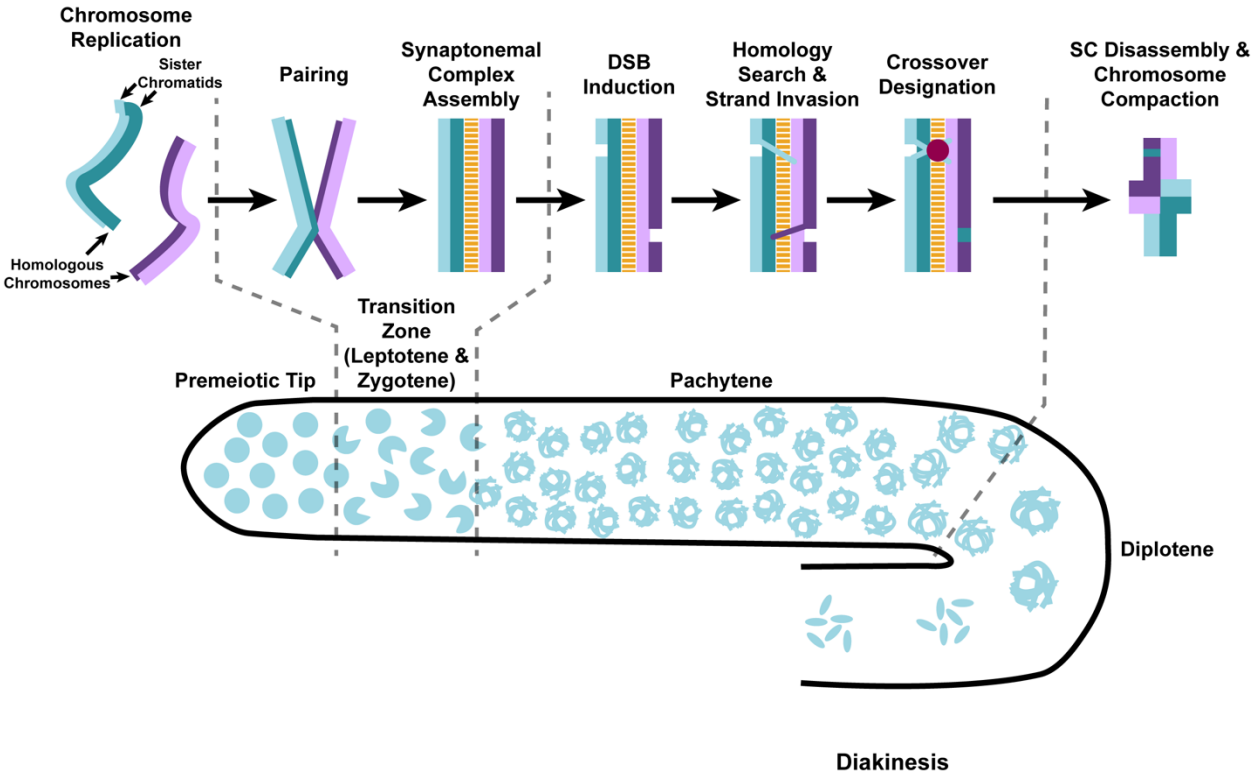

Figure 1.1. Outline of meiotic progression in the *C. elegans* germline. Depicted is a cartoon of a *C. elegans* germline in which oocyte nuclei (light blue circles) process through the gonad beginning in the left tip (premeiotic) to the right (diplotene/diakinesis) as they also progress through meiotic prophase I. Above are representations of the meiotic events which occur within nuclei at respective meiotic stages. Dashed grey lines demarcate transition points in the germline at which specific meiotic stages and events occur.

mechanisms to preserve genome integrity. In diplotene and diakinesis, meiotic 'bivalents' organized around the crossovers to facilitate accurate segregation at the meiosis I and II divisions.

The nematode *Caenorhabditis elegans* has proven to be a powerful model for understanding the molecular mechanisms underpinning meiosis and aging (Garcia-Muse and Boulton 2007; Mack *et al.* 2018). Adult *C. elegans* animals exist as two sexes – hermaphrodites which produce spermatocytes within a specific window of larval development and oocytes throughout their adult reproductive span, and males which produce exclusively spermatocytes (Albert Hubbard and Greenstein 2000). Thus, *C. elegans* further enables comparative studies between spermatogenesis and oogenesis in adult animals. Further, robust genetic toolkits have been developed in *C. elegans*, facilitating rapid genetic engineering and tissue-specific transgene expression using CRISPR/Cas9 genome editing (Dokshin *et al.* 2018).

In particular, the *C. elegans* germline is a potent system for understanding germ cell development (Hubbard and Greenstein 2005). *C. elegans* germ cells are proliferated from a stem cell pool in the distal tip of the gonad and move along the distal-proximal axis they progress through meiosis (Figure 1.1) (Hubbard and Schedl 2019). Thus, oocytes at all stages of meiotic prophase I are available within the gonad simultaneously. This organization facilitates assessment of 3D cytological features in meiotic nuclei either through live imaging of fluorescently labeled proteins or fixed preparations using immunofluorescence. Additionally, the rate at which oocytes move through the germline is known (Jaramillo-Lambert *et al.* 2007; Rosu *et al.* 2011; Cahoon and Libuda 2021). Together, these features of *C. elegans* reproductive physiology facilitate unique reverse-timecourse approaches for assessing how oocytes throughout prophase I respond to discrete stimuli. These experiments are performed by subjecting a parent hermaphrodite to a treatment, such as radiation or heat stress, and then assessing the consequences of that stimulus in resultant progeny laid in specific windows following that treatment (Rosu *et al.* 2011).

The genetic tools and physiological features of *C. elegans* together make it an ideal model for understanding the mechanisms required for engagement of specific DNA repair outcomes during meiosis and how these pathways are differentially regulated during the course of prophase I. In this thesis, I exploit *C. elegans* to further our understanding of how two key decisions in meiosis are made: 1) How do meiotic cells choose which DNA repair pathway will be engaged to resolve a DSB?; and, 2) How do meiotic cells choose recombination repair templates (homologous chromosome vs. sister chromatid)?

The first decision: Which DNA repair pathway?

Cells may engage many independent pathways to resolve DSBs with varying degrees of accuracy (Figure 1.2) (Reviewed in Gartner and Engebrecht 2022). In meiosis, DSBs are primarily repaired via recombination, which utilizes base pair homology to identify accurate repair templates and conserves sequence identity in the final repair product. Error prone pathways are also available to resolve DSBs at the risk of introducing mutations (Gartner and Engebrecht 2022). While mutagenic DNA repair pathways may generate *de novo* deleterious sequence changes in the genome, some forms of error prone repair are kinetically faster than recombination and can avoid errors in resolving DSBs in repetitive genomic regions (Mao *et al.*

2008). Error prone pathways can therefore be advantageous over recombination in some contexts. To preserve genome integrity, cells must regulate engagement of both recombination and error-prone pathways to ensure efficient and accurate DSB resolution.

During meiosis, DSBs are designated to be resolved by recombination via specific processing steps early in their repair. Following DSB induction, the 5' ends of the DSB are resected to yield 3' single-strand DNA (ssDNA) overhangs (Figure 1.2). These 3' ends are then loaded with the conserved recombinase RAD-51 (Colaiácovo *et al.* 2003; Alpi *et al.* 2003). RAD-51 facilitates homology search to identify a recombination repair template and additionally protects resected DNA from being erroneously repaired by error-prone pathways (So *et al.* 2022). Upon identification of a homologous repair template, the invading ssDNA strand displaces the noncomplementary strand of its double-stranded DNA (dsDNA) repair template, creating a structure known as a D-loop (Figure 1.2).

Following strand invasion, RAD-51 is removed and DNA polymerases extend the invading end of the DSB utilizing the complementary dsDNA template. The invading strand may then be ejected by helicases to complete repair as a noncrossover in a pathway called 'synthesis-dependent strand annealing' (SDSA) (Van Brabant *et al.* 2000; Bachrati *et al.* 2006; Hu *et al.* 2007) (Figure 1.2). Alternately, the displaced strand of the dsDNA repair template in the D-loop may engage the second end of the DSB, forming a classical joint molecule structure called a double-Holliday junction (dHJ) (Holliday 1964) (Figure 1.2). In mid/late pachytene, a specific subset of dHJs accumulate pro-crossover proteins (Kelly *et al.* 2000; Yokoo *et al.* 2012; Cahoon *et al.* 2019) and are eventually cleaved by nucleases to yield crossover events (Agostinho *et al.* 2013; O'Neil *et al.* 2013; Saito *et al.* 2013) (Figure 12). dHJ intermediates not designated to become obligate crossovers have been suggested to be resolved as noncrossover products (Crown *et al.* 2014) (Figure 1.2). However, a growing body of evidence in multiple species suggests that noncrossovers are primarily formed via SDSA (Hunter 2015).

To preserve genome integrity as well as facilitate proper chromosome segregation, recombination is heavily favored as a repair pathway during *C. elegans* meiosis (Gartner and Engebrecht 2022). Mutants which disrupt resection or homology search, however, become dependent upon error-prone mechanisms for DSB repair (Yin and Smolikove 2013; Macaisne *et al.* 2018), suggesting that these alternative pathways act as 'back up mechanisms' in meiotic prophase I. Three major error-prone repair pathways are known to be available during *C. elegans*

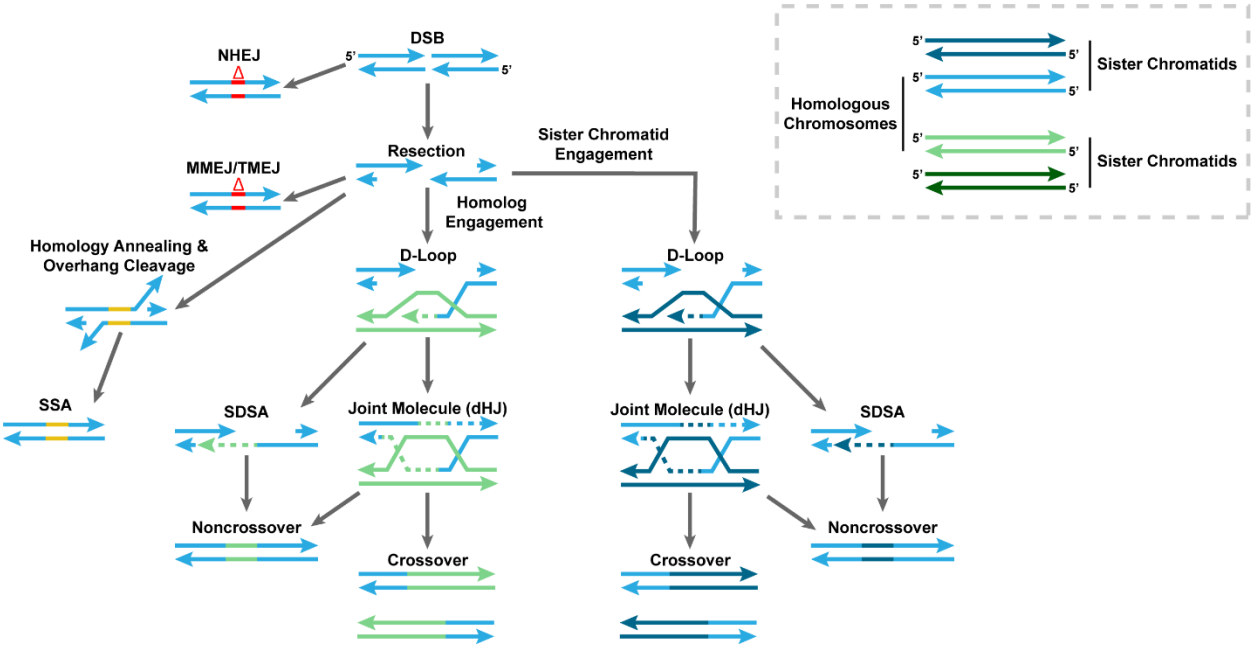

Figure 1.2. DNA repair pathways in the *C. elegans* germline. Depicted is a cartoon of DNA repair mechanisms which may be engaged to repair DSBs during *C. elegans* meiosis. Acronyms used include: dHJ (double-Holliday junction), D-loop (displacement loop), MMEJ (microhomology-mediated end joining), NHEJ (non-homologous end joining), SDSA (synthesis-dependent strand annealing), SSA (single-strand annealing), and TMEJ (theta mediated end joining).

meiosis: non-homologous end joining (NHEJ), microhomology mediated end joining (MMEJ), and single-strand annealing (SSA).

Similar to DSBs repaired via recombination, DSBs intended for NHEJ repair are also designated early in DSB processing. Following DSB induction, the CKU-70/80 heterodimer binds to DSB ends and facilitates their direct ligation by the specialized ligase LIG-4 (Figure 1.2) (Clejan *et al.* 2006; Lemmens *et al.* 2013). DNA ligation in NHEJ is error prone and risks introducing small lesions 1-4bp in size (Gartner and Engebrecht 2022). Meiotic cells bias DSB repair towards recombination, however, by removing bound CKU-70/80 from DSB ends via the CtIP homolog COM-1 (Lemmens *et al.* 2013).

MMEJ utilizes short stretches (1-20bp) of microhomology exposed on resected DNA to anneal and ligate DSB ends at the expense of introducing small insertions and deletions (Figure 1.2) (Seol *et al.* 2018; Ramsden *et al.* 2022). In *C. elegans* meiosis, MMEJ is primarily enacted through the activity of the polymerase θ homolog POLQ-1 (theta-mediated end joining, TMEJ) (Van Schendel *et al.* 2015). Polymerase θ exhibits both helicase and polymerase activity to

facilitate microhomology annealing and gap filling respectively (Ramsden *et al.* 2022; Gartner and Engebrecht 2022). While TMEJ is both active in the *C. elegans* germline and responsible for most small indels incurred in germ cells (Van Schendel *et al.* 2015), the molecular mechanisms regulating TMEJ engagement during meiosis remain largely unknown.

SSA is engaged when long regions of complementary sequence (>30bp), which are exposed by resectioning on both ends of a DSB, directly anneal (Figure 1.2) (Bhargava *et al.* 2016). Following strand annealing, the nonhomologous 3' DNA overhangs are cleaved by the Rad1 nuclease homolog XPF-1 and the DSB ends are ligated (Figure 1.2) (Gartner and Engebrecht 2022). SSA is therefore intrinsically error-prone and always yields deletions, as any sequence between the flanking complementary homology is removed in the final repaired product.

How error prone repair is prevented to ensure DSBs are repaired by recombination during meiosis, as well as how error-prone repair pathways are engaged when recombination is defective, remain essential questions in the study of meiotic genome integrity. Analysis of mutations incurred in a wide array of DNA repair mutant backgrounds has revealed that many *C. elegans* proteins differentially contribute to DNA damage repair (Volkova *et al.* 2020). Many of these complexes, including the tumor suppressor BRCA1 and structural maintenance of chromosomes 5/6 (Smc5/6), are widely conserved and have been shown to be vital in preventing error prone repair in *C. elegans* (Volkova *et al.* 2020; Kamp *et al.* 2020). Thus, illumination of these proteins' functions in the *C. elegans* germline may enable broad insights into mechanisms preserving genome integrity across phyla.

The second decision: Which recombination repair template?

When a DSB has been designated for repair by recombination, a second vital choice must be made: which DNA template (a.k.a recombination partner) will be engaged? There are two available repair partners in meiotic prophase I: the sister chromatid and the homologous chromosome (Humphryes and Hochwagen 2014). Mitotic DSBs incurred in interphase are heavily biased towards recombination with the sister chromatid, presumably due to the close spatial proximity of the DSB and the sister chromatid (Nasmyth and Haering 2009; Kim *et al.* 2010). In meiosis this pattern is inverted, with the majority of DSBs engaging the homologous chromosome instead of the sister chromatid (Kim *et al.* 2010). Work in budding yeast has

identified many players which regulate bias towards the homolog during meiosis. These regulators include proteins composing the chromosome axis (Kim *et al.* 2010), the meiotic kinase Mek1 (Niu *et al.* 2005; Terentyev *et al.* 2010), the meiotic cohesin Rec8 (Kim *et al.* 2010), and the recombinase Dmc1 (Cloud *et al.* 2012).

The conservation of mechanisms conveying homolog template bias has proven challenging to directly test, as quantifying partner choice requires the capacity to assess both interhomolog and intersister repair in meiotic cells. As homologous chromosomes are frequently polymorphic, interhomolog engagements are readily detectible by sequencing recombination products for nucleotide conversions which arise during repair. Since sister chromatids share perfect sequence identity, sequencing-based approaches have failed to capture and detect intersister repair products. Well established 2D gel electrophoresis and Southern blotting techniques enable detection of recombination intermediates between homologs and sister chromatids at specific loci in budding yeast (Goldfarb and Lichten 2010; Humphryes and Hochwagen 2014), but these techniques have not proven translatable to studies in metazoan systems. Thus, the putative engagement of intersister repair and the mechanisms which may regulate this pathway remain undetermined in metazoan meiosis.

Recent evidence in *C. elegans* suggests that chromosome organization may contribute to regulation of repair template engagement. DNA-FISH of specific loci in meiotic chromosome spreads indicates that sister chromatids are not symmetrically organized, potentially disfavoring engagement of the sister as a repair template (Woglar *et al.* 2020). Further, mutants for the *C. elegans* Rec8 homolog incorrectly assemble the SC between sister chromatids and form intersister crossovers at elevated rates (Cahoon *et al.* 2019; Almanzar *et al.* 2021), suggesting that this protein may have a similar function in worms and budding yeast. Access to the homolog as a repair template and the requirements for DSB repair are also known to change during the course of meiotic prophase I (Hayashi *et al.* 2007; Rosu *et al.* 2011), as the homologous chromosome only available as a repair template in early stages of meiotic prophase I. Meiotic DSBs are nonetheless resolved in mutants which are deficient in interhomolog recombination (MacQueen *et al.* 2002; Colaiácovo *et al.* 2003). This evidence has contributed to a hypothesis that the sister chromatid may be engaged in late prophase I to resolve DSBs. The absence of a reliable method to assess homolog-independent recombination outcomes presents a fundamental

limitation to testing this hypothesis and identifying mechanisms regulating metazoan meiotic recombination partner choice.

Illuminating mechanisms of meiotic homolog-independent DSB repair

Understanding the engagement and regulation of DSB repair pathways requires the capacity to detect all possible repair outcomes. Interhomolog recombination may be detected through polymorphism conversions in recombination products and error prone repair pathway engagement can be identified through the presence of *de novo* mutations. Since intersister repair products are indistinguishable from undamaged DNA in most contexts, intersister recombination is effectively "invisible" by sequencing-based methods. To enable the direct detection of homolog-independent recombination, I developed a recombination assay which enables the identification and sequence analysis of both crossover and noncrossover recombination products with the sister chromatid or same DNA molecule at a known locus in the *C. elegans* genome. Using this assay, I demonstrate that intersister/intrachromatid crossover and noncrossover repair is engaged in *C. elegans* meiosis and is the exclusive recombination pathway in late meiotic prophase I. Moreover, I use this assay to identify conserved DNA repair protein complexes (Rad1/XPF nuclease, structural maintenance of chromosomes 5/6, and the tumor suppressor BRCA1) which regulate intersister/intrachromatid repair outcomes. Through these studies, I further uncover meiosis-stage specific regulatory mechanisms limiting engagement of error prone DNA repair pathways.

To facilitate cytological study of DSB repair protein dynamics within the *C. elegans* germline, I additionally developed an image analysis pipeline which enables quantification of DSB repair proteins in individual meiotic nuclei and contextualization of those nuclei based on their meiotic stage and progression through the germline. Utilizing this pipeline, I identified mechanisms which contribute to meiotic defects during *C. elegans* reproductive aging. Taken together, my thesis work unveils novel mechanisms of DNA repair preserving intergenerational genome integrity in the immortal germline.

CHAPTER II

MEIOTIC DNA BREAK REPAIR CAN UTILIZE HOMOLOG-INDEPENDENT CHROMATID TEMPLATES IN *C. ELEGANS*

Published in *Current Biology* April 2021

Erik Toraason, Anna Horaceek, Cordell Clark, Marissa L. Glover, Victoria L. Adler, Tolkappiyan Premkumar, Alina Salagean, Francesca Cole, and Diana E. Libuda

Summary

During meiosis, the maintenance of genome integrity is critical for generating viable haploid gametes (Ann Handel and Schimenti 2010). In meiotic prophase I, double-strand DNA breaks (DSBs) are induced and a subset of these DSBs are repaired as interhomolog crossovers to ensure proper chromosome segregation. DSBs not resolved as crossovers with the homolog must be repaired by other pathways to ensure genome integrity (Gray and Cohen 2016). To determine if alternative repair templates can be engaged for meiotic DSB repair during oogenesis, we developed an assay to detect sister and/or intra-chromatid repair events at a defined DSB site during *Caenorhabditis elegans* meiosis. Using this assay, we directly demonstrate that the sister chromatid or the same DNA molecule can be engaged as a meiotic repair template for both crossover and noncrossover recombination, with noncrossover events being the predominant recombination outcome. We additionally find that the sister or intra-chromatid substrate is available as a recombination partner for DSBs induced throughout meiotic prophase I, including late prophase when the homolog is unavailable. Analysis of noncrossover conversion tract sequences reveals that DSBs are processed similarly throughout prophase I. We further present data indicating that the XPF-1 nuclease functions in late prophase to promote sister or intra-chromatid repair at steps of recombination following joint molecule processing. Despite its function in sister or intra-chromatid repair, we find that *xpf-1* mutants do not exhibit severe defects in progeny viability following exposure to ionizing radiation. Overall, we propose that *C. elegans* XPF-1 may assist as an intersister or intrachromatid resolvase only in late prophase I.

Results and Discussion.

Engagement of the sister chromatid in meiotic DSB repair

During meiotic prophase I, double-strand DNA breaks (DSBs) are induced across the genome (Ann Handel and Schimenti 2010). A subset of DSBs must be repaired as interhomolog

crossovers to ensure accurate chromosome segregation, and the remaining DSBs are repaired through other mechanisms (Lao and Hunter 2010). While the homolog is the preferred recombination template in meiotic prophase I (Lao and Hunter 2010), access to the homolog is shut down in mid-late pachytene stage (Rosu *et al.* 2011). Several studies have hypothesized that after access to the homolog is shut down, there is a regulated switch in template preference from the homolog to the sister chromatid during late meiotic prophase I to ensure the repair of any remaining DSBs prior to the meiotic divisions (Hayashi *et al.* 2007; Rosu *et al.* 2011; Lemmens *et al.* 2013). Studies in *Saccharomyces cerevisiae* indicate the sister chromatid can be engaged during meiosis (Goldfarb and Lichten 2010) and multiple lines of evidence have suggested that the sister chromatid may be engaged as a meiotic DSB repair template to repair these remaining DSBs in metazoan meiosis (Hayashi *et al.* 2007; Robert *et al.* 2008; Rosu *et al.* 2011), but the perfect sequence identity shared between sister chromatids has precluded direct testing of this hypothesis in metazoans.

To determine whether the sister chromatid or the same chromatid can be engaged as a repair template during *C. elegans* meiosis, we developed a non-allelic intersister/intrachromatid repair assay (ICR assay; Figures 2.1A and S2.1) that utilizes controlled excision of a Mos1 transposon to induce a single DSB within a genetic reporter that detects repair events using a non-allelic truncated cassette on the sister chromatid or same chromatid as a template. Similar to other repair assays in *S. cerevisiae* meiosis (Fasullo and Davis 1987; Kadyk and Hartwell 1992) and mammalian mitosis (Johnson *et al.* 1999; Pierce *et al.* 1999; Johnson and Jasin 2000), our ICR assay is composed of two tandem reporter sequences. In our assay, the upstream copy encodes a truncated GFP allele driven by a *myo-3* promoter (body wall expression). The downstream copy is driven by a *myo-2* promoter (pharynx expression) and is disrupted with the *Drosophila* Mos1 transposable element (Bessereau *et al.* 2001). Upon heat shock-induced expression of Mos1 transposase (Robert and Bessereau 2007), excision of the Mos1 transposon produces a single DSB (Rosu *et al.* 2011). Previous studies determined the frequency of Mos1 excision with this heat-induced method to be 28% of *C. elegans* germ cell nuclei and that Mos1 is likely not to excise in both sister chromatids (see supplement of Rosu *et al Science* 2011 (Rosu *et al.* 2011)) (Engels *et al.* 1990; McVey *et al.* 2004; Davis *et al.* 2005; Rosu *et al.* 2011). Repair of the Mos1-induced DSB via nonallelic intersister or intrachromatid recombination yields restoration of functional GFP sequence and GFP+ progeny. The tissue-specific expression of the

resultant functional GFP indicates which recombination pathway is engaged: 1) an intersister or intrachromatid noncrossover will generate functional *pmyo-2::*GFP expressed in the pharynx; and, 2) a deletion product indicative of an intersister or intrachromatid crossover will produce *pmyo-3::*GFP expressed in the body wall muscle. While homology-directed single strand annealing (SSA) could also generate a deletion product, 1367 bp of sequence would need to be resected for this mechanism to occur and data in this manuscript indicates that SSA is likely not responsible for these products. Further, intersister crossover recombination has been demonstrated in *C. elegans* (Almanzar *et al.* 2021). Although the ICR assay cannot definitively distinguish between an intersister or an intrachromatid event, we suggest the assay is very likely detecting intersister events based on evidence for intersister repair in *S. cerevisiae* (Goldfarb and Lichten 2010) and strong evidence indicating use of intersister repair in *C. elegans* (Hayashi *et al.* 2007; Adamo *et al.* 2008; Rosu *et al.* 2011; Lemmens and Tijsterman 2011; Macaisne *et al.* 2018; Almanzar *et al.* 2021). Since allelic recombination will not restore functional GFP sequence, the ICR assay will not detect every sister chromatid or intrachromatid repair event but it does detect nonallelic recombination outcomes, thereby enabling direct detection of such events in *C. elegans*.

The ICR assay was performed in hermaphrodites heterozygous for the assay at a locus previously assessed for interhomolog repair (exon 6 of *unc-5*; (Rosu *et al.* 2011)) (see Methods). Since there is no GFP sequence on the homolog in this context, recombination repair of the Mos1-induced DSB is restricted to sister chromatid or intrachromatid events. With this assay, we observed both noncrossover and crossover GFP+ recombinants at an overall frequency of 0.69% of all progeny (including progeny that did not experience a Mos-1 induced DSB; 95% confidence interval (CI) 0.550-0.863%), which represents the frequency of nonallelic recombination at this locus in oocytes at meiotic stages from leptotene/zygotene (transition zone) through late pachytene and diplotene at the time of DSB induction by Mos1 transposition (Figure 2.1B top). Notably, noncrossover events were the predominant repair outcome from the ICR assay (85.3% of GFP+ recombinants, Table S2.1 top). This data directly demonstrates that the sister chromatid or same DNA molecule can be engaged as a DSB repair template in *C. elegans* meiosis and enables the assessment of this meiotic DNA repair pathway for the first time in a metazoan.

We next wanted to test for the hypothesized switch in template bias from the homolog to the sister chromatid during late meiotic prophase I (Hayashi *et al.* 2007; Rosu *et al.* 2011; Lemmens *et al.* 2013). Similar to a previous *C. elegans* assay which assessed interhomolog repair during meiosis (interhomolog repair assay; Figure 2.1B bottom and Table S2.1 bottom) (Rosu *et al.* 2011), the ICR assay can determine the stages of meiotic prophase I in which the sister chromatid can be engaged as a repair template. Given the established timing of meiotic prophase progression for *C. elegans* oogenesis, progeny laid in the 22-58 hour timepoints were derived from oocytes spanning entry into meiotic prophase I through mid-pachytene at the time of heat shock (Mos1 excision), while the oocytes yielding progeny at the 10-22 hour time point were at late pachytene/diplotene (Jaramillo-Lambert *et al.* 2007; Rosu *et al.* 2011). While neither the interhomolog assay nor ICR assay detect whether a DSB is repaired within the same meiotic stage it was induced, we can still determine the latest window in which a repair template is available. Specifically, DSBs induced during the 22+ hour time points ('interhomolog window') and not the 10-22 hour time point ('non-interhomolog window') can be repaired with the homolog (Figure 2.1B bottom, Table S2.1) (Rosu *et al.* 2011), the ICR assay demonstrates that DSBs induced at different times throughout meiotic prophase can be repaired using the sister chromatid or same DNA molecule, and that such repair occurs at similar frequencies regardless of the timing of DSB induction (Figure 2.1B top, Table S2.1). Thus, while engagement of the homolog is restricted to a specific window of meiotic prophase I, the sister chromatid or same chromatid may be engaged as a repair template for DSBs induced throughout meiotic prophase I. This data further demonstrates that intersister or intrachromatid repair becomes the preferred recombination pathway in late meiotic prophase I when the homolog is no longer readily engaged for repair (10-22 hours post-heat shock, Figure 2.1B). Moreover, we observed both noncrossover and crossover recombinant progeny at all timepoints (Figure 2.1B top), indicating that DSBs induced throughout meiotic prophase I may be repaired by intersister/intrachromatid crossover and noncrossover recombination pathways. Crossover recombinants are specifically enriched in the non-interhomolog window (10-22hr post heat shock) compared to the interhomolog window (Fisher's Exact Test $p=0.041$). These results indicate that a late pachytene transition increases DSB resolution by intersister/intrachromatid crossover recombination.

XPF-1 nuclease promotes intersister/intrachromatid repair

We next investigated the role of the resolvase XPF-1 in intersister and intrachromatid recombination. XPF-1 is the *C. elegans* homolog of the XPF/RAD1 nuclease and acts semi-redundantly with other nucleases to resolve meiotic interhomolog crossovers (Saito *et al.* 2009, 2013; Agostinho *et al.* 2013; O'Neil *et al.* 2013). XPF-1 is also required for single-strand annealing (SSA), a mutagenic homology-directed repair pathway which may be engaged upon exposure of >30bp of repeated sequence on each resected ssDNA strand of a damaged chromosome and results in deletion of sequences between tandem repeats (Lemmens and Tijsterman 2011; Manandhar *et al.* 2015; Bhargava *et al.* 2016). As the ICR assay contains tandem GFP cassettes (Figure 2.1A), engagement of SSA to resolve Mos1-induced DSBs could yield progeny with a phenotype that may be interpreted as an intersister/intrachromatid crossover event. To both assess the role of XPF-1 in intersister/intrachromatid repair and determine whether our assay is identifying SSA-mediated DSB repair, we performed the ICR assay in an *xpf-1(tm2842)* mutant, which exhibits normal rates of ovulation and likely does not significantly affect the timing of meiotic prophase progression (Figure S2.2A).

Neither the overall recombinant frequency nor the proportion of crossover progeny in *xpf-1* mutants differed from wild-type within the interhomolog window (Figure 2.2B and Tables S2.1 and S2.2, Fisher's Exact Test $p>0.05$). However, there was a decrease in the total frequency of recombinants in the non-interhomolog window at 10-22 hours post-heat shock (Figure 2.2, Fisher's Exact Test $p=0.004$), including crossover recombinant progeny. If the ICR assay was primarily detecting SSA repair, ablation of *xpf-1* should result in a severe reduction of 'crossover' progeny without altering observed frequencies of noncrossover progeny. Therefore, the occurrence of crossover recombinants in the *xpf-1* mutant suggests SSA does not significantly contribute to the detected ICR assay repair outcomes. This result is not surprising, as multiple *C. elegans* studies demonstrate that mutagenic DNA repair pathways, including SSA, are only frequently utilized for meiotic DSB repair in mutants where homologous recombination is impeded (Robert *et al.* 2008; Lemmens *et al.* 2013; Yin and Smolikove 2013; Macaisne *et al.* 2018; Bae *et al.* 2019). Notably, intersister crossovers were also cytologically observed in the accompanying publication (Almanzar *et al.* 2021), reinforcing the model that the crossover progeny we observe are likely derived from bona fide intersister crossovers. Overall, our data suggests that XPF-1 promotes meiotic sister chromatid and/or intrachromatid repair specifically

in late meiotic prophase I. Since XPF-1 functions to resolve interhomolog joint molecules in *C. elegans* meiosis (Saito *et al.* 2009, 2013; Agostinho *et al.* 2013; O'Neil *et al.* 2013), XPF-1 may also act to cleave intersister/intrachromatid joint molecules to yield crossover and noncrossover products at this late meiotic stage.

Mechanisms of intersister/intrachromatid recombination

Recombination mechanisms can be inferred from gene conversion tracts, which are DNA sequence changes that arise from nonreciprocal exchanges during recombination repair with a polymorphic template. To reveal mechanisms of meiotic intersister/intrachromatid repair, we engineered polymorphisms in the two tandem GFP cassettes within the ICR assay, thereby enabling detection of conversion tracts from recombination between nonallelic GFP sequences (Figure 2.3A). Wild-type intersister/intrachromatid noncrossover events displayed tracts ranging from a single to multiple polymorphism conversions spanning 567bp of sequence (Figure 2.3B). In all of these tracts, the polymorphism most proximal to the site of Mos1 excision (12bp downstream) was always converted, indicating that recombination intermediates remain local to the site of DSB induction and/or that this marker is frequently incorporated within the resection area (Figure 2.3B). This result is also reminiscent of *S. cerevisiae* mitotic repair of HO-mediated DSBs where there is preferential conversion of markers proximal to the DSB site (Hicks *et al.* 2010), likely due to the proofreading activity of polymerase delta. With this polymorphism density, we did not observe restoration tracts arising from recombination in wild type animals, which are unconverted polymorphisms flanked by conversion events indicative of multiple template engagement, heteroduplex DNA mismatch correction, or nucleotide excision of joint molecules during recombination (Fleck *et al.* 1999; Crown *et al.* 2014; Marsolier-Kergoat *et al.* 2018) (Figure 2.3B). Although interhomolog conversion tracts in other organisms suggest frequent joint molecule migration and strand switching (Marsolier-Kergoat *et al.* 2018; Peterson *et al.* 2020), our results suggest intersister/intrachromatid noncrossover repair in *C. elegans* possibly may not involve extensive migration from the DSB site. Future experiments in a mismatch repair mutant (*e.g. msh-2* mutant) or an ICR assay with a higher density of polymorphisms could reveal additional molecular signatures and evidence of template switching during these events.

To assess whether processing of intersister/intrachromatid recombination intermediates changes during meiotic progression, we compared tracts generated at different stages of prophase

I (Figures 2.3B, 2.3C). The length of a conversion tract can be influenced by 5' strand resection, joint molecule migration, extent of strand synthesis, and mismatch repair of heteroduplex sequences (Yin and Petes 2014; Ertl *et al.* 2017). Comparing the minimum conversion tract lengths of our wild-type intersister/intrachromatid noncrossover tracts, we note that the proportion of 'short' tracts converted only at one polymorphism and 'long' tracts ≥96bp in length are similar within both the interhomolog and non-interhomolog windows (interhomolog window 76.1% 'short' tracts 95% CI 62.1-86.1%, non-interhomolog window 72.7% 'short' tracts 95% CI 51.8-86.1%, Figure 2.3C, Fisher's Exact Test $p>0.05$), suggesting that DSB processing during intersister/intrachromatid noncrossover recombination repair is likely similar throughout prophase I.

XPF-1 does not influence intersister/intrachromatid noncrossover conversion tracts

Similar to wild-type, the most DSB proximal polymorphism remained converted in every *xpf-1* mutant intersister/intrachromatid noncrossover tract we sequenced (Figure 2.3B). However, we identified a single restoration tract arising from an interhomolog window noncrossover tract in our *xpf-1* mutant dataset (Figure 2.3B, asterisk). While this single event is not sufficient evidence that restoration tracts are specific to or enriched in *xpf-1* mutants, our identification of this tract demonstrates that complex recombination events occur in *C. elegans* meiosis. The proportion of 'short' (1bp) and 'long' (≥96bp) noncrossover conversion tracts arising from *xpf-1* mutants were similarly indistinguishable from wild-type (interhomolog window 80.0% 'short' tracts 95% CI 67.0-88.8%, non-interhomolog window 70% 'short' tracts 95% CI 39.7-89.2%, Figure 2.3C, Fisher's Exact Test interhomolog and non-interhomolog windows $p>0.05$). While our limited sample in the non-interhomolog window limits our interpretation of tract length proportions at this timepoint, the similar proportion of 'short' and 'long' tracts in the interhomolog window in both wild type and *xpf-1* mutants suggests that XPF-1 may function after joint molecule processing by acting as a resolvase to promote intersister/intrachromatid repair in late meiotic prophase I.

XPF-1 is not required for progeny viability following irradiation

To establish whether defects in intersister/intrachromatid recombination at specific stages of meiotic prophase I is required for fertility, we exposed young adult *xpf-1* mutant hermaphrodites to ionizing radiation, which induces DSBs, and performed a reverse time-course to assess effects on brood viability of damage induced at specific meiotic stages. Mutants for *xpf-*

1 exhibited a mild but significant reduction in brood viability upon exposure to 5000 Rads of ionizing radiation only within the interhomolog window (22-46 hour timepoint, Figure 2.4, Mann-Whitney U test p=0.037). While our ICR assay demonstrates that XPF-1 promotes intersister/intrachromatid repair in the non-interhomolog window, *xpf-1* mutants were not radiation-sensitive in late meiotic prophase I.

One possibility is that XPF-1 might distinguish between DSBs generated from transposition versus ionizing irradiation. Alternately, this discrepancy in ionizing radiation sensitivity and intersister/intrachromatid repair frequencies in *xpf-1* mutants could reflect that defects late in meiotic recombination intermediate resolution do not necessarily impact progeny viability. A recent study found that during *Drosophila* and mammalian mitosis, theta-mediated end joining (TMEJ) can process joint molecules in a resolvase-deficient background (Carvajal-Garcia *et al.* 2020). TMEJ is active during *C. elegans* meiosis and is the primary mechanism responsible for the formation of small deletions in the *C. elegans* germline (Van Schendel *et al.* 2015). A study which profiled mutations in *xpf-1* mutants demonstrated that nematode germ cells deficient in XPF-1 are susceptible to incurring small deletions in response to ionizing radiation (Volkova *et al.* 2020). Thus, mutants in DSB repair components such as XPF-1 that affect intersister/intrachromatid recombination late in joint molecule resolution may be less impactful on fertility due to DSB resolution by alternative and error prone repair pathway(s). Notably, sensitivity to ionizing radiation has been utilized as an important indicator for mutants deficient in intersister repair (Adamo *et al.* 2008; Bickel *et al.* 2010). Our data indicates that the ICR assay can further elucidate functions of proteins in meiotic DSB repair.

Conclusions

In this study, we detected recombination between sister chromatids and/or the same chromatid, thereby demonstrating that intersister/intrachromatid DNA repair can be engaged during meiosis. Additionally, we generated and analyzed intersister/intrachromatid conversion tracts to assess mechanisms of these types of events. We further show that the XPF nuclease is differentially engaged within meiotic prophase I to promote intersister/intrachromatid repair. From our data, we propose that XPF-1 nuclease acts downstream of recombination intermediate processing to promote intersister/intrachromatid repair during late meiotic prophase I. Multiple repair pathways likely work with or in parallel to XPF-1 to promote meiotic

intersister/intrachromatid recombination, and our ICR assay enables future elucidation of these interactions.

Acknowledgements

We thank the CGC (funded by National Institutes of Health (NIH) P40 OD010440) for strains. We thank A. Villeneuve, C. Cahoon, and N. Kurhanewicz for comments on the manuscript. We also thank K. Sugioka for his insights into the long-range interactions of the myosin promoters within the ICR assay. We also thank O. Rog and D. Almanzar for sharing their manuscript and data prior to publication. This work was supported by the National Institutes of Health T32GM007413 and Advancing Science in America (ARCS) Foundation Award to ET; National Institutes of Health R25HD070817 to CC, AH, and AS; National Institutes of Health R01HD098129 to FC and, National Institutes of Health R00HD076165 and R35GM128890 to DEL. TP was supported by the Cockrell Endowment Fellowship. DEL is also a recipient of a March of Dimes Basil O'Connor Starter Scholar award and Searle Scholar Award.

Author Contributions

E.T., A.H., C.C., M.L.G., V.L.A., T.P., and A.S. conducted experiments; E.T. performed statistical analyses; E.T., T.P., F.C., and D.E.L. designed the experiments and analyzed the data. E.T. and D.E.L. wrote the paper.

Declaration of Interests

The authors declare that they have no competing interests.

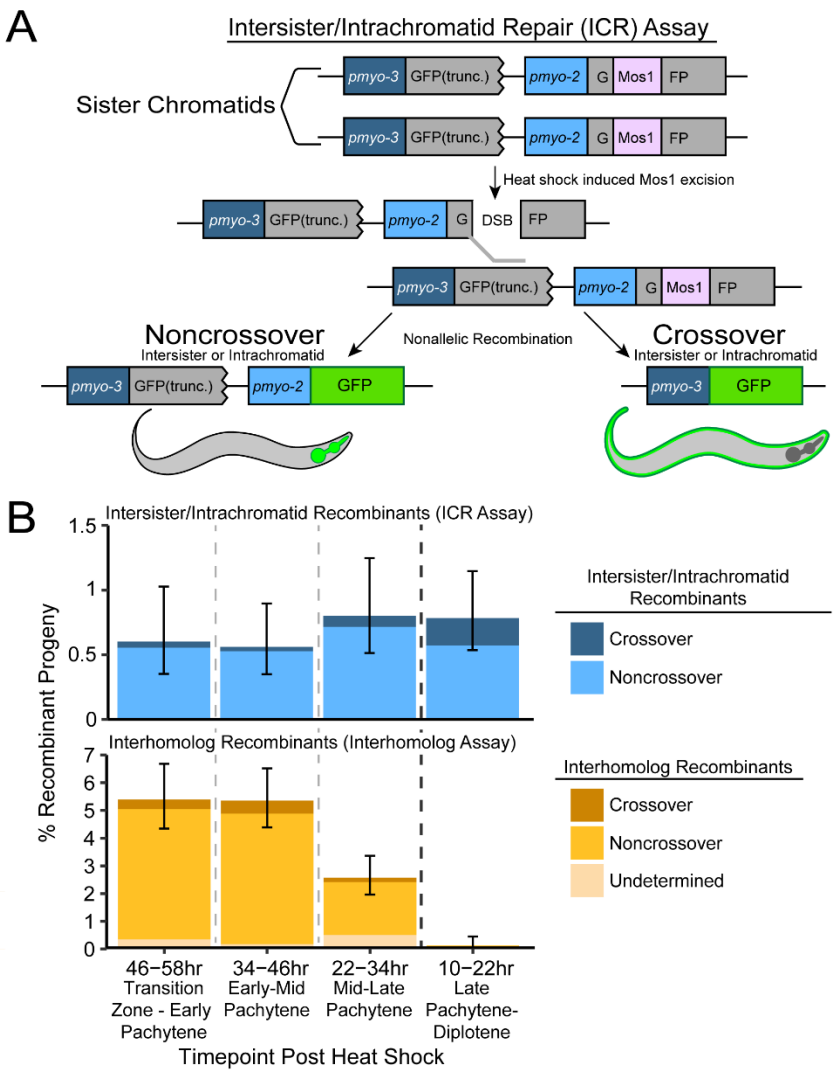

FIGURE 2.1. Intersister/intrachromatid repair can be engaged to resolve DSBs in meiotic prophase I. (A) Cartoon diagram of the intersister/intrachromatid repair (ICR) assay. The ICR assay is composed of two tandem GFP cassettes. The upstream GFP is driven by a *pmyo-3* (body wall) promoter and is truncated, while the downstream GFP is driven by a *pmyo-2* (pharynx) promoter and is interrupted by a Mos1 *Drosophila* transposon. Excision of Mos1 yields a single DSB. Repair of this DSB by intersister or intrachromatid recombination will yield GFP+ progeny. Figure S2.1A depicts how intrachromatid repair could be engaged within the ICR assay. See Figures S2.1B-S2.1D and S2.5 for confirmation of both ICR assay integration and noncrossover progeny genotypes. (B) Frequency of recombinant progeny identified in the ICR assay (top) and interhomolog assay (bottom) (Rosu *et al.* 2011). Total progeny scored n=ICR assay/interhomolog assay; 10-22hrs n=3317/1625; 22-34 hrs n=2372/1989; 34-46hrs n=3032/1721; 46-58hrs n=2159/1477; (Table S2.1). Stacked bar plots represent the overall percent of living progeny that exhibit the indicated recombinant phenotype within a specific time point following heat shock. Error bars represent 95% binomial confidence intervals. Dashed vertical lines delineate between time points scored, while the dark black dashed line delineates between the 'interhomolog window' (22-58hr post heat-shock) and 'non-interhomolog window' (10-22hr post heat-shock).

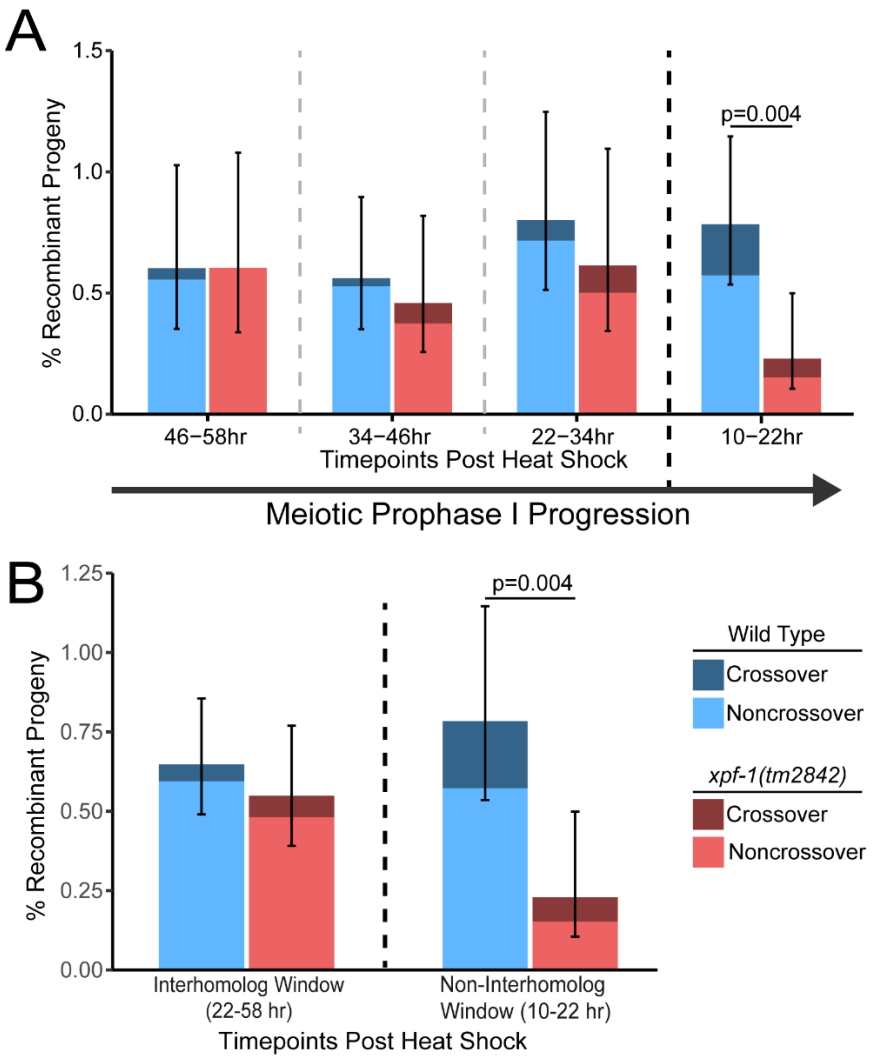

FIGURE 2.2. XPF-1 promotes intersister/intrachromatid repair in late meiotic prophase I. (A) Frequency of ICR assay recombinant progeny in wild-type and *xpf-1(tm2842)* mutants at each scored time point following heat shock. Total progeny scored n=wild-type/*xpf-1*; 10-22hrs n=3317/2618; 22-34 hrs n=2372/1793; 34-46hrs n=3032/2400; 46-58hrs n=2159/1819 (Tables S2.1 and S2.2). Both wild-type and *xpf-1(tm2842)* have similar rates of meiotic prophase progression (Figure S2.2A). (B) Frequency of recombinant progeny identified in the ICR assay within binned windows of prophase I defined by observation of recombinants in the Interhomolog assay. n=wild-type/*xpf-1*; interhomolog window n=7563/6012; non-interhomolog window n= 3317/2618; 22-34 hrs (Tables S2.1 and S2.2). Stacked bars represent the overall percent of living progeny that exhibit the indicated recombinant phenotype within the labeled time interval following heat shock. Error bars represent 95% binomial confidence intervals. P values were calculated by Fisher's Exact Test. Dashed vertical lines delineate between time points scored, while the dark black dashed line delineates between the 'interhomolog window' (22-58hr post heat-shock) and 'non-interhomolog window' (10-22hr post heat-shock).

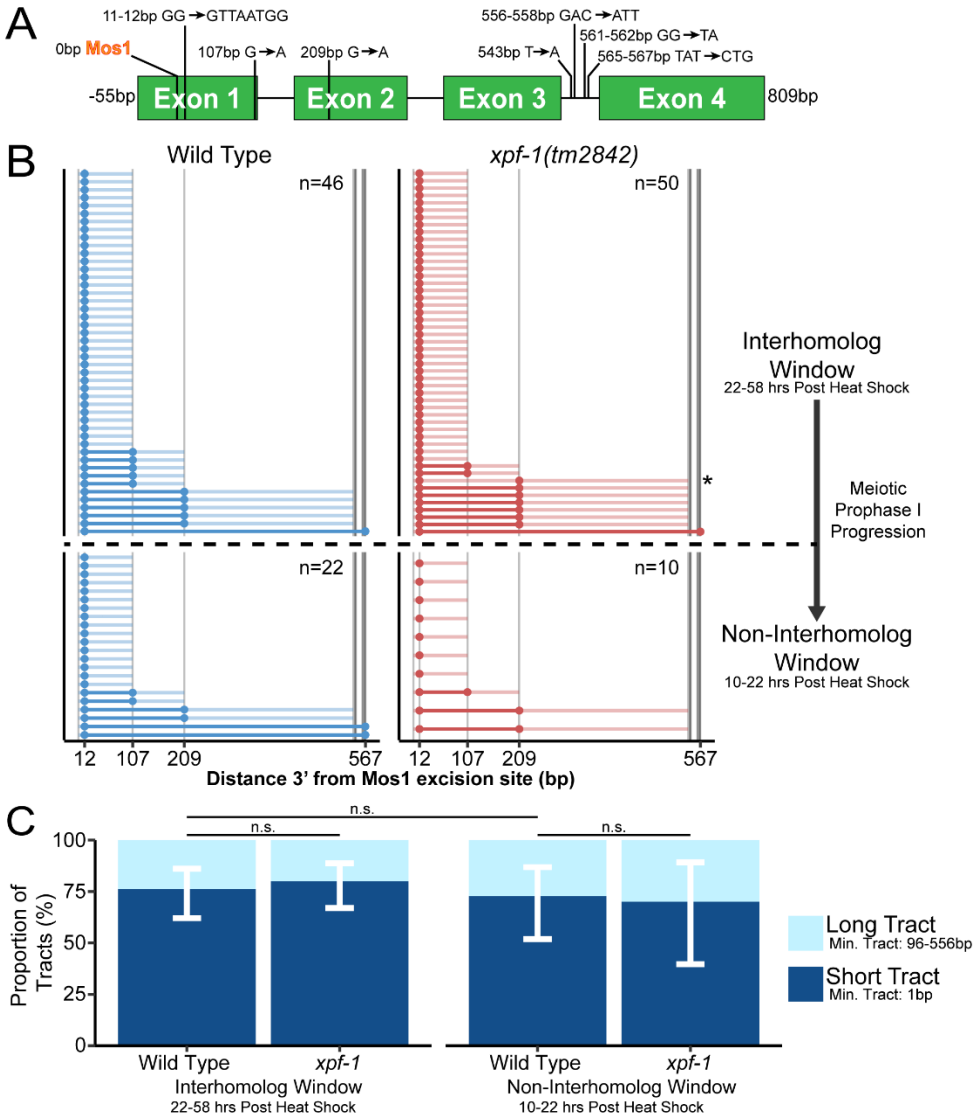

FIGURE 2.3. XPF-1 does not influence intersister/intrachromatid conversion tract length. (A) Scale cartoon of ICR assay GFP cassette with annotated polymorphisms. The polymorphisms of the *pmyo-2::*GFP sequence are listed to the left of each arrow, while the sequence of the *pmyo-3::GFP* polymorphism is listed to the right of each arrow. Positions of polymorphisms in bp are relative to the site of Mos1 excision. (B) Converted polymorphisms within ICR assay wild-type and *xpf-1(tm2842)* ICR assay noncrossover recombinant loci. Each horizontal line represents the sequenced locus of a single recombinant. High opacity lines connect contiguous converted polymorphisms within a single tract and represent minimum tract length, while the low opacity lines represent the range between converted and the most proximal non-converted polymorphism. See Figure S2.3 for crossover conversion tract data. (C) Stacked bar plots showing the proportion of 'short' (1bp minimum tract length) and 'long' (≥96bp minimum tract length). P values calculated by Fisher's Exact Test.

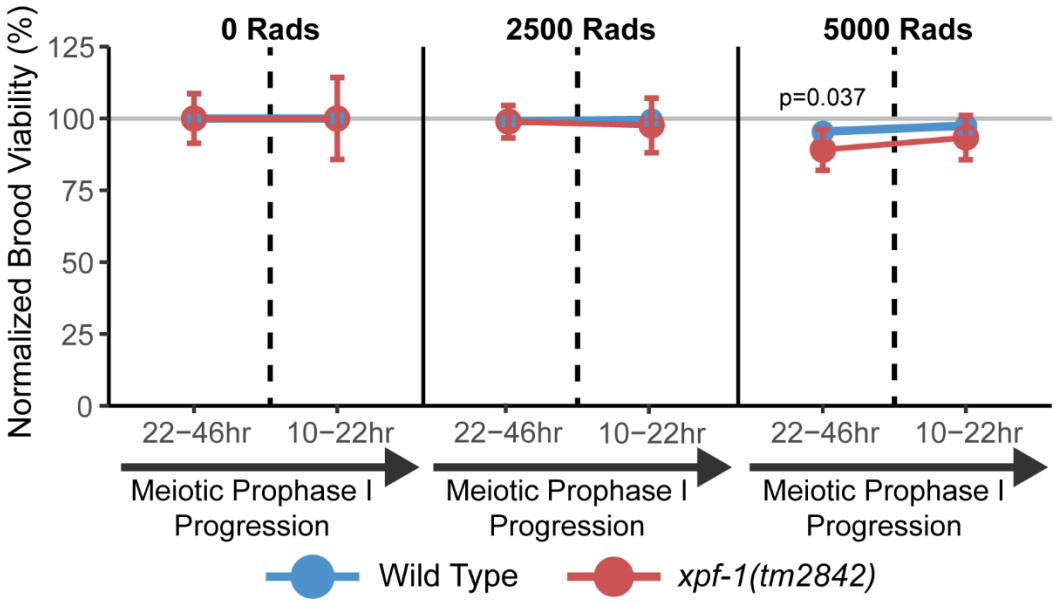

FIGURE 2.4. XPF-1 is not required for brood viability in response to ionizing radiation. Mean brood viability of young adult hermaphrodites exposed to 0, 2500, or 5000 Rads of ionizing radiation, normalized to the mean brood viability for each genotype and timepoint scored in the absence of ionizing radiation (0 Rads treatment). Broods of n=15 parent hermaphrodites of each respective genotype were scored for each irradiation treatment dose. Vertical dashed lines delineate between timepoints representing damage induced during the interhomolog window (22-46 hrs) and timepoints representing damage induced during the non-interhomolog window (10-22 hrs). Error bars represent standard deviation. Brood viabilities of each condition without normalization are displayed in Figure S2.2B.

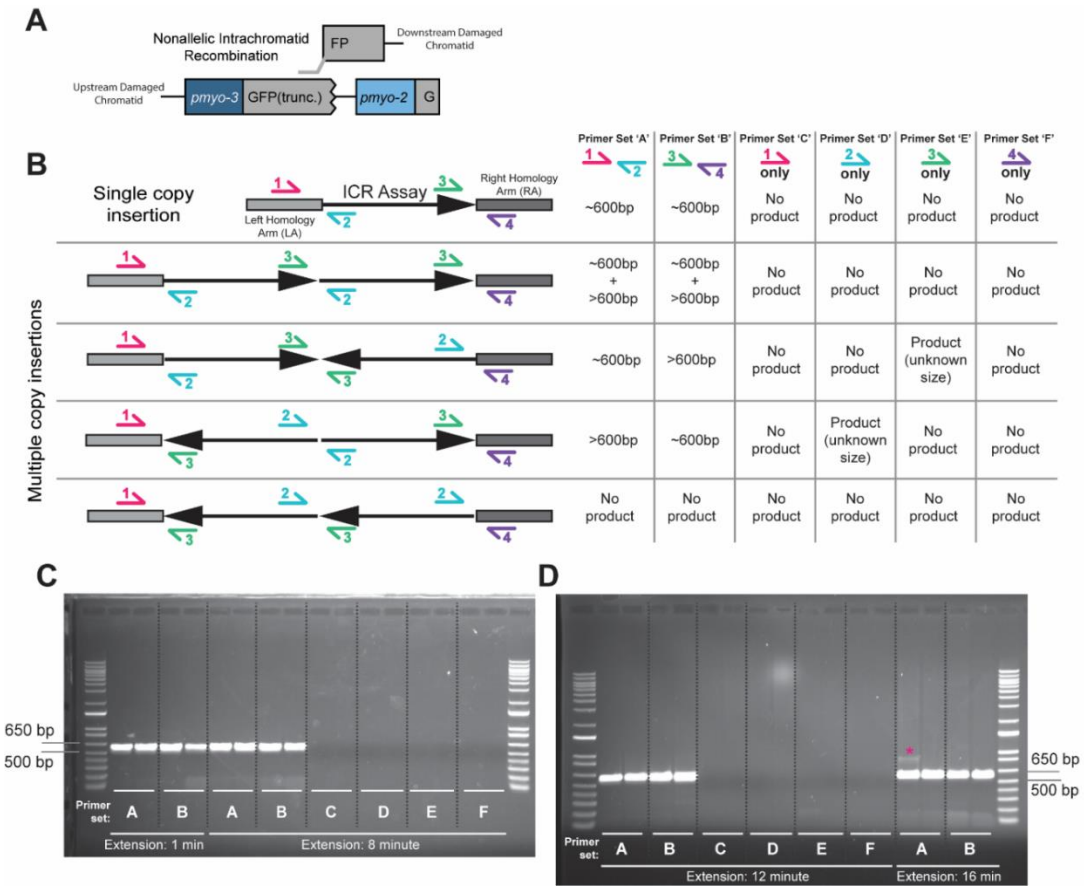

FIGURE S2.1. Confirmation of single copy integration of the intersister/intrachromatid repair (ICR) assay. Related to Figure 2.1. (A) Alternate mechanism for Figure 2.1A depicting DSB repair in the ICR assay by intrachromatid repair. If intrachromatid repair is engaged to resolve the DSB, the resected DNA strand would invade the GFP(trunc.) sequence upstream of the DSB within the damaged chromatid. (B) Diagram of the predicted ICR assay insertion targeted to *unc-5* on Chromosome IV of the *C. elegans* genome and schematics of possible single and tandem insertions of the ICR assay and PCR primer locations for detecting these possibilities. The grey boxes depict the upstream and downstream sequence used to target the ICR assay for integration at the *unc-5* locus, while the black arrow represents the ICR cassette. Primer 1 is a forward primer in the 3' end of the left homology arm on the *C.elegans* genome, and Primer 2 is a reverse primer positioned in the 5' end of the ICR cassette. Similarly, Primer 3 is a forward primer at the 3' end of the ICR cassette, while Primer 4 is a reverse primer positioned towards the 5' end of the right homology arm. Together, Primers 1+2 (Set 'A') and Primers 3+4 (Set 'B') span the genome-cassette junction on the 5' and 3' end of the cassette, respectively. Set 'A' amplicon's expected size is 596bp while set 'B' is 593bp. Reaction sets with primer(s) added in each set are detailed in the schematic table on the right. (C,D) PCR confirmation that ICR assay construct is integrated once with correct orientation at *unc-5*. PCRs were performed in duplicates with the indicated primer sets and extension times to detect any evidence of tandem insertions ≤10kb apart. Irrespective of the amplification duration, only set A or B produced a product and the observed product is consistent with the expected size (~600bp). None of the single primers amplified a product. One non-specific band is sporadically observed (red asterisk). Thus, the ICR assay is likely inserted as a single copy and in the correct orientation.

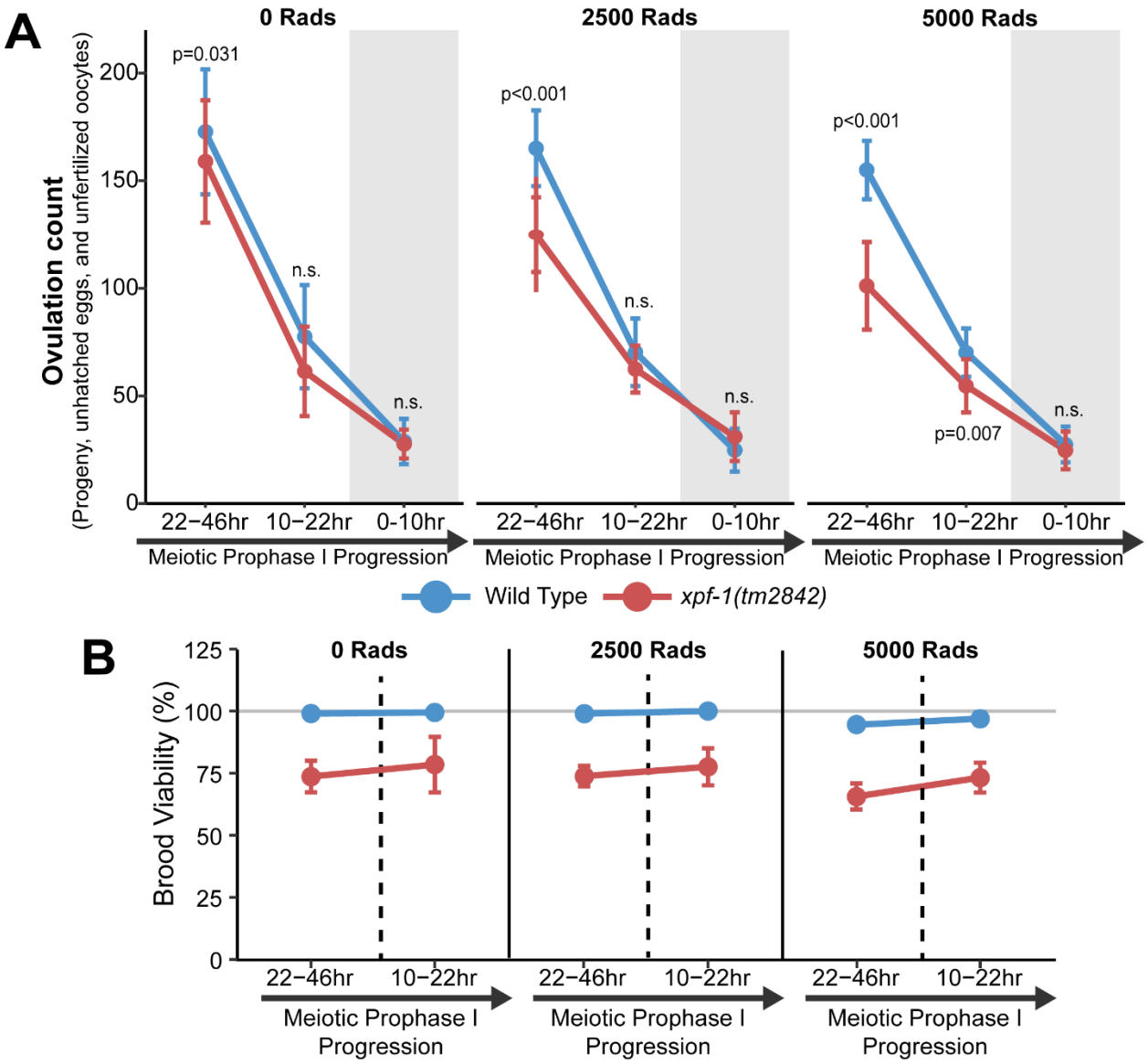

FIGURE S2.2. Ovulation rate and brood viability of wild type and *xpf-1* following ionizing radiation treatment. Related to Figure 2.4. Reproductive statistics of n=15 parent hermaphrodites of each respective genotype were scored for each irradiation treatment dose. (A) Mean ovulation counts (living progeny, unhatched eggs, and unfertilized oocytes) of young adult hermaphrodites exposed to 0, 2500, or 5000 Rads of ionizing radiation. Ovulation counts of n=15 parent hermaphrodites of each respective genotype were scored for each irradiation treatment dose. Shaded timepoints indicate timepoints not included in the interhomolog or non-interhomolog windows. Error bars represent standard deviations. p values were calculated by Mann-Whitney U test. (B) Mean brood viability of young adult hermaphrodites exposed to 0, 2500, or 5000 Rads of ionizing radiation. Vertical dashed lines delineate between timepoints representing the interhomolog window (22-46 hrs) and timepoints representing the non-interhomolog window (10-22hrs). Error bars represent standard deviations.

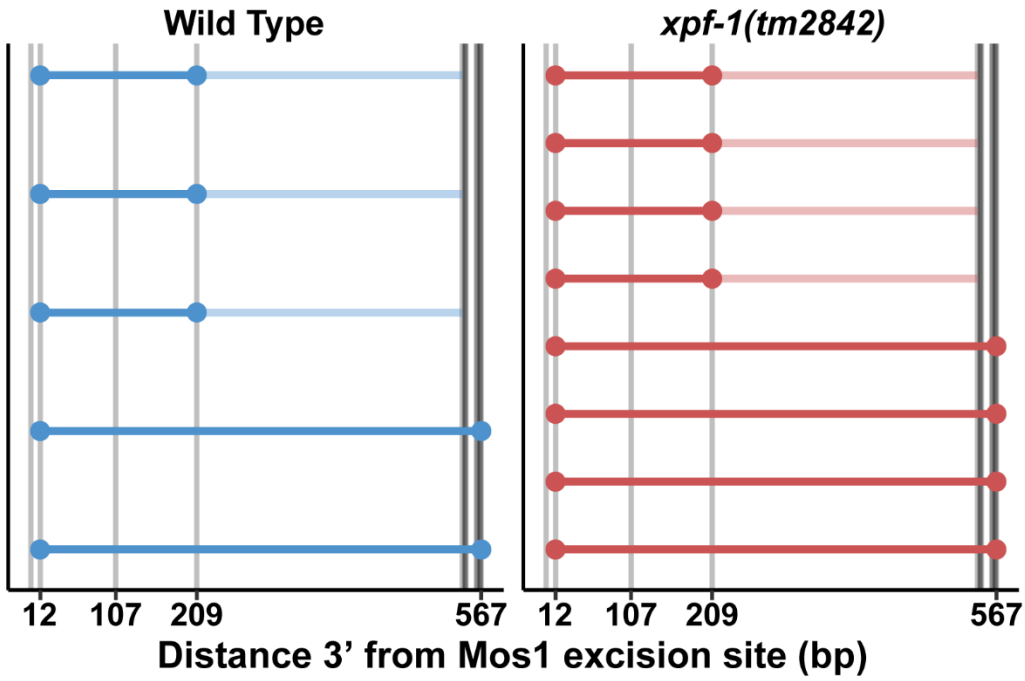

FIGURE S2.3. Intersister/intrachromatid crossover conversion tracts. Related to Figure 2.3. Converted polymorphisms within ICR assay wild-type and *xpf-1(tm2842)* ICR assay crossover recombinant loci. Each horizontal line represents the sequenced locus of a single recombinant. High opacity lines connect contiguous converted polymorphisms within a single tract and represent minimum tract length, while the low opacity lines represent the range between converted and the most proximal non-converted polymorphism.

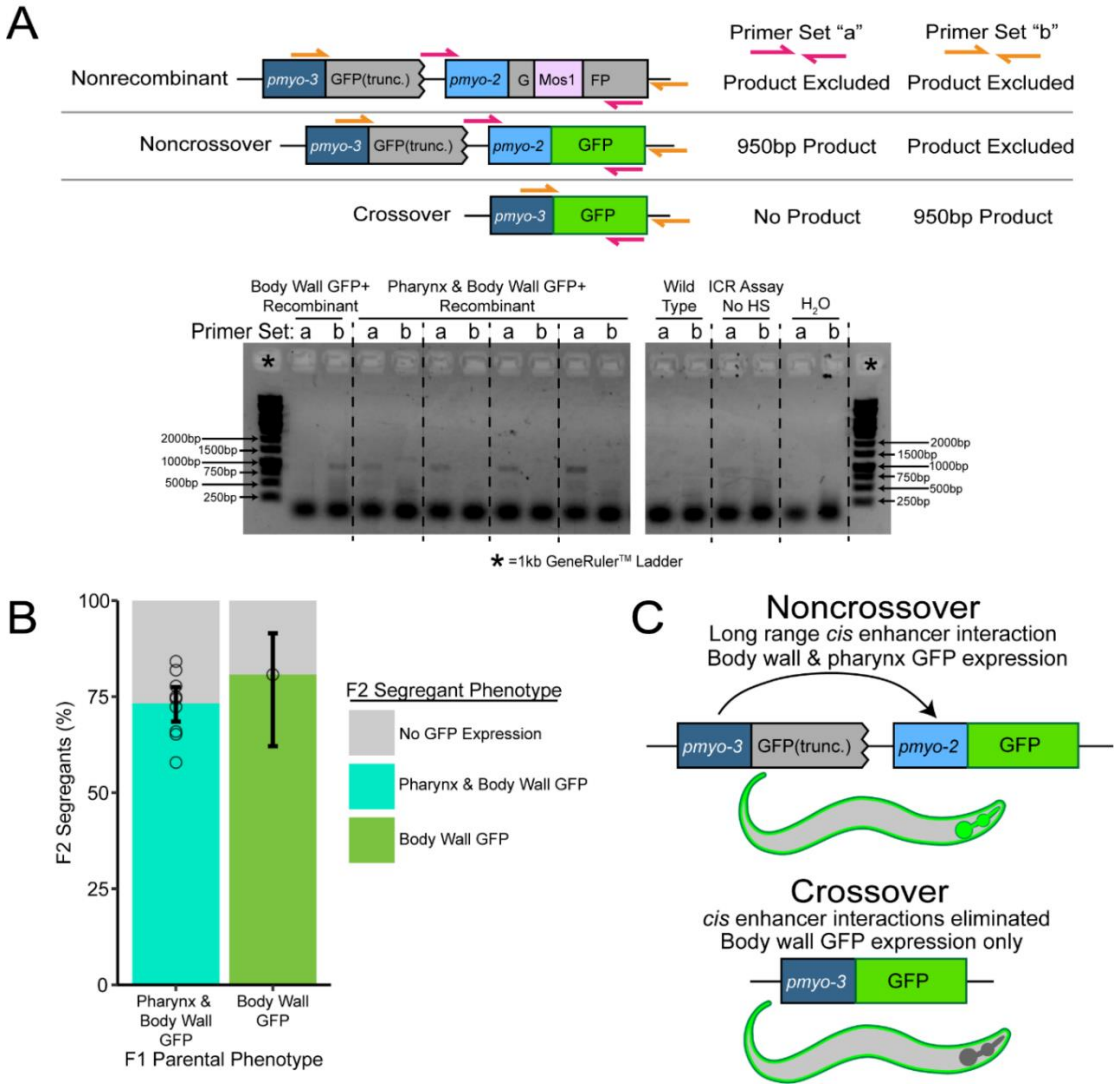

FIGURE S2.4. Intersister/intrachromatid repair assay recombinant progeny expressing GFP in multiple tissues are likely single noncrossovers events. Related to Figure 2.1, STAR methods. The design of the ICR assay predicts that recombinant progeny should exhibit either body wall or pharynx GFP expression (Figure 2.1A). However, the majority of pharynx GFP+ progeny also expressed GFP in the body wall. (A) PCR screening of recombinant progeny demonstrates expected crossover and noncrossover products in body wall and body wall + pharynx GFP expressing recombinants. 'PCR product restricted' indicates primer sets unable to amplify the given sequence based on the extension time of the PCR cycle. Wells in ethidium bromide stained agarose gel marked with asterisks were loaded with 1kb GeneRuler DNA ladder. (B) Both body wall and body wall + pharynx expression phenotypes segregate in ratios consistent with dominant Mendelian traits arising from a single locus (Chi Square Test of Goodness of Fit p>>0.05 for both parental phenotypes). Error bars represent 95% Binomial confidence intervals, bars indicate proportion of segregants of each phenotype across all broods scored. Circles represent the proportion of segregants with respective phenotypes from the broods of individual F1 recombinant hermaphrodites scored. (C) Body wall + Pharynx GFP expression likely arises from known long-range enhancer activity between *myo-2* and *myo-3* promoter sequences (Okkema *et al.* 1993).

Recombination Frequency Counts of ICR Assay in Wild-type					
Timepoint post Heat Shock	Total Progeny	Noncrossover (Intersister/ Intrachromatid)	Crossover (Intersister/ Intrachromatid)	% Recombinant Progeny (95% CI)	% Crossovers (95% CI)
10-22 hours	3317	19	7	0.78% (0.54-1.15%)	26.9% (13.7-46.1%)
22-34 hours	2372	17	2	0.80% (0.51-1.25%)	10.5% (2.9-31.4%)
34-46 hours	3032	16	1	0.56% (0.35-0.90%)	5.8% (1.0-27.0%)
46-58 hours	2159	12	1	0.60% (0.35-1.03%)	7.7% (1.4-33.3%)
58-70 hours	1190	8	1	0.76% (0.40-1.43%)	12.5% (2.0-43.5%)
Interhomolog Window (22-58 hours)	7563	45	4	0.65% (0.49-0.86%)	8.1% (3.2-19.2%)
Total	10880	64	11	0.69% (0.55-0.86%)	14.7% (8.4-24.4%)

Recombination Frequency Counts of Interhomolog Assay				
Timepoint post Heat Shock	Total Progeny	Total Recombinant Progeny (Crossover:Noncrossover/)	% Recombinant (95% CI)	% CO (95% CI)
10-22 hours	1625	2 (0:2)	0.12% (0.03-0.45%)	0% (0-65.8%)
22-34 hours	1989	51 (3:38)	2.56% (1.96%-3.36%)	7.3% (2.5-19.4%)
34-46 hours	1721	92 (8:81)	5.35% (4.38-6.51%)	8.9% (4.6-16.7%)
46-58 hours	1447	78 (5:68)	5.40% (4.34%-6.68%)	6.8% (3.0-15.1%)
58-70 hours	710	19 (2:15)	2.68% (1.72%-4.14%)	11.8% (3.3-34.3%)
Interhomolog Window (22-58 hours)	5157	221 (16:187)	4.29% (3.77-4.87%)	7.9% (4.9-12.4%)
Total	6782	223 (16:189)	3.29% (2.9-3.7%)	7.8% (4.9-12.3%)

TABLE S2.1. Recombination frequency counts of ICR assay and Interhomolog assay performed in wild-type animals. Related to Figure 2.1.

Recombination Frequency Counts of *xpf-1(tm2842)* ICR Assay					
Timepoint post Heat Shock	Total Progeny	Noncrossover (Intersister/ Intrachromatid)	Crossover (Intersister/ Intrachromatid)	% Recombinant (95% CI)	% CO (95% CI)
10-22 hours	2618	4	2	0.23% (0.11-0.50%)	33.3% (9.7-70%)
22-34 hours	1793	9	2	0.61% (0.34-1.1%)	18.2% (5.1-47.7%)
34-46 hours	2400	9	2	0.46% (0.26-0.82%)	18.2% (5.1-47.7%)
46-58 hours	1819	11	0	0.61% (0.39-1.1%)	0% (0-25.9%)
58-70 hours	813	4	0	0.49% (0.19-0.13%)	0% (0-49.0%)
Interhomolog Window (22-58 hours)	6012	29	4	0.55% (0.39-0.77%)	12.1% (4.8-27.3%)
Total	8630	33	6	0.45% (0.33-0.62%)	15.4% (7.2-29.7%)

TABLE S2.2. Recombination frequency counts of ICR assay performed in *xpf-1(tm8242)* animals. Related to Figure 2.2.

STAR Methods

RESOURCE AVAILABILITY

Lead Contact

Requests for further information, reagents, or resources should be directed to the lead contact, Diana E. Libuda (dlibuda@uoregon.edu).

Materials Availability

All strains and reagents generated for this dataset are available upon request.

Data and Code Availability

The published article includes all ICR assay datasets generated or analyzed in this study. Datasets detailing the per-hermaphrodite brood viability and ovulation counts used to generate Figure 24 and Supplemental Figure 2.2 are available upon request.

EXPERIMENTAL MODEL AND SUBJECT DETAILS

Caenorhabditis elegans

C. elegans strains used in this study were maintained at 15°C or 20°C on nematode growth medium (NGM) plates and were fed the OP50 *Escherichia coli* bacterial strain. Experiments

were performed only on *C. elegans* strains that had been maintained at 20°C for a minimum of two generations.

C. elegans strains used in this study were obtained from the *Caenorhabditis* Genetics Center (CGC) or were generated by crossing and/or CRISPR/Cas9 genome editing. Genetic crosses were performed by placing L4 stage male and hermaphrodite nematodes on NGM plates with OP50 at 20°C and screening for cross progeny after 3-4 days. Genotypes of strains generated by crossing were confirmed by PCR. DLW23 was generated by crossing YE57 males to DLW14 hermaphrodites. DLW82 was generated by crossing TG1660 hermaphrodites were crossed to YE57 males to generate males carrying the *xpf-1(tm2842)* allele balanced by the mIn1 balancer. These F1 *xpf-1*/*mIn1* males were then crossed to DLW14.

Strains generated by CRISPR/Cas9 genome editing were backcrossed to remove any off-target mutations that may have been incurred. The strain carrying the integrated intersister/intrachromatid repair (ICR) assay sequence, DLW14, was backcrossed three times to EN909.

METHOD DETAILS

Intersister/intrachromatid Repair (ICR) Assay Construction

The intersister/intrachromatid (ICR) assay plasmid pMG1 was constructed by integrating *pmyo-3* sequence from pCFJ104 (Jorgensen Lab) into the synthetic plasmid pDL23 (GenScript) by Gibson assembly (SGI-DNA) and PCR stitching. Plasmids pMG3 and pMG14 expressing Cas9 and CRISPR guide RNAs (pMG3 protospacer 5'-GAGUAGUUCAGGAUCUGG-3', pMG14 protospacer 5'-GUUGUUGAAUGUGGUAGAGG-3') targeting *unc-5* were generated by modifying pJW1285 (Jorgensen Lab) using PCR stitching. All plasmid sequences were confirmed by Sanger sequencing (Sequetech).

CRISPR/Cas9 C. elegans Genome Editing

CRISPR/Cas9 genome editing to integrate the ICR assay into the *unc-5* locus on Chromosome IV of the *C. elegans* genome was performed by injecting the germlines of adult N2 hermaphrodites with a plasmid mix (100ng/µL pMG1, 30ng/µL pMG3, 30ng/µL pMG14). F1 progeny of injected hermaphrodites were screened for uncoordinated movement (Unc) phenotypes, indicating editing at the *unc-5* locus. Integration of the ICR assay was confirmed by PCR, and the entire integrant construct sequence was confirmed by Sanger sequencing (Sequetech).

ICR assay copy number verification

DNA was isolated from adult DLW14 hermaphrodites using a DNeasy Blood and Tissue Kit (Qiagen) following a modified version of the Kaganovich Lab Genomic DNA Isolation using Qiagen kit protocol. 100 adult DLW14 hermaphrodites were placed into 200 µL of M9 buffer and were washed 2x by centrifuging at 2500xg for 1 minute, removing ~150µL of supernatant, and then resuspending the pelleted hermaphrodites in an additional ~150µL of M9 buffer. Following washes, the hermaphrodites were centrifuged at 2500xg for 1 minute, ~180µL of supernatant was removed, and the hermaphrodites were resuspended in 200µL ATL buffer (DNeasy kit) and then were frozen at -80°C overnight. The next day, the hermaphrodites were freeze thawed 3x using liquid Nitrogen and a 65°C water bath. 20µL of Proteinase K (New England Biolabs) was added and the lysed worm solution was incubated at 56°C for 2 hours. 8uL of RNAse A (Sigma Aldrich) was added and the solution was incubated at room temperature for 5 minutes. 200µL of AL buffer (DNeasy kit) and the solution was incubated for 10 minutes at 56°C. 200µL of 100% ethanol was then added, and the solution was vortexed. Remaining steps of the protocol followed the published Qiagen kit instructions. All DNA was eluted from a single column in 50µL of ddH_2O and was stored at -20°C until used.

The schematic to detect duplications is outlined in Figure S2.1. The primers used are as follows: Primer 1 (5'- GCGGACTCCTCTCGGATAGT-3'), Primer 2 (5'- GGGCGTGGAACTCCTTATCA-3'), Primer 3 (5'- TGAGGTACCAGTTCAGAGGA-3'), Primer 4 (5'- TGAAGTCCGCTATTACAATGAAGT-3'). Primer 1 and 2 amplifies the left genome-construct junction, while primers 3 and 4 amplifies the right genome construct junction. The annealing temperatures were determined empirically. Each 8 mL reaction PCR mix contained: 1x buffer (10x: 450mM Tris-HCl pH 8.8, 110mM $(NH_4)_2SO_4$, 45mM $MgCl_2$, 67mM b-mercaptoethanol, 44mM EDTA, 10mM each: dATP, dTTP, dGTP, and dCTP, and 1.13mg/ml non-acetylated BSA), 12.5mM Tris base, 0.2mM of each primer, 0.25U of Taq, and 0.05U of Pfu polymerase. The reaction mixture was then subjected to extension times, as denoted in Figure S2.1. In independent assays, this DNA-PCR reaction mix produce amplicons of >10kb reliably.

Intersister/intrachromatid Repair (ICR) Assay

Parent (P0) hermaphrodites for ICR assays were generated by crossing. L4 stage P0 hermaphrodites were picked 16-18 hours before heat shock and incubated overnight at 15°C. To improve progeny yields at later timepoints, where the abundance of hermaphrodite sperm limits

brood size, N2 young adult males were added to these plates in some replicates of the ICR assay. Heat shock was performed by placing P0 hermaphrodites in an air incubator (refrigerated Peltier incubator, VWR Model VR16P) at 34°C for one hour. Following heat shock, hermaphrodites were incubated at 20°C for 10 hours and then were picked to individual NGM plates seeded with OP50. Data in Tables S2.1 and S2.2 contain data for time courses with 12 hour time points and pooled times points (details outlined below).

For the time course with 12 hour time points (10-22 hrs, 22-34 hrs, 34-46 hrs, 46-58 hrs, and 58-70hrs): After 12 hours (for which the plate contained F1 progeny for the 10-22 hr time point), each P0 hermaphrodite was transferred to a new NGM plate. P0 hermaphrodites were similarly passaged to new NGM plates every 12 hours for a total of 6 transfers. NGM plates with P0 hermaphrodites were maintained at 20°C, while NGM plates with F1 progeny only were placed at 15°C.

For time course with pooled time points encompassing the non-interhomolog window (10-22 hrs) and the interhomolog window (22-58 hrs): After 12 hours (for which the plate contained F1 progeny for the 10-22 hr time point), each P0 hermaphrodite was transferred to a new NGM plate for 36 hrs. After this 36 hrs (for which the plate contained F1 progeny for the 22-58 hr time point) P0 hermaphrodites were discarded. NGM plates with P0 hermaphrodites were maintained at 20°C, while NGM plates with F1 progeny only were placed at 15°C.

F1 progeny were maintained at 15°C for 36-48 hours. ~18 hours before scoring for fluorescence, F1 progeny were placed in a 25°C incubator to enhance GFP expression. F1 progeny were scored for fluorescence using an Axio Zoom V16 fluorescent dissection microscope (Zeiss). F1s that expressed GFP in the pharynx, body wall, or both were transferred to individual plates for single worm lysis (as described in Intersister/intrachromatid Repair (ICR) Assay Conversion Tract Analysis methods). All other progeny were removed from the plate and discarded. If all F1 progeny were in larval developmental stages at the time of scoring, dead eggs and unfertilized oocytes on the plates were additionally quantified.

We noted that the majority of recombinant progeny with *pmyo-2* (pharynx) GFP expression also exhibited *pmyo-3* (body wall) GFP fluorescence. To determine if this expression pattern arose from a single locus, we assayed the segregation of GFP phenotypes in F2 progeny arising from pharynx and body wall GFP expressing ICR assay progeny (Figure S2.5). The ratios of segregation were consistent with Mendelian inheritance of a single locus (Figure S2.5B). PCR

genotyping of progeny with both *pmyo-2* (pharynx) and *pmyo-3* (body wall) GFP expression produced products consistent with the presence of noncrossover/intrachromatid recombination events specifically (Figure S2.5A). Previous work has demonstrated that both the *pmyo-2* and *pmyo-3* promoters contain enhancers that alter the specificity of the other respective promoter's expression pattern (Okkema *et al.* 1993). We therefore suggest that recombinants with both pharynx and body wall GFP expression patterns arise from the enhancer activity of the upstream *myo-3* promoter in noncrossover recombinants (Figure S2.5C). Progeny exhibiting both pharynx and body-wall GFP expression were scored as noncrossover/chromatid recombinants in all recombination frequency calculations.

We also found that a fraction of F1 ICR assay progeny exhibited weak fluorescence phenotypes only in a portion of the pharynx, body wall, or both tissues. These progeny were transferred to individual plates and maintained at 20°C. F2 progeny were visually screened for inheritance of a fluorescent phenotype. No partial tissue fluorescent F1 was ever observed to produce fluorescent progeny, indicating that these fluorescent phenotypes are a product of somatic Mos1 excision and subsequent DNA repair and are not the result of bona fide meiotic recombination. Partially fluorescent F1s were categorized as nonrecombinant when determining frequencies of meiotic sister chromatid recombination.

The ICR assay was replicated a minimum of three times for each genotype.

While performing ICR assays in N2 and *xpf-1(tm2842)* backgrounds in which the *unc-5(lib1)* and KrIs14 transgenes were inherited from a hermaphrodite, we observed a spontaneous change in results encompassing: (1) reduced recombinants at the 10-22 hour timepoint following heat shock; and, (2) severe embryonic lethality amongst progeny laid 22+ hours following heat shock. We were able to successfully restore function of the ICR assay by performing cross schemes to ensure that the parent hermaphrodites heat shocked in the ICR assay inherited their *unc-5(lib1)* allele and KrIs14 transgene from a male. We therefore recommend that future ICR assays only be performed on parent hermaphrodites who inherit these transgenes from a male. For descriptions of both cross schemes, see 'Crosses to Generate Strains for the ICR Assay'.

Crosses to Generate Strains to Perform the ICR Assay

1) N2 (wild-type) with ICR assay transgenes inherited from hermaphrodite: Parent hermaphrodites were generated by crossing: (1) DLW14 hermaphrodites x N2 males to generate F1 *unc-5(lib1)*/+ IV; KrIs14/+ V hermaphrodites.

2) N2 (wild-type) with ICR assay transgenes inherited from male: Parent hermaphrodites were generated by crossing: (1) N2 males x DLW14 hermaphrodites to generate F1 *unc-5(lib1)*/+ IV; KrIs14/+ V males, (2) F1 males x CB791 hermaphrodites to generate *unc-5(lib1)*/*unc-5(e791)* IV; KrIs14/+ V hermaphrodites.
3) *xpf-1* with ICR assay transgenes inherited from male: Parent hermaphrodites were generated by crossing: (1) YE57 males x TG1660 hermaphrodites to generate *xpf-1(tm2842)*/mIn1 II males, (2) F1 males x DLW75 hermaphrodites to generate *xpf-1(tm2842)*/mIn1 II; *unc-5(lib1)*/+ IV; KrIs14/+ V males, (3) F2 males x DLW82 hermaphrodites to generate *xpf-1(tm2842)*/ *xpf-1(tm2842)* II; *unc-5(lib1)*/*unc-5(e791)* IV; KrIs14/+ V hermaphrodites.

Intersister/intrachromatid Repair (ICR) Assay Conversion Tract Analyses

Genomes of fluorescent recombinant F1 progeny or the fluorescent F2 segregants of isolated recombinant F1 progeny from ICR assays were extracted by single worm lysis. Individual hermaphrodites were picked into single 10μL aliquots of worm lysis buffer (50mM KCl, 10mM TrisHCl pH 8.2, 2.5mM $MgCl_2$, 0.45% IGEPAL, 0.45% Tween20, 0.3μg/μL proteinase K in ddH_2O). Each suspended worm was then serially frozen and thawed three times by immersion in a 95% ethanol and dry ice bath followed by a 65°C water bath. Each lysate was incubated at 60°C for one hour and then incubated at 95°C for 15 minutes to heat inactivate proteinase K. Final lysates were diluted with 10μL of ddH_2O.

Recombinant loci were PCR amplified using OneTaq 2x Master Mix (New England Biolabs). Specificity of PCR reactions was determined by gel electrophoresis. Desired amplicons were extracted by PCR purification (Zymo PCR Purification Kit) if only one band was observed by electrophoresis, or gel extraction (Thermo Scientific Gel Extraction Kit) if multiple amplicons were observed. Purified amplicons were submitted for Sanger sequencing (Sequetech) with sequencing primers specific to the locus (see Key Resources table). Sequencing files were aligned to reference GFP sequences with Benchling alignment software to detect converted polymorphisms.

The most efficient and effective primer set for amplifying *pmyo-2* (pharynx) GFP+ loci was DLO822 + DLO823. In addition, *pmyo-2* (pharynx) GFP+ loci were amplified using DLO640 + DLO641. The most efficient and effective primer set for amplifying crossover loci was DLO824+DLO546.

Not all fluorescent progeny lysed were able to be PCR amplified or successfully sequenced. We were able to completely sequence 68/87 wild-type NCO recombinants, 5/14 wild-type CO recombinants, 60/70 *xpf-1(tm2842)* NCO recombinants, and 10/14 *xpf-1(tm2842)* CO recombinants.

Interhomolog Assay

The interhomolog assay was replicated following the protocol outlined in Rosu, Libuda, and Villleneuve *Science* 2011. In brief, parent (P0) hermaphrodites for interhomolog assays were generated by crossing AV554 males to CB791 hermaphrodites to generate *dpy-13(e184sd) unc-5(ox171::Mos1)/+ unc-5(e791)* IV; KrIs14/+ V F1 progeny. Heat shock was performed by placing P0 hermaphrodites in an air incubator (refrigerated Peltier incubator, VWR Model VR16P) at 34°C for one hour. Following heat shock, hermaphrodites were incubated at 20°C for 10 hours and then were picked to individual NGM plates seeded with OP50. After 12 hours each P0 hermaphrodite was transferred to a new NGM plate. P0 hermaphrodites were similarly passaged to new NGM plates every 12 hours for a total of 6 transfers. Following transfer, the number of eggs laid by each hermaphrodite was scored. ~48-60 hours following transfer, F1 progeny were scored for recombinant phenotypes. For details in determining noncrossover and crossover progeny, see Rosu, Libuda, and Villeneuve *Science* 2011.

Ionizing radiation treatment and quantification of both brood viability and ovulation rates

L4 stage hermaphrodites were picked 16-18 hours before irradiation and incubated overnight at 15°C. Irradiation was performed using a ^{137}Cs source (University of Oregon). Following irradiation, hermaphrodites were singled to individual NGM plates with OP50 lawns and were maintained at 20°C. At 10hrs and 46hrs following irradiation, the hermaphrodites were transferred to new NGM plates seeded with OP50. The proportion of hatched F1 progeny, dead eggs, and unfertilized oocytes were scored 36-48 hours following hermaphrodite removal. Brood viability was calculated as (Hatched Progeny) / (Hatched Progeny + Dead Eggs). Normalized brood viability was calculated by dividing the brood viability of each irradiated hermaphrodite within each scored timepoint (10-22 hrs, 22-46 hrs) by the mean brood viability of unirradiated hermaphrodites. Brood viability experiments were replicated three times for each genotype and irradiation dose, with the broods of n=5 hermaphrodites scored per replicate. To ensure that ovulation was similar between all genotypes assessed, progeny and unfertilized oocytes laid 0-10

hrs following irradiation treatment were additionally scored but were not included in brood viability calculations or analyses.

Quantification of ICR assay F2 segregant phenotypes

Fluorescent recombinant ICR assay progeny were identified following the protocols described above using a total of 28 parent hermaphrodites generated through cross scheme #2. However, instead of performing the full time course, parent hermaphrodites were discarded following the 22-34hr timepoint. n=11 F1 progeny were identified that expressed GFP both in the body wall and in the pharynx and n=1 F1 progeny was identified that expressed GFP in the body wall only. Each of these recombinants was placed on an individual NGM plate seeded with OP50 and was incubated at 20°C. Each recombinant was monitored daily to determine if it had laid eggs. If >30 eggs were visible on the plate or the F1 recombinant was visually egg laying defective, identified by internal egg hatching inside of the F1, the F1 recombinant was lysed for PCR analysis (Figure S2.4A). F2 segregants were maintained at 20°C for an additional 24 hours, and then were scored for fluorescent phenotypes using an Axio Zoom V16 fluorescent dissection microscope (Zeiss).

QUANTIFICATION AND STATISTICAL ANALYSIS

All statistics were calculated in R (v4.0.3). Data wrangling was performed using the Tidyverse package (v1.3.0). Proportions of recombinant intersister/intrachromatid repair assay or interhomolog repair assay progeny and proportions of ‘short’ and ‘long’ conversion tracts (Figure 2.1B, Figure 2.2, Figure 2.3C) were compared using Fisher’s Exact Test. Brood viability between timepoints within the same genotype and between genotypes within the same timepoints were compared using Mann-Whitney U tests (Figure 2.4). Segregation ratios of F2 progeny from F1 ICR assay recombinants (Figure S2.4B) were compared to an expected distribution for mendelian segregation of a dominant phenotype arising from a single locus (75% parental phenotype, 25% no GFP expression) by Chi Square Tests of Goodness of Fit. For all tests, statistical significance was determined as a p value equal to or less than 0.05 following correction for multiple comparisons, if applicable. 95% confidence intervals (Figure 2.1B, Figure 2.2, Figure 2.3C, Figure S2.4B, Table S2.1, Table S2.2) were calculated using the DescTools package (v0.99.30).

Table S2.3 Key Resources

REAGENT or RESOURCE	SOURCE	IDENTIFIER
Bacterial and Virus Strains		
OP50 *Escherichia coli*	CGC	OP50
TOP10 *Escherichia coli* chemically competent cells	Invitrogen	C4040-06
Chemicals, Peptides, and Recombinant Proteins		
≥99.8% pure Tris base (Tris[hydroxymethyl]aminomethane or Trimethamine)	Bio-Rad	Cat#1610716EDU; CAS 77-86-1
Dimethylsulfoxide ≥99.9% (DMSO)	VWR	97063-136; CAS 67-68-5
GeneRuler 1kb Ladder	ThermoFisher Scientific	Cat#SM0311
Hydrochloric Acid, Certified ACS Plus, 36.5 to 38.0% (HCl)	ThermoFisher Scientific	40233; CAS 7647-01-0
IGEPAL® CA-630	Sigma-Aldrich	Cat#I8896; CAS 9002-93-1
Magnesium chloride (MgCl2)	Sigma-Aldritch	Cat#M8266; CAS 7786-30-3
OneTaq Quick-Load 2X Master Mix w/ Standard Buffer	New England Biolabs	Cat#M0486
Potassium Chloride (KCl)	VWR	Cat#MK6858-04; CAS 7447-40-7
Proteinase K, Molecular Biology Grade	New England Biolabs	Cat#P8107S
RNAse A	Sigma Aldrich	Cat#R6148
Tween® 20	Sigma-Aldrich	Cat#P9416; CAS 9005-64-5
Tris-HCl	Sigma	Cat#93363, CAS 1185-53-1
Ammonium Sulfate $(NH_4)_2SO_4$	Sigma	Cat#A4915, CAS 7783-20-2
Magnesium chloride (MgCl2)	Sigma	Cat#M9272, CAS 7791-18-6
β-mercaptoethanol	Sigma	Cat#63689, CAS 60-24-2
EDTA	Sigma	Cat#03690, CAS 60-00-4
dNTPs	Sigma	Cat#DNTP100A
non-acetylated BSA	Ambion/Life Technologies	Cat#AM2616
Tris base	Fluka	Cat#08656
Cloned Pfu DNA polymerase	Agilent	Cat#600154
Kapa Taq polymerase	Kapa Biosystems	Cat#BK1002

Table S2.3 Key Resources, continued

REAGENT or RESOURCE	SOURCE	IDENTIFIER
Experimental Models: Organisms/Strains		
C. elegans: Strain AV554 (*dpy-13(e184sd) unc-5(ox171::Mos1)*/ nT1 (*qIs51*) IV; *KrIs14(Phsp-16.48*::MosTransposase; *lin-15B*; *Punc-122*::GFP) / nT1 (*qIs51*) V)	Villeneuve Lab	AV554
C. elegans: Strain CB791 (*unc-5(e791)* IV)	Caenorhabditis Genetics Center	CB791
C. elegans: Strain DLW14 (*unc-5(lib1* [intersister repair assay *Pmyo-3*::GFP(-) + *unc-119(+)* + *Pmyo-2::GFP(Mos1)*]) IV; *KrIs14(Phsp-16.48*::MosTransposase; *lin-15B*; *Punc-122*::GFP) V)	This Study	DLW14
C. elegans DLW75: Strain (*xpf-1(tm2842)* II; *unc-5(lib1* [intersister repair assay *Pmyo-3*::GFP(-) + *unc-119(+)* + *Pmyo-2::GFP(Mos1)*]) IV; *KrIs14(Phsp-16.48*::MosTransposase; *lin-15B*; *Punc-122*::GFP) V)	This Study	DLW75
C. elegans: Strain DLW82 (*xpf-1(tm2842)* II; *unc-5(e791)* IV)	This Study	DLW82
C. elegans: Strain EN909 (*KrIs14(Phsp-16.48*::MosTransposase; *lin-15B*; *Punc-122*::GFP) V)	CGC	EN909
C. elegans: Strain N2 (Wild-type)	CGC	N2
C. elegans: Strain TG1660 (*xpf-1(tm2842)* II)	CGC	TG1660
Oligonucleotides		
DLO546 (5'-AGTTGGTAATGGTAGCGACC-3')	This Study	DLO546
DLO638 (5'-ACGAAGGAGGGTAGGTGTTG-3')	This Study	DLO638
DLO640 (5'-TTGAGCCGGCTTCTTCACTA-3')	This Study	DLO640
DLO641 (5'-TTAGAAGTCAGAGGCACGGG-3')	This Study	DLO641
DLO695 (5'-TGGCCAAAGGACCCAAAG-3')	This Study	DLO695
DLO822 (5'-ATTTTAACCCTCGGGGTACG-3')	This Study	DLO822
DLO823 (5'-TCCATGCCATGTGTAATCCCA-3')	This Study	DLO823
DLO824 (5'-AGATCCATCTAGAAATGCCGGT-3')	This Study	DLO824
Recombinant DNA		
pMG1	This Study	pMG1
pMG3	This Study	pMG3
pMG13	This Study	pMG13
pDL23	GenScript	pDL23
pJW1285	Jorgensen Lab	pJW1285
pCFJ104	Jorgensen Lab	pCFJ104

Table S2.3 Key Resources, continued

REAGENT or RESOURCE	SOURCE	IDENTIFIER
Software and Algorithms		
Benchling Align Sequences Tool	Benchling	https://help.benchling.com/en/
DescTools [v0.99.37]	R package	https://cran.r-project.org/web/packages/DescTools/index.html
Illustrator	Adobe	https://www.adobe.com/
reshape2 [v1.4.4]	R package	https://cran.r-project.org/web/packages/reshape2/index.html
RStudio	RStudio Team	https://rstudio.com/
Tidyverse	R package	https://www.tidyverse.org/
Other		
QIAquick PCR Purification Kit	Qiagen	28104
Monarch® PCR & DNA Cleanup Kit	New England Biolabs	T1030S
DNeasy Blood and Tissue Kit	Qiagen	69504
GeneJET Gel Extraction Kit	Thermo Fisher	R1341
Gibson Assembly HiFi 1 Step Master Mix	SGI-DNA	GA1100-03

CHAPTER III

BRCA1/BRC-1 and SMC-5/6 REGULATE DNA REPAIR PATHWAY ENGAGEMENT IN *C. ELEGANS* MEIOSIS

Erik Toraason, Alina Salagean, David Almanzar, Ofer Rog, and Diana E. Libuda. *In preparation.*

Abstract

Preservation of genome integrity between generations is vital for reproductive success. During meiosis, the tumor suppressor BRCA1/BRC-1 and structural maintenance of chromosomes 5/6 (SMC-5/6) complex are known to promote high fidelity DSB repair, but the specific DNA repair outcomes these proteins regulate remain unknown. To define the roles of BRC-1 and SMC-5/6 in regulating meiotic DSB repair, we exploited the nematode *Caenorhabditis elegans* to perform a combination of genetic, cytological, and functional DNA repair in *brc-1* and *smc-5* mutants. We demonstrate that both BRC-1 and SMC-5/6 repress intersister crossover recombination, but show that BRC-1 is uniquely required for long intersister/intrachromatid noncrossover gene conversion. We further provide evidence that BRC-1 specifically inhibits error prone repair of DSBs induced at mid pachytene. By assessing the susceptibility of *brc-1, smc-5,* and *smc-5;brc-1* mutants to exogenous DNA damage, we show that meiotic cells become more dependent upon BRC-1 and SMC-5/6 to repair DSBs in late meiotic prophase I. These experiments further reveal that functional BRC-1 enhances DSB repair defects in *smc-5* mutants, in part via its role in repressing theta mediated end joining. Taken together, our study illuminates functions of BRC-1 and SMC-5/6 which regulate DNA repair outcomes in the immortal germline.

Introduction

Meiosis is the specialized form of cell division by which most sexually reproducing organisms generate haploid gametes. In a diploid organism, each meiotic cell begins prophase I with four copies of the genome – two homologous chromosomes and an identical replicate of each homolog called a sister chromatid. As mutations incurred in the gamete genome may have deleterious impacts on resultant progeny, it is crucial that genome integrity be maintained during meiosis. Despite this risk, meiotic cells intentionally induce DNA double strand breaks (DSBs) by the highly conserved topoisomerase-like protein Spo11 (Keeney *et al.* 1997). A limited subset

of DSBs must engage the homologous chromosome as a recombination partner and be resolved as a crossover event, which forges a physical connection between homologs that facilitates accurate chromosome segregation at the meiosis I division. DSBs are incurred in excess of the number of eventual crossovers, therefore other pathways must be utilized to repair residual DSBs. How meiotic cells regulate repair pathway engagement to accurately and efficiently resolve DSBs is a critical question in the field of genome integrity.

As the number of interhomolog crossover events are limited, the majority of meiotic DSBs are repaired through interhomolog noncrossover recombination mechanisms (Hunter 2015). Evidence in *Drosophila* has suggested that joint molecule intermediates between homologous chromosomes can be processed to generate noncrossover recombination products (Crown *et al.* 2014). Work in budding yeast, mammals, and *Arabidopsis*, however, indicates that the majority of interhomolog noncrossovers are generated via synthesis-dependent strand annealing (SDSA) with the homolog (Hunter 2015). In SDSA, the resected end of the DSB invades a repair template, synthesizes new sequence, dissociates from its repair template, and finally utilizes the synthesized sequence to anneal to the other resected end of the DSB. Only one end of the DSB invades a repair template during single SDSA, while double SDSA occurs when both DSB ends synthesize new sequence from a repair template before annealing.

Meiotic DSBs may also be resolved by recombination with the sister chromatid (Goldfarb and Lichten 2010; Toraason *et al.* 2021a; Almanzar *et al.* 2021). In budding yeast, intersister recombination is disfavored so as to promote DSB repair with the homologous chromosome (Humphryes and Hochwagen 2014). In metazoan meiosis, however, the engagement of intersister repair has proven challenging to detect and quantify. While recombination between polymorphic homologs may be readily studied via sequence conversions in final repair products, the near identical sequences of sister chromatids preclude the detection of intersister recombination by sequencing approaches. Recently, two methods have been developed in the nematode *Caenorhabditis elegans* to enable direct detection of homolog-independent meiotic recombination (Toraason *et al.* 2021a; Almanzar *et al.* 2021). Toraason *et al.* 2021a constructed an intersister/intrachromatid repair (ICR) assay, which exploits nonallelic recombination at a known locus in the genome to identify homolog-independent repair events in resultant progeny. Almanzar *et al.* 2021 designed an EdU labeling assay to cytologically identify sister chromatid exchanges (SCEs) in compacted chromosomes at diakinesis. Together, these studies

demonstrated that: 1) homolog-independent meiotic recombination occurs in *C. elegans*; 2) the sister chromatid and/or same DNA molecule is the exclusive recombination repair template in late prophase I; and, 3) intersister crossovers are rare and represent a minority of homolog-independent recombination products (Toraason *et al.* 2021a; Almanzar *et al.* 2021).

While meiotic cells primarily utilize recombination to resolve DSBs, error prone repair pathways are also available in meiosis to repair DSBs at the expense of introducing *de novo* mutations (Gartner and Engebrecht 2022). These error-prone mechanisms are repressed to promote recombination repair, but become activated in mutants which disrupt recombination (Lemmens *et al.* 2013; Yin and Smolikove 2013; Macaisne *et al.* 2018; Kamp *et al.* 2020). Non-homologous end joining (NHEJ), which facilitates the mutagenic ligation of blunt DNA ends by the DNA ligase IV homolog LIG-4, is active in the *C. elegans* germline (Yin and Smolikove 2013; Macaisne *et al.* 2018). Recent studies have indicated that microhomology-mediated end joining facilitated by the DNA polymerase θ homolog POLQ-1 (theta-mediated end joining, TMEJ) is the primary pathway by which small mutations are incurred in *C. elegans* germ cells (Van Schendel *et al.* 2015). Despite these results, neither NHEJ nor TMEJ are required for successful meiosis (Lemmens *et al.* 2013; Kamp *et al.* 2020), thereby indicating recombination is sufficient for meiotic DSB repair and gamete viability under normal conditions.

The structural maintenance of chromosomes 5/6 complex and tumor suppressor BRCA1 (SMC-5/6 and BRC-1 respectively in *C. elegans*) regulate meiotic DSB repair in *C. elegans* (Bickel *et al.* 2010; Hong *et al.* 2016; Li *et al.* 2018; Kamp *et al.* 2020). SMC-5/6 is vital for preservation of meiotic genome integrity, as *C. elegans* mutants for *smc-5* exhibit a transgenerational sterility phenotype. Although null mutations of *smc-5, smc-6,* and *brc-1* revealed that they are not required for viability in *C. elegans* (Bickel *et al.* 2010; Li *et al.* 2018), both SMC-5/6 and BRC-1 are required for complete DSB repair, as *smc-5* and *brc-1* null mutants display meiotic chromosome fragmentation at diakinesis indicative of unresolved DNA breaks (Bickel *et al.* 2010). BRC-1 has also been shown to repress error prone DSB repair via NHEJ and TMEJ (Li *et al.* 2020; Kamp *et al.* 2020). SMC-5/6 and BRC-1 may promote genome integrity in part by facilitating efficient recombination, as *smc-5* and *brc-1* mutants exhibit persistent DSBs marked by the recombinase RAD-51 (Boulton *et al.* 2004; Adamo *et al.* 2008; Bickel *et al.* 2010; Kamp *et al.* 2020), suggesting that early recombination steps are delayed in these mutants. Despite these apparent DNA repair defects, interhomolog crossover formation is

largely unaffected by *smc-5* and *brc-1* mutation (Adamo *et al.* 2008; Bickel *et al.* 2010; Li *et al.* 2018). Taken together, these data support the hypothesis that SMC-5/6 and BRC-1 may be required for intersister repair in *C. elegans.*

Multiple lines of evidence indicate that SMC-5/6 and BRC-1 genetically interact to regulate DSB repair. The frequency of chromosome fragments at diakinesis in *smc-5* and *brc-1* mutants are not additive in the double *smc-5;brc-1* mutant context, which indicates that SMC-5/6 and BRC-1 may share some DSB repair functions (Bickel *et al.* 2010). Other experiments, however, suggest opposing functions for SMC-5/6 and BRC-1, as both the mitotic DNA replication defects in *smc-5* mutants and the synthetic lethality of *smc-5;him-6* (BLM helicase) double mutants are suppressed by *brc-1* mutation (Wolters *et al.* 2014; Hong *et al.* 2016). The specific steps of recombination regulated by SMC-5/6 and BRC-1 which intersect to influence DNA repair outcomes remain unknown.

To determine the DSB repair functions of SMC-5/6 and BRC-1 which regulate DNA repair outcomes during *C. elegans* meiosis, we employed a multipronged approach utilizing genetic assays, cytology, sequence analysis of recombinant loci, and functional DSB repair assays in *smc-5* and *brc-1* mutants. We find that SMC-5/6 and BRC-1 function to repress meiotic intersister crossover recombination, and further demonstrate that BRC-1 specifically regulates homolog-independent noncrossover intermediate processing. Through these experiments, we also identify a BRC-1 meiosis-stage specific function in preventing mutagenic DSB repair at mid pachytene. By assessing germ cell capacity to resolve exogenous DSBs, we demonstrate that meiotic nuclei become more dependent on SMC-5/6 and BRC-1 for DSB repair in late stages of meiotic prophase I. Finally, we reveal that *smc-5* mutant DSB repair defects are enhanced by functional BRC-1, which impedes gamete viability in part by repressing error prone repair pathways. Taken together, our study defines specific functions and interactions of BRC-1 and SMC-5/6 in regulating meiotic DSB repair outcomes across meiotic prophase I.

Results

BRC-1 restricts intersister crossovers

To directly assess the functions of BRC-1 in homolog-independent DSB repair, we employed the recently developed intersister/intrachromatid (ICR) assay (Toraason *et al.* 2021a; c). The ICR assay enables: 1) the controlled generation of a single DSB in *C. elegans* meiotic

nuclei via heat shock inducible mobilization of a Mos1 transposon (Bessereau *et al.* 2001; Robert and Bessereau 2007); 2) detection of this DSB's repair with the sister chromatid or same DNA molecule by GFP fluorescence in resultant progeny; and, 3) delineation of homolog-independent crossover and noncrossover recombination outcomes (Toraason *et al.* 2021a). Since the *C. elegans* germline is organized in a spatial-temporal gradient in which nuclei move progressively through the stages of meiotic prophase I along the distal-proximal axis (Jaramillo-Lambert *et al.* 2007; Rosu *et al.* 2011; Cahoon and Libuda 2021), oocytes at all stages of meiotic prophase I can be affected simultaneously by a specific treatment, such as heat shock or irradiation. Since the rate of meiotic progression in the *C. elegans* germline is known (Jaramillo-Lambert *et al.* 2007; Rosu *et al.* 2011; Cahoon and Libuda 2021), we can score resultant progeny at specific timepoints post heat shock to distinguish oocytes which incurred a Mos1-excision induced DSB at the stages of prophase I when the homologous chromosome is available as a repair partner (the 'interhomolog window', leptotene-mid pachytene, 22-58hr post heat shock) from the stages when the homolog is not readily engaged for DSB repair (the 'non-interhomolog window', late pachytene-diplotene, 10-22hr post heat shock) (Rosu *et al.* 2011).

We performed the ICR assay in a *brc-1(xoe4)* mutant, which ablates the entire *brc-1* coding sequence (Li *et al.* 2018). If BRC-1 is required for efficient intersister repair, then we expected the overall frequency of ICR assay GFP+ progeny to be reduced. Contrary to this hypothesis, we found that GFP+ progeny were elevated at all interhomolog window timepoints and were not reduced within the non-interhomolog window (Figure S3.1A, Table S3.1). This result could be explained by multiple effects, such as altered repair template bias, and therefore does not necessarily represent an overall increase in intersister/intrachromatid repair in *brc-1* mutants (see Methods). Regardless of the absolute number of ICR assay GFP+ progeny, we identified both crossover and noncrossover recombinant progeny at all timepoints scored (Supplemental Figure 3.1A), demonstrating that BRC-1 is not required for intersister/intrachromatid crossover or noncrossover repair. Notably, the overall proportion of crossover progeny among recombinants identified was increased at all timepoints scored

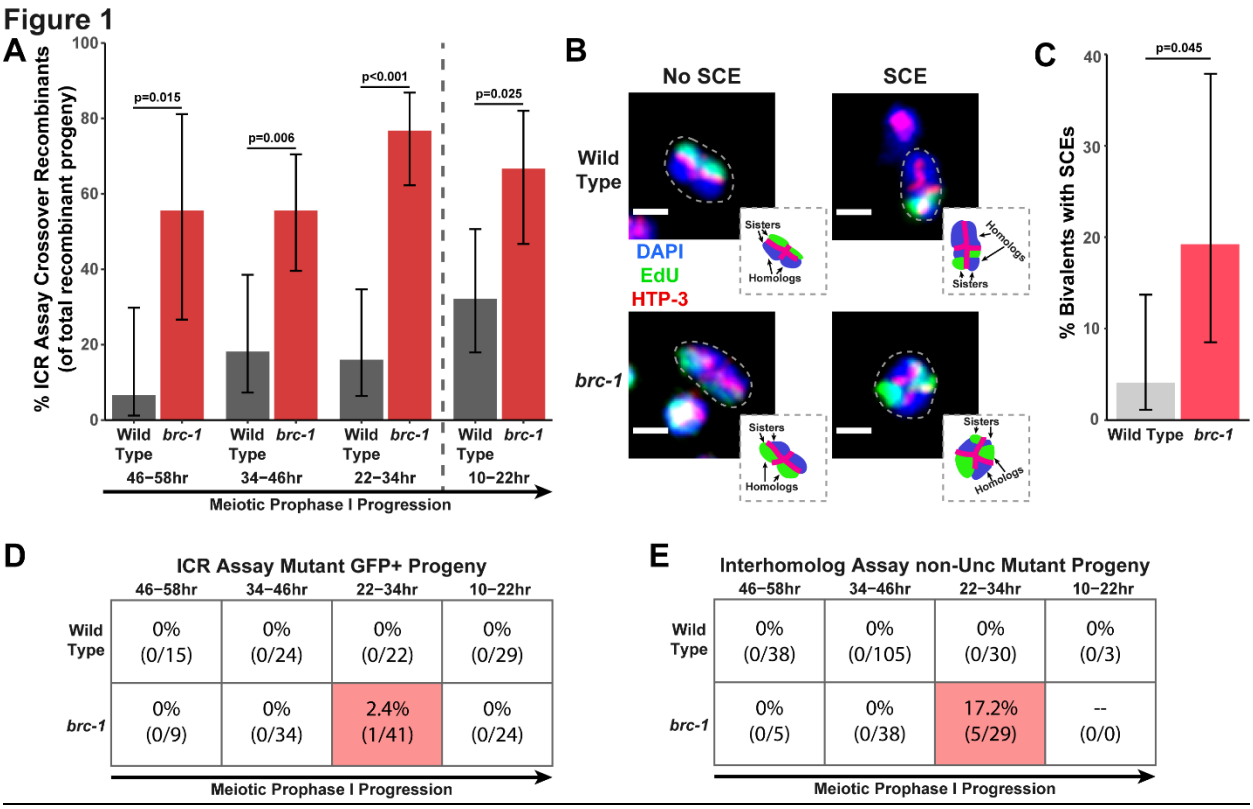

Figure 3.1. BRC-1 suppresses intersister crossovers and error-prone repair. A) Bar plot displaying the percent of crossover recombinant progeny identified in wild type and *brc-1* ICR assays out of all recombinant progeny scored. Frequencies of recombinants identified overall in ICR assays is displayed in Figure S3.1A and specific counts are denoted in Table S3.1. B) Images of wild type and *brc-1(xoe4)* mutant bivalent chromosomes displaying an absence or presence of SCEs. Scale bars represent 1µm. Dashed bordered insets contain cartoon depictions of the SCE and non-SCE bivalents which are outlined with dashed lines in the images to aid in visualizing exchange events. C) Frequency of SCEs identified among wild type (n=49) or *brc-1* mutant (n=26) bivalents scored. D-E) Tables displaying the percent of sequenced GFP+ progeny in wild type and *brc-1* ICR assays (D) or non-Unc progeny IH assays (E) which showed signatures of mutagenic repair. Numbers in parentheses indicate the number of mutant worms out of the total number of sequenced progeny. Shaded boxes indicate timepoints in which mutant progeny were identified. The overall frequency of interhomolog assay non-Unc progeny is displayed in Figure S3.2A-B and specific interhomolog assay counts are denoted in Table S3.2. In all panels, error bars represent 95% Binomial confidence intervals, dashed vertical lines delineate between timepoints within the interhomolog window (22-58hr post heat shock) and non-interhomolog window (10-22hr post heat shock), and p values were calculated using Fisher's Exact Test.

(Figure 3.1A), suggesting that BRC-1 functions in *C. elegans* meiosis to repress intersister/intrachromatid crossover events.

To confirm that intersister crossovers are more frequent in a *brc-1* mutant, we employed a recently developed cytological assay which utilizes EdU incorporation to visualize sister chromatid exchanges (SCEs) in compacted diakinesis chromosomes (Figure 3.1B) (Almanzar *et al.* 2021, 2022). While SCEs are found in only 4.1% of bivalents in a wild type background (2/49 bivalents scored, 95% Binomial CI 1.1-13.7%) (Almanzar *et al.* 2021), we detected SCEs at an elevated rate of 19.2% in a *brc-1(xoe4)* mutant (Figure 3.1B-C, 5/26 bivalents scored, 95% Binomial CI 8.5-37.9%, Fisher's Exact Test p=0.045). When we compared the levels of SCEs cytologically identified with the frequency of ICR assay crossovers generated from DSBs within the interhomolog window, the elevated frequency of SCEs (4.7 fold increase) closely mirrored the relative increase in crossovers as a proportion of all recombinants observed in the *brc-1* mutant ICR assay (4.6 fold increase). Taken together, these results demonstrate that BRC-1 functions to suppress intersister crossover recombination during *C. elegans* meiosis.

BRC-1 is not required for interhomolog recombination

Since BRC-1 acts to suppress crossover recombination between sister chromatids, we next assessed if *brc-1* mutants exhibited defects in interhomolog recombination, including interhomolog crossovers. To assess the overall rates of interhomolog noncrossover and crossover recombination, we employed an established interhomolog (IH) recombination assay (Rosu *et al.* 2011) which enables: 1) controlled generation of a single DSB in meiotic nuclei via heat-shock inducible Mos1 excision (Robert and Bessereau 2007); 2) identification of interhomolog DSB repair of the induced DSB by reversion of an uncoordinated movement 'Unc' phenotype (non-Unc progeny, see Methods); and, 3) delineation of interhomolog noncrossover and crossover repair outcomes (see Methods). Previous research has established that mutagenic DSB repair in the IH assay can also produce non-Unc progeny which are

Supplemental Figure 1
Intersister/Intrachromatid Repair (ICR) Assay

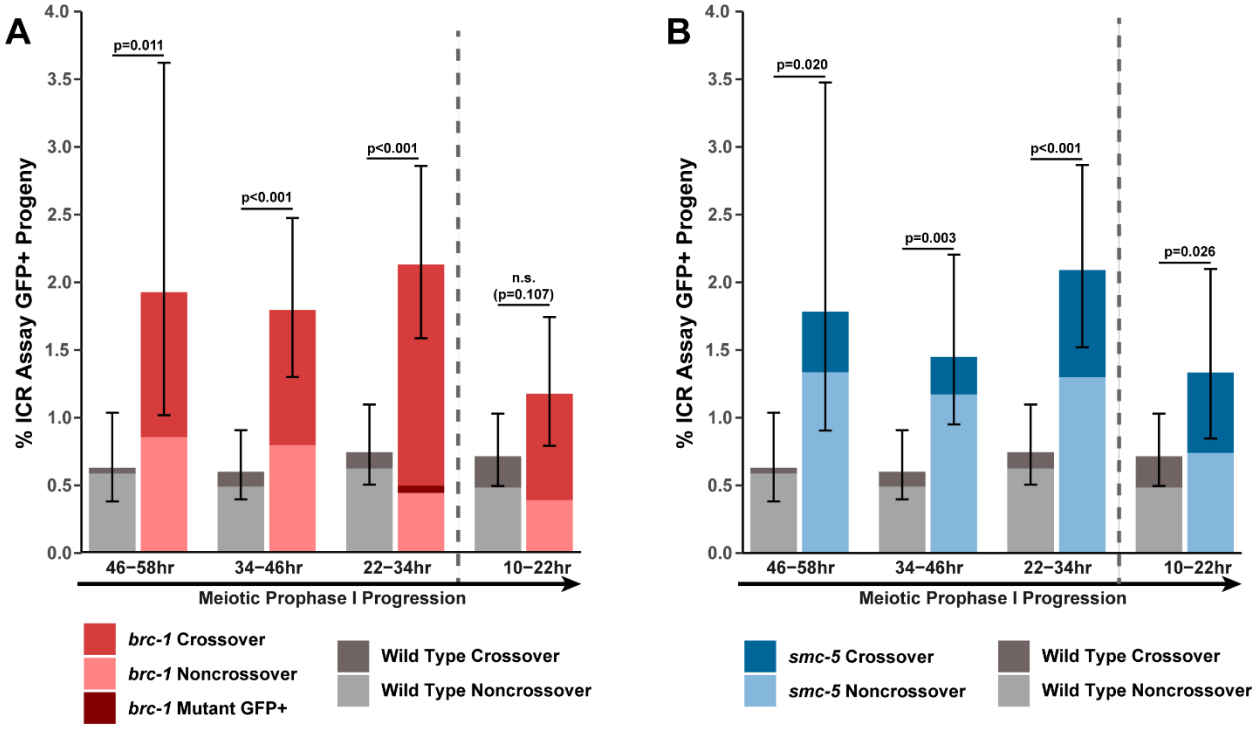

Figure S3.1. Intersister/intrachromatid repair (ICR) assay GFP+ progeny are elevated in *brc-1* and *smc-5* mutants. Stacked bar plots displaying the percent of all progeny scored in wild type and *brc-1* (A) or *smc-5* (B) ICR assays which were determined to be GFP+ noncrossover recombinants, crossover recombinants, or mutants. Specific progeny counts are displayed in Table S3.1. Error bars represent the 95% Binomial confidence intervals for the frequencies of GFP+ progeny. P values were calculated by Fisher's Exact test. Vertical dashed lines demarcate the interhomolog window (22-58hr post heat shock) and non-interhomolog window (10-22hr post heat shock) timepoints.

Supplemental Figure 2

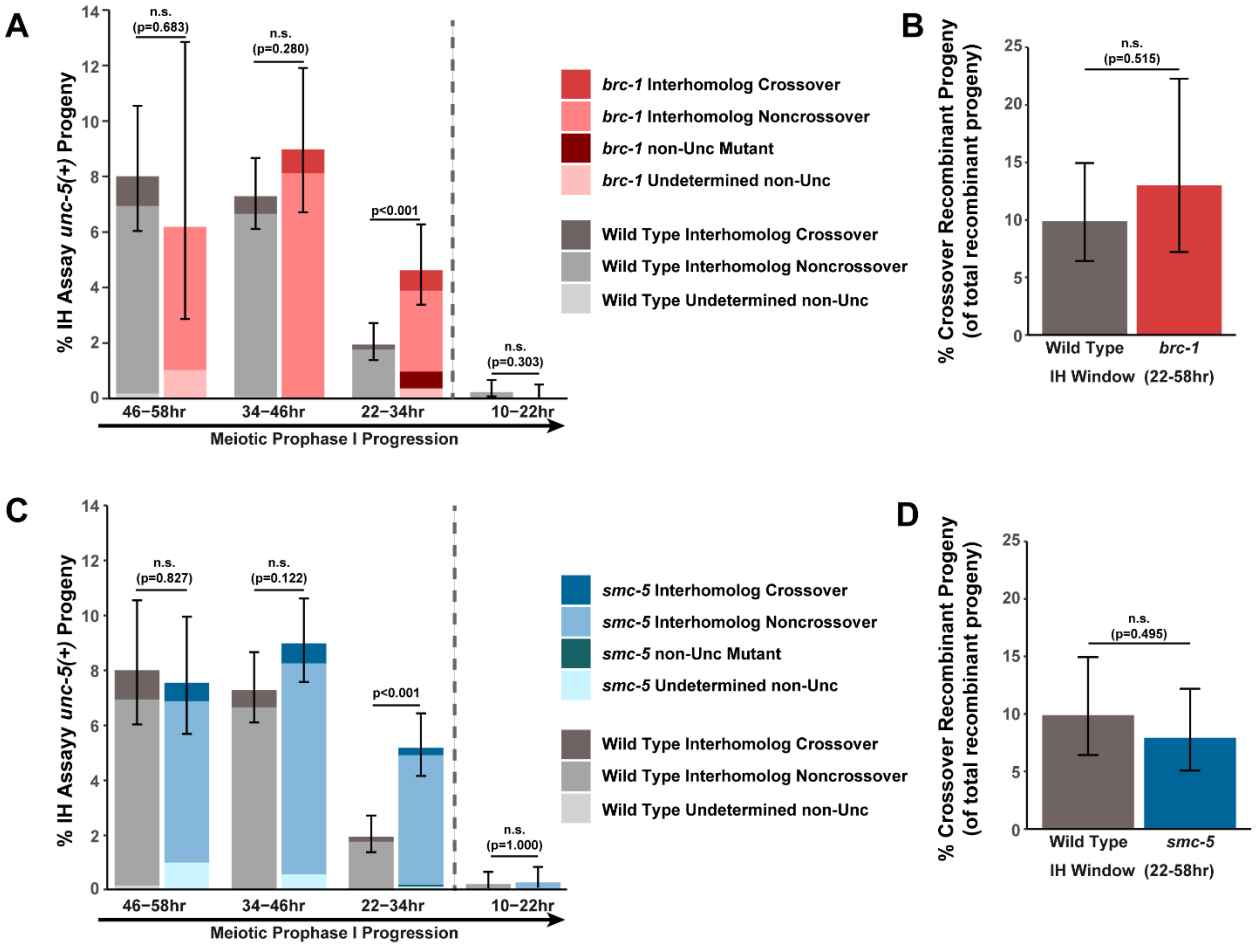

Figure S3.2. Interhomolog repair is largely unperturbed in *brc-1* and *smc-5* mutants. A) Stacked bar plots displaying the percent of all progeny scored in wild type and *brc-1* IH assays which were determined to be noncrossover recombinants, crossover recombinants, non-Unc mutants, or undetermined non-Unc. B) Percent of all recombinant progeny identified within the interhomolog window of wild type and *brc-1* IH assays which were crossover recombinants. C) Stacked bar plots displaying the percent of all progeny scored in wild type and *smc-5* IH assays which were determined to be noncrossover recombinants, crossover recombinants, non-Unc mutants, or undetermined non-Unc. D) Percent of all recombinant progeny identified within the interhomolog window of wild type and *smc-5* IH assays which were crossover recombinants. Specific progeny counts of all IH assays are displayed in Table S3.2. Error bars represent the 95% Binomial confidence intervals for the frequencies of non-Unc progeny. P values were calculated by Fisher's Exact test. Vertical dashed lines demarcate the interhomolog window (22-58hr post heat shock) and non-interhomolog window (10-22hr post heat shock) timepoints.

phenotypically indistinguishable from noncrossover recombinants (Robert *et al.* 2008). While error prone repair events are rare in a wild type context (Robert *et al.* 2008), *brc-1* mutants are known to incur small mutations more frequently (Kamp *et al.* 2020). We therefore sequenced the repaired *unc-5* locus of putative noncrossover non-Unc progeny in the IH assay to confirm whether the repaired sequence matched the homolog repair template or indicated mutations at the site of Mos1 excision (see Methods). Non-Unc progeny which we were unable to sequence were designated as 'undetermined non-Unc'.

When we performed the IH assay in the *brc-1* mutant, we observed a significant increase in the proportion of non-Unc progeny only at the 22-34hr timepoint, which corresponds to the mid pachytene stage of meiosis and the end of the interhomolog window (Figure S3.2A, Table S3.2, Fisher's Exact Test $p<0.001$). This result may indicate a slight delay in the rate of meiotic progression in *brc-1* mutants (Rosu *et al.* 2011). However, the overall frequency of non-Unc progeny was not elevated relative to wild type within the non-interhomolog window (Figure S3.2A, 10-22hr post heat shock, Fisher's Exact Test $p=0.303$), indicating that ablation of *brc-1* does not severely impact meiotic prophase I progression.

When we compared the ratio of crossover and noncrossover recombinant progeny within the interhomolog window between wild type and *brc-1* mutants, we saw that the frequency of interhomolog crossovers was not significantly altered (Supplemental Figure 3.2B, Fisher's Exact Test $p=0.515$). This result mirrors recombination assays previously performed in *brc-1* mutants which provided no evidence for the presence of additional crossovers (Li *et al.* 2018). Thus, our data supports a role for BRC-1 in regulating crossover recombination specifically between sister chromatids.

BRC-1 prevents mutagenic DNA repair in mid pachytene

In both the ICR and IH assays performed in *brc-1* mutants, we identified progeny which exhibited molecular signatures of mutagenic DSB repair at the Mos1 excision site (Figure 3.1D-E, Figure S3.1A, Figure S3.2A, Table S3.1). These events were only identified within the 22-34hr timepoint, which is composed of nuclei in mid pachytene at the time of Mos1 excision. In the ICR assay, mutants were identified as 2.4% (95% Binomial CI 0.4-12.5%) of all sequenced GFP+ progeny at the 22-34hr time point. In the IH assay, 13.2% (95% Binomial CI 7.6-34.5%) of all sequenced non-Unc progeny at the 22-34hr time point were identified as mutant (Figure 3.1D-E). Notably, we only sequenced GFP+ and non-Unc progeny in the ICR and IH assays

respectively. The frequency of error prone pathway utilization in a *brc-1* mutant is therefore likely much greater than our results suggest, as we could not detect mutations which disrupt the GFP or *unc-5* open reading frames.

One of the five mutant *brc-1* IH assay non-Unc mutants we sequenced carried two distinguishable mutagenic repair products. These two mutations likely represent the outcomes of both a meiotic DSB repair event and an additional somatic repair event in the progeny. We have previously observed analogous somatic Mos1 excision events in F1 progeny in the ICR assay (Toraason *et al.* 2021a; c). As we cannot distinguish the source of the respective repair events, this mutant was excluded from subsequent sequence analysis. Of the meiotic lesions we identified among *brc-1* IH assay progeny, 75% (3/4 mutations, 95% CI 30.0-95.4%) exhibited one or more complementary nucleotides on both ends of the deletion (Figure S3.3B). This frequency is greater than what we would expect given the surrounding sequence following Mos1 excision, as only 26.2% of random in frame deletions within 34nt of the site of Mos1 excision would share one or more complementary nucleotides on either end of the DSB.

The single mutant identified among *brc-1* ICR assay GFP+ progeny displayed a particularly striking rearrangement (Figure S3.3A) which can be parsimoniously inferred to have been formed by strand invasion and extension of both ends of the DSB with a repair template followed by end joining. The position of the putative end joining event in this instance shared 3nt of homology on either end of the DSB, suggesting a similar mechanism for resolution as the mutations incurred in the IH assay. Regions of microhomology present on either end of small (<50bp) deletions are characteristic of theta mediated end joining (TMEJ) (Van Schendel *et al.* 2015). A previous study demonstrated that the rate of TMEJ-mediated germline mutagenesis is elevated in *brc-1* mutants (Kamp *et al.* 2020). Our data is concordant with elevated TMEJ engagement in *brc-1* mutants and further reveals that the function of BRC-1 in preventing mutagenic repair events is specifically vital in the mid pachytene stage of meiotic prophase I.

SMC-5/6 restricts intersister crossovers

The SMC-5/6 DNA damage complex has been hypothesized to function in homolog-independent DSB repair in *C. elegans* (Bickel *et al.* 2010). To directly assess the functions of

Supplemental Figure 3

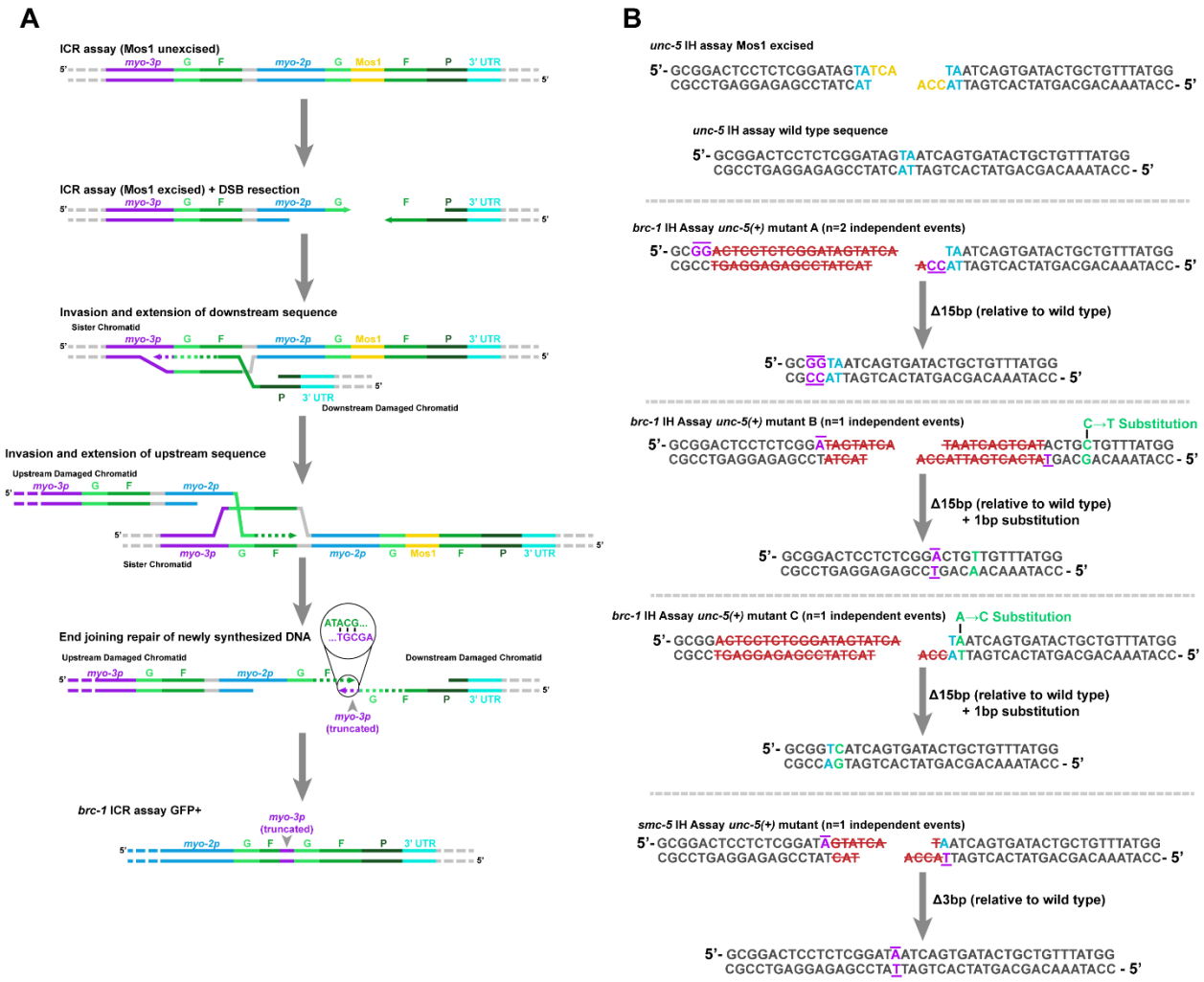

Figure S3.3. Illustrations of mutants identified in ICR and IH assays. A) Illustrated depiction of ICR assay GFP+ mutant identified in a *brc-1* mutant background (Figure S3.1, Table S3.1). The partial tandem duplication produced (bottom) can best be parsimoniously explained by two independent strand invasion and extension events on either end of the DSB. For simplicity, intersister recombination is depicted in this diagram. However, intrachromatid templates could also have been engaged to produce the final product. B) Illustrations of *unc-5* lesions identified in IH assay non-Unc progeny in *brc-1* or *smc-5* mutants. Specific mutation signatures are separated by horizontal dashed grey lines. The wild type *unc-5* locus sequence at the site of Mos1 excision and the DSB product generated by Mos1 excision are displayed on the top of panel B. Blue letters indicate a duplicated TA at the site of Mos1 insertion in the *unc-5(ox171)* locus, while yellow letters indicate the 3nt 3' overhangs left following Mos1 excision (Robert *et al.* 2008). In the panels displaying mutations identified, purple letters with bars indicate complementary bases flanking the deletion site. Red letters struck through with red lines indicate bases in the damaged locus which were deleted to produce the final product. Green letters indicate sites of nucleotide substitution mutations.

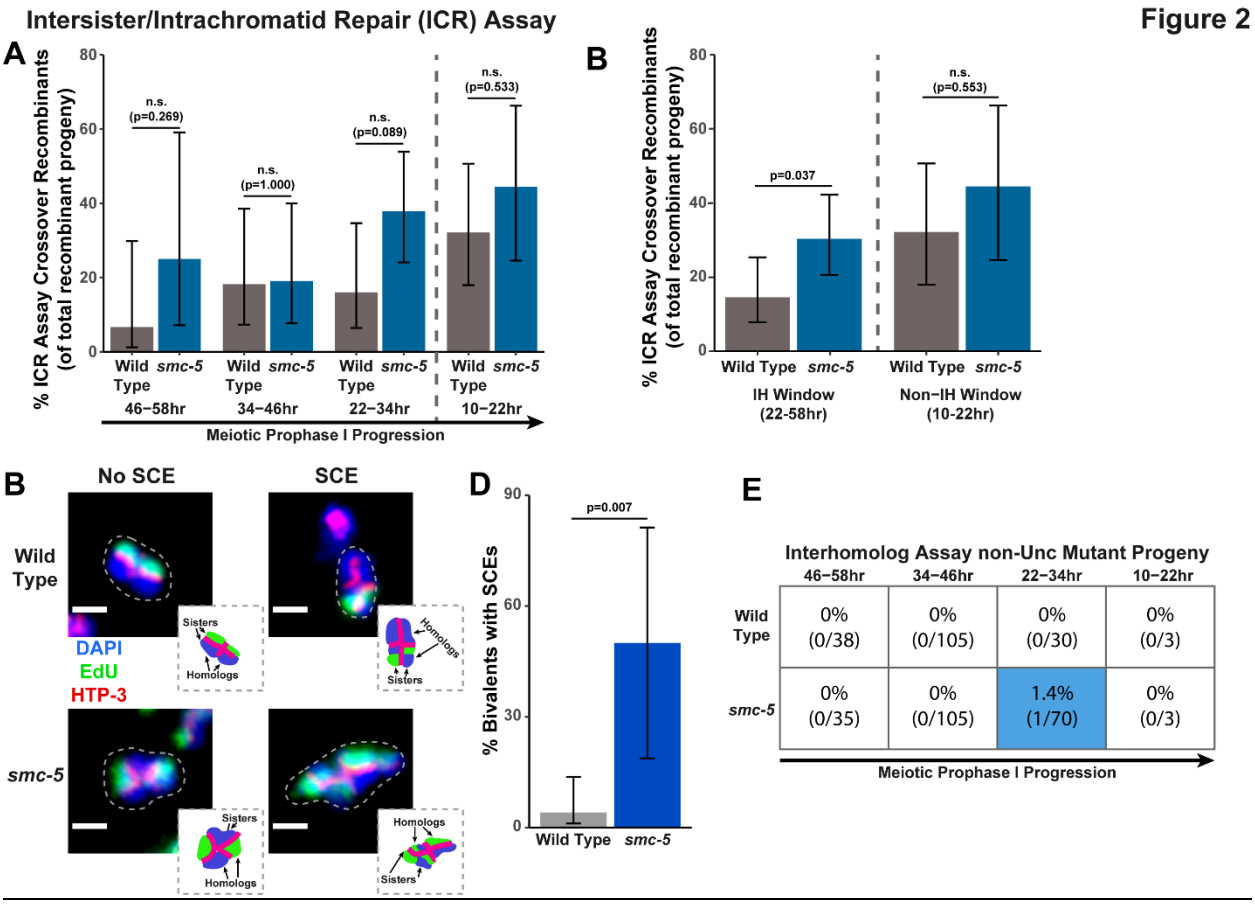

Figure 3.2. SMC-5/6 suppresses intersister crossovers. A) Bar plot displaying the percent of crossover recombinant progeny identified in wild type and *smc-5* ICR assays out of all recombinant progeny scored within individual 12 hour timepoint periods. Frequencies of recombinants identified overall in ICR assays is displayed in Figure S3.1B and specific counts are denoted in Table S3.1. B) Bar plot displaying the percent of crossover recombinant progeny identified in wild type and *smc-5* ICR assays out of all recombinant progeny scored within the interhomolog window (22-58hr post heat shock) and non-interhomolog window (10-22hr post heat shock). C) Images of wild type and *smc-5(ok2421)* mutant bivalent chromosomes displaying an absence or presence of SCEs. Scale bars represent 1μm. Dashed bordered insets contain cartoon depictions of the SCE and non-SCE bivalents which are outlined with dashed lines in the images to aid in visualizing exchange events. D) Frequency of SCEs identified among wild type (n=49) or *smc-5(ok2421)* mutant (n=6) bivalents scored. E) Table displaying the percent of sequenced non-Unc progeny in wild type and *smc-5* IH assays which showed signatures of mutagenic repair. Numbers in parentheses indicate the number of mutant worms out of the total number of sequenced progeny. Colored boxes indicate timepoints in which mutant progeny were identified. The overall frequency of interhomolog assay non-Unc progeny is displayed in Figure S3.2C-D and specific interhomolog assay counts are denoted in Table S3.2. In all panels, error bars represent 95% Binomial confidence intervals, dashed vertical lines delineate between timepoints within the interhomolog window (22-58hr post heat shock) and non-interhomolog window (10-22hr post heat shock), and p values were calculated using Fisher's Exact Test.

the structural maintenance of chromosomes 5/6 (SMC-5/6) complex in homolog-independent DSB repair, we performed the ICR assay in the *smc-5(ok2421)* null mutant. The *smc-5(ok2421)* deletion allele disrupts the final 6 exons of the 11 exons in the *smc-5* coding sequence and prevents SMC-5/6 complex assembly, as evidenced by both biochemical and cytological experiments (Bickel *et al.* 2010). SMC-5/6 is therefore not required for viability in *C. elegans*, unlike many other organisms (Aragón 2018). Similar to the *brc-1* mutant, we found that the frequency of GFP+ progeny in the ICR assay was elevated at all timepoints scored in *smc-5(ok2421)* null mutants (Figure S3.1B, Table S3.1). As mentioned above and in the Methods, this result does not necessarily represent an absolute increase in the rate of intersister/intrachromatid recombination (see Methods). Importantly, we did identify both crossover and noncrossover recombinants at all timepoints scored, demonstrating that SMC-5/6 is not required for noncrossover nor crossover homolog-independent repair (Figure S3.1B, Table S3.1).

To determine if SMC-5/6 regulates engagement of intersister/intrachromatid recombination outcomes, we examined the proportion of *smc-5* ICR assay crossover recombinants as a proportion of all recombinants identified. While the proportion of crossovers was not significantly different than wild-type within the individual 12-hour timepoints we scored (Figure 3.2A), the frequency of crossover recombinants in *smc-5* mutants was significantly elevated within the interhomolog window overall (Figure 3.2B, Fisher's Exact Test p=0.037). Thus, our data suggests that a function of SMC-5/6 is to prevent homolog-independent crossovers arising from DSBs induced in early stages of meiotic prophase I.

To cytologically affirm the results of our ICR assay, we assessed the frequency of SCEs in *smc-5(ok2421)* mutants by examining EdU labeled chromatids at diakinesis. Mutants for *smc-5* are known to have defects in chromosome compaction and produce misshapen bivalents (Bickel *et al.* 2010; Hong *et al.* 2016). These defects made the majority of bivalents uninterpretable in the EdU labeling assay. Nonetheless, even among a limited sample, we identified SCEs in 50% of scored bivalents (Figure 3.2C-D, 3/6 bivalents scored, 95% Binomial CI 18.8-81.2%, Fisher's Exact Test p=0.007) as compared to only 4.1% of wild type bivalents (2/49 bivalents scored, 95% Binomial CI 1.1-13.7%) (Almanzar *et al.* 2021). This EdU labeling data in the *smc-5(ok2421)* null mutant represents a 12.2 fold increase in the rate of SCEs, which is notably more extreme than the 2.1 fold increase in the proportion of crossover recombinants

observed in the IH window in our *smc-5* ICR assay data. Nevertheless, both our ICR assay and EdU labeling experiments support a function for SMC-5/6 in repressing intersister crossing over during *C. elegans* meiosis.

SMC-5/6 is not required for interhomolog recombination

To determine if the SMC-5/6 complex regulates interhomolog recombination, we performed the IH assay in the *smc-5(ok2421)* null mutant. We identified both interhomolog crossover and noncrossover recombinants in the IH assay (Figure S3.2C, Table S3.2), indicating that SMC-5/6 is not required for either of these recombination pathways. Similar to *brc-1* mutants, we noted elevated non-Unc progeny at the 22-34hr time point in *smc-5* mutants, implying that meiotic prophase progression may be slightly delayed when SMC-5/6 function is lost (Figure S3.2C, Fisher's Exact Test $p<0.001$). Notably, non-Unc progeny were not increased in the non-interhomolog window in *smc-5* mutants, suggesting that the progression of meiotic prophase I was not drastically altered in this genetic context (Figure S3.2C, Fisher's Exact Test $p=1.000$). The proportion of crossover recombinants among all recombinants identified also was not altered in an *smc-5* mutant (Figure S3.2D, Fisher's Exact Test $p=0.495$). Thus, our data does not support a function for SMC-5/6 in ensuring efficient interhomolog recombination.

Among all sequenced ICR and IH assay GFP+ and non-Unc progeny isolated in *smc-5* mutants, we identified only one mutagenic DSB repair event at the 22-34hr timepoint of the IH assay (Figure 3.2E, Figure 3.2C, Figure S3.3B, Table S3.2). Moreover, the frequency of *smc-5* non-Unc mutants which we detected at this timepoint (1.32% of all sequenced non-Unc progeny, 95% Binomial CI 0.2-7.1%) is lower than the frequency observed in *brc-1* mutants (Fisher's Exact Test $p=0.015$). Previously, profiling of meiotic mutagenic DNA repair events in *smc-6* mutants revealed that large structural variations are a primary class of mutations which arise in SMC-5/6 deficient germlines (Volkova *et al.* 2020). In our *smc-5* ICR and IH assays, a greater frequency of DSBs may have been resolved by mutagenic repair, but if these products disrupted the coding sequence in GFP or *unc-5* respectively, then they would have escaped detection in our assays.

BRC-1 promotes the formation of long homolog-independent noncrossover conversion tracts

Since we identified functions for BRC-1 and SMC-5/6 in regulating intersister crossover recombination, we wanted to determine if recombination intermediate processing is altered in

brc-1 and *smc-5* mutants. Evaluation of sequence conversions have informed much of our understanding of recombination intermediate processing (Szostak *et al.* 1983; Pâques and Haber 1999; Marsolier-Kergoat *et al.* 2018; Ahuja *et al.* 2021). The ICR assay was engineered to contain multiple polymorphisms spanning 12bp to 567bp 3' from the site of Mos1 excision, enabling conversion tract analysis of homolog-independent recombination (Toraason *et al.* 2021a). In a wild type context, 74.2% of ICR assay noncrossover conversion tracts within the interhomolog window are 'short', which we define as tracts with a sequence conversion only at the most proximal polymorphism 12bp downstream from the site of Mos1 excision (Figure 3.4A, 3.4C, wild type 74.2% short tracts 95% CI 62.6-83.3%). In contrast to 74.2% of wild type noncrossover tracts during the interhomolog window being classified as 'short', 96.6% of *brc-1* noncrossover tracts during the interhomolog window were 'short' (*brc-1* interhomolog window 96.6% short tracts 95% CI 82.8-99.4%, Fisher's Exact Test p=0.010). During the non-interhomolog window, a null mutation of *brc-1* had no effect on the proportion of 'short' noncrossover tracts (Figure 3.3A, 3.3C, wild type 72.7% short tracts 95% CI 51.8-86.8%; *brc-1* 87.5% short tracts 95% CI 52.9-97.8%, Fisher's Exact Test p=0.638), thereby indicating that BRC-1 likely affects the mechanisms of noncrossover formation only during the interhomolog window.

We previously showed that wild type intersister/intrachromatid crossover conversion tracts in *C. elegans* tend to be larger than noncrossovers, with a median minimum conversion tract length (the distance from the most proximal to the most distal converted polymorphisms in bp) for intersister/intrachromatid crossovers being 198bp (Figure 3.3B) (Toraason *et al.* 2021a). Based on this median length for intersister/intrachromatid crossovers, we defined 'short' ICR assay crossover tracts as ≤198bp in length. We found that the proportion of 'short' crossover tracts was not altered by *brc-1* mutation within the interhomolog window (Figure 3.3B, 3.3D, wild type 80.0% short tracts 95% CI 62.7-90.5%; *brc-1* 74.1% short tracts 95% CI 61.1-83.9%, Fisher's Exact Test p=1.00) nor within the non-interhomolog window (Figure 3.3B, 3.3D, wild type 55.6% short tracts 95% CI 37.3-72.4%; *brc-1* 68.8% short tracts 95% CI 44.4-58.8%, Fisher's Exact Test p=0.657). Taken together, these results support a model in which BRC-1 regulates mechanisms of intersister/intrachromatid noncrossover recombination (and not crossover recombination) in the early stages of meiotic prophase I.

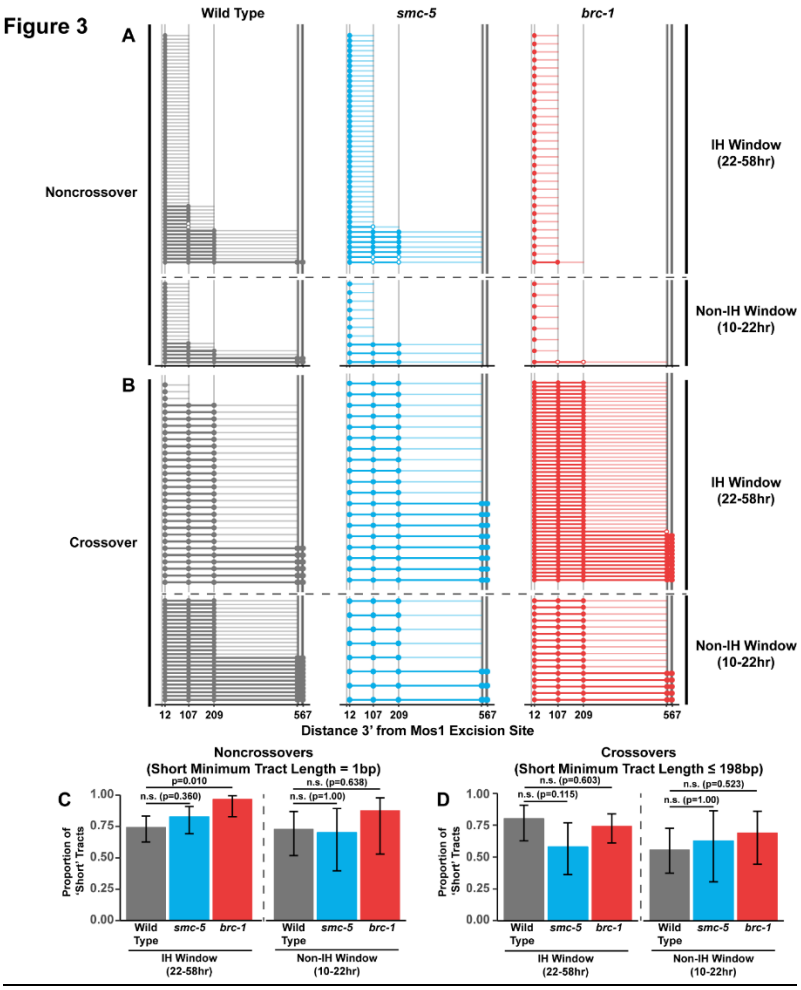

Figure 3.3. BRC-1 is required for long noncrossover gene conversion. A-B) Plots of conversion tracts sequenced from recombinant ICR assay loci. Vertical grey lines indicate the positions of polymorphisms in the ICR assay with bp measurements given 3' relative to the site of Mos1 excision (Toraason *et al.* 2021a; c). Each horizontal line represents a single recombinant sequenced, ordered from smallest tract to largest tract within the interhomolog and non-interhomolog windows. Filled in points represent fully converted polymorphisms, while points with white interiors represent heteroduplexed DNA sequences identified in conversion tracts. High opacity horizontal lines within plots represent the minimum conversion tract length, or the distance from the most proximal to the most distal converted polymorphisms. Low opacity horizontal lines indicate the maximum conversion tract, extending from the most distal converted polymorphism to its most proximal unconverted polymorphism. Tracts from noncrossover recombinants are displayed in A, while tracts from crossover recombinants are displayed in B. C-D) Frequency of small noncrossover tracts (C, minimum tract length 1bp converted at only the 12bp polymorphism) or small crossover tracts (D, minimum tract length 198bp) as a proportion of all tracts identified from progeny laid within the interhomolog and non-interhomolog windows. Error bars represent the 95% binomial confidence intervals of these proportions and p values were calculated using Fisher's Exact Test. In all panels, dashed grey lines delineate between the interhomolog window (22-58hr post heat shock) and non-interhomolog window (10-22hr post heat shock) timepoints.

SMC-5/6 does not regulate the extent of homolog-independent gene conversion

To assess if SMC-5/6 influences recombination intermediates, we compared *smc-5* mutant ICR assay conversion tracts to their wild type counterparts. We found that ICR assay noncrossover conversion tracts in *smc-5* mutants exhibited a similar proportion of 'short' tracts to wild type in both the interhomolog (Figure 3.3A, 3.3C, wild type 74.2% short tracts 95% CI 62.6-83.3%; *smc-5* 82.6% short tracts 95% CI 69.3-90.9%, Fisher's Exact Test p=0.360) and non-interhomolog windows (Figure 3.3A, 3.3C, wild type 72.7% short tracts 95% CI 51.8-86.8%; *smc-5* 70% short tracts 95% CI 39.7-89.2%). Thus, SMC-5/6 does not have a strong effect on the extent of noncrossover gene conversion in intersister/intrachromatid repair.

When we compared the proportion of 'short' *smc-5* ICR assay crossover tracts to wild type , we similarly observed that there is no significant difference in the proportion of short and long crossover tracts in either the interhomolog (Figure 3.3B, 3.3D, wild type 80.0% short tracts 95% CI 62.7-90.5%; *smc-5* 57.9% short tracts 95% CI 36.3—76.9%, Fisher's Exact Test p=1.00) or non-interhomolog windows (Figure 3.3B, 3.3D, wild type 55.6% short tracts 95% CI 37.3-72.4%; *smc-5* 62.5% short tracts 95% CI 30.6-86.3%, Fisher's Exact Test p=1.00). Taken together, these results do not support a function for SMC-5/6 in regulating the extent of noncrossover and crossover gene conversion which yields functional GFP repair products.

In our wild type, *brc-1*, and *smc-5* ICR assay conversion tracts, we additionally noted multiple instances of heteroduplex DNA in our sequencing (Figure 3.4A, 3.4B). DNA heteroduplex is a normal intermediate when recombination occurs between polymorphic templates but is usually resolved by the mismatch repair machinery. Our observation of these events across genotypes suggests that at a low frequency, mismatch repair may fail to resolve heteroduplex DNA during the course *C. elegans* meiotic DSB repair.

BRC-1 and SMC-5/6 genetically interact in resolving exogenous DSBs

To determine whether the regulation of homolog-independent DSB repair involves interactions between SMC-5/6 and BRC-1, we assessed how *smc-5(ok2421);brc-1(xoe4)* double mutants respond to DSBs. Since genetically balanced *smc-5;brc-1* double mutants can still acquire mutations and become progressively sterile over the course of a few generations (see Methods), we were unable to assess DSB repair in this double mutant with the ICR and IH assays, which require multi-generational crosses (see Methods) (Toraason *et al.* 2021c). To minimize the impact of this reproductive dysfunction phenotype and test for the genetic

interactions of SMC-5/6 and BRC-1 in ensuring efficient DSB repair, we instead assessed the resilience of *smc-5*, *brc-1*, and *smc-5;brc-1* mutant gametes to exogenous DSBs induced by ionizing radiation. Accordingly, we treated wild type, *smc-5*, *brc-1*, and *smc-5;brc-1* mutant adult hermaphrodites with 0, 2500, or 5000 Rads of ionizing radiation and assayed the resultant progeny derived from their irradiated oocytes for larval viability (Figure S3.4A). We scored embryos which successfully hatched into larvae following irradiation and calculated brood viability (defined as the proportion of all eggs laid which hatch into larvae) as a proxy measure for each genotype's capacity to resolve exogenous DNA damage in meiosis. Importantly, we scored brood viability over a similar reverse time course as was done in our ICR and IH assays following irradiation (see Methods), enabling us to identify meiosis-stage specific DNA repair defects in these mutants.

While performing these irradiation experiments, we noted variation in the brood viabilities of individual genotypes (Figure S3.4A), which indicates differences in baseline fertility. This baseline disparity for the unirradiated cohorts posed a challenge in interpreting the effects of ionizing radiation on brood viability, as the resilience of an irradiated cohort will be affected by both baseline fertility defects as well as the effects of the exogenous DNA damage that we sought to quantify. Further, the responses of individual hermaphrodites to ionizing radiation treatment were heterogeneous in some genotypes (Figure S3.4A). To estimate the effect of ionizing radiation on brood viability and to account for inter-hermaphrodite variance in our analysis, we employed a hierarchical statistical modeling approach using our dataset (Figure 3.4B, see Methods). From this analysis, we calculated a metric termed 'gamma' for each genotype, representing the sensitivity of a given genotype to ionizing radiation (Figure 3.4B, see Methods). A gamma estimate of 1 indicates that irradiation has no effect on brood viability, while a gamma estimate of 0 indicates that all progeny of a genotype are inviable following irradiation.

Figure 4

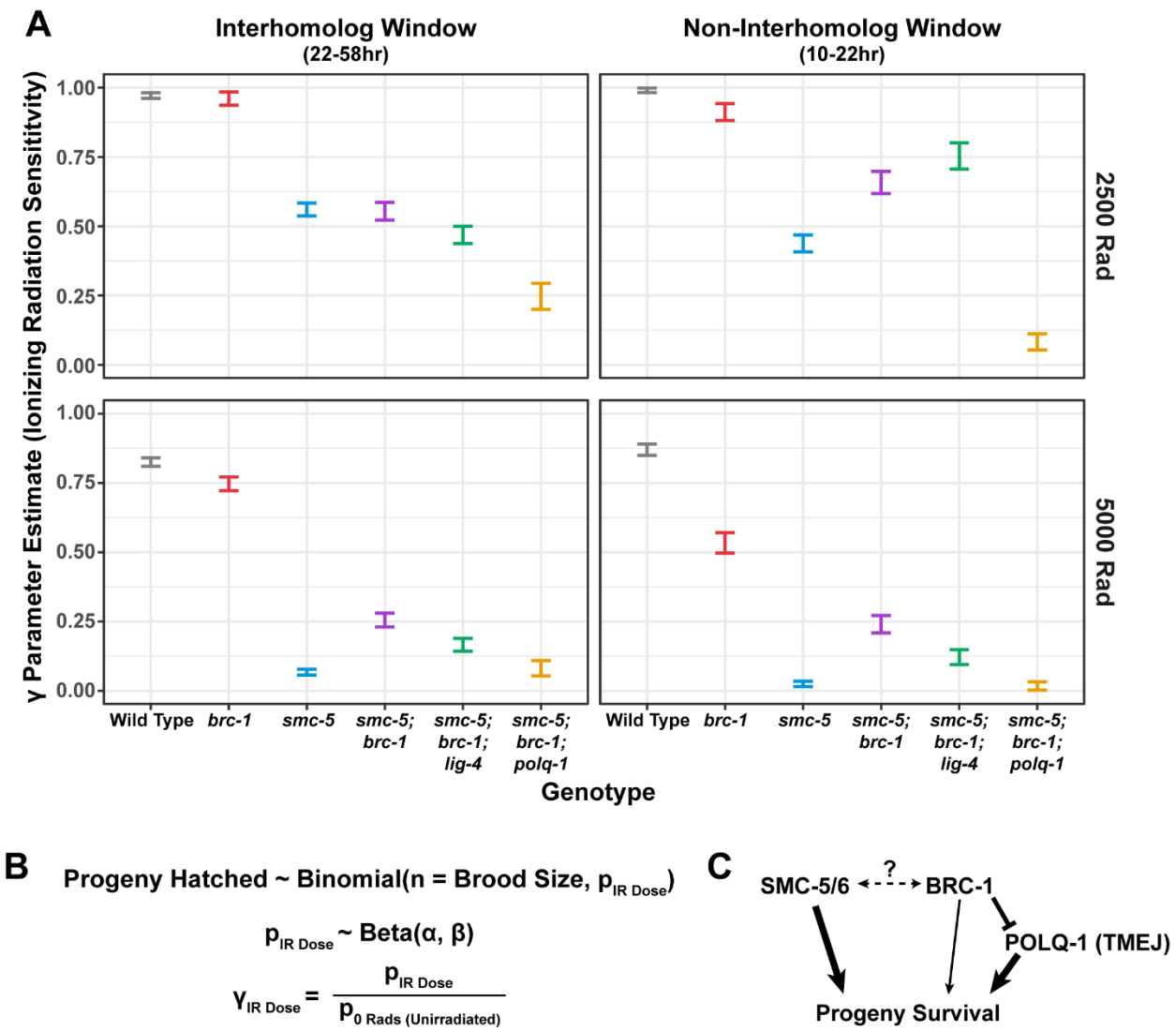

Figure 3.4. Interactions of SMC-5/6 and BRC-1 in meiotic DSB repair following irradiation. A) Gamma parameter estimates of genotype sensitivity to ionizing radiation of given doses. Vertical error bars represent the 95% credible interval of the gamma estimate for each genotype at the given dose of irradiation exposure. The brood viabilities of hermaphrodites used in this analysis are displayed in Figure S3.4A. Counts of progeny survival following irradiation are denoted in Table S3.3, S3.4. B) Outline of beta binomial model framework used to generate panel A. See Methods for details. C) Genetic interaction diagram inferred from estimates presented in panel A. SMC-5/6 and BRC-1 both contribute to progeny viability following meiotic exposure to exogenous DSBs. However, BRC-1 also inhibits error prone repair, which can compensate for the DSB defects of *smc-5* mutants when *brc-1* is also ablated.

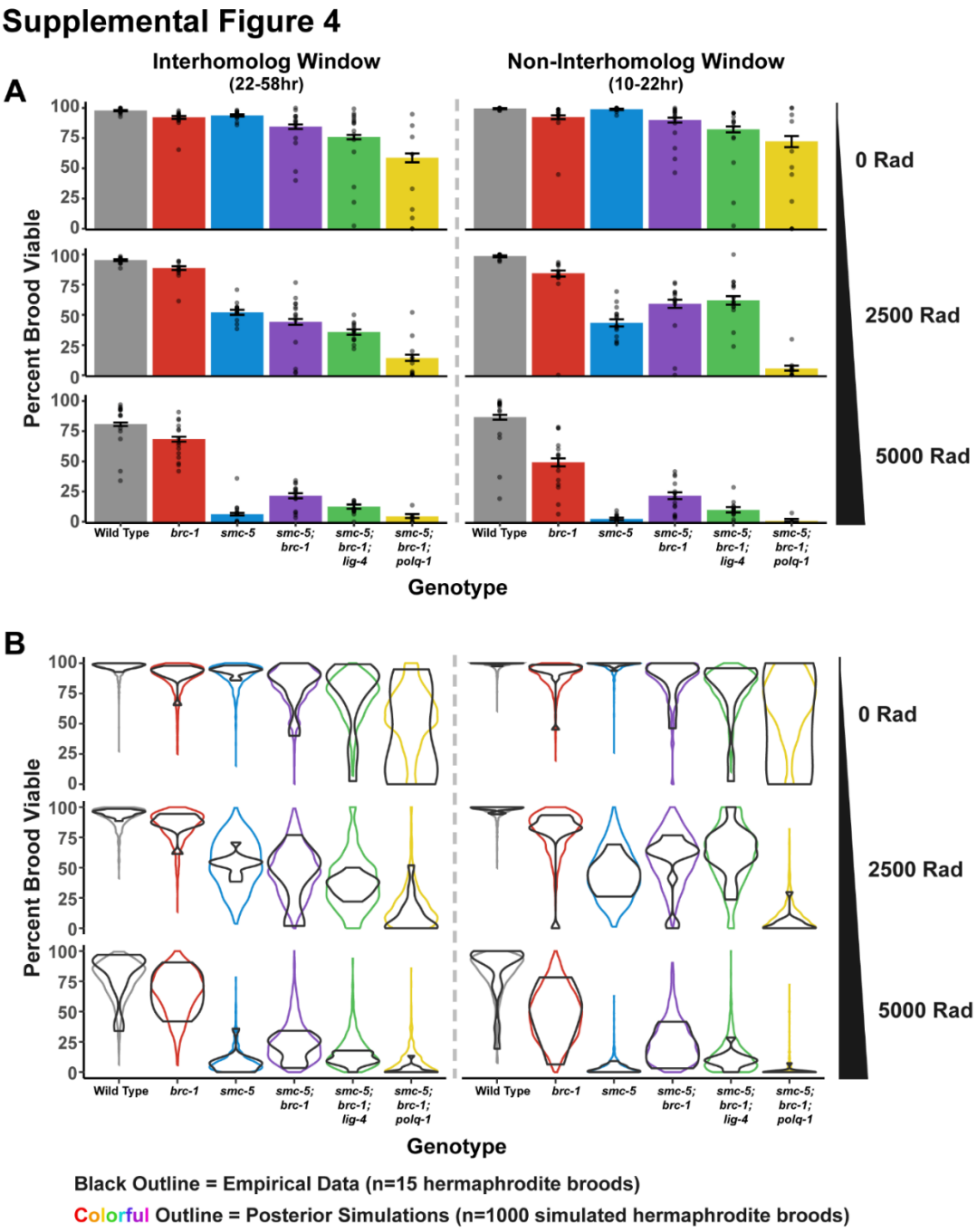

Figure S3.4. Brood viability results following irradiation. A) Brood viability results following irradiation at doses of 0, 2500, or 5000 Rads. Bars represent the population brood viability, while points represent the brood viabilities of individual hermaphrodites scored. Error bars indicate 95% Binomial confidence intervals of the population brood viability. Specific counts are presented in Table S3.3, S3.4. B) Violin plots of empirical brood viabilities from individual hermaphrodites scored (displayed as points in A) and posterior simulations from the Beta-Binomial model fit to the data (Figure 3.4A, see Methods). In all panels, vertical dashed grey lines separate interhomolog (22-58hr post heat shock) and non-interhomolog window (10-22hr post heat shock) timepoints.

To assess the differential sensitivities of *smc-5*, *brc-1*, and *smc-5;brc-1* mutants across meiotic prophase I, we compared the 95% credible intervals of the gamma estimates for each genotype within the interhomolog and the non-interhomolog windows for both moderate (2500 Rads) and high (5000 Rads) irradiation doses (Figure 3.4A). Across all irradiation doses and timepoints, we note that loss of *smc-5* conveys a greater sensitivity to exogenous DNA damage than loss of *brc-1* (Figure 3.4A), emphasizing that the SMC-5/6 complex prevents catastrophic defects following exogenous DNA damage induction. Moreover, the sensitivity of both single mutants to ionizing radiation is greater in the non-interhomolog window than in the interhomolog window (Figure 3.4A). This result demonstrates that meiotic cells are more dependent upon these complexes to resolve DSBs when the homolog is unavailable as a repair template.

At 2500 Rad of ionizing radiation, we found that mutation of both *smc-5* and *brc-1* differentially impacted radiation resilience within the interhomolog and non-interhomolog windows. In the interhomolog window, the *smc-5;brc-1* double mutant and *smc-5* single mutant gamma estimates overlap, indicating that loss of BRC-1 does not alter *smc*-5 mutant sensitivity at this timepoint (Figure 3.4A). Further, *brc-1* mutant gamma estimates are indistinguishable from wild type within the interhomolog window (Figure 3.4A); therefore, the absence of an interaction may reflect the dispensability of BRC-1 in early prophase I for progeny survival when DNA damage levels are not extreme. In the non-interhomolog window, however, we observe a striking resilience to exogenous DSBs in *smc-5;brc-1* double mutants as compared to *smc-5* single mutants (Figure 3.4A). This synthetic resilience is recapitulated across meiotic prophase I at 5000 Rads of ionizing radiation in *smc-5;brc-1* double mutants (Figure 3.4A). Thus, our data indicates that DNA damage sensitivity observed in *smc-5* mutants is enhanced by BRC-1-mediated functions.

BRC-1 is known to repress both NHEJ and TMEJ in multiple organisms, including *C. elegans* (Huen *et al.* 2010; Li *et al.* 2020; Kamp *et al.* 2020). We hypothesized that error prone repair pathways may be activated in *smc-5;brc-1* double mutants to resolve DSBs and abrogate the DNA repair defects associated with *smc-5* mutation. To test whether NHEJ and/or TMEJ contribute to the ionizing radiation resilience observed in *smc-5;brc-1* double mutants, we created *smc-5;brc-1;lig-4* and *smc-5;brc-1;polq-1* triple mutants which are defective in NHEJ and TMEJ respectively. We found that *smc-5;brc-1;lig-4* mutants exhibited only mild effects on

radiation sensitivity compared to the *smc-5;brc-1* double mutant alone (Figure 3.4A). At 2500 Rads of radiation, the gamma estimate of *smc-5;brc-1;lig-4* triple mutants in the interhomolog window was slightly reduced relative to *smc-5;brc-1* double mutants, indicating that NHEJ only subtly contributes to progeny survival in early prophase I (Figure 3.4A). Inversely, *smc-5;brc-1;lig-4* mutants were more resilient to radiation than the *smc-5;brc-1* double mutant in the non-interhomolog window, indicating that NHEJ may deleteriously impact the viability of nuclei at this stage. Triple *smc-5;brc-1;lig-4* mutants exhibit slightly reduced gamma estimates throughout prophase I following exposure to 5000 Rads of radiation compared to *smc-5;brc-1* double mutants (Figure 3.4A). Thus, our data indicates that the contributions of NHEJ to embryonic viability in *smc-5;brc-1* mutants differ depending on the meiotic stages of nuclei and extent of DNA damage. At moderate doses of radiation, NHEJ promotes gamete viability in early meiotic prophase I but may have negative effects in late prophase I. Conversely, as the levels of DNA damage increase, NHEJ provides a consistently beneficial effect to progeny survival in *smc-5;brc-1* mutants. Moreover, the effect of *lig-4* mutation is insufficient to fully account for the synthetic resilience of the *smc-5;brc-1* double mutant compared to *smc-5* mutants alone, suggesting that NHEJ is not the primary mechanism of DNA repair in meiotic cells when both SMC-5/6 and BRC-1 are lost.

In contrast to the subtle effects on DNA repair produced in our *smc-5;brc-1;lig-4* mutant, we observed a striking effect at all doses and timepoints scored in a *smc-5;brc-1;polq-1* mutant as compared to the *smc-5;brc-1* mutant. Even at the moderate dose of 2500 Rads, loss of POLQ-1 caused dramatic sensitization of *smc-5;brc-1* mutants to ionizing radiation (Figure 3.4A). This effect was particularly strong in the non-interhomolog window, where *smc-5;brc-1;polq-1* mutants were nearly sterile following ionizing radiation treatment regardless of irradiation dose (Figure 3.4A). These results strongly indicate that *smc-5;brc-1* deficient germ cells exposed to exogenous DNA damage are dependent upon TMEJ for fertility.

Taken together, the results of our irradiation analysis indicate that both SMC-5/6 and BRC-1 contribute to gamete viability following ionizing radiation treatment, with loss of SMC-5/6 having far greater consequences for the gamete than loss of BRC-1 (Figure 3.4C). As *brc-1* mutation confers synthetic resilience to radiation in *smc-5* mutants, we provide evidence that some functions of BRC-1 contribute to the meiotic DSB repair defects associated with *smc-5* mutation (Figure 3.4C). Further, we find that TMEJ is vital to radiation resilience in *smc-5;brc-1*

mutants, suggesting that this pathway compensates for the DNA repair deficiencies incurred when SMC-5/6 and BRC-1 are both lost (Figure 3.4C). Repression of TMEJ by BRC-1 may therefore be deleterious to reproductive success in *smc-5* mutants by enabling more severe DNA repair errors to occur.

BRC-1 localization is independent of SMC-5/6

To determine whether the genetic interactions we observed between BRC-1 and SMC-5/6 in our irradiation experiments coincide with a dependency on SMC-5/6 for proper BRC-1 localization, we first examined GFP::BRC-1 by immunofluorescence in both wild type and *smc-5* mutant germlines. Similar to previous studies (Janisiw *et al.* 2018; Li *et al.* 2018), we observed that BRC-1 localizes as a nuclear haze in the premeiotic tip through early pachytene and becomes associated with the synaptonemal complex during the progression of pachytene in wild type germlines (Figure S3.5). In late pachytene, BRC-1 relocates to the short arms of the bivalents, where it can be visualized at diplotene as short tracks on the compacted chromosome arms (Figure S3.5). When we examined *smc-5* mutants, the general pattern of GFP::BRC-1 localization across meiotic prophase was similar to wild type, except in the premeiotic tip where GFP::BRC-1 formed bright foci (Figure S3.5). Given that BRD-1, the obligate heterodimeric partner of BRC-1, was found to form a similar localization in *smc-5* mutants (Wolters *et al.* 2014), the bright GFP::BRC-1 foci in the pre-meiotic tip likely mark BRC-1 localization to collapsed replication forks (Bickel *et al.* 2010; Wolters *et al.* 2014). Our data therefore indicate normal localization of BRC-1 does not require SMC-5/6.

To assess if BRC-1 changes localization in response to exogenous DSBs, we exposed wild type and *smc-5* mutant germlines to 5000 Rads of ionizing radiation and again examined germline GFP::BRC-1 by immunofluorescence. We found that the general pattern of GFP::BRC-1 localization appeared normal in both wild type and *smc-5* mutants following irradiation (Figure S3.5). Taken together, our results suggest that BRC-1 localization is not altered following the induction of exogenous DSBs even when SMC-5/6 complex function is lost.

SMC-5/6 localization is independent of BRC-1

To determine whether SMC-5/6 localization is dependent upon BRC-1, we generated an endogenous *smc-5* allele which codes for the auxin-inducible degron (AID*) and 3xFLAG epitope tags on the C terminus (*smc-5(syb3065[AID*::3xFLAG])*). The *smc-5(syb3065)* allele

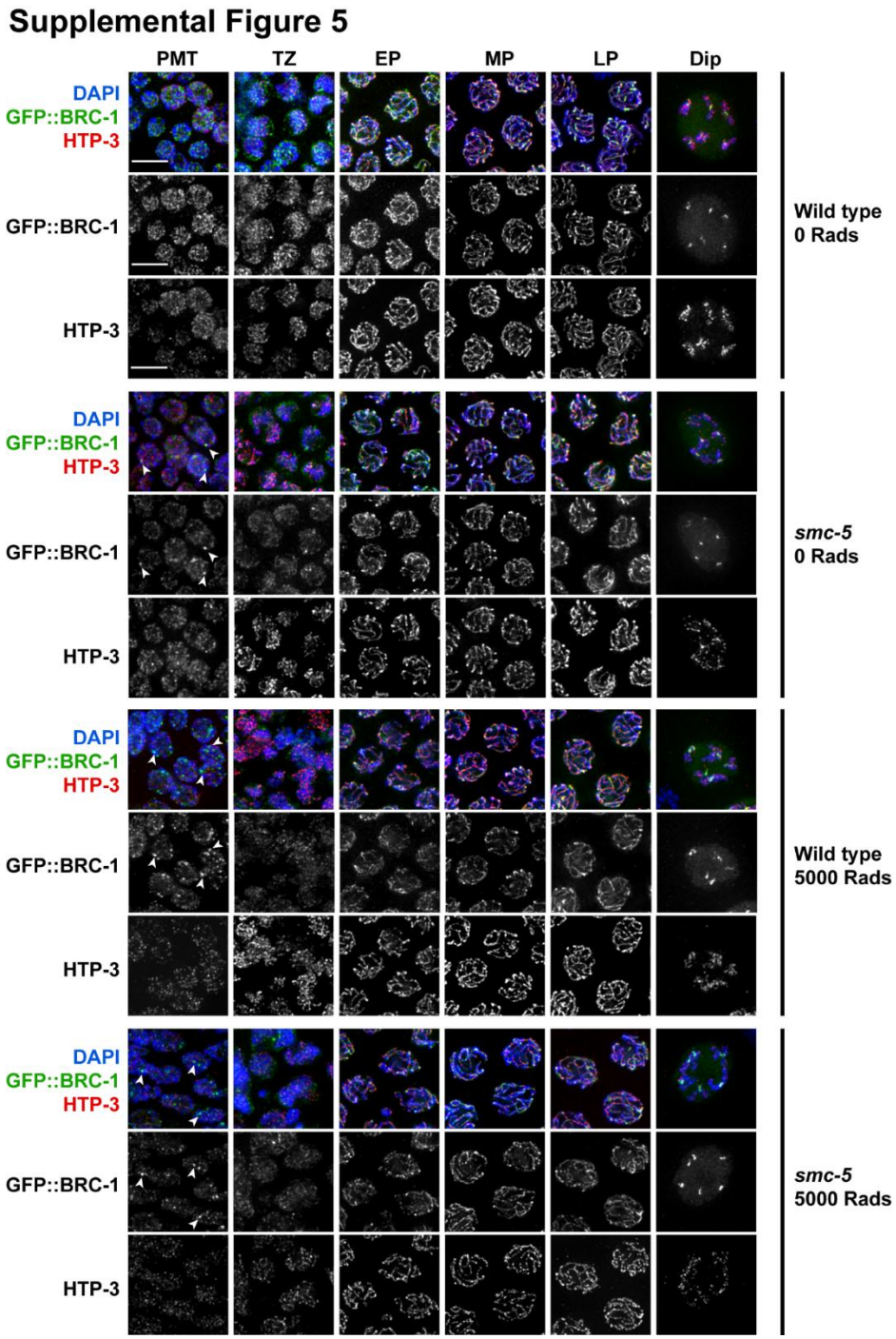

Figure S3.5. SMC-5/6 is not required for GFP::BRC-1 localization. Deconvolved widefield images of germline nuclei stained for GFP (GFP::BRC-1), chromosome axis protein HTP-3, and DAPI (DNA) in a wild type or *smc-5(ok2421)* mutant background and treated with 0 or 5000 Rads of ionizing radiation. Scale bars represent 5μm. Stages of meiotic nuclei were determined based on DAPI morphology and are listed on the top of the figure (PMT = premeiotic tip, TZ = transition zone, EP = early pachytene, MP = mid pachytene, LP = late pachytene, Dip = Diplotene). Arrowheads indicate GFP::BRC-1 foci.

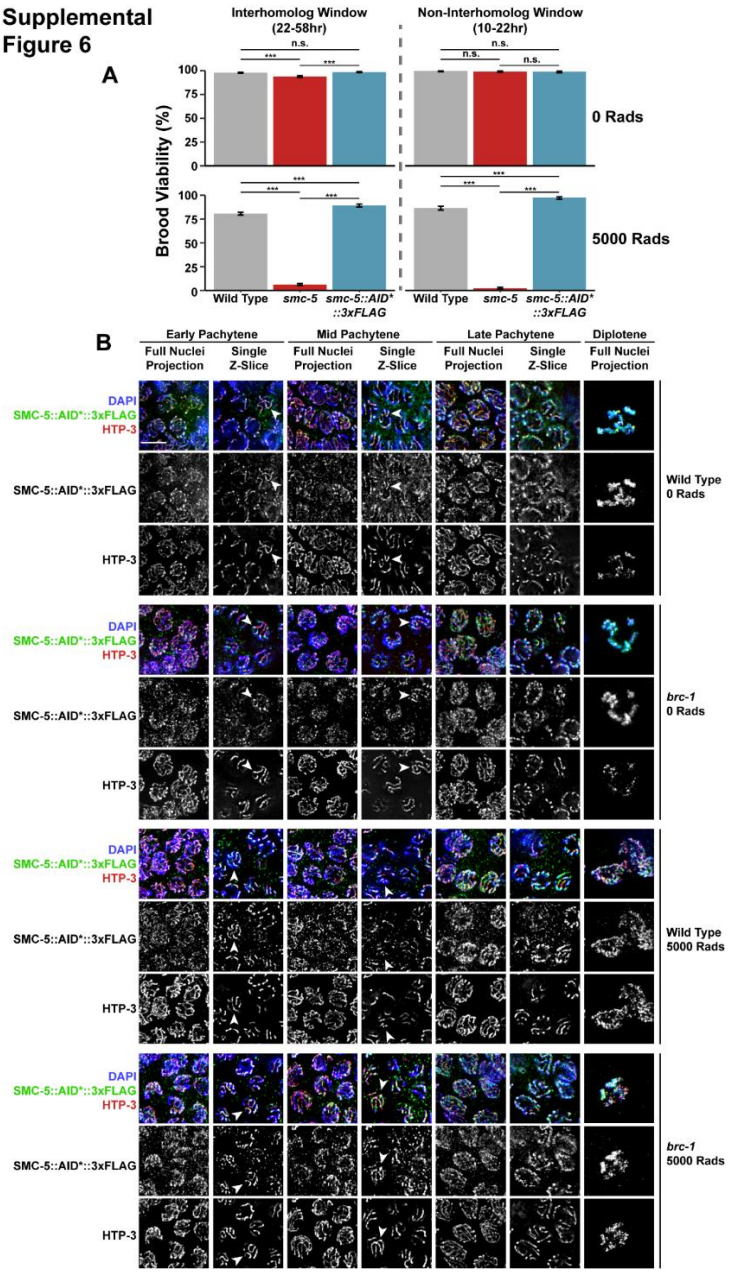

Figure S3.6. BRC-1 is not required for SMC-5::AID*::3xFLAG localization. A) Brood viability of wild type, *smc-5(ok2421)*, and *smc-5(syb3065)* hermaphrodites exposed to 0 or 5000 Rads of ionizing radiation. Bars represent the population brood viability of each strain. P values were calculated by Fisher's Exact Test (n.s. = not significant $p>0.05$, *** $p<0.001$). Error bars represent the 95% Binomial confidence interval of the brood viability estimate. B)Deconvolved images of germline nuclei stained for AID* (SMC-5::AID*::3xFLAG), chromosome axis protein HTP-3, or DAPI (DNA) in a wild type or *brc-1(xoe4)* mutant background and treated with 0 or 5000 Rads of ionizing radiation. Scale bars represent 5µm. Stages of meiotic nuclei are determined based on DAPI morphology and are listed at the top of the figure. For each image, a max intensity projection of whole nuclei and single z-slices are displayed to demonstrate the relative localization of SMC-5 and HTP-3. Arrowheads indicate examples of colocalization between HTP-3 and SMC-5::AID*3xFLAG.

Supplemental Figure 7

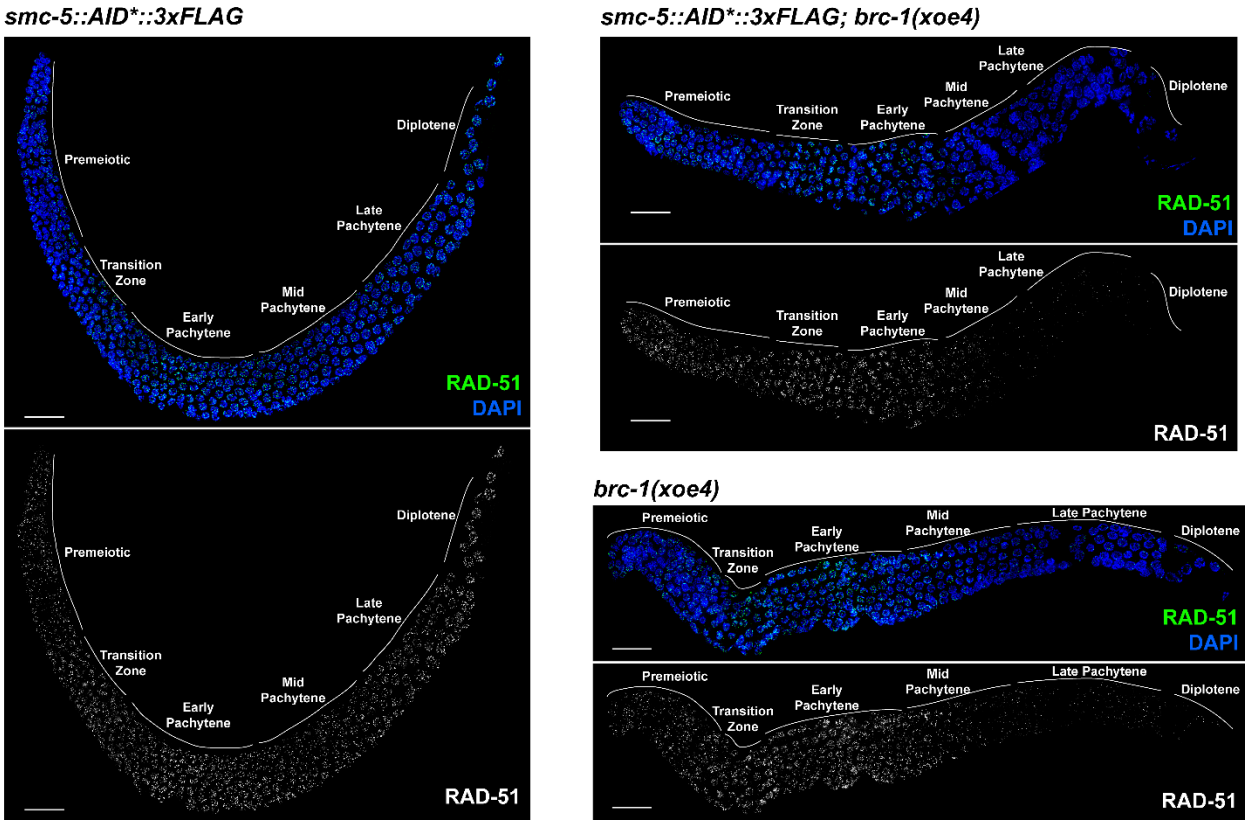

Figure S3.7. SMC-5::AID*::3xFLAG does not inhibit RAD-51 localization to irradiation-induced DSBs. Deconvolved images of whole extruded germlines stained for RAD-51 and DAPI. All germlines were exposed to 5000 Rads of ionizing radiation and were dissected within 1 hour of the radiation treatment. Loss of *brc-1* impedes RAD-51 localization in mid/late pachytene (Janisiw *et al.* 2018; Li *et al.* 2018), and this phenotype is not recapitulated nor enhanced by the *smc-5(syb3065)* allele. Grey lines and labels demarcate the mitotic and meiotic stages of the germline. Scale bars represent 20µm.

did not confer sensitivity to ionizing radiation nor an alteration in RAD-51 loading, suggesting that the tag does not impair SMC-5/6 complex function (Figures S3.6A and S3.7). We examined the localization of SMC-5::AID*::3xFLAG in both wild type and *brc-1* mutants (Supplemental Figure S3.6B). Contrary to a prior study that indicates SMC-5/6 localizes to the chromatin throughout meiotic prophase (Bickel *et al.* 2010), we found that SMC-5 staining in early and mid pachytene was primarily localized to the chromosome axis, marked with HTP-3 (Figure S3.6B). This localization pattern changed upon entry into late pachytene when SMC-5 appears more punctate and less specific to the axis (Figure S3.6B). Similar to the previous analysis (Bickel *et al.* 2010), we found SMC-5 localizes to the chromatin on the compacting bivalent chromosomes at diplotene (Figure S3.6B). The pattern of SMC-5 localization was not disrupted in a *brc-1*

mutant, and similarly was not altered following exposure to 5000 Rads of ionizing radiation (Figure S3.6). Thus, the localization of SMC-5/6 does not depend upon the activity of BRC-1 and is not altered following induction of exogenous DNA damage at the levels we tested.

Discussion

Meiotic cells must coordinate DNA repair pathway engagement to ensure both formation of interhomolog crossovers and repair of all DSBs. The highly conserved proteins SMC-5/6 and BRC-1 promote accurate DSB repair, but the specific DNA repair steps that these proteins regulate have remained unclear. We find that SMC-5/6 and BRC-1 both act to repress intersister crossovers, and further demonstrate that BRC-1 specifically influences noncrossover intermediate processing. We also observe that mutants for *brc-1* incur DNA repair defects at mid pachytene, as evidenced by increased engagement of error prone repair pathways. By comparing the germ cell resilience of *smc-5*, *brc-1*, and *smc-5;brc-1* mutants to ionizing radiation, we show that SMC-5/6 and BRC-1 are especially important for DSB repair in late meiotic prophase I. Further, we reveal that BRC-1 enhances the meiotic DNA repair defects of *smc-5* mutants and provide evidence that this interaction is in part underpinned by BRC-1 dependent repression of TMEJ. Taken together, our study illuminates specific functions and interactions of highly conserved DNA repair complexes in promoting germline genome integrity.

Functions of BRC-1 in *C. elegans* meiotic DNA repair

The work presented in this study demonstrates that meiotic cells deficient in BRC-1 exhibit multiple DNA repair defects, including reduced noncrossover conversion tract length, elevated rates of intersister crossovers, and engagement of error prone DSB repair mechanisms at the mid-pachytene stage. What functions of BRC-1 may underpin these phenotypes? Accumulating evidence in other model systems supports roles for BRCA1 in regulating many early steps in recombination including DSB resection, strand invasion, and D-loop formation (Chen *et al.* 2008; Chandramouly *et al.* 2013; Cruz-García *et al.* 2014; Zhao *et al.* 2017; Kamp *et al.* 2020). We propose that perhaps some of these functions of BRC-1 are conserved in *C. elegans*.

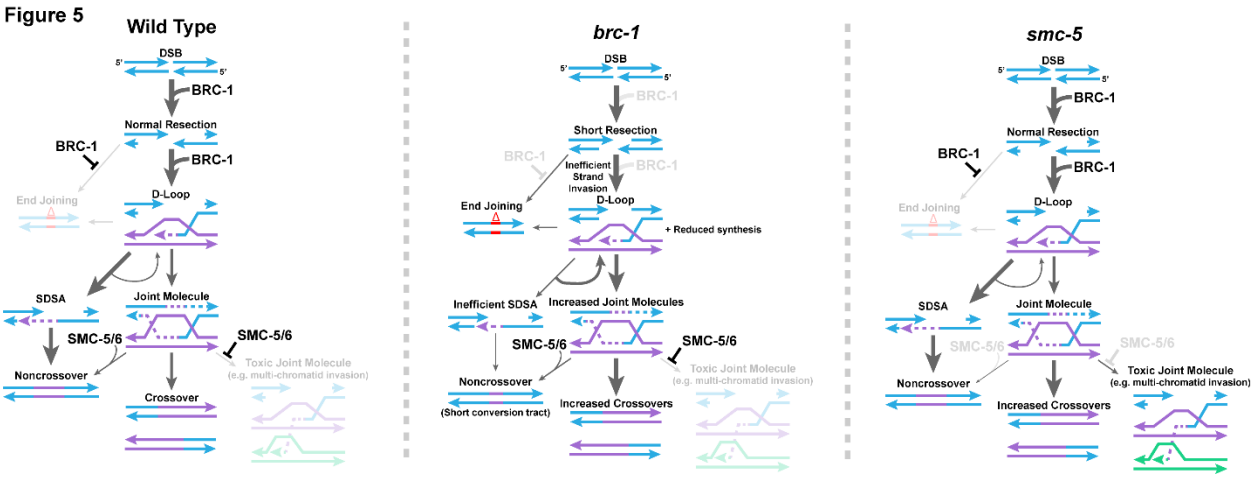

Figure 3.5. Model of BRC-1 and SMC-5/6 function in *C. elegans* intersister DSB repair. Displayed is a proposed model for the functions of BRC-1 and SMC-5/6 in regulating intersister DSB repair in the *C. elegans* germline. Under wild type conditions, BRC-1 promotes efficient resection of the damaged chromatid (blue) and facilitates strand invasion and extension with the sister chromatid (purple). BRC-1 also inhibits TMEJ either through direct antagonism of this pathway or indirectly by promoting efficient recombination. Following strand extension, the majority of D-loop intermediates are dissolved and repaired through SDSA, which is efficient due to BRC-1 promoted resection of the second end of the DSB. A minority of D-loops will proceed to form joint molecules, which may potentially be preferentially resolved as noncrossovers via the action of SMC-5/6 or as crossovers in an SMC-5/6 independent manner. In addition, SMC-5/6 inhibits the formation of toxic joint molecule intermediates, such as multi-chromatid joint molecules. In a *brc-1* mutant, DSBs are not resected to wild type levels and strand invasion is inefficient. Reduced resection limits the efficiency of second end capture in SDSA, reducing noncrossovers through this pathway. Further, limited strand extension reduces the extent of gene conversion in noncrossovers generated by successful SDSA. Failure in SDSA leads to increased DSB reinvasion of repair templates, contributing to the tandem duplications observed in mutants for BRCA1 (Chandramouly *et al.* 2013; Kamp *et al.* 2020). In addition, either due to absence of direct inhibition by BRC-1 or inefficiencies in recombination, end joining (particularly TMEJ) becomes activated to resolve DSBs. However, reduced resection does not inhibit joint molecule formation, leading to more of these intermediates which are preferentially resolved as crossovers. Finally, in an *smc-5* mutant, early steps in DSB repair proceed normally. However, absence of SMC-5/6 results in unconstrained joint molecule formation, including toxic intermediates. Failure in SMC-5/6 action to promote noncrossover repair further increases the proportion of joint molecules which are resolved as crossovers.

While a growing body of research in budding yeast, mammalian systems, and *Arabidopsis* suggests that SDSA is the primary pathway for the formation of noncrossovers in meiosis (Hunter 2015), the mechanisms by which *C. elegans* noncrossover recombination occurs is unknown. Distinguishing between recombination mechanisms underlying noncrossover repair requires the reliable identification of heteroduplex DNA sequences on both sides of the DSB. As the current version of the ICR assay is unable to consistently detect heteroduplex DNA on both sides of the DSB, we are unable to delineate the recombination pathway which produces intersister/intrachromatid noncrossovers. Despite this caveat, the unique effect of *brc-1* mutation on the extent of ICR assay noncrossover gene conversion, but not crossover gene conversion, suggests that homolog-independent noncrossovers arise from a distinct intermediate from crossovers in *C. elegans*. This result is consistent with a model in which SDSA is a primary mechanism of intersister noncrossover recombination in the *C. elegans* germline (Figure 3.5).

The size of an SDSA noncrossover conversion tract depends upon the extent of heteroduplex DNA present following strand annealing, which is primarily determined by the length of DNA strand extension (Keelagher *et al.* 2011; Guo *et al.* 2017; Marsolier-Kergoat *et al.* 2018). Human BRCA1 promotes strand invasion and D-loop formation (Zhao *et al.* 2017), which may influence the efficiency of strand extension. Our conversion tract data raises the possibility that BRC-1 influences the formation and/or stability of strand invasion intermediates, thereby promoting the formation of long ICR assay noncrossover gene conversion events (Figure 3.5).

Our data also demonstrate that *brc-1* mutants exhibit elevated intersister crossovers. If BRC-1 only functions to promote strand invasion and D-loop formation, then we expected *brc-1* mutation to reduce intersister crossovers and not increase their occurrence. Previous studies have also suggested that BRCA1/BRC-1 regulates DSB resection, and we propose that this function better accounts for the observed increase in intersister crossovers (Chandramouly *et al.* 2013; Kamp *et al.* 2020). Specifically, studies have posited that BRCA1-promoted long range DSB resection may be important for the efficiency of SDSA by ensuring sufficient single stranded DNA is exposed on the second end of the DSB to facilitate strand annealing (Chandramouly *et al.* 2013; Kamp *et al.* 2020). While sufficient resection may be critical in resolving noncrossovers, work in budding yeast has shown that long range resection is not required for the efficient formation of joint molecules (Zakharyevich *et al.* 2010). Thus, reduced length of DNA

resection due to a *brc-1* mutation may impede SDSA and therefore increase the probability that DSBs will form joint molecule intermediates, thereby promoting intersister crossover outcomes.

Reduced resection in conjunction with inefficient strand invasion and synthesis during recombination may further explain the ectopic engagement of TMEJ observed in *brc-1* mutants (Kamp *et al.* 2020). Short range resection provides sufficient substrate for TMEJ (Ramsden *et al.* 2022), which in combination with inefficient homology search may provide more opportunity for TMEJ engagement. BRC-1 is also required in late meiotic prophase I for the loading and/or maintenance of RAD-51 at irradiation induced DSBs (Janisiw *et al.* 2018; Li *et al.* 2018). Defects in RAD-51 localization may further exacerbate the likelihood of error prone DSB repair at these meiotic stages. Overall, our data is consistent with a model in which BRC-1 promotes multiple DSB repair steps, including resection and the formation of early strand invasion intermediates, to facilitate intersister noncrossover repair (Figure 3.5).

Functions of SMC-5/6 in *C. elegans* meiotic DSB repair

Our experiments demonstrate that SMC-5/6 acts to repress intersister crossover recombination in the early stages of meiotic prophase I. We do not find evidence, however, of prominent roles for SMC-5/6 in regulating ICR assay conversion tracts nor limiting error prone repair outcomes. These relatively subtle phenotypes appear at first incongruous with the known severe defects associated with loss of SMC-5/6 in *C. elegans*, which include chromosome fragmentation, large mutations, and transgenerational sterility (Bickel *et al.* 2010; Volkova *et al.* 2020). The ICR and IH assay experiments, however, are limited to the detection of DSB repair outcomes which encode a functional protein product. Thus, many of the severe mutations associated with SMC-5/6 deficiency may disrupt the coding sequence in the ICR or IH assays and therefore escape our detection (Volkova *et al.* 2020).

In budding yeast, Smc5/6 prevents the accumulation of toxic interchromosomal attachments and recombination intermediates (Xaver *et al.* 2013; Lilienthal *et al.* 2013; Copsey *et al.* 2013). Prior evidence in *C. elegans* suggests that some of these functions are likely conserved, as double mutants for *smc-5* and the BLM helicase homolog *him-6* are sterile and display chromatin bridges indicative of persistent interchromosomal attachments (Hong *et al.* 2016). This synthetic phenotype suggests that these two complexes act in parallel to prevent the accumulation of joint molecules. A previous study (Almanzar *et al.* 2021) and the data we present here reveal that both SMC-5/6 and HIM-6 repress intersister crossovers. The synthetic

sterility associated with loss of both SMC-5/6 and HIM-6 then may be a product of parallel functions for these proteins in limiting and/or resolving joint molecules. Although BLM is known to play multiple roles in regulating recombination, a core function of this helicase is in antagonism of joint molecule formation and promotion of noncrossover recombination (McVey *et al.* 2004; Weinert and Rio 2007; Schvarzstein *et al.* 2014). SMC-5/6 in *C. elegans* meiosis may therefore act as a second line of defense to ensure the elimination of inappropriate joint molecule intermediates which have formed more stable configurations (Figure 3.5). Under this model, we would expect accumulation of intersister joint molecules in an *smc-5* mutant and therefore elevated intersister crossovers, as observed in our *smc-5* ICR assay and EdU labeling experiments. Our observation that *smc-5* mutation does not alter ICR assay conversion tracts is also consistent with a model in which SMC-5/6 influences recombination following joint molecule formation. Taken together, our data indicates that SMC-5/6 is not required for homolog-independent meiotic recombination and instead reveals a function for this complex in limiting crossover exchanges between sister chromatids.

Temporal regulation of error-prone meiotic DSB repair

In both the ICR and IH assays we performed in *brc-1* mutants and in the IH assay we performed in *smc-5* mutants, we identified mutagenic repair events specifically at the 22-34hr timepoint, corresponding to oocytes in mid pachytene at the time of Mos1-excision induced DSB formation. Further, the repair events we identified frequently displayed microhomologies flanking the deletion site – a characteristic signature of TMEJ. While our dataset cannot definitively demonstrate that these events are the product of TMEJ, previous evidence and the nature of the break repair products strongly suggest that they originate from this pathway (Kamp *et al.* 2020). The limited temporal window in which we identified these events suggests that the activity of TMEJ may be relegated to later stages of meiotic prophase I. There are a number of important events which coincide at the mid/late pachytene transition of *C. elegans* meiosis, including a MAP kinase phosphorylation cascade, designation of interhomolog crossovers, a switch from RAD-50 dependence to independence for loading of RAD-51 to resected DNA, and loss of access to the homolog as a ready repair template (Church *et al.* 1995; Kritikou *et al.* 2006; Hayashi *et al.* 2007; Lee *et al.* 2007; Rosu *et al.* 2011; Yokoo *et al.* 2012; Nadarajan *et al.* 2016). These events may correspond to a switch in cellular "priorities" from ensuring interhomolog recombination to promoting repair of all residual DSBs even through error prone mechanisms.

By repairing all residual DSBs (even in the wake of sequence errors), germ cells avoid catastrophic chromosome fragmentation during the meiotic divisions.

During the mid to late pachytene transition, an important function of BRC-1 (and to a lesser extent SMC-5/6) may be to prevent TMEJ either by antagonizing this pathway or facilitating efficient recombination. Our irradiation experiments revealed that both *brc-1* and *smc-5* mutant oocytes exhibit greater sensitivity to exogenous DNA damage in late stages of prophase I, suggesting that cellular requirements for efficacious DSB repair change during the transition to late pachytene. Moreover, during the late pachytene stage, several changes regarding BRC-1 occur: 1) BRC-1 protein localization changes; and, 2) BRC-1 is required to load (and/or stabilize) RAD-51 filaments. These changes in localization and function of BRC-1 at mid/late pachytene coincide with an increase in mutagenic DSB repair events with characteristic TMEJ signatures. Our irradiation experiments revealed that *smc-5;brc-1* double mutant oocytes throughout prophase I are dependent upon TMEJ DNA polymerase θ homolog *polq-1* for viability. If BRC-1 functions which repress TMEJ (Kamp *et al.* 2020) are specific to late prophase, then this result suggests that many DSBs in *smc-5;brc-1* mutants induced in early prophase may not be repaired until mid/late pachytene, when TMEJ is active. Spatiotemporal transcriptomic analysis has shown that *polq-1* is expressed throughout meiotic prophase I (Tzur *et al.* 2018). As we only identified error-prone resolution of DSBs induced at mid pachytene, our findings raise the possibility that BRC-1 independent mechanisms may repress TMEJ in early/mid pachytene. Our results in *brc-1* mutants therefore lay the groundwork for future research delineating the temporal regulation of error-prone meiotic DSB repair. Taken together, our study reveals that the engagement of error-prone and recombination DSB repair pathways are differentially regulated during the course of *C. elegans* meiotic prophase I.

Interaction between BRC-1 and SMC-5/6 in meiotic DNA repair

Our irradiation experiments assessing the viability of *smc-5*, *brc-1*, and *smc-5;brc-1* mutant oocytes reveal that functional BRC-1 enhances the DNA repair defects of *smc-5* mutants. By further ablating error prone repair pathways, we also demonstrated that *smc-5;brc-1* mutants are dependent upon TMEJ for viability following irradiation. However, this genetic interaction does not coincide with changes in either SMC-5/6 or BRC-1 localization in respective mutants. Taken together, we suggest that the observed genetic relationships between BRC-1 and SMC-5/6 are likely not derived from direct interaction between these complexes, nor action on shared

substrates, but rather arise from their respective sequential roles in regulation of DSB repair. A similar model was proposed by Hong *et al.* 2016 which postulated that early recombination defects in *brc-1* mutants may alleviate the toxic recombination intermediates formed in *smc-5;him-6* double mutants. We expand upon this model to demonstrate that this genetic relationship observed in *smc-5;him-6;brc-1* mutants is recapitulated in *smc-5;brc-1* double mutants, indicating that this interaction is not unique to the triple mutant context.

How might DNA repair defects in *brc-1* mutants ameliorate genomic instability associated with *smc-5* mutation? If *smc-5* mutants accumulate toxic joint molecules, then we would expect deficiencies in earlier recombination steps to limit the formation of these problematic intermediates and therefore alleviate the effects of *smc-5* mutation. Our analysis of homolog independent recombination in *brc-1* mutants revealed phenotypes which are consistent with this protein regulating both DSB resection and strand invasion. Work in budding yeast has shown that the additional ssDNA generated by long range resectioning of a DSB is used for homology search (Chung *et al.* 2010). Inefficient resection in *brc-1* mutants may reduce the extent of homology which could anneal to heterologous templates and contribute to toxic joint molecules (Figure 3.5). Conversely, resection defects of *brc-1* mutants could increase the risk for toxic recombination intermediates in *smc-5* mutants by limiting the efficiency of SDSA and therefore biasing DSBs to form joint molecules. However, compromised strand invasion and D-loop formation in *brc-1* mutants could also limit the capacity for DSBs to form multi-chromatid engagements. Finally, increased TMEJ activity in *smc-5;brc-1* mutants could resolve DSBs before they form recombination intermediates, thereby bypassing requirements for SMC-5/6 in DSB repair. In summation, our study reveals an interplay between BRC-1 and SMC-5/6 in regulating meiotic DSB repair.

Acknowledgements

We thank the CGC (funded by National Institutes of Health P40 OD010440) for providing strains. We also thank J. Engebrecht for generously sharing strains carrying the *brc-1(xoe4)* and *GFP::brc-1* alleles. We thank C. Cahoon, A. Naftaly, and N. Kurhanewicz for thoughtful comments on this manuscript. This work was supported by the National Institutes of Health T32GM007413 and Advancing Science in America (ARCS) Foundation Award to E.T; National Institutes of Health R25HD070817 to A.S.; Genetics Training Grant 5T32M007464-42 to

D.E.A.; a Pilot Project Award from the American Cancer Society, 1R355GM128804 grant from NIGMS, and start-up funds from the University of Utah to O.R.; and National Institutes of Health R00HD076165 and R35GM128890 to D.E.L. D.E.L. is also a recipient of a March of Dimes Basil O'Connor Starter Scholar award and Searle Scholar Award.

Competing Interests

The authors declare no conflicts of interest.

Materials and Methods

Caenorhabditis elegans strains and maintenance

Caenorhabditis elegans strains were maintained at 15°C or 20°C on nematode growth medium (NGM) plates seeded with OP50 bacteria. All experiments were performed in the N2 genetic background of *C. elegans* and animals were maintained at 20°C for at least two generations preceding an experiment.

Strains used in this study include:

N2 (wild type)

AV554 (*dpy-13(e184sd) unc-5(ox171::Mos1)*/ nT1 (qIs51) IV; KrIs14 (*phsp-16.48::MosTransposase*; *lin-15B*; *punc-122::GFP*) / nT1 (qIs51) V)

CB791 (*unc-5(e791)* IV), DLW14 (*unc-5(lib1*[ICR assay *pmyo-3::GFP(-)*; *unc-119(+)*; *pmyo-2::GFP(Mos1)*]) IV; KrIs14 (*phsp-16.48::MosTransposase*; *lin-15B*; *punc-122::GFP*) V)

DLW23 (*smc-5(ok2421)*/mIn1 [*dpy-10(e128)* mIs14] II; *unc-5(lib1*[ICR assay *pmyo-3::GFP(-)*; *unc-119(+)*; *pmyo-2::GFP(Mos1)*]) IV; KrIs14 (*phsp-16.48::MosTransposase*; *lin-15B*; *punc-122::GFP*) V)

DLW81 (*smc-5(ok2421)*/mIn1[*dpy-10(e128)* mIs14] II; *unc-5(e791)* IV)

DLW131 (*smc-5(ok2421)*/mIn1[*dpy-10(e128)* mIs14] II; *lig-4(ok716) brc-1(xoe4)* III)

DLW134 (*smc-5(ok2421)*/mIn1[*dpy-10(e128)* mIs14] II; *polq-1(tm2572) brc-1(xoe4)* III)

DLW137 (*smc-5(ok2421)*/mIn1 [mIs14 *dpy-10(e128)*] II; *brc-1(xoe4)* III)

DLW157 (*brc-1(xoe4)* III; *unc-5(e791)* IV)

DLW175 (*smc-5(syb3065* [::AID*::3xFLAG]*)* II; *brc-1(xoe4)* III)

DLW182 (*smc-5(ok2421)*/mIn1[*dpy-10(e128)* mIs14] II; *GFP::brc-1* III)

DLW202 (*smc-5(ok2421)*/mIn1 [*dpy-10(e128)* mIs14] II; *dpy-13(e184sd) unc-5(ox171::Mos1)*/ nT1 (qIs51) IV; KrIs14 [*phsp-16.48::MosTransposase*; *lin-15B?*; *punc-122::GFP*]/nT1 (qIs51) V)

DLW203 (*brc-1(xoe4)* III; *dpy-13(e184sd) unc-5(ox171::Mos1)*/ nT1 (qIs51) IV; KrIs14 [*phsp-16.48::MosTransposase*; *lin-15B*; *punc-122::GFP*]/nT1 (qIs51) V)

JEL515 (*GFP::brc-1* III)

JEL730 (*brc-1(xoe4)* III)

PHX3065 (*smc-5(syb3065* [::AID*::3xFLAG]*)* II)

YE57 (*smc-5(ok2421)*/mIn1 [mIs14 *dpy-10(e128)*] II)

Double and triple mutants which carried the *smc-5(ok2421)* and *brc-1(xoe4)* alleles incurred mutations within ~6-10 generations of propagation, as indicated by progeny with movement defects, body morphology defects, or the presence of male offspring. To minimize the risk of *de novo* suppressor or enhancer mutations influencing the phenotypes we observed in these mutants, we froze stocks of these double and triple mutants at -80°C within 3 generations of the strains' construction. All experiments using these strains were carried out on stocks which had been maintained for less than 1-2 months. If a strain began to segregate mutant phenotypes, a new isolate of the freshly generated strain was thawed from frozen stocks.

CRISPR/Cas9 genome editing

CRISPR/Cas9 genome editing was performed by SUNY Biotech to generate the *smc-5(syb3065)* allele in which the endogenous sequence of *smc-5* is modified at its C terminus to code for both an AID* tag (peptide sequence PKDPAKPPAKAQVVGWPPVRSYRKNVMVSCKSSGGPEAAAFVK) and a 3xFLAG tag (peptide sequence DYKDHDGDYKDHDIDYKDDDDK). The coding sequence of *smc-5*, the AID* tag, and the 3xFLAG tag were respectively connected by flexible GAGS peptide linkers. The repair template for this insertion was synthesized as a single strand oligo and was injected with Cas9 enzyme and a single guide RNA targeting the 12th exon of the *smc-5* locus. Successful integration was confirmed by PCR and Sanger sequencing. CRISPR edited strains were backcrossed three times to N2 before experiments were performed.

***C. elegans* brood viability assays and Bayesian hierarchical modeling analysis**

L4 stage hermaphrodite nematodes of each genotype to be scored were isolated 16-18hrs before irradiation was to be performed and were maintained at 15°C on NGM plates seeded with OP50.

These worms were then exposed to 0, 2500, or 5000 Rads of ionizing radiation from a Cs^{137} source (University of Oregon). Following irradiation, n=5 hermaphrodites of each genotype and treatment combination were placed onto individual NGM plates seeded with OP50 and were maintained at 20°C. At 10hrs, 22hrs, and 46hrs post irradiation, the irradiated hermaphrodites were transferred to new NGM plates seeded with OP50. 58hrs after irradiation, the parent hermaphrodites were discarded. The proportion of F1 progeny which hatched, did not hatch ('dead eggs' indicating embryonic lethality), or were unfertilized on each plate was scored 36-48hrs after the removal of the parent hermaphrodite from a plate. The brood size of each hermaphrodite was calculated as (hatched progeny) + (dead eggs). Brood viability at each timepoint was calculated as (hatched progeny) / (brood size). Brood viability assays were performed in triplicate with the exception of *smc-5(syb3065)*, which was replicated twice with n=5 hermaphrodites scored for each radiation treatment in each replicate.

Brood viabilities of individual hermaphrodites for each given genotype and irradiation treatment were analyzed using RStan (Stan Development Team 2021). The brood viability data of individual hermaphrodites (h) for each genotype (g), timepoint scored (t), and irradiation treatment (i) was fit to a Beta-Binomial model:

$$\text{Hatched Progeny}_{g,t,i,h} \sim \text{Binomial}(\text{n} = \text{Brood size}_{g,t,i,h}, \text{p}_{g,t,i})$$

$$\text{p}_{g,t,i} \sim \text{Beta}(\alpha_{g,t,i}, \beta_{g,t,i})$$

A metric (termed "gamma") for the effect of ionizing radiation on the observed brood viability of each genotype was calculated in the Generated Quantities block during MCMC sampling from the posterior probability distribution of the parameter p, defined as:

$$\text{gamma}_{g,t,i} = \frac{\text{p}_{g,t,i}}{\text{p}_{g,t,0\ \text{Rads}}}$$

In addition to the model fit statistics output from Stan, model fit was assessed by posterior simulations. The expected brood viability for 1000 parent hermaphrodites from each genotype, timepoint, and irradiation treatment were simulated (Figure S3.4B). For each simulated parent hermaphrodite, a brood size was sampled from the empirical data of the corresponding experimental group, values for α and β were sampled from the respective posterior probability distributions, and a value for p was simulated from a Beta distribution with shape parameters α and β. The number of hatching progeny were simulated ~Binomial (brood size, p).

Intersister/intrachromatid repair assay (ICR Assay)

ICR assays were performed as described in (Toraason *et al.* 2021a; c). Parent (P0) hermaphrodites for the ICR assay for each genotype were generated by crossing (see cross schemes detailed below).

ICR assay cross schemes:

1) Wild type (N2): P0 hermaphrodites were generated by crossing: (1) N2 males to DLW14 hermaphrodites to generate *unc-5(lib1)*/+ IV; KrIs14/+ V males; (2) F1 males to CB791 hermaphrodites to generate *unc-5(lib1)/unc-5(e791)* IV; KrIs14/+ V hermaphrodites.

2) *brc-1* mutant: P0 hermaphrodites were generated by crossing: (1) JEL730 males to DLW156 hermaphrodites to generate *brc-1(xoe4)* III; *unc-5(lib1)*/+ IV; KrIs14/+ V males; (2) F1 males to DLW157 hermaphrodites to generate *brc-1(xoe4)* III; *unc-5(lib1)*/*unc-5(e791)* IV; KrIs14/+ V hermaphrodites.

3) *smc-5* mutant: P0 hermaphrodites were generated by crossing: (1) YE57 males to DLW23 hermaphrodites to generate *smc-5(ok2421)*/mIn1 II; *unc-5(lib1)*/+ IV; KrIs14/+ V males; (2) F1 males to DLW81 hermaphrodites to generate *smc-5(ok2421)* II; *unc-5(lib1)*/*unc-5(e791)* IV; KrIs14/+ V hermaphrodites.

In brief, P0 hermaphrodites of the desired genotype were isolated 16-18hrs before heat shock and were maintained at 15°C. Heat shock was performed in an air incubator (refrigerated Peltier incubator, VWR Model VR16P) for one hour. The P0 worms were then allowed to recover at 20°C for nine hours. P0 hermaphrodites were placed onto individual NGM plates seeded with OP50 and maintained at 20°C. 22hrs, 34hrs, and 46hrs after heat shock, the P0 worms were transferred to new NGM plates seeded with OP50. 58hrs after heat shock, P0 hermaphrodites were removed from their NGM plates and discarded. Plates with P0 hermaphrodites were maintained at 20°C, while plates with F1 progeny were placed at 15°C.

F1 progeny were scored for GFP fluorescence ~54-70hrs after the P0 hermaphrodite was removed. ~18hrs before scoring, plates with F1 progeny were placed at 25°C to enhance GFP expression. Fluorescent phenotype scoring was performed on a Axio Zoom v16 fluorescence stereoscope (Zeiss). F1 progeny which expressed recombinant fluorescence phenotypes were isolated and lysed for sequencing (see Sequencing and analysis of ICR assay conversion tracts). Nonrecombinant progeny were discarded. If all progeny on a plate were in larval developmental

stages at the time of scoring, then the number of dead eggs and unfertilized oocytes were additionally recorded.

ICR assays in *brc-1(xoe4)* and *smc-5(ok2421)* mutants were replicated 4 times and the broods of at least 20 parent hermaphrodites scored in each replicate. The ICR assay in a wild type genetic background was performed once and combined with previous data (Toraason *et al.* 2021a).

Sequencing and analysis of ICR assay conversion tracts

Recombinant ICR assay progeny were placed in 10µL of 1x Worm Lysis Buffer for lysis (50mM KCl, 100mM TricHCl pH 8.2, 2.5mM $MgCl_2$, 0.45% IGEPAL, 0.45% Tween20, 0.3µg/µL proteinase K in ddH_2O) and were iteratively frozen and thawed three times in a dry ice and 95% EtOH bath and a 65°C water bath. Samples were then incubated at 60°C for one hour and 95°C for 15 minutes to inactive the proteinase K. Final lysates were diluted with 10µL ddH2O. Conversion tracts were PCR amplified using OneTaq 2x Master Mix (New England Biolabs). Noncrossover recombination products were amplified using forward primer DLO822 (5'-ATTTTAACCCTTCGGGGTACG-3') and reverse primer DLO823 (5'-TCCATGCCATGTGTTAATCCCA-3'). Crossover recombination products were amplified using forward primer DLO824 (5'-AGATCCATCTAGAAATGCCGGT-3') and reverse primer DLO546 (5'-AGTTGGTAATGGTAGCGACC-3'). PCR products were run on an Agarose gel and desired bands were isolated by gel extraction (QIAquick Gel Extraction Kit, New England Biolabs) and were eluted in ddH_2O. Amplicons were submitted for Sanger sequencing (Sequetech) with three primers. Noncrossovers were sequenced using DLO822, DLO823, and DLO1077 (5'-CACGGAACAGGTAGGTTTTCCA-3') and crossovers were sequenced using DLO824, DLO546, and DLO1077.

Sanger sequencing chromatograms were analyzed using Benchling alignment software (Benchling) to determine converted polymorphisms. Heteroduplex DNA signals were identified by two prominent peaks in the chromatogram at the site of a known polymorphism. Putative heteroduplexed samples were PCR amplified and submitted for sequencing a second time for confirmation as described above.

Samples which produced PCR products of the expected size but did not yield interpretable sequencing were subsequently analyzed using TOPO cloned amplicons. ICR assay locus amplicons were PCR amplified as described above but were immediately cloned into pCR2.1 vector using the Original TOPO-TA^{TM} Cloning Kit^{TM} (Invitrogen) following kit instructions.

Putative successful amplicon clones were identified by PCR amplification using 2xOneTaq Master Mix (New England Biolabs) with primers DLO883 (5'-CAGGAAACAGCTATGACCATG-3') and DLO884 (5'-TGTTAAAACGACGGCCAGGT-3'). Plasmids containing amplicon inserts were isolated from 2mL LB+Amp cultures using the GENEJET Miniprep kit (Fischer Scientific) and were submitted for Sanger sequencing (Sequetech) using primers DLO883 and DLO884.

To acquire additional wild type ICR assay crossover tracts for our analyses, three "bulk" replicates of the wild type ICR assay were performed following the protocol described in the 'Intersister/intrachromatid repair assay' with the following exceptions: 1) n=3 hermaphrodites were passaged together on individual plates during the experiment; 2) transfers were only performed at 10hr, 22hr, and 46 hr following heat shock; and, 3) plates were screened for body wall GFP+ crossover recombinants but the frequency of pharynx GFP+ and GFP- nonrecombinant progeny were not scored. Body wall GFP+ crossover progeny were lysed and following the preceeding protocol.

Not all lysed recombinant yielded successful PCR products or sequences. Of the additional wild type ICR assay recombinants sequenced for this manuscript, 11 of 11 noncrossover and 52 of 52 crossover lysates were successfully sequenced. Among lysates from *brc-1* mutant ICR assays, 37 of 37 noncrossover and 70 of 73 crossover lysates were successfully sequenced. Among lysates from *smc-5* mutant ICR assays, 56 of 56 noncrossover and 27 of 28 crossover lysates were successfully sequenced.

Interhomolog assay (IH assay)

IH assays were performed as described in (Rosu *et al.* 2011). In brief, P0 hermaphrodites were generated by crossing (see cross schemes detailed below).

IH assay cross schemes:

1) Wild type (N2): P0 hermaphrodites were generated by crossing: (1) N2 males to AV554 hermaphrodites to generate *dpy-13(e184sd) unc-5(ox171::Mos1)*/+ IV; KrIs14/+ V males; (2) F1 males to CB791 hermaphrodites to generate *dpy-13(e184sd) unc-5(ox171::Mos1)*/*unc-5(e791)* IV; KrIs14/+ V hermaphrodites.

2) *brc-1* mutant: P0 hermaphrodites were generated by crossing: (1) JEL730 males to DLW203 hermaphrodites to generate *brc-1(xoe4)* III; *dpy-13(e184sd) unc-5(ox171::Mos1)*/+ IV;

KrIs14/+ V males; (2) F1 males to DLW157 hermaphrodites to generate *brc-1(xoe4)* III; *dpy-13(e184sd) unc-5(ox171::Mos1)*/*unc-5(e791)* IV; KrIs14/+ V hermaphrodites.

3) *smc-5* mutant: P0 hermaphrodites were generated by crossing: (1) YE57 males to DLW23 hermaphrodites to generate *smc-5(ok2421)*/mIn1 II; *dpy-13(e184sd) unc-5(ox171::Mos1)*/+ IV; KrIs14/+ V males; (2) F1 males to DLW81 hermaphrodites to generate *smc-5(ok2421)* II; *dpy-13(e184sd) unc-5(ox171::Mos1)*/*unc-5(e791)* IV; KrIs14/+ V hermaphrodites.

The heat shock and timing at which parent hermaphrodites were transferred to new NGM plates was performed identically to the ICR assay (see 'Intersister/Intrachromatid repair assay (ICR assay)' above). However, the number of eggs and unfertilized oocytes laid by each hermaphrodite was recorded immediately following the removal of the parent hermaphrodite at each timepoint and plates carrying F1 progeny were maintained at 20°C. Plates were scored for F1 wild type moving (non-Unc) progeny ~84-96hrs after parent hermaphrodites were removed. F1 Unc progeny were discarded.

F1 non-Unc progeny were placed on single NGM plates seeded with OP50 bacteria. Dpy non-Unc progeny (putative noncrossover recombinants) were lysed following the protocol described in 'Sequencing and analysis of SCR assay conversion tracts'. If Dpy non-Unc progeny died before the time of lysis and had laid F2 progeny, non-Unc segregant F2s were lysed instead. Non-Dpy non-Unc progeny (putative crossover recombinants) were allowed to lay F2 progeny. If progeny were laid and Dpy non-Unc F2 segregants were identified, these Dpy non-Unc F2s were lysed and the F1 was inferred not to be a crossover recombinant. If >50 F2 progeny were on the plate and no Dpy non-Unc segregants were identified, the F1 was assumed to be a crossover recombinant and no worms were lysed. If very few progeny were laid and no Dpy non-Unc segregants were identified, the F1 non-Unc or its non-Unc F2 offspring were lysed and subsequently subjected to PCR genotyping analysis using OneTaq 2x Master Mix (New England Biolabs) to determine the genotype of *unc-5* and *dpy-13*. The presence of Mos1 in the *unc-5* locus was assessed using primers DLO987 (5'-TCTTCTTGCCAAAGCGATTC-3') and DLO1082 (5'-TTCTCTCCGAGCAATGTTCC-3'). The *dpy-13* locus was assessed using primers DLO151 (5'-ATTCCGGATGCGAGGGAT-3') and DLO152 (5'-TCTCCTCGCAAGGCTTCTGT-3'). Lysed F1 nUnc nDpy progeny were inferred to be crossover recombinants if the worms 1) carried the Mos1 transposon at the *unc-5* locus and were

heterozygous for the *dpy-13(e184)* allele, or; 2) did not carry the Mos1 transposon at the *unc-5* locus and were homozygous wild type for *dpy-13.*

The *unc-5* locus was amplified for sequencing by PCR using OneTaq 2x Master Mix (NEB) with primers DLO1081 (5'-TCTTTTCAGGCTTTGGCACTG-3') and DLO1082. PCR products were run on an agarose gel and desired bands were isolated by gel extraction (QIAquick Gel Extraction Kit, New England Biolabs) and were eluted in ddH_2O. These amplicons were submitted for Sanger sequencing (Sequetech) with primer DLO1082 or DLO150 (5'-GTTCCATGTTTGATGCTCCAAAAG-3'). Sanger sequencing chromatograms were compared to the wild type *unc-5* sequence using Benchling alignment software. Samples which showed a reversion to wild-type *unc-5* sequence at the site of Mos1 excision were inferred to be noncrossover recombinants. Samples which showed mutations that preserved the reading frame of the *unc-5* locus were considered 'mutant non-Unc'.

Samples which showed mixed sequences despite a clear amplicon being generated in the PCR were subsequently TOPO cloned, as described in 'Sequencing and analysis of ICR assay conversion tracts', except that the amplicon used in the reaction was generated using primers DLO1081 and DLO1082.

Not all interhomolog assay non-Unc progeny were able to be confirmed as recombinants by sequencing. Of the wild type IH assay non-Unc progeny identified, 176 of 178 putative noncrossovers were successfully sequenced. Among lysates from *brc-1* mutant IH assays, 72 of 76 putative noncrossovers were successfully sequenced. Among lysates from *smc-5* mutant IH assays, 213 of 229 putative noncrossovers were successfully sequenced. Non-Unc progeny whose *unc-5* DNA repair events could not be identified by sequencing were considered 'undetermined non-Unc' in subsequent analyses of this data.

EdU Sister Chromatid Exchange Assay

EdU Sister Chromatid Exchange assays were performed as described in (Almanzar *et al.* 2021, 2022).

Immunofluorescence localization of SMC-5/6 and BRC-1

Immunofluorescence was performed as in (Libuda *et al.* 2013) or (Howe *et al.* 2001). For both protocols, L4 staged hermaphrodites were isolated 18-22hrs before dissection and maintained at 20°C on NGM plates seeded with OP50. Nematodes which were irradiated preceding an immunofluorescence experiment were exposed to a Cs^{137} source (University of Oregon) were

dissected less than an hour after following irradiation. Samples prepared for GFP::BRC-1 visualization were dissected in 1x Egg Buffer (118 mM NaCl, 48 mM KCl_2, 2 mM $CaCl_2$, 2 mM $MgCl_2$, 25 mM HEPES pH7.4, 0.1% Tween20) and were fixed in 1x Egg Buffer with 1% paraformaldehyde for 5 min on a Superfrost Plus slide (VWR). Samples prepared for SMC-5::AID*::3xFLAG visualization were dissected in 1x Sperm Salts (50mM PIPES pH7, 25mM KCl, 1mM $MgSO_4$, 45mM NaCl, 2mM $CaCl_2$) and an equal volume of 1x Sperm Salts with 3% paraformaldehyde was applied for 5 min before samples were affixed to a Superfrost Plus slide (VWR). For both protocols, gonads were then flash frozen in liquid nitrogen and the cover slip was removed. Germlines stained for GFP::BRC-1 were then fixed for 1 min in ice cold MeOH and then were washed in 1x PBST (1x PBS, 0.1% Tween20), while germlines stained for SMC-5::AID*::3xFLAG were fixed for 1 min in ice cold 95% EtOH and then were washed in 1xPBST* (1x PBS, 0.5% Triton-X100, 1mM EDTA pH8). Slides were then washed 3x in PBST or PBST* respectively before being placed in Block (1xPBST or 1xPBST* with 0.7% bovine serum albumin) for at least 1 hour.

Primary antibody staining was performed by placing 50µL of antibody diluted in PBST for samples in which GFP::BRC-1 or RAD-51 were to be visualized or PBST* if the sample was to be stained for SMC-5::AID*::3xFLAG (see below for specific dilutions of primary antibodies). A parafilm coverslip was placed on each sample and the slides were incubated for 16-18hrs in a dark humidifying chamber. Slides were then washed 3x in PBST or PBST* for 10 min. 50µL of secondary antibody diluted in PBST for samples in which GFP::BRC-1 or RAD-51 were to be visualized or PBST* if the sample was to be stained for SMC-5::AID*::3xFLAG (see below for specific dilutions of primary antibodies) was then placed on each slide. Slides were incubated for 2hrs in a dark humidifying chamber with a parafilm coverslip. Slides were then washed 3x in PBST or PBST* for 10 min in a dark chamber. 50µL of 2µg/mL DAPI was then applied to each slide. Slides were incubated in a dark humidifying chamber with parafilm coverslips for 5 min. Slides were then washed 1x in PBST or PBST* for 5 min in a dark chamber before being mounted in VectaShield with a No. 1.5 coverslip (VWR) and sealed with nail polish.

Slides were maintained at 4°C until imaging. All slides stained for SMC-5::AID*::3xFLAG were imaged within 48 hours of mounting. Immunofluorescence images were acquired at 512x512 pixel dimensions on an Applied Precision DeltaVision microscope. All images were acquired in 3D using Z-stacks at 0.2µm intervals and were deconvolved with Applied Precision softWoRx

deconvolution software. Individual images of whole germlines were stitched as 3D Z-stacks in FIJI using the Grid/Collection Stitching plugin (Preibisch *et al.* 2009) or as maximum intensity projections using Photoshop (Adobe). The intensity levels of images displayed in this manuscript were adjusted in Photoshop for clarity.

The following primary antibodies were used in this study at the given dilutions: Chicken αRAD-51 (1:1000; (Kurhanewicz *et al.* 2020)), Mouse αmini-AID M214-3 (1:500, MBL International), Rat αHTP-3 (1:1000, this study), Rabbit αGFP (1:500 (Yokoo *et al.* 2012)).

Antibody Generation

The HTP-3 antibody used in this study was generated from an identical C-terminal segment of the HTP-3 protein (synthesized by GenScript) as was used by (MacQueen *et al.* 2005). Antibodies were produced in rats and affinity purified by Pocono Rabbit Farms.

Statistics

All statistics were calculated in R (v4.0.3). Specific tests utilized are described in text or in the figure legends. Data wrangling was performed using the Tidyverse (v1.3.0). Bayesian hierarchical models were fit using Rstan (v2.21.2). Binomial Confidence Intervals were calculated using the DescTools package (v 0.99.38).

Table S3.1. Intersister/intrachromatid repair assay progeny counts

Genotype	Time-point	Total Progeny	Total GFP+	NCO	CO	GFP+ Mutant	%GFP+	% COs (of total Recombinant)	% Mutant (of all GFP+)
Wild Type	10-22hr	3921	28	19	9	0	0.71	32.14	0
Wild Type	22-34hr	3359	25	21	4	0	0.74	16	0
Wild Type	34-46hr	3664	22	18	4	0	0.6	18.18	0
Wild Type	46-58hr	2383	15	14	1	0	0.63	6.67	0
brc-1(xoe4)	10-22hr	2042	24	8	16	0	1.18	66.67	0
brc-1(xoe4)	22-34hr	2017	43	9	33	1	2.13	76.74	2.33
brc-1(xoe4)	34-46hr	2005	36	16	20	0	1.8	55.56	0
brc-1(xoe4)	46-58hr	467	9	4	5	0	1.93	55.56	0
smc-5(ok2421)	10-22hr	1350	18	10	8	0	1.33	44.44	0
smc-5(ok2421)	22-34hr	1771	37	23	14	0	2.09	37.84	0
smc-5(ok2421)	34-46hr	1450	21	17	4	0	1.45	19.05	0
smc-5(ok2421)	46-58hr	449	8	6	2	0	1.78	25	0

Table S3.2. Interhomolog repair assay progeny counts

Genotype	Time-point	Total Progeny	non-Unc Progeny	CO	NCO	Non-Unc Mutant	Undetermined non-Unc	% non-Unc	% Mutant (of all non-Unc)	% COs (of all Recombinants)
Wild Type	10-22hr	1308	3	0	3	0	0	0.23	0	0
Wild Type	22-34hr	1695	33	3	30	0	0	1.95	0	9.09
Wild Type	34-46hr	1592	116	10	105	0	1	7.29	0	8.7
Wild Type	46-58hr	562	45	6	38	0	1	8.01	0	13.64
brc-1(xoe4)	10-22hr	758	0	0	0	0	0	0	NA	NA
brc-1(xoe4)	22-34hr	823	38	6	24	5	3	4.62	13.16	20
brc-1(xoe4)	34-46hr	468	42	4	38	0	0	8.97	0	9.52
brc-1(xoe4)	46-58hr	97	6	0	5	0	1	6.19	0	0
smc-5(ok2421)	10-22hr	1031	3	0	3	0	0	0.29	0	0
smc-5(ok2421)	22-34hr	1466	76	4	69	1	2	5.18	1.32	5.48
smc-5(ok2421)	34-46hr	1369	123	10	105	0	8	8.98	0	8.7
smc-5(ok2421)	46-58hr	596	45	4	35	0	6	7.55	0	10.26

Table S3.3. Irradiation brood viability progeny counts (Single and Double Mutants).

Genotype	Treatment	Window	Progeny Hatched	Dead Eggs	Unfertilized Oocytes	Brood Viability
Wild Type	0 Rad	IH Window	2460	54	433	0.97852
Wild Type	0 Rad	Non-IH Window	1342	7	0	0.994811
Wild Type	2500 Rad	IH Window	2736	134	565	0.95331
Wild Type	2500 Rad	Non-IH Window	1136	16	0	0.986111
Wild Type	5000 Rad	IH Window	2267	540	422	0.807624
Wild Type	5000 Rad	Non-IH Window	959	148	0	0.866305
brc-1(xoe4)	0 Rad	IH Window	1761	148	621	0.922472
brc-1(xoe4)	0 Rad	Non-IH Window	1036	85	1	0.924175
brc-1(xoe4)	2500 Rad	IH Window	1460	184	529	0.888078
brc-1(xoe4)	2500 Rad	Non-IH Window	690	128	1	0.843521
brc-1(xoe4)	5000 Rad	IH Window	1374	634	524	0.684263
brc-1(xoe4)	5000 Rad	Non-IH Window	423	436	2	0.492433
smc-5(ok2421)	0 Rad	IH Window	2616	173	525	0.937971
smc-5(ok2421)	0 Rad	Non-IH Window	1176	12	0	0.989899
smc-5(ok2421)	2500 Rad	IH Window	1169	1077	274	0.520481
smc-5(ok2421)	2500 Rad	Non-IH Window	476	623	0	0.433121
smc-5(ok2421)	5000 Rad	IH Window	137	2064	80	0.062244
smc-5(ok2421)	5000 Rad	Non-IH Window	23	988	0	0.02275
smc-5(ok2421); brc-1(xoe4)	0 Rad	IH Window	1224	224	335	0.845304
smc-5(ok2421); brc-1(xoe4)	0 Rad	Non-IH Window	746	82	6	0.900966
smc-5(ok2421); brc-1(xoe4)	2500 Rad	IH Window	725	916	570	0.441804
smc-5(ok2421); brc-1(xoe4)	2500 Rad	Non-IH Window	480	331	1	0.591862
smc-5(ok2421); brc-1(xoe4)	5000 Rad	IH Window	333	1220	281	0.214424
smc-5(ok2421); brc-1(xoe4)	5000 Rad	Non-IH Window	182	667	0	0.21437
smc-5(phx3065)	0 Rad	IH Window	1997	31	63	0.984714
smc-5(phx3065)	0 Rad	Non-IH Window	717	9	0	0.987603
smc-5(phx3065)	5000 Rad	IH Window	1508	179	15	0.974235
smc-5(phx3065)	5000 Rad	Non-IH Window	605	16	0	0.893894

Table S3.4. Irradiation brood viability progeny counts (Triple Mutants).

Genotype	Treatment	Window	Progeny Hatched	Dead Eggs	Unfertilized Oocytes	Brood Viability
smc-5(ok2421); brc-1(xoe4); lig-4(ok716)	0 Rad	IH Window	1654	524	298	0.759412
smc-5(ok2421) ;brc-1(xoe4); lig-4(ok716)	0 Rad	Non-IH Window	754	162	0	0.823144
smc-5(ok2421); brc-1(xoe4); lig-4(ok716)	2500 Rad	IH Window	677	1217	169	0.357445
smc-5(ok2421); brc-1(xoe4); lig-4(ok716)	2500 Rad	Non-IH Window	458	281	0	0.619756
smc-5(ok2421); brc-1(xoe4); lig-4(ok716)	5000 Rad	IH Window	169	1187	146	0.124631
smc-5(ok2421); brc-1(xoe4); lig-4(ok716)	5000 Rad	Non-IH Window	68	633	0	0.097004
smc-5(ok2421); brc-1(xoe4); polq-1(tm2572)	0 Rad	IH Window	401	282	268	0.587116
smc-5(ok2421); brc-1(xoe4); polq-1(tm2572)	0 Rad	Non-IH Window	261	100	15	0.722992
smc-5(ok2421); brc-1(xoe4); polq-1(tm2572)	2500 Rad	IH Window	101	609	132	0.142254
smc-5(ok2421); brc-1(xoe4); polq-1(tm2572)	2500 Rad	Non-IH Window	27	459	1	0.055556
smc-5(ok2421); brc-1(xoe4); polq-1(tm2572)	5000 Rad	IH Window	30	640	71	0.044776
smc-5(ok2421); brc-1(xoe4); polq-1(tm2572)	5000 Rad	Non-IH Window	2	300	8	0.006623

CHAPTER IV

AUTOMATED AND CUSTOMIZABLE QUANTITATIVE IMAGE ANALYSIS OF WHOLE *CAENORHABDITIS ELEGANS* GERMLINES

Published in *Genetics* January 2021

Erik Toraason, Victoria L. Adler, Nicole A. Kurhanewicz, Acadia DiNardo, Adam M. Saunders, Cori K. Cahoon, and Diana E. Libuda

Abstract

Arranged in a spatial-temporal gradient for germ cell development, the adult germline of *Caenorhabditis elegans* is an excellent system for understanding the generation, differentiation, function, and maintenance of germ cells. Imaging whole *C. elegans* germlines along the distal-proximal axis enables powerful cytological analyses of germ cell nuclei as they progress from the pre-meiotic tip through all the stages of meiotic prophase I. To enable high-content image analysis of whole *C. elegans* gonads, we developed a custom algorithm and pipelines to function with image processing software that enables: 1) quantification of cytological features at single nucleus resolution from immunofluorescence images; and, 2) assessment of these individual nuclei based on their position within the germline. We demonstrate the capability of our quantitative image analysis approach by analyzing multiple cytological features of meiotic nuclei in whole *C. elegans* germlines. First, we quantify double strand DNA breaks (DSBs) per nucleus by analyzing DNA-associated foci of the recombinase RAD-51 at single-nucleus resolution in the context of whole germline progression. Second, we quantify the DSBs that are licensed for crossover repair by analyzing foci of MSH-5 and COSA-1 when they associate with the synaptonemal complex during meiotic prophase progression. Finally, we quantify P-granule composition across the whole germline by analyzing the colocalization of PGL-1 and ZNFX-1 foci. Our image analysis pipeline is an adaptable and useful method for researchers spanning multiple fields utilizing the *C. elegans* germline as a model system.

Introduction

Reproduction in many sexually reproducing organisms requires the formation of haploid gametes. Gametes originate from germ cells that divide and differentiate to generate a germline, which is also known as the “totipotent” or “immortal” cell lineage due to its ability to pass on its genetic information to the next generation (Hubbard and Schedl 2019). Studies of germ cells in

multiple systems have revealed molecular mechanisms of germ cell development, function, and maintenance. Over the past several decades, the use of genetics and cytology has been instrumental for understanding fundamental aspects of germ cell biology.

For germ cell studies, the *Caenorhabditis elegans* germline provides unique manipulation and visualization advantages (Hubbard and Greenstein 2000; Hubbard and Greenstein 2005). In adult hermaphrodites, there are two complete tube-shaped gonads that each form a U-shape when contained within the adult animal (Hubbard and Schedl 2019). Within the adult hermaphrodite germline, ~1000 germ cell nuclei are positioned around the circumference of the tube and are arranged in a spatial-temporal gradient according to developmental stage along the distal-proximal axis. At the distal end of the gonad (pre-meiotic tip or proliferative zone), mitotically-cycling nuclei move proximally until they reach the leptotene/zygotene region that commits them to enter meiosis, the specialized cell division that generates haploid gametes. This entry into meiosis is termed the "transition zone" and the germ cells begin differentiating to form mature oocytes. The transition zone is classically identified by crescent-shaped DAPI morphology due to the polarized active movement of chromosomes; however, in certain mutant situations that affect chromosome pairing or germ cell proliferation, this region with distinct DAPI morphology may be either absent or extended (*e.g. hal-2* and *syp-1)* (MacQueen *et al.* 2002; Zhang *et al.* 2012). Following the transition zone, germ cell nuclei enter pachytene stage where chromosomes are no longer undergoing rapid polarized movement and instead assume a cage-like appearance. After pachytene, chromosomes begin the condensation process in the diplotene stage and eventually fully condense to form six DAPI-staining bodies (one for each set of homologs) at diakinesis. This "pipeline" of germ cell development in the *C. elegans* gonad has enabled the visualization of all stages of germ cell development simultaneously within a single germline, thereby making this model system a powerful tool for cytological approaches.

Cytological studies of the *C. elegans* germline illuminate key aspects of meiosis, including chromosome pairing, recombination, regulation of DNA damage responses, and apoptosis in gamete production (Garcia-Muse and Boulton 2007; Hillers *et al.* 2017; Cahoon and Libuda 2019) . The spatial-temporal organization of the germline can be used to define the timing and/or progression of these events throughout meiotic prophase I in *C. elegans* (Garcia-Muse and Boulton 2007; Jaramillo-Lambert *et al.* 2007; Hillers *et al.* 2017). For example, localization and quantification of foci composed of meiotic recombination proteins established

the timing and steps of DNA repair events in the *C. elegans* germline (Yokoo *et al.* 2012; Schvarzstein *et al.* 2014; Woglar and Villeneuve 2018; Cahoon and Libuda 2019). Further, quantification of these foci within the germ cell nuclei can indicate changes in the frequency of these specific DNA repair events both in wild type and mutant contexts. Overall, quantitative image analysis of whole germlines have been instrumental in revealing roles for specific genes in meiotic DNA repair (Garcia-Muse and Boulton 2007).

Germ cell differentiation and fertility in *C. elegans* require the germline to assemble RNA/protein condensates called P granules. These membraneless organelles are perinuclear during the majority of germ cell development and are involved in silencing germline transcription via small RNA pathways (Seydoux 2018; Putnam *et al.* 2019; Ouyang *et al.* 2019). For nearly 40 years, cytology and genetics have played critical roles in studies of P granules. In 1982, P granules were originally identified by immunofluorescence imaging that revealed the existence of granules in the *C. elegans* P cell lineage, which exclusively gives rise to the germline (Strome and Wood 1982). Subsequent high-resolution microscopy, live imaging, and fluorescence recovery after photobleaching studies have revealed the components, dynamics, and liquid-like properties of P granules (Seydoux 2018; Putnam *et al.* 2019; Ouyang *et al.* 2019). Further, analysis of whole adult gonads stained for P granule structures reveal that some components of these membraneless organelles can undergo morphological changes during meiotic prophase I progression (Uebel *et al.* 2020), further suggesting possible changes in function during oogenesis.

While both qualitative and quantitative microscopy approaches are currently employed to study the *C. elegans* germline, the variation in the chromosome morphology throughout the germline and technical variability from affixing dissected gonads affixed to microscope slides have limited high-content automated analysis of germline features. Some powerful computational methods exist for analyzing images taken of specific regions of the germline, such as the distal region where germ cell proliferation occurs (Lee *et al.* 2016; Crittenden *et al.* 2019), but these methods are limited to germlines (whole or specific regions) that affix in a straight/linear orientation. Due to limitations of existing automated image analysis methods for non-linear whole gonads, many research groups still rely on time consuming and laborious manual efforts for quantifying features of germ cells within whole *C. elegans* germlines. To expedite and expand quantitative image analysis of the whole *C. elegans* germline, we developed a high-content, automated

method using custom algorithms that function with image processing software. This method enables quantitative image analysis of cytological features of single nuclei within non-linear whole *C. elegans* gonads. Further, this computational pipeline permits analysis and data visualization of individual nuclei based on their position within the germline. Here we describe and validate our computational method by analyzing images of multiple features of germ cell nuclei undergoing meiotic prophase I progression within the context of an entire *C. elegans* germline.

Results

Gonad Analysis Pipeline for fluorescent image analysis of whole *C. elegans* germlines

The *C. elegans* germline presents many challenges for automated quantification of cytological data. Due to the non-linear three-dimensional (3D) shape of both undissected and dissected gonads, it has been difficult to computationally: 1) distinguish individual nuclei within an imaged gonad; and, 2) contextualize quantitative features of individual nuclei based on their position in the gonad and during specific stages of meiotic prophase I. Further, the freedom of dissected gonads to adopt multiple shape conformations when affixed to a microscope slide or coverslip presents an additional challenge for automating computational analysis of large numbers of dissected gonads. To overcome these challenges, we constructed a Gonad Analysis Pipeline using image quantification software in conjunction with custom scripts implemented in MATLAB and R to enable high-throughput quantification of germline features at single nucleus resolution, while maintaining information regarding the relative position of these nuclei within the *C. elegans* germline. For all of our analyses, we acquired and utilized 3D immunofluorescence images of dissected, fixed *C. elegans* germlines using established protocols that preserve the 3D architecture of the germline (Figures 4.1A, 4.1B; Materials and Methods). Since high-resolution analysis of whole *C. elegans* gonads requires acquisition of multiple 3D images to encompass their entire distal-proximal length, we stitched the individual 3D images together into a single reconstruction of the imaged germline using either Imaris Stitcher or an image stitching plugin in FIJI (see Materials and Methods; (Preibisch *et al.* 2009)). Individual nuclei within the gonad were defined using Surface in Imaris with the DNA stain DAPI (see below). Due to the arrangement of nuclei in some germlines, a subset of nuclei (~23%) were unable to be computationally identified and were subsequently removed from the dataset

(Figures 4.1B, 4.1C). A caveat of removing these nuclei is that specific germline regions could be under sampled ($p<0.001$ Chi Square Test of Goodness of Fit, Figures S4.1A, S4.1B); however, we found that combining the datasets of at least two germlines was sufficient to enable even sampling of nuclei across the germline from the pre-meiotic tip to the end of late pachytene ($p=0.422$, Chi Square Test of Goodness of Fit, Figure S4.1C). From our imaged gonads (which capture the top 25-30% of the germline along the dorsal-ventral axis; see Materials and Methods), we computationally identified an average of 146.3±16.9 nuclei per germline (n=4 gonads). Overall, ~15% of the germline nuclei contained in a single gonad arm are captured by this method using our particular images of the top dorsal portion of each gonad, and are evenly sampled from all regions of the germline. These results indicate the ability of this pipeline to identify and analyze large numbers of nuclei from whole gonads.

To demarcate the conformation of each gonad from the distal tip (premeiotic) to proximal end (late pachytene), we drew contiguous line segments down the center of each germline (Figure 4.1D). Using this method, we designated each stage of meiotic prophase I along this segmented line based on DNA morphology: the premeiotic zone, transition zone (encompassing leptotene and zygotene), and pachytene. Since some mutant germlines lack some of these cytological features (*e.g.* absence of polarized chromosomes characteristic of transition zone nuclei), we developed an algorithm to approximate the relative germline position of each nucleus independent of DNA morphology (Figure 4.1E). This algorithm (called the "Gonad Linearization Algorithm") approximates the position of each nucleus along the length of the germline based on its orientation relative to the line drawn along the center of the gonad. To calculate the position of each nucleus, the Gonad Linearization Algorithm identifies the best fit perpendicular intersection point for the position of each nucleus relative to the central line segments (see perpendicular arrows projecting from each nucleus to the central line in Figure 4.1D). This analysis allows us to recontextualize individual nuclei from 3D space into a one-dimensional (1D) space, enabling assessment of nucleus features based on position in the gonad as nuclei progress through meiotic prophase I.

To assess the ability of the Gonad Linearization Algorithm to accurately align nuclei through the germline, we applied the algorithm to a simulated dataset of 100 'germlines.' Each simulated 'germline' contained 100 simulated 'nuclei' dispersed along the lengths of the 'germline' (Figure S4.2A). We found that, for most simulated 'germlines,' >90% of the 'nuclei'

were accurately assigned to the correct line segment, and that correctly aligned nuclei recapitulated the order in which they were simulated along the length of the 'germline' ($p<0.001$, $R2=1$, Linear regression analysis, Figures S4.2B, S4.2C). Even in the case of incorrect assignment of a 'nucleus' to a line segment, the deviation of the placement of each 'nucleus' in the context of the whole gonad was 0.00±3.7% on average, and all were <10% (Figure S4.2D). In addition, we have included within the algorithm a way to manually correct the assignment of these incorrectly assigned nuclei. These data illustrate the accuracy and customizability of the Gonad Linearization Algorithm for analysis of diverse conformations of dissected gonads.

Quantification of DNA-associated proteins at single nucleus resolution

Manual quantification of foci within nuclei from whole *C. elegans* gonads is a laborious, rate-limiting step during image analysis. To validate our Gonad Analysis Pipeline's automated quantification of meiotic features, we first quantified classic markers that are involved in double strand DNA break (DSB) formation and repair. The recombinase RAD-51 loads at sites of DSBs in meiotic nuclei (Colaiácovo *et al.* 2003; Lemmens and Tijsterman 2011). The number of RAD-51 foci within germline nuclei can indicate either the extent of DSB induction and/or the efficiency of DSB repair during meiotic prophase I progression (Bickel *et al.* 2010; Rosu *et al.* 2013). DSB-2 promotes DSB induction, and accumulates on meiotic chromatin in the final stages of the transition zone and early pachytene when RAD-51 forms numerous foci (Rosu *et al.* 2013; Stamper *et al.* 2013).

To quantify RAD-51 within an entire germline, we implemented our Gonad Analysis Pipeline adapted with a custom MATLAB script in combination with the Gonad Linearization Algorithm. First, we identified nuclei within the germline using DAPI (see Methods for details). A custom MATLAB script (called Spots to Surfaces) was used to: 1) identify the RAD-51 foci (spots) that were associated with each individual nucleus (surface); and 2) provide a readout of foci per nucleus. Then after drawing line segments along the length of the gonad, the Gonad Linearization Algorithm was used to transform the position of each nucleus and the RAD-51 foci (spots) associated with that nucleus on to that 1D line. This transformation generated data from a single germline that contained both the number of spots associated with each nucleus and the relative position of each nucleus along the length of the germline. In addition to scoring the number of RAD-51 foci for each nucleus, we further calculated the mean intensity of DSB-2

staining with each nucleus using Imaris (Figure 4.2A). From these analyses, we are able to observe the complete dynamics of DNA repair at a single nucleus resolution.

To determine the accuracy of our high-throughput Gonad Analysis Pipeline method for nuclear-associated foci quantification, we manually scored RAD-51 foci in a blinded subset of representative nuclei taken from whole gonad images (Figure 4.2B; n=70 nuclei). The mean deviation between automated and manual foci quantification was 0.05±1.21, and the number of foci per nucleus quantified by Imaris software correlated well with the number of foci scored manually ($p<0.001$, Adjusted $R^2 = 0.91$, Linear Regression Analysis, Figure 4.2B). Thus, across a population of nuclei, our Gonad Analysis Pipeline yields reliable statistics for the number of foci associated with individual *C. elegans* germline nuclei.

Using the Gonad Analysis Pipeline, we assessed the distribution of RAD-51 along the length of the germline (Figure 4.2C) in wild-type and mutant contexts. In concordance with previous studies of wild-type germlines (Colaiácovo *et al.* 2003; Rosu *et al.* 2013; Stamper *et al.* 2013), we observe most nuclei with one or more RAD-51 foci within the central ~50% of the germline (Figure 4.2C), corresponding to the end of the transition zone through mid-pachytene stages of meiosis I (Figure 4.1D). In addition, we assessed mutants which displayed aberrant meiotic recombination. Null mutants for the topoisomerase-like protein SPO-11 are unable to generate endogenous meiotic DSBs and exhibit few RAD-51 foci throughout meiotic prophase I (Colaiácovo *et al.* 2003); Figure S4.4A). Our quantification of a *spo-11(me44)* null mutant hermaphrodite germline reflects this phenotype, with 93.3% of nuclei analyzed (125/139 nuclei) exhibiting no RAD-51 foci (Figure S4.4C, top). Null mutants of the recombination protein RAD-54 are unable to unload RAD-51 from DSBs during pachytene, resulting in elevated and persistent RAD-51 foci ((Mets and Meyer 2009; Rosu *et al.* 2011; Nottke *et al.* 2011); Figure S4.4B). When we quantified RAD-51 foci per nucleus in a *rad-54(ok615)* null mutant hermaphrodite germline using the Whole Gonad Pipeline, we also observed elevated and persistent RAD-51 foci during meiotic prophase I progression (Figure S4.4C, bottom). Our dataset illustrates that the number of DSBs per nucleus in a *rad-54* mutant is dramatically higher than wild-type (Figure S4.4C), with the highest number of DSBs in a single nucleus (83 RAD-51 foci in a single nucleus) located most proximally in the germline. Taken together, these data demonstrate the flexibility of using the Gonad Analysis Pipeline to quantify DNA damage repair foci across different mutant contexts.

To further assess the functionality and accuracy of our image quantification method, we quantified the association between RAD-51 and DSB-2 on a single nucleus basis. Similar to RAD-51, the per-nucleus normalized mean intensity of DSB-2 within germlines was also highest in the central 50% of the germline (Figure 4.2C). To dissect this relationship further, we binned the DSB-2 and RAD-51 data into two bins based on when DSB-2 is loaded to chromatin in early prophase (transition zone-early pachytene) or offloaded from chromatin in late prophase (mid-late pachytene) (Rosu *et al.* 2013). Overall, higher DSB-2 intensity is correlated with increased numbers of RAD-51 foci (Figure S4.3). Notably, we observed a stronger correlation in early prophase (Spearman's ρ 0.785 95% CI 0.721-0.836, p value < 0.001, Spearman's rank correlation test) than in late prophase (Spearman's ρ 0.389 95% CI 0.225-0.532, p value < 0.001, Spearman's rank correlation test), supporting the reported function of DSB-2 to promote DSB induction during early pachytene by creating a DSB-permissive state when loaded onto chromatin (Rosu *et al.* 2013). Taken together, these results demonstrate the capability of the Gonad Analysis Pipeline to quantify the relationships of cytological features at single nucleus resolution

Quantification of meiotic chromosome structure-associated foci at single nucleus resolution

Next we used the Gonad Analysis Pipeline to quantify foci associated with specific steps in DSB repair that occur along meiotic chromosome axis structures. While many proteins are involved in establishing a crossover during meiosis, we focused on quantifying the localization pattern of two proteins that are loaded after the initial strand invasion steps of recombination. The MutS homolog MSH-4/5 and cyclin-like COSA-1 localize to intermediate steps in the meiotic DSB repair process and are required for crossover recombination events between homologous chromosomes (Kelly *et al.* 2000; Colaiácovo *et al.* 2003; Yokoo *et al.* 2012; Woglar and Villeneuve 2018). In early-mid pachytene, MSH-5 has been observed to form many dim foci before late pachytene, when both COSA-1 and MSH-5 localize to 6 foci, marking the positions of the obligate crossover for each of the six *C. elegans* chromosomes. Studies have demonstrated that the synaptonemal complex – a proteinaceous structure that assembles between homologous chromosomes during meiosis – recruits MSH-5 and COSA-1 in *C. elegans* (Macqueen and Villeneuve 2001; Colaiácovo *et al.* 2003; Jantsch *et al.* 2004; Bhalla *et al.* 2008; Libuda *et al.* 2013; Cahoon *et al.* 2019).

We adapted the Gonad Analysis Pipeline to determine the number of MSH-5 and COSA-1 foci associated with the synaptonemal complex protein, SYP-1 throughout the germline (Figures 4.3A, 4.3B). For this approach, SYP-1 staining was used instead of DAPI to generate surfaces for each individual nucleus. Next, we identified MSH-5 or GFP::COSA-1 foci, then used the Spots to Surface MATLAB script to identify the foci associated with each SYP-1 surface, and finally approximated the positions of these SYP-1 surfaces along the germline using the Gonad Linearization Algorithm. As the synaptonemal complex is not fully assembled until the end of the transition zone, we did not identify any SYP-1 objects in the first segmented portion of each analyzed germline, which corresponds to the pre-meiotic region (Figure 4.3C). In total, we identified the SYP-1 surfaces of 167 individual nuclei in a single germline stained with SYP-1 and MSH-5, and 168 individual nuclei in a single germline stained with SYP-1 and GFP::COSA-1. As previously reported (Yokoo *et al.* 2012; Woglar and Villeneuve 2018), MSH-5 forms >6 foci per meiotic nucleus in early-mid pachytene. Then in late pachytene (the final ~25% of the germline), GFP::COSA-1 forms bright, robust foci and both MSH-5 and COSA-1 foci counts converge to ~6 foci per nucleus, which corresponds to the 6 total crossovers formed per nucleus (Yokoo *et al.* 2012). Notably, MSH-5 and COSA-1 foci in late pachytene have been found to be brighter than those observed earlier in meiotic prophase I (Yokoo *et al.* 2012; Woglar and Villeneuve 2018). Since Imaris software enables flexible thresholding of puncta based on signal intensity, it is possible to limit analysis specifically to these bright foci by changing the threshold cutoff (Figure S4.5). Overall, these results demonstrate the capability of our approach to identify nuclear structures, as well as to quantitate the subnuclear association of specific meiotic proteins with specific chromosome structures at single-nucleus resolution.

Quantification of perinuclear structures across the *C. elegans* germline

To demonstrate the ability of our method to assess extranuclear features of the *C. elegans* germline, we adapted our Gonad Analysis Pipeline to identify and quantify P granule structures that assemble within the perinuclear space of germ cells. P granules are liquid-like condensates associated with nuclear pore complexes in the *C. elegans* germline that process small RNAs (Seydoux 2018). For our analysis of P granules, we analyzed two components of P granules: PGL-1 and ZNFX-1. PGL-1 is a core component of P granules that is required for fecundity (Strome and Wood 1982; Kawasaki *et al.* 1998). ZNFX-1 is a P granule component required for

effective transcript silencing in the germline and colocalizes with PGL-1 perinuclear foci in the germline (Ishidate *et al.* 2018; Wan *et al.* 2018).

To analyze the localization of PGL-1 and ZNFX-1 P granule components throughout the adult germline (Figure 4.4A), we adapted our Gonad Analysis Pipeline to initially identify and quantify the number of individual perinuclear PGL-1 and ZNFX-1 foci by creating surfaces of each focus in Imaris (Figure 4.4A). In total, we identified n=4543 PGL-1 foci and n=3842 ZNFX-1 foci (Figure 4.4B). Then, we applied the Gonad Linearization Algorithm to approximate the position of these foci relative to their progression through the germline (Figure 4.4B). To understand the relationship between PGL-1 and ZNFX-1, we determined the proportion of colocalized PGL-1 and ZNFX-1 along the germline in a sliding window representing 10% of total gonad length (Figure 4.4C). Throughout meiotic prophase I, >50% of PGL-1 and ~75% of ZNFX-1 foci are consistently colocalized. However, in late prophase I, the frequency of PGL-1 colocalization increases to ~75%. From our analysis, we also found that throughout the germline, PGL-1 foci were more frequently found unassociated with ZNFX-1 than ZNFX-1 was found unassociated with PGL-1 (Figure 4.4D). Together, these results agree with previous findings indicating the colocalization of these two components within the *C. elegans* hermaphrodite germline (Ishidate *et al.* 2018; Wan *et al.* 2018).

To assess the accuracy of the Gonad Analysis Pipeline in determining colocalization frequencies, we also compared the association between MSH-5 and RAD-51 foci, which mark distinct recombination intermediates and rarely interact in germ nuclei (Schvarzstein *et al.* 2014; Woglar and Villeneuve 2018) (Figure S4.6). We found that ~6-7% of MSH-5 and RAD-51 are colocalized (Figure S4.6B). Importantly, we found that the distributions of distances between colocalized MSH-5 foci with their associated RAD-51 focus, as well as between non-colocalized MSH-5 foci with the nearest RAD-51 focus, are not discretely separated (Figure S4.6C). This result indicates that proximity alone does not determine colocalization, therefore supporting the accuracy of the Gonad Analysis Pipeline in identifying interactions between germline features. Overall, our data demonstrates the adaptability and customizability of the Gonad Analysis Pipeline to quantitate the changes in colocalization frequency throughout the whole *C. elegans* germline.

To test whether our method could quantify additional structural features of P granules, we quantified and compared the volume/size of individual PGL-1 and ZNFX-1 P granules to the

volume/size of P granules with colocalized PGL-1 and ZNFX-1. From our analysis across meiotic prophase I, we found that the volume of foci that were colocalized were larger than individualized foci for both proteins assessed ($p<0.001$, Mann-Whitney U test, Figure 4.4D). When we examined the mean volume of PGL-1 and ZNFX-1 foci in a sliding window representing 10% of total gonad length (Figure 4.4E), we observed that P granules with colocalization of PGL-1 and ZNFX-1 were consistently larger in volume than those granules that did not have both components present. This result may indicate that the inclusion of multiple P granule components possibly results in a synergistic increase the volume of a granule. Taken together, we have demonstrated that our approach enables high-throughput analysis of germline granules and provides support for a model in which the composition and features of individual P granules may change throughout meiotic prophase I progression.

Discussion

In this study, we demonstrate the utility of a customizable computational pipeline, called the Gonad Analysis Pipeline, developed to perform automated quantification of features within (or associated with) individual nuclei with reference to the position of the nuclei in the *C. elegans* gonad. Specifically, we adapt and use the Gonad Analysis Pipeline to quantify foci per nucleus, foci associated with chromosome structures, and foci colocalization frequencies across whole adult *C. elegans* hermaphrodite gonads from the pre-meiotic tip to late pachytene. This pipeline yields datasets concordant with previous observations for known features of meiotic prophase I (Colaiácovo *et al.* 2003; Rosu *et al.* 2011, 2013; Nottke *et al.* 2011; Yokoo *et al.* 2012; Schvarzstein *et al.* 2014; Ishidate *et al.* 2018; Wan *et al.* 2018; Woglar and Villeneuve 2018). Additionally, many *C. elegans* mutants defective in key meiotic events such as synapsis and pairing can have aberrant DNA morphology and disruption of normal meiotic stage progression. These defects make it difficult to use DNA morphology to discern the specific transitions between meiotic stages and challenging to categorically delineate nuclei within those germline contexts. Our automated Gonad Analysis Pipeline provides a consistent metric utilizing position along the normalized gonad length for comparative analysis of mutants to wildtype germlines.

While analyses presented here assess nuclei from the pre-meiotic tip to late pachytene of the *C. elegans* germline, our pipeline can also be extended to include more proximal portions of

the germline for quantitative analyses of other germline features. For example, P granules display a dynamic localization pattern throughout the germline, changing from cytoplasmic localization in the distal region of the germline to a more perinuclear localization in the more proximal region of the germline (Seydoux 2018). Our computational pipeline could be adapted to quantify these changes in P granule localization across the entire *C. elegans* germline and perform comparative studies of these nucleus-cytoplasm localization dynamics between wild type and mutant contexts. Additionally, several studies have found dynamic changes to the localization of specific synaptonemal complex components during meiotic prophase progression (Martinez-Perez *et al.* 2008; Severson *et al.* 2009; Tzur *et al.* 2012; Nadarajan *et al.* 2016). Our pipeline can also be utilized to quantify these changes in the chromosome axis and the synaptonemal complex from transition zone through diakinesis.

Our analyses demonstrate how small customizable changes to the Gonad Analysis Pipeline can enable quantification at multiple levels from the entire germline to single nuclei. Further changes can enable the additional quantifications of cytological objects, such as sphericity, intensity, and relative distance between objects. Utilization of these other quantifiable metrics enables a comprehensive analysis of many germ cell features, including the quantification of chromosome pairing for fluorescence in situ hybridization (FISH) experiments, assembly and disassembly of chromosome structures, and protein dynamics during live cell imaging. In particular for live imaging, the pipeline could assess changes in numerous metrics such as velocity, mean square displacement, duration, volume, and sphericity of objects over time for all nuclei during oogenesis and contextualize these statistics based on nuclear position within the germline. These types of adaptations of our Gonad Analysis Pipeline for live imaging may prove particularly powerful for quantification of the liquid-like properties and dynamics of P granules in the adult germline, especially in response to different stresses or aging.

The present study focuses on adult hermaphrodite germlines, however, the Gonad Analysis Pipeline can also be used to analyze larval germlines and adult male germlines. An increasing number of studies are demonstrating the power of performing comparative analyses between oogenesis and spermatogenesis in *C. elegans* to identify important sexual dimorphic features of meiosis (Jaramillo-Lambert *et al.* 2007; Van *et al.* 2016; Cahoon and Libuda 2019; Li *et al.* 2020). Spermatogenesis in the germlines of *C. elegans* males is also organized in a spatial-temporal gradient (Shakes *et al.* 2009) and can easily be analyzed by our pipeline, thereby aiding

both studies of spermatogenesis as well as sexual dimorphism of germ cell development. Additionally, this approach and protocol could be adapted to use with other tissues and organisms. For example, many developing tissues do not follow a straight line, such as the epithelium of the *Drosophila* wing disc, and this protocol can be used to linearize elements within the developing tissue that might help to reveal different aspects of cellular migration and development.

Taken together, we have generated and validated an automated and customizable image analysis resource for the *C. elegans* germline community. Our Gonad Analysis Pipeline enables standardized quantification of diverse features of the *C. elegans* gonad. Moreover, our approach is flexible and could be applied to analyze features of other tissues composed of cells organized along a linear gradient.

Acknowledgements

We thank A. Villeneuve for antibodies, the CGC (funded by National Institutes of Health (NIH) P40 OD010440) for strains, and Adele Adamo for providing the pET30a plasmid. We thank the members of the Libuda Lab for many insightful and helpful discussions in refining this method. We also thank A. Villeneuve for encouraging us to write up and publish this method. This work was supported by the National Institutes of Health T32GM007413 to ET and AD; National Institutes of Health F32GM130006 to NAK; Jane Coffin Childs Postdoctoral Fellowship to CKC; and National Institutes of Health R35GM128890 Award to DEL. DEL is also a recipient of a March of Dimes Basil O'Connor Starter Scholar award and Searle Scholar Award.

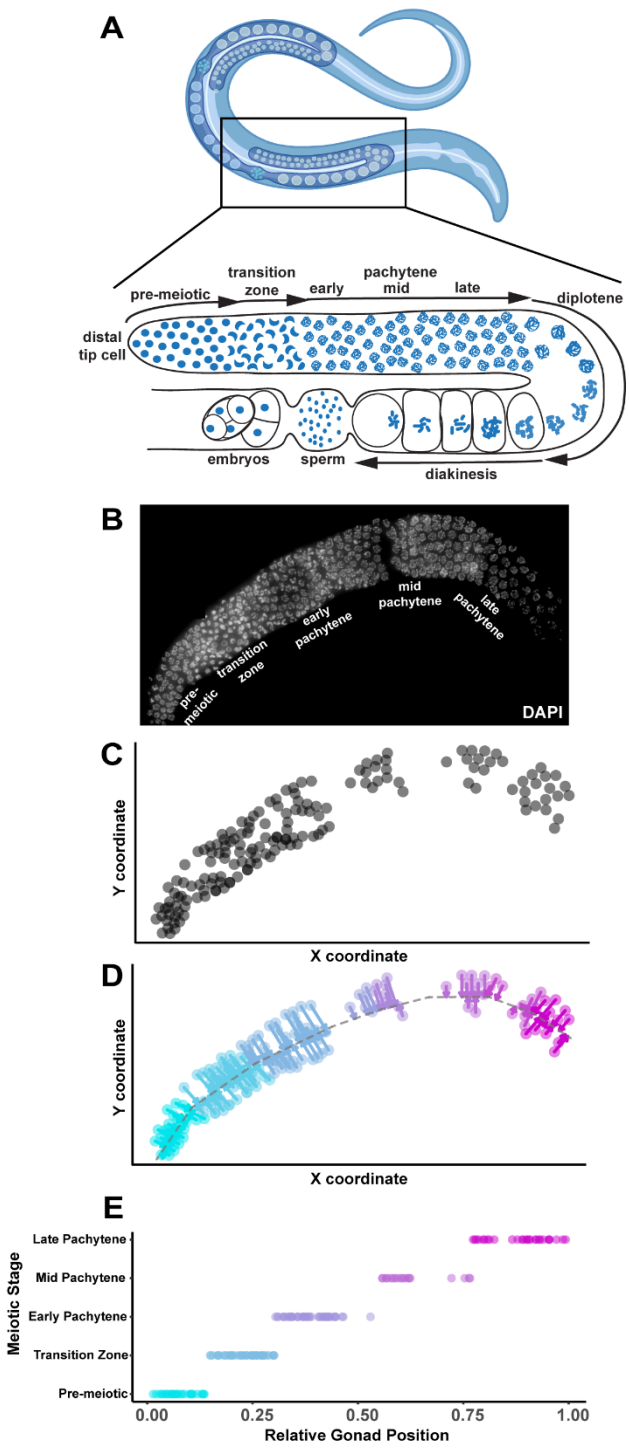

Figure 4.1. Gonad Linearization Algorithm transforms and orients 3D-nuclei within a non-linear *C. elegans* gonad onto a one-dimensional axis. We designed a custom algorithm (called the "Gonad Linearization Algorithm") to enable the assessment of individual *C. elegans* nuclei relative to their position within a germline. (A) Cartoon of adult hermaphrodite worm (top panel; made with Biorender) with zoom in of one gonad arm (lower panel) with nuclei (blue) and indicated stages of meiosis based on DNA morphology (B) Dissected *C. elegans* hermaphrodite germline with DNA stained using DAPI (white). Specific meiotic stages were determined by DNA morphology. (C) 2D coordinate positions (units arbitrary) of individual whole nuclei (gray circles) within a *C. elegans* germline. Whole nuclei and respective coordinate positions were defined using Imaris. Nuclei found to be overlapping or only partially imaged were eliminated from analysis. Nuclei that were not able to be computationally oriented were also removed from analysis. (D) Application of the Gonad Linearization Algorithm transforms the coordinates of nuclei onto a central axis line drawn through the germline, approximating the progression of nuclei through the germline based on their position along that line. (E) Normalizing the total length of line segments drawn through the center of the gonad enables standardized assessment of individual nuclei contextualized by their progression through the germline. Line segments were specifically placed to delineate the premeiotic zone and transition zone based on DAPI morphology of chromosomes. Early, mid, and late pachytene were defined on this graph by dividing the remaining normalized germline length into equal thirds.

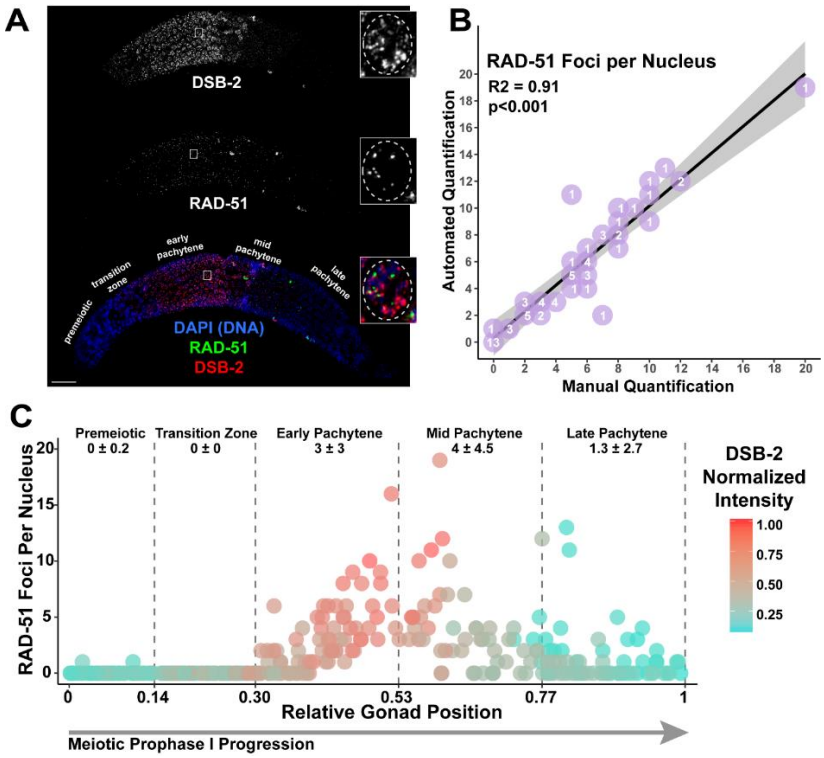

Figure 4.2. Gonad Analysis Pipeline enables germline-wide single nucleus assessment of double-strand DNA break (DSB) levels. (A) Immunofluorescence image of a C. elegans hermaphrodite germline stained with DAPI (DNA; blue), DSB-2 (red), and RAD-51 (green). Scale bar represents 20 μm. Inset images display a representative mid-pachytene nucleus with characteristic DSB-2 and RAD-51 staining. The location of inset image within the whole germline image is indicated by a white box on the whole germline image. For clarity, a dashed line is used in the inset image to emphasize the region of the image containing the nucleus of interest. Specific meiotic stages were determined by DNA morphology. (B) Comparison of data from automated quantification of RAD-51 foci associated with individual nuclei to data from manual quantification of RAD-51 foci within those same nuclei analyzed by the automated system (n =70 nuclei derived from three separate germlines). The number listed on each point (purple) indicates the number of nuclei scored with that result. The linear regression line is displayed as a black line, whereas the gray-shaded area represents the 95% confidence interval of this analysis. (C) Visualization of RAD-51 foci counts and DSB-2 normalized mean fluorescence intensity of individual nuclei across gonads (n =2). The RAD-51 foci counts and DSB-2 normalized intensity values of 295 individual nuclei are displayed. DSB-2 mean intensity was normalized within analyzed gonads by the highest recorded DSB-2 mean fluorescence intensity among nuclei. Normalized DSB-2 intensity is indicated with a color gradient from red (highest intensity) to blue (lowest intensity). Vertical dashed lines indicate the average position in which nuclei within each gonad transition between each successive stage of meiotic prophase I (as indicated by text in the figure), determined by DAPI morphology. The deviation between these transition points was <0.01 between the germlines. Numbers below the text demarcating each respective meiotic stage in the germline indicate the mean number of RAD-51 foci ± the standard deviation of RAD-51 foci among nuclei within that region.

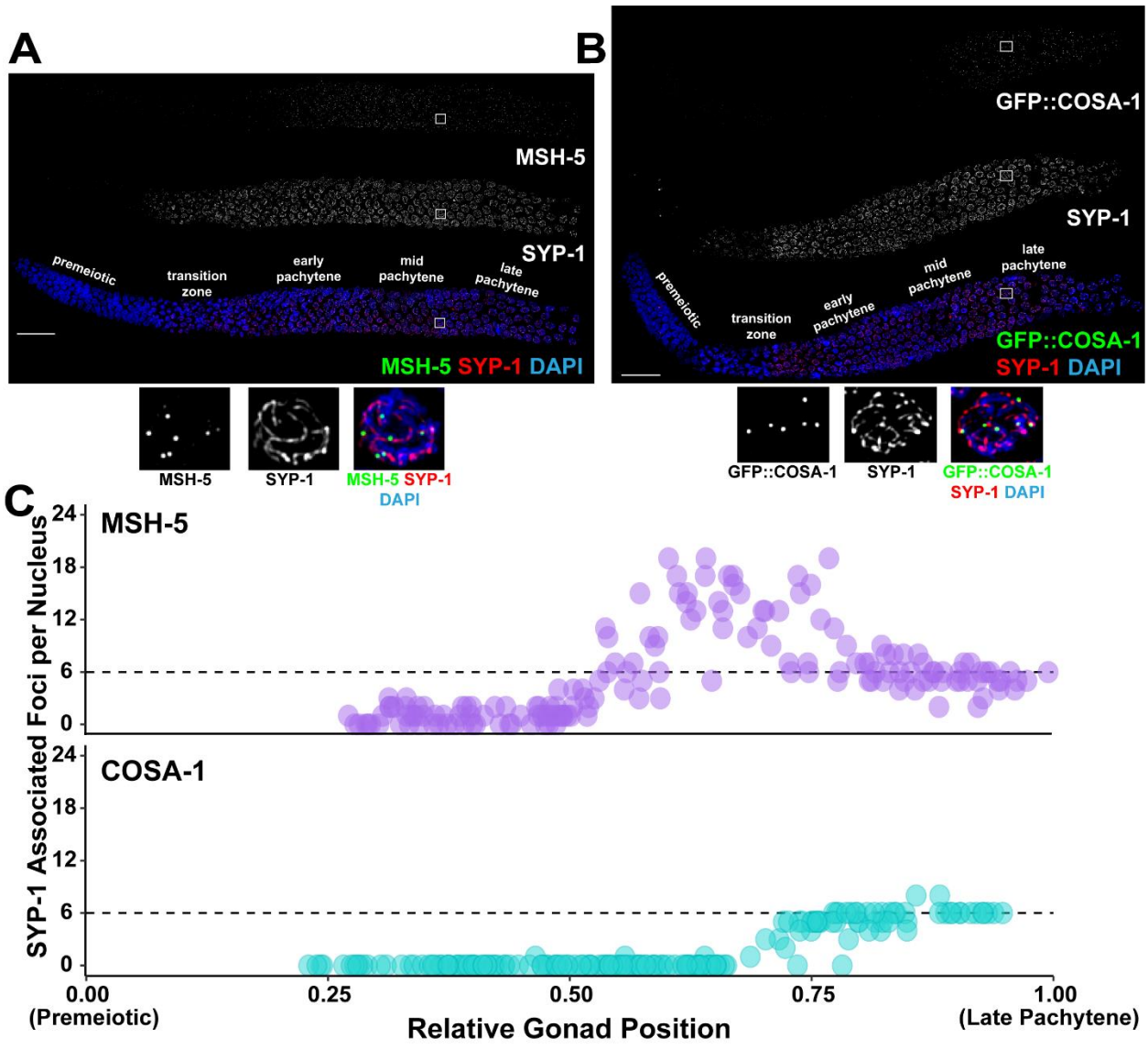

Figure 4.3. Single-nucleus analysis of meiotic recombination markers along the meiotic chromosome axis. Immunofluorescence images of a C. elegans hermaphrodite germline stained with either (A) DAPI (DNA; blue), MSH-5 (green), and SYP-1 (red), or (B) DAPI (blue), GFP::COSA-1 (green), and SYP-1 (red). Scale bar represents 20 µm. Inset images display representative late pachytene nuclei. The location of these inset images within the germline image are indicated by white boxes on the whole gonad images. Specific meiotic stages were determined by DNA morphology. (C) Visualization of numbers of MSH-5 (purple) or GFP::COSA-1 (blue) foci associated with SYP-1 within individual nuclei across the germlines displayed in A-B. As nuclei progress through meiotic prophase I, the number of MSH-5 and COSA-1 spots converge at 6 foci per nucleus in the latter part of the **g**ermline, consistent with the reported number of MSH-5 and COSA-1 foci marking the 6 crossover sites in late pachytene (Yokoo *et al.* 2012).

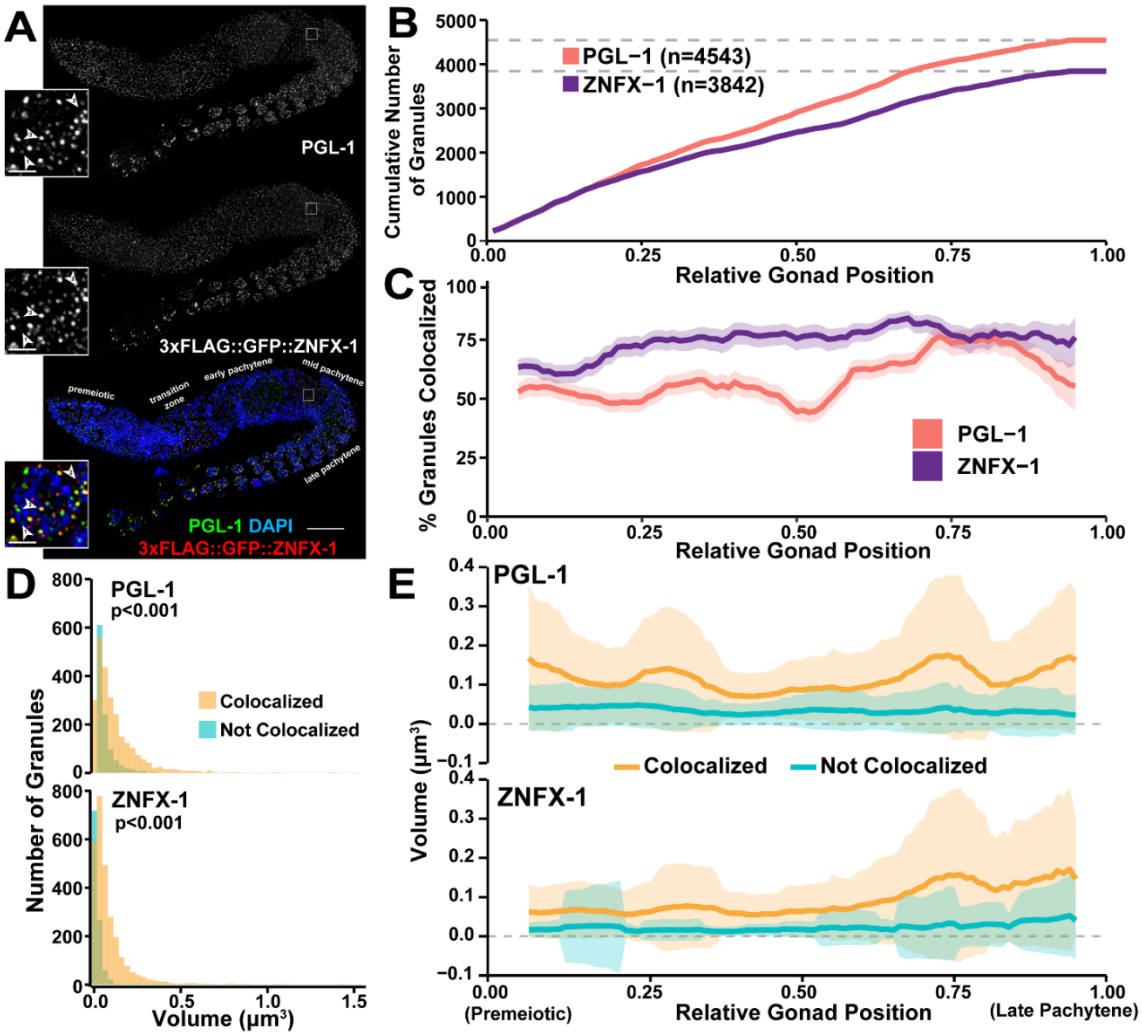

Figure 4.4. Assessment of P-granule components across meiotic prophase I. (A) Immunofluorescence image of a C. elegans hermaphrodite germline stained with DAPI (DNA), PGL-1 (green), and 3xFLAG::GFP::ZNFX-1 (red). Specific meiotic stages were determined by DNA morphology. Inset images show a single mid-pachytene nucleus. The location of these inset nuclei within the original whole germline image are indicated by white boxes on the whole gonad images. Numbered arrowheads, respectively, indicate examples of: (1) a PGL-1 focus not colocalized with ZNFX-1, (2) a ZNFX-1 focus not colocalized with PGL-1, and (3) colocalized PGL-1 and ZNFX-1 foci. The scale bar in the whole germline image represents 20 μm, whereas the scale bars in the insets represent 2 μm. (B) Cumulative number of PGL-1 and ZNFX-1 foci identified across the germline. (C) Percent of total PGL-1 and ZNFX-1 foci which are, respectively, colocalized within a sliding window representing 10% of total germline length. Shaded area represents 95% Binomial Confidence Interval. (D) Histograms displaying the distribution of PGL-1 and ZNFX-1 foci volumes, distinguishing between foci colocalized (yellow) or not colocalized (blue) with other respective protein. P values were calculated from comparisons between colocalized and non-colocalized focus volumes by Mann–Whitney U test. (E) Mean volume of PGL-1 and ZNFX-1 foci in a sliding window representing 10% of total germline length, distinguishing between foci which are (yellow) or are not (blue) colocalized. Shaded area represents standard deviation.

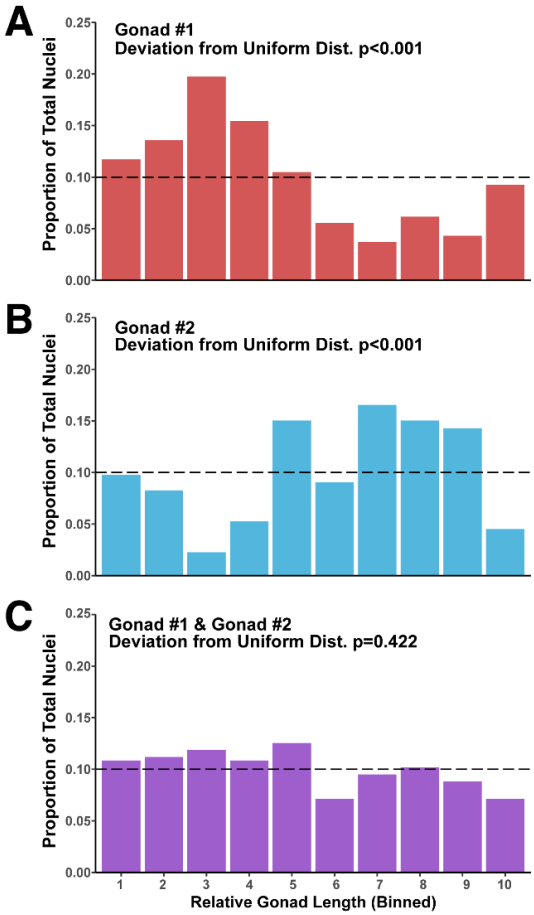

Figure S4.1. Position of individual nuclei within whole germlines identified for computational analysis. Bar plots representing the proportion of nuclei in ten equal bins across the lengths of the two gonads analyzed in Figure 4.2. P values in all panels were calculated by Chi Square Test of Goodness of Fit (expected frequency 0.1 in each bin). (A-B) Number of nuclei within bins across the lengths of analyzed individual germlines. The distribution of nuclei computationally identify by the Whole Gonad Pipeline along the length of each gonad was nonuniform. (C) Number of nuclei within bins of combined gonads analyzed in panels A-B. The distribution of nuclei within bins is indistinguishable from a uniform distribution by this same test when the nuclei from the two germlines are taken together.

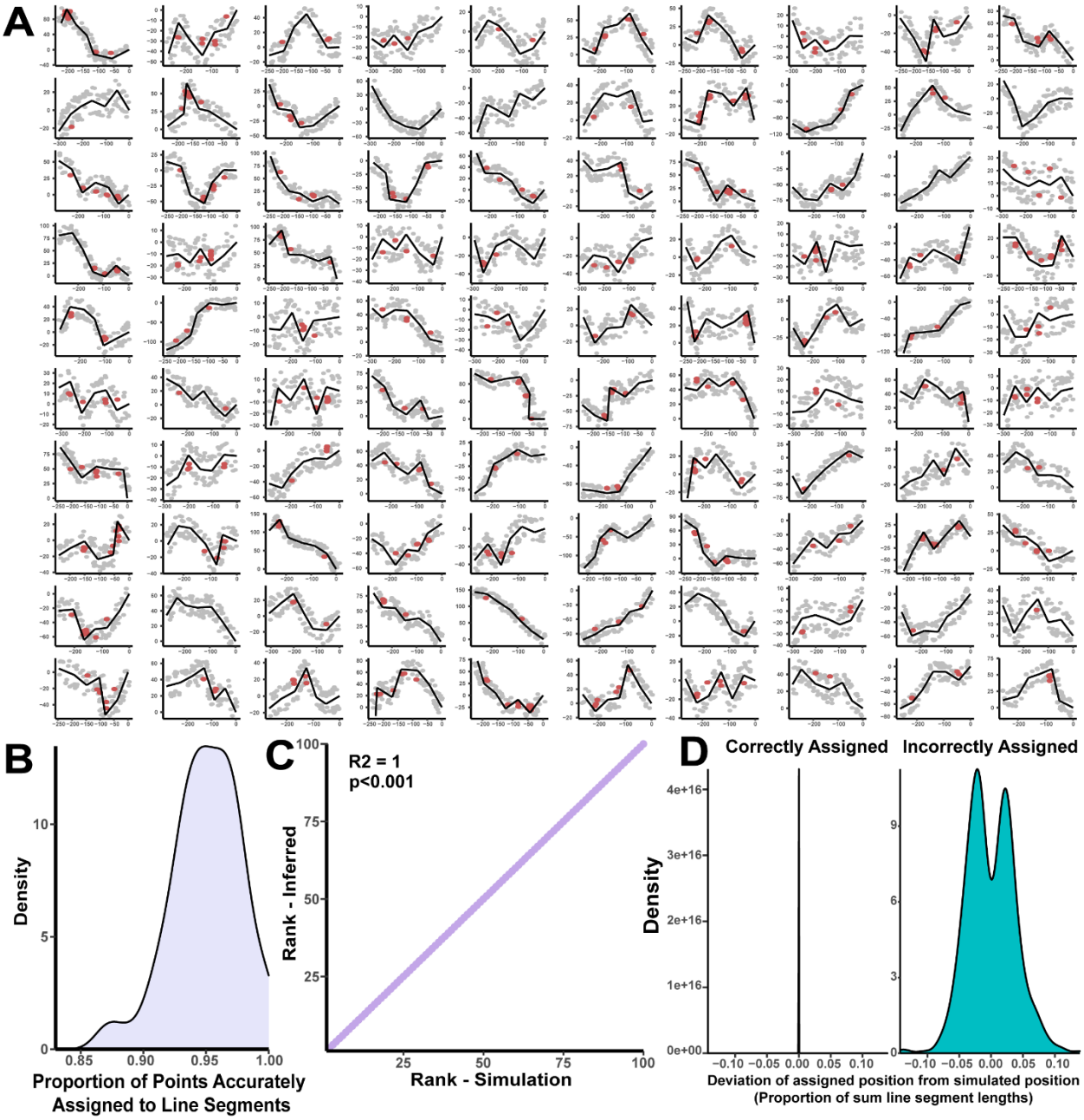

Figure S4.2. Validation of Gonad Linearization algorithm. (A) Plots of simulated dataset of 100 'germlines' each with 100 'nuclei' points dispersed along their lengths. Points were realigned to the central lines using the Gonad Linearization algorithm, and points that were aligned to the correct line segment are marked in grey while points marked in red were aligned to the incorrect line segment. (B) Density plot demonstrating the distribution of accuracy of point alignment to line segments among the 100 individual simulated 'gonads'. (C) Comparison of the known rank order of correctly aligned spots to the rank order of spots as determined by the Gonad Linearization algorithm. R2 and p values were calculated by linear regression analysis. (D) Calculation of the deviation of assigned positions as determined by the Gonad Linearization algorithm from 'actual' known positions from the original simulation.

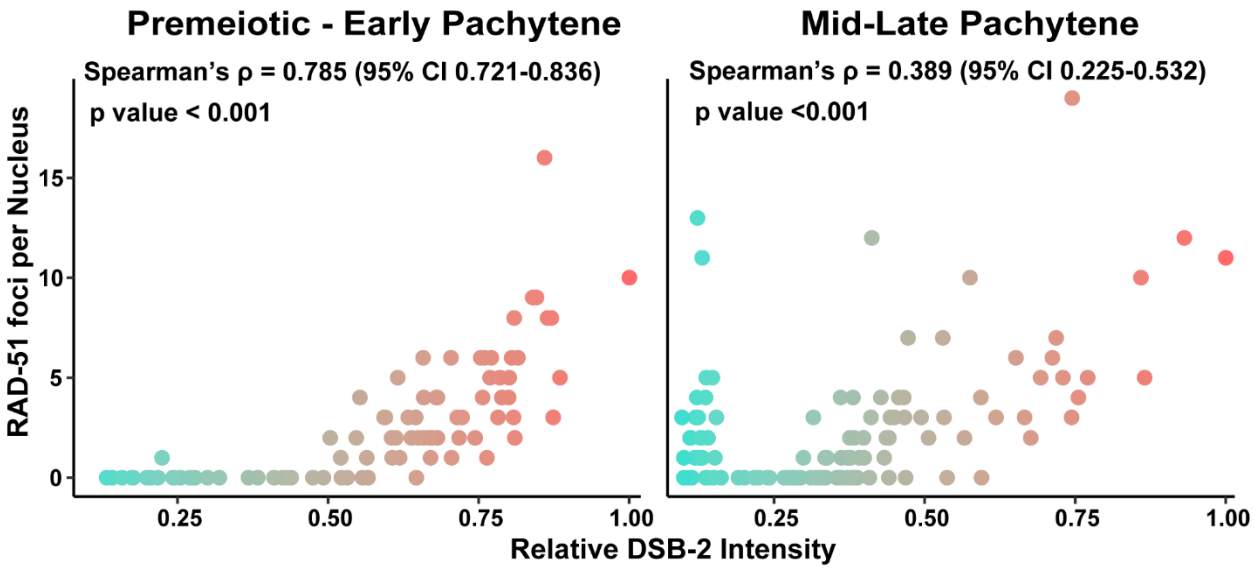

Figure S4.3. DSB-2 normalized intensity per nucleus correlates with RAD-51 foci per nucleus. Assessment of nonparametric correlation by Spearman correlation tests between RAD-51 foci per nucleus and normalized DSB-2 staining intensity among nuclei within the premeiotic through early pachytene stages, and in mid- through late pachytene stages. Specific meiotic stages determined based on DNA morphology.

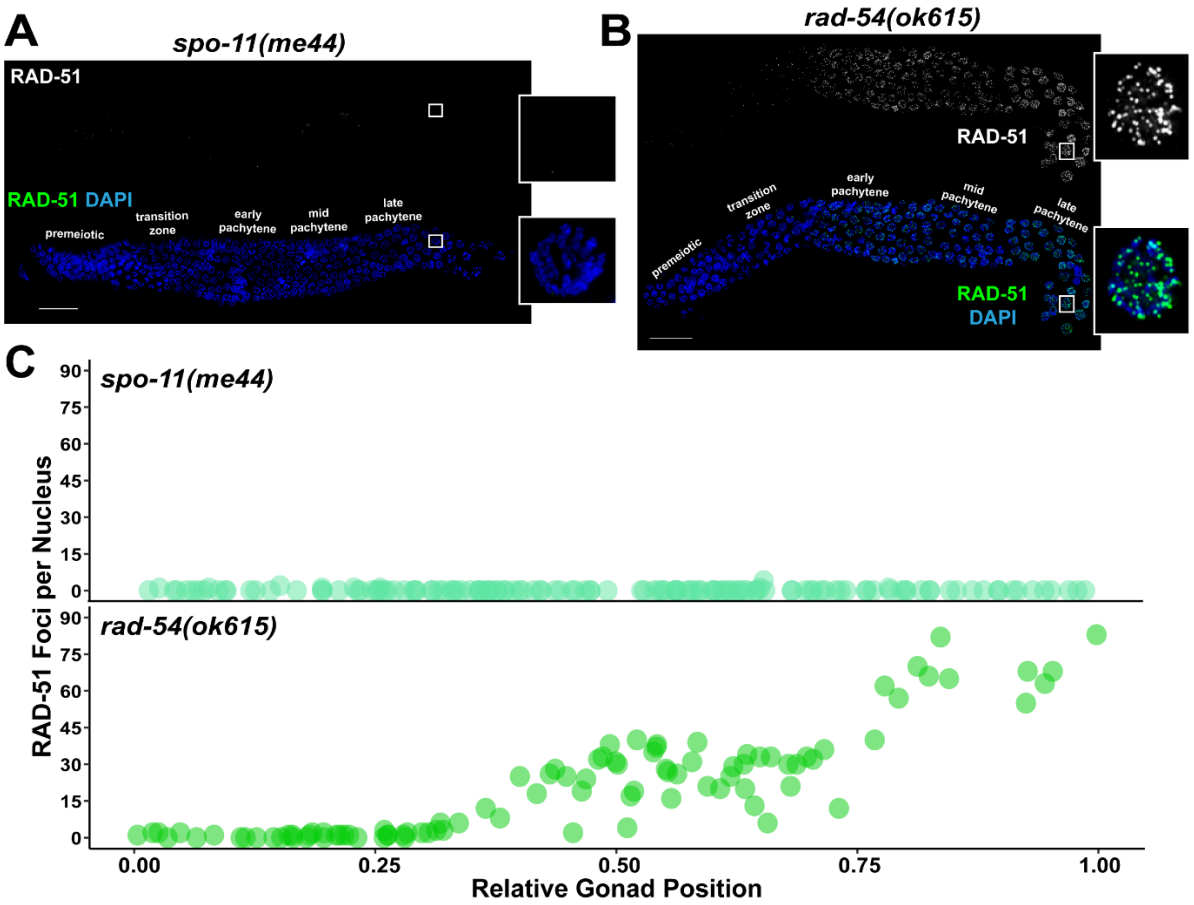

Figure S4.4. RAD-51 foci per nucleus quantification in meiotic mutants. Immunofluorescence images of (A) a *spo-11(me44)* null mutant hermaphrodite germline (no endogenous DSBs made during meiotic prophase I progression), and (B) a *rad-54(ok615)* null mutant hermaphrodite germline (RAD-51 cannot be unloaded during meiotic prophase I progression) stained with DAPI (DNA; blue) and RAD-51 (green). Scale bar represents 20μm. Inset images display representative late pachytene nuclei. The position these nuclei are located within the germline are indicated by white boxes on the whole gonad images. Specific meiotic stages determined based on DNA morphology. Image in (B) is an immunofluorescence image from a supplemental figure in Rosu *et al.*, *Science* 2011 that has been requantified utilizing the method described in this manuscript. (C) Visualization of numbers of RAD-51 foci associated with individual nuclei across the germlines displayed in A-B. Mutants deficient in *spo-11* are unable to induce meiotic DNA breaks, resulting in very few DSBs observed within the germline (Colaiácovo *et al.* 2003). Mutants for *rad-54* are unable to complete DSB repair, and so exhibit elevated and persistent RAD-51 marked DSBs (Mets and Meyer 2009; Rosu *et al.* 2011; Nottke *et al.* 2011).

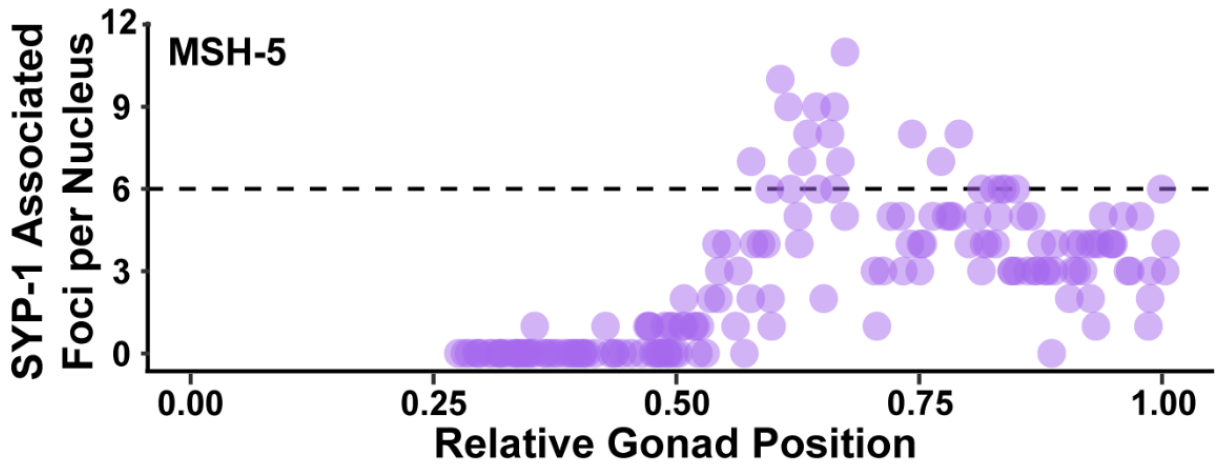

Figure S4.5. Quantification of 'bright' MSH-5 foci associated with the chromosome axes of individual meiotic nuclei. Visualization of numbers of MSH-5 foci associated with SYP-1 within individual nuclei across the germline displayed in Figure 4.3A. As MSH-5 foci are known to become brighter in late prophase I, we restricted our analysis to account for only the brightest foci in the germline. This dataset, composed of identical nuclei to those quantified in the top panel of Figure 4.3C, demonstrates the flexible capacity of Imaris software in conjunction with our Whole Gonad Pipeline to specifically identify and quantify specific subpopulations of meiotic biological features.

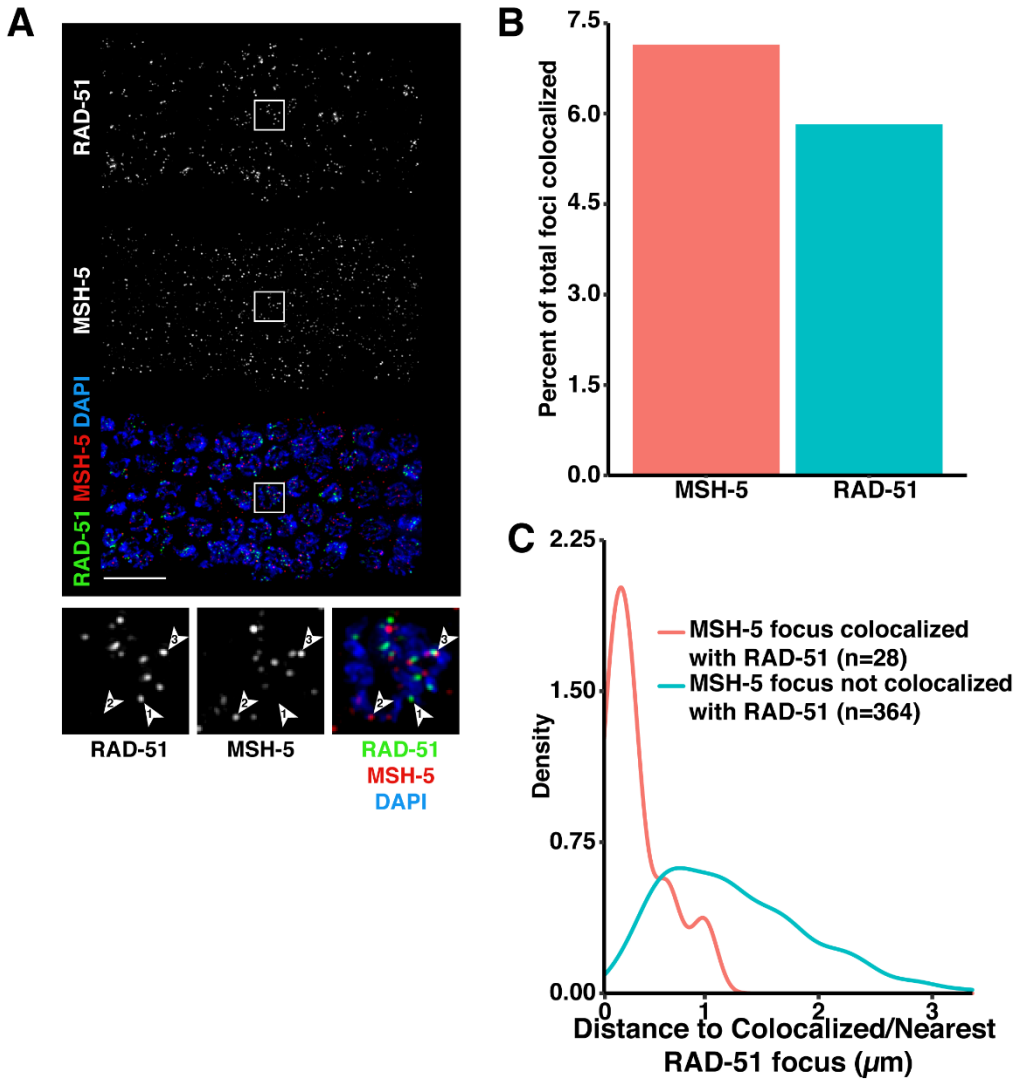

Figure S4.6. Colocalization analysis of meiotic features which infrequently colocalize. To determine the accuracy of our colocalization analysis (Figure 4.4), we assessed the association of MSH-5 and RAD-51, which mark distinct recombination intermediates and rarely colocalize (Schvarzstein *et al.* 2014). (A) Immunofluorescence image of a *C. elegans* hermaphrodite germline stained with DAPI (DNA; blue), RAD-51 (green), and MSH-5 (red). Our analysis focused on early-mid pachytene where MSH-5 and RAD-51 foci are most frequently observed in the same nuclei. Scale bar represents 10μm. Inset images display a representative early pachytene nucleus. The position at which this nucleus is located within the germline is indicated by white boxes on the gonad images. Numbered arrowheads respectively indicate examples of: (1) a RAD-51 focus not colocalized with MSH-5, (2) a MSH-5 focus not colocalized with RAD-51, and (3) colocalized RAD-51 and MSH-5 foci. (B) Proportion of MSH-5 (7.1%; 28/392) and RAD-51 (5.8%; 28/481 foci) foci determined to be colocalized with the respective other protein foci. (C) Density plot displaying the distributions of distances between MSH-5 foci and their respective colocalized RAD-51 focus, or between non-colocalized MSH-5 foci and the nearest RAD-51 focus.

Materials and Methods

Caenorhabditis elegans strains and maintenance

C. elegans strains were maintained under standard conditions on nematode growth medium (NGM) plates at 20°C with OP50 *Escherichia coli* bacteria lawns. All experiments were performed in the N2 background of *C. elegans* (CGC).

Strains used in this study include N2 (wild type), AV157 (*spo-11(me44)/nT1 [unc-?(n754) let-? qIs50]* (IV; V), AV630 (meIs8[*unc-119(+) pie-1p*::GFP::*cosa-1*] II), VC531 (*rad-54*&*snx-3(ok615)* I/hT2 [*bli-4(e937) let-?(q782) qIs48]* I;III), and YY916 (*znfx-1(gg544[3xflag::GFP::znfx-1])* II.).

Immunofluorescence

Immunofluorescence was performed as in (Libuda *et al.* 2013). At 18-22 hours before dissection, L4 stage hermaphrodite worms were isolated and maintained at 20°C on NGM plates seeded with OP50. Gonads were dissected in 30µL of egg buffer (118mM NaCl, 48mM KCl_2, 2mM $CaCl_2$, 2mM $MgCl_2$, 25mM HEPES pH7.4, 0.1% Tween20) and were fixed in egg buffer with 1% paraformaldehyde for 5 minutes on a Superfrost Plus slide (VWR). Gonads were then flash frozen in liquid N_2 and the cover slip was removed. For germlines stained for DSB-2, RAD-51, MSH-5, or GFP::COSA-1, the slide was placed in -20°C MeOH for 1 minute and then was washed in PBST (1x PBS, 0.1% Tween20). For germlines stained for PGL-1 and ZNFX-1, the slide was placed in -20°C MeOH for 10 minutes, then in -20°C acetone for 5 minutes, and then was washed in PBST. Slides were washed 3x in 1xPBST for 5 minutes before being place in block (1xPBS, 0.1% Tween20, 0.7% Bovine Serum Albumin) for 1 hour. 50µL of diluted primary antibody (in 1xPBST; see below for individual antibody concentrations) was applied to each slide and allowed to stain overnight in a dark humidifying chamber with a parafilm coverslip. At 16-18 hours after application of primary antibody, slides were washed 3x in PBST for 10 minutes. 50µL of diluted secondary antibody (in 1xPBST; see below for individual antibody concentrations) was applied to each slide and allowed to stain for 2 hours in a dark humidifying chamber with a parafilm coverslip. Slides were washed 3x in PBST for 10 minutes in a dark chamber and then 50µL of 2µg/mL of DAPI in ddH_2O was added to each slide and incubated for 5 minutes in a dark humidifying chamber with a parafilm coverslip. Slides were washed in PBST for 5 minutes in a dark chamber and then were mounted in VectaShield with a No. 1.5 coverslip (VWR) and sealed with nail polish. Slides were maintained at 4°C prior to

imaging (as described below). The following primary antibodies were utilized in this study at the listed concentrations: polyclonal chicken αRAD-51 (1:1000, this study, see below), αDSB-2 (1:5000; (Rosu *et al.* 2013)), αMSH-5 (1:10,000, Novus #3875.00.02), polyclonal chicken αGFP (1:2000, Abcam #ab13790), monoclonal mouse αPGL-1 K76 (1:20, Developmental Studies Hybridoma Bank), polyclonal guinea pig SYP-1 (1:250; (Macqueen and Villeneuve 2001)), and polyclonal rabbit GFP (1:1000; (Yokoo *et al.* 2012)). Secondary staining was performed with goat antibodies conjugated to Alexa Fluors 488 and 555 targeting the primary antibody species (1:200, Invitrogen).

Antibody production

Our RAD-51 antibody was generated from a His-tagged fusion protein expressed by Genscript from plasmid pET30a containing the entire RAD-51S coding sequence (1385 bp, GenBank accession number AF061201 (Rinaldo *et al.* 1998; Colaiácovo *et al.* 2003)). Antibodies were produced in chicken and affinity purified by Pocono Rabbit Farms.

Image Acquisition

Immunofluorescence slides were imaged at 512 × 512 or 1024 x 1024 pixel dimensions on an Applied Precision DeltaVision microscope with a 63x lens and a 1.5x optivar. To ensure analysis of the highest resolution germline images, we imaged the top ~quarter of the germline along the dorsal-ventral axis that encompassed whole nuclei closest to the coverslip, but our pipeline can be utilized for analysis of gonads imaged through entire dorsal-ventral axis. Images were acquired as Z-stacks at 0.2 μm intervals and deconvolved with Applied Precision softWoRx deconvolution software.

Gonad Analysis Pipeline

Below is a detailed section describing the method. A step-by-step protocol published with the manuscript is available as File S1. For the latest step-by-step protocol of this method, please go to the publication section of www.libudalab.org. The ability to resolve foci or cellular features using this protocol depends on the microscopy method used to capture the images. For this study, widefield microscopy combined with deconvolution was used to generate the gonad images for a resolution limit of 200 nm (see above "Image Acquisition" method section). To resolve objects less than 200 nm apart with this protocol, users will need to use superresolution microscopy techniques, such as structured illumination microscopy (SIM), stochastic optical reconstruction microscopy (STORM), or stimulated depletion microscopy (STED).

Identification of nuclei within whole gonad images: 3D images were tiled using the Imaris Stitcher software (Bitplane) or the Grid/Collection Stitching plugin in FIJI with regression threshold of 0.7 (this value was raised or lowered depending on the stitching results) (Preibisch *et al.* 2009). If images were not accurately aligned by the Imaris Stitcher algorithm, they were manually adjusted before proceeding with analysis. Individual nuclei within stitched gonads were identified by DAPI as Surface objects. When using DAPI staining to define Surface objects, the changing morphology of nuclei within the germline required different sets of parameters to be utilized. Nuclei spanning from the distal premeiotic tip through the final 5 rows of pachytene were defined using Smooth 0.15, Background 3.5, Seed Point Diameter 2-3, and Volume Filter 8-55. Late pachytene nuclei (nuclei in the 5 rows preceding diplotene) were defined using Smooth 0.15, Background 4, Seed Point Diameter 3-4, and Volume Filter 10-50. Manual thresholding and specific values for Seed Point Diameter and Volume Filter were defined for each gonad within the indicated ranges. Defined Surfaces were then split to designate individual nuclei using the Imaris Surfaces Split module. Nuclei which were either partially imaged or overlapping with another nucleus, were eliminated from analysis.

Identification of SYP-1 surfaces in whole gonad images: In 3D stitched gonad images (see 'Identification of nuclei within whole gonad images', above) Individual SYP surfaces were defined using Absolute Intensity (enabled), Smooth (0.22), Background (N/A), Seed Point Diameter (N/A), and Volume Filter (deleted surfaces less than 0.5μm). If multiple individual surfaces were generated to represent the SYP-1 staining of a single given nucleus, then these surfaces were manually unified.

Quantification of DSB-2 normalized mean staining intensity: DSB-2 mean staining intensity per nucleus was calculated in Imaris following definition of single nuclei as surface objects using DAPI signal (see "Identification of nuclei within whole gonad images" section). As image acquisition settings differed between imaged germlines but were consistent within the same germline, the DSB-2 mean intensity of each nucleus was normalized by dividing the mean intensity of each nucleus by the highest mean intensity among nuclei within a gonad.

Quantification of meiotic recombination foci: RAD-51, MSH-5, and GFP::COSA-1 foci were defined from stitched whole gonad images (see "Identification of nuclei within whole gonad images" section) using the Create Spots tool in Imaris (Bitplane) with the settings Estimated XY Diameter 0.1, Model PSF-elongation 1.37, and Background Subtraction enabled. To determine

the number of RAD-51 foci per nucleus by determining based on proximity of defined Spots to Surfaces, we used a custom "Finds Spots Close to Surface" MATLAB module (Threshold value 1; see "Data and Code Availability" section for link to download module). The number of SYP-1 associated MSH-5 or GFP::COSA-1 foci per nucleus was also determined using the "Finds Spots Close to Surface" module (Threshold value 0.1).

Quantification of PGL-1 and ZNFX-1 foci: PGL-1 and ZNFX-1 foci were defined as Surface objects in Imaris (Bitplane) with the settings Smooth (Not enabled), Background 0.513, Seed Point Diameter (Not enabled), and Volume Filter (foci > 0.1μM). In late pachytene, the large variance in different P granule sizes required the generation of a separate additional set of "large" surfaces with the settings Smooth (Not enabled), Background 0.513, Seed Point Diameter (Not Enabled), and Volume Filter A (0.1μm – 2μm) for Filter B (0.1μm – 12μm). To ensure that moderately sized PGL-1 and ZNFX-1 foci were not counted twice in this analysis, we generated unique intensity channels to identify overlapping 'small' and 'large' PGL-1 and ZNFX-1 surfaces. If a "small" and "large" PGL-1 or ZNFX-1 surface was found to share a unique intensity value, indicating that they were occupying the same volume in the 3D reconstructed image, the "small" surface was excluded, as the "large" surface better represented the image.

Colocalization analysis: To determine if foci (PGL-1 and ZNFX-1 Figure 4.4, RAD-51 and MSH-5 Supplemental Figure 4.6) colocalized, we applied the Shortest Distance Calculation function in Imaris to identify and replicate surfaces separated by 0μm. These overlapping surfaces were then given unique colocalization identity intensity channels. A focus was considered "co-localized" in all analyses if two or more foci of different types (PGL-1 and ZNFX-1; or, MSH-5 and RAD-51) with the same unique colocalization intensity value could be identified in the exported data. For colocalization analysis, MSH-5 and RAD-51 foci were identified as surface objects, following a protocol identical to the one described in "Quantification of PGL-1 and ZNFX-1 foci."

Gonad Linearization algorithm

To assess nuclei based on their position within the gonad, we used an algorithm (called "Gonad Linearization" algorithm) implemented in R to approximate the progression of nuclei through the *C. elegans* germline as a linearly ordered sequence beginning at the premeiotic tip and terminating at the end of pachytene. For a link to download the Gonad Linearization algorithm,

see “Data and Code Availability” section of Methods. To delineate the orientation of the gonad, a series of connected line segments marking the approximate center of the gonad were drawn on the stitched germline image using the Imaris Measurement tool. When possible, specific measurement points were placed at positions indicating transitions between meiotic stages based on DAPI nuclei morphology, specifically marking the beginning of the premeiotic zone, transition zone, pachytene, and end of pachytene.

Each line segment drawn through the germline was defined by the coordinates of its respective start (x_i,y_i) and end (x_j,y_j) points. The standard equation [$0=Ax + By + C$] of each line segment $\bar{IJ}$ was calculated such that:

$$A_{\bar{IJ}} = \left(\frac{y_j - y_i}{x_j - x_i}\right)$$

$$B_{\bar{IJ}} = -1$$

$$C_{\bar{IJ}} = y_i - x_i\left(\frac{y_j - y_i}{x_j - x_i}\right)$$

To determine whether the position of a nucleus within the gonad could be well approximated as a position on a given line segment, we calculated the perpendicular intersection point of a vector drawn from the position of the nucleus to each line segment. The perpendicular intersection point (x_p,y_p) of a nucleus at position (x_n,y_n) to a line $\bar{IJ}$ was calculated as:

$$x_p = \frac{y_n - \left(\frac{-x_n}{A_{\bar{IJ}}}\right) - C_{\bar{IJ}}}{A_{\bar{IJ}} - \left(\frac{-1}{A_{\bar{IJ}}}\right)}$$

$$y_p = \left(\frac{-x_p}{A_{\bar{IJ}}}\right) + y_n - \left(\frac{-x_n}{A_{\bar{IJ}}}\right)$$

The transformed coordinate position (x_p,y_p) of a nucleus was considered well approximated if the distances from the start position of the line segment (x_i,y_i) to (x_p,y_p) and the distance from the end position of the line segment (x_j,y_j) to (x_p,y_p) were smaller than the total length of the line segment $\bar{IJ}$. If multiple line segments met this criteria, the correct line segment was inferred to be the one for which the distance from the nucleus’ original position (x_n,y_n) to its perpendicular intersection point (x_p,y_p) was the shortest.

The above method of assigning nuclei to segments was sufficient for all germlines analyzed in this study. However, the specific arrangement of nuclei around the central gonad axis in the

context of the whole germline conformation may lead to nuclei being incorrectly aligned according to these criteria. To ameliorate this potential problem, we included a stringency parameter in our algorithm, which increases the permissible distance nuclei may be assigned to a particular line segment. If increasing the stringency parameter from its default value of 0 is not sufficient to enable more accurate nuclei assignment, nuclei can also be manually assigned to line segments.

Once all nuclei had been assigned transformed coordinate positions, the sum length of all contiguous line segments drawn through a germline, as well as the sum distance of all line segments from the most proximal point to each transformed nucleus position, were calculated. Each length measurement was normalized to the total length of all line segments drawn through the germline to calculate relative gonad position, where a position of 0 corresponded to the start of the premeiotic tip and position 1 corresponded to the end of late pachytene.

Validation of nucleus positioning by the Gonad Linearization algorithm

100 'gonads' were simulated by iteratively generating six consecutive line segments with lengths ~Normal(50,5) and angles of intersection ~Normal(180,30). 100 points were simulated along the sum length of the line segments for each gonad ~Uniform(0,sum line segment lengths). Each point was then transposed perpendicularly to its line segment a distance ~Normal(10,3). These transposed 'nucleus' positions were then realigned to the line segments using the Gonad Linearization algorithm and were subsequently analyzed to determine goodness of fit.

Statistics

All statistics were calculated in R (v4.0.3). Data wrangling was performed using the Tidyverse package (v1.3.0). Nonparametric correlations between DSB-2 normalized staining intensity and RAD-51 focus counts (Supplemental Figure 4.3) were assessed by Spearman correlation tests with confidence intervals calculated using the DescTools package (v0.99.30). Comparisons of RAD-51 focus manual and automated quantification (Figure 4.2B) and the rank order of simulated nucleus position data (Supplemental Figure 4.1C) were performed by linear regression analysis. The 95% Binomial confidence interval for the proportion of colocalized PGL-1 and ZNFX-1 granules (Figure 4.4C) was calculated using the DescTools package. Volumes of PGL-1 and ZNFX-1 (Figure 4.4D) foci were compared by Mann-Whitney U test.

Data and Code Availability

All strains and antibodies available upon request. File S1 contains a step-by-step protocol for the Gonad Analysis Pipeline at the time of this manuscript's publication. The latest step-by-step protocol for the Gonad Analysis Pipeline can be found at www.libudalab.org in the publication section. The "Gonad Linearization" algorithm and "Finds Spots Close to Surface" MATLAB module are available at github.com/libudalab/Gonad-Analysis-Pipeline.

CHAPTER V

AGING AND SPERM SINGALS ALTER DNA DAMAGE INDUCTION AND REPAIR IN THE *C. ELEGANS* GERMLINE

Erik Toraason*, Victoria L. Adler*, and Diana E. Libuda. *In preparation.*

*Indicates co-authorship

Abstract

Female reproductive aging is associated with decreased oocyte quality and fertility. The nematode *C. elegans* is a powerful system for understanding the biology of aging and exhibits age-related reproductive defects that are analogous to those observed in many mammals, including dysregulation of DNA repair. *C. elegans* germline function is influenced simultaneously by both reproductive aging and signals triggered by limited supplies of sperm, which are depleted over chronological time. To delineate the causes of DNA damage repair defects in aged *C. elegans* germlines, we assessed both DNA double strand break (DSB) induction and repair during meiotic prophase progression in aged germlines which were depleted of self-sperm or mated. We find that germline DSB induction is dramatically reduced only in hermaphrodites which have exhausted their endogenous sperm, suggesting that a signal due specifically to sperm depletion downregulates DSB formation. We also find that DSB repair is delayed in aged germlines regardless of whether hermaphrodites had either a reduction in sperm supply or an inability to endogenously produce sperm. These results demonstrate that in contrast to DSB induction, DSB repair defects are a feature of *C. elegans* reproductive aging independent of sperm presence. Finally, we show that the ubiquitin E2 ligase variant UEV-2 is required for efficient DSB repair specifically in young germlines, implicating this protein in regulation of DNA repair during reproductive aging. In summary, our study demonstrates that DNA repair defects are a feature of *C. elegans* reproductive aging and uncovers parallel mechanisms regulating efficient DSB formation in the immortal germline.

Introduction

Genome integrity must be preserved during gamete development, as any genetic defects incurred may have detrimental effects on progeny or fertility. Meiosis, the specialized cell division that generates haploid gametes such as eggs and sperm, utilizes specific DNA repair

pathways to both ensure accurate chromosome segregation and preserve genomic integrity. During early meiotic prophase I, DNA double-strand breaks (DSBs) are intentionally induced across the genome by the conserved topoisomerase-like protein Spo11 (Keeney *et al.* 1997; Dernburg *et al.* 1998). A specific subset of these breaks must be repaired by recombination as crossovers, creating the physical connections between homologous chromosomes required for accurate chromosome segregation. Failure to repair meiotic DSBs accurately and efficiently can contribute to infertility or risk the formation of *de novo* germline mutations.

Gamete quality is negatively impacted in organisms of advanced chronological age (Broekmans *et al.* 2007). In many organisms, oocyte quality in particular declines starkly with maternal age (Luo *et al.* 2009, 2010; Moghadam *et al.* 2022). Oocyte aging is associated with conserved phenotypic changes, including loss of sister chromatid cohesion, dysregulation of DNA repair gene expression, and derepression of heterochromatin and retroviral elements (Luo *et al.* 2010; Achache *et al.* 2021; Raices *et al.* 2021; Chatzidaki *et al.* 2021; Wasserzug-Pash *et al.* 2022).

The nematode *Caenorhabditis elegans* is a key model system for the study of aging biology, including age-related infertility (Mack *et al.* 2018). *C. elegans* hermaphrodites (which produce oocytes as adults) undergo reproductive senescence due to declining oocyte quality and incur many of the defects observed in the aging mammalian ovary (Andux and Ellis 2008; Luo *et al.* 2009, 2010; Achache *et al.* 2021). Unlike many mammalian systems, however, which generate oocytes *in utero* and hold them in dictyate arrest until ovulation, *C. elegans* hermaphrodites continuously produce new oocytes during their adult reproductive period (Albert Hubbard and Greenstein 2000). Mitotic proliferation and ovulation of oocytes is dependent upon signals from sperm, which are stored at the end of the germline in a specialized compartment called the 'spermatheca' (Mccarter *et al.* 1999; Cinquin *et al.* 2016). "Obligate female" mutants, which do not produce sperm, therefore exhibit dramatically slowed germline proliferation and progression (Doniach and Hodgkin 1984; Schedl and Kimble 1988; Mccarter *et al.* 1999; Cinquin *et al.* 2016). The *C. elegans* germline is organized in a spatial temporal gradient wherein oocytes mitotically proliferate at the distal tip and move proximally through the germline as they progress through meiotic prophase I (Albert Hubbard and Greenstein 2000).Thus, oocyte nuclei at all stages of meiotic prophase I are simultaneously present in the adult germline and enable

assessment of meiotic events which are dynamic across prophase, such as the induction and repair of DSBs.

Multiple lines of evidence suggest that preservation of genome integrity is important for the maintenance of oocyte quality during reproductive aging. Human females carrying DNA repair protein variants exhibit extended fertility (Ruth *et al.* 2021). *C. elegans* mutants with extended reproductive periods are also resilient to exogenous DNA damage and upregulate genes associated with DNA repair (Luo *et al.* 2010). Further, recent evidence demonstrated that DNA damage and repair are altered in aged *C. elegans* germlines (Achache *et al.* 2021; Raices *et al.* 2021). By the fourth day of adulthood, *C. elegans* oocyte nuclei exhibit fewer programmed DSBs, delayed loading of recombination proteins, and increased engagement of error-prone repair mechanisms (Achache *et al.* 2021; Raices *et al.* 2021).

Sperm also regulate *C. elegans* germline physiology and reproduction. *C. elegans* hermaphrodites produce sperm only during a late stage in larval development (L'Hernault 2006). By the third to fourth day of adulthood, these sperm are depleted, which leads to a premature cessation of reproduction in *C. elegans* hermaphrodites (Luo *et al.* 2010). Sperm depletion also induces broad transcriptional remodeling independent of aging processes, resulting in a 'female-like' transcriptional profile (Angeles-Albores *et al.* 2017). Mating extends the hermaphrodite reproductive span on average to the sixth day of adulthood, after which declining oocyte quality limits fertility (Luo *et al.* 2010). Mating and even exposure to males, however, also induces deleterious responses in hermaphrodites leading to premature demise (Maures *et al.* 2014; Shi and Murphy 2014). It remains unknown how reproductive aging, signaling induced by the presence or depletion of sperm, and mating intersect to regulate meiotic processes in aged *C. elegans* germlines.

To define DNA repair defects which are specific to reproductive aging, we assayed levels of DSB formation and repair in the meiotic oocytes of aged mated and unmated *C. elegans* hermaphrodites, as well as feminized germline mutants that do not produce sperm (*fog-2* mutants). We demonstrate that while the depletion of sperm downregulates DSB induction in aged germlines, delayed DSB repair is a shared feature of aging germlines independent of sperm presence. Finally, we identify the ubiquitin E2 ligase variant protein UEV-2 as a putative regulator of DNA repair during germline aging. Taken together, our work distinguishes DNA

repair defects specific to reproductive aging and identifies parallel mechanisms regulating gamete quality in the immortal germline.

Methods

Caenorhabditis elegans strains and maintenance

Caenorhabditis elegans strains were maintained at 20°C on nematode growth medium (NGM) plates seeded with OP50 *Escherichia coli* bacteria. All experiments were performed in the N2 genetic background. Strains used in this experiment include AV761 (*GFP::cosa-1* II; *spo-11(me44)* IV/ nT1[qIs51]), AV676 (*GFP::cosa-1* II; *fog-2(q71)* V), N2 (wildtype), CB4108 (*fog-2(q71)* V), DLW135 (*uev-2(gk960600gk429008gk429009);rgr-1(gk429013)* III), DLW199 (libIsX[*pie-1p::uev-2::unc-54 3'UTR*] III:7007600), N2 (wild type), VC30168 (Million Mutation Project strain carrying *uev-2(gk960600)*), and WBM1119 (wbmIs60 [*pie-1p::3XFLAG::dpy-10 crRNA::unc-54* 3'UTR] (III:7007600)).

In experiments with aged animals, L4 hermaphrodites were isolated and maintained on NGM plates seeded with OP50 in the absence of males. Strains which produced self progeny were transferred to new NGM plates seeded with OP50 2 days post-L4 to prevent overconsumption of food from F1 progeny. At this transfer, if the experimental cohort was to be mated, young adult male N2 worms were additionally added to these plates at a ratio of ~1.5-2 males per hermaphrodite. Mated hermaphrodites were again transferred to new NGM plates with OP50 ~20-26 hours after males were added and male animals were discarded.

Strain DLW135 was generated by backcrossing VC30168 to N2 10 times. VC30168 was created by the Million Mutations Project (Thompson *et al.* 2013) and carried many mutations in addition to the *uev-2(gk960600)* allele of interest. Following backcrossing, mutations on Chromosomes I, II, IV, V, and X were assumed to have been eliminated. To determine the success of backcrossing on removing undesired mutations *in cis* with *uev-2* on Chromosome III, we assessed the presence of known flanking mutations to *uev-2(gk960600gk429008gk429009)*. Presence of the upstream most proximal genic mutation to *uev-2*, *pho-9(gk429005)*, was assessed via PCR amplification using OneTaq 2x Master Mix (forward primer DLO1142 5'-ACCCATTTCCCATTCAATCA-3' reverse primer DLO1143 5'-TTGTAATCTGCCCCAAAAGG-3') and subsequent HpaII restriction digest (New England Biolabs). DLW135 carried a wild type allele of *pho-9*, indicating that the region of Chromosome

III upstream of *uev-2* was successfully reverted to wild-type sequence by recombination. However, the closely linked (~1 cM) downstream allele *rgr-1(gk429013)* was preserved in DLW135, as confirmed by Sanger sequencing (Sequetech) of a PCR amplified region of the *rgr-1* locus using OneTaq 2x Master Mix (forward primer DLO1140 5'-TGGAATGGGACTTCCTCTTG-3' reverse primer DLO1141 5'-TTTCCAAAAGCCAGGACATC-3') isolated using a GeneJET PCR Purification kit (ThermoFisher). The *rgr-1(gk429013)* allele is a single base pair substitution resulting in a S360N missense mutation. RGR-1 is a Mediator complex subunit involved in transcriptional activation that is required for embryonic viability (Shim *et al.* 2002). S360N does not disrupt a predicted functional domain, and mutants carrying *rgr-1(gk429013)* survive embryogenesis and are fertile, indicating that this mutation does not severely disrupt function of the RGR-1 protein. As RGR-1 is not known to play a role in DNA damage repair, and *uev-2* has been previously demonstrated to modulate germline sensitivity to DNA damage (Luo *et al.* 2010), the phenotypes we observed using DLW135 in this manuscript are not best explained by the presence of the *rgr-1(gk429103)* mutation. For simplicity, DLW135 mutants are referred to as '*uev-2* mutants' in the text of this manuscript.

CRISPR/Cas9 genome editing

Strain DLW199 was generated using the SKILODGE transgenic system (Silva-García *et al.* 2019). WBM1119 was injected with 40ng/μL pRF4 purified plasmid, 40ng/μL purified PCR amplicon of the full *uev-2* coding sequence with 35bp homology arms to the wbmIs60 landing site (Phusion polymerase, forward primer DLO1144 5'-tcccaaacaattaaaaatcaaattttcttttccagATGCGAAGACGTAGCAACAG-3' reverse primer DLO1154 5'-taattggacttagaagtcagaggcacgggcgcgagatgTTAGTTTTCGATGTCAATTGGT-3'), 0.25 μg/μL Cas9 enzyme (IDT), 100ng/μL tracrRNA (IDT), and 56ng/μL crRNA DLR002 (5'-GCUACCAUAGGCACCACGAG-3'). Dpy F1 progeny were isolated and screened for insertion at the wbmIs60 locus by PCR following the SKILODGE recommended protocols (primers CGSG130, CGSG117 (Silva-García *et al.* 2019)).

The candidate insertion identified among progeny from the above injected hermaphrodites contained an undesired additional 43bp of sequence between the 5' 3xFLAG tag of the edited wbmIs60 landing site and the start codon of the *uev-2* coding sequence. The strain carrying this insertion allele was backcrossed 3x to N2 and was CRISPR/Cas9 edited again to remove the

undesired 5' sequence. Worms were injected with 0.25 μg/μL Cas9 (IDT), 100ng/μL tracrRNA (IDT), 28ng/μL gRNA DLR022 (5'-GAUCUUUAUAAUCACCGUCA-3'), 28ng/μL gRNA DLR023 (5'-UGUUGCUACGUCUUCGCAUC-3'), 25ng/μL ssODN donor DLO1173 (5'-AACAATTAAAAATCAAATTTTCTTTTCCAGATGCGGAGGCGAAGTAATAGACAATATGTTGATCTCTCATATTTTCGCGAAAC-3'), and 40ng/μL purified pRF4 plasmid. Successful removal of the 3xFLAG sequence and undesired 43bp inserted sequence were confirmed by PCR and Sanger sequencing (Sequetech).

Nematode irradiation

C. elegans worms were maintained at 20°C on NGM plates seeded with OP50 prior to and following irradiation. Irradiation was performed using a Cs^{137} source (University of Oregon).

Immunofluorescence sample preparation and microscopy

Immunofluorescence samples were prepared as in (Libuda *et al.* 2013). Nematodes were dissected in 1x Egg Buffer (118 mM NaCl, 48 mM KCl_2, 2 mM $CaCl_2$, 2 mM $MgCl_2$, 25 mM HEPES pH7.4, 0.1% Tween20) and were fixed in 1x Egg Buffer with 1% paraformaldehyde for 5 min on a SuperFrost Plus slide (VWR). Slides were then flash frozen in liquid nitrogen and the cover slip was removed before the slides were placed in ice cold methanol for 1 minute. Slides were washed in 1xPBST (1x PBS, 0.1% Tween20) 3x for 10 minutes before they were placed in Block (1xPBST with 0.7% bovine serum albumin) for a minimum of one hour. 50μL of primary antibody diluted in PBST (see below for specific antibody dilutions) was then placed on each slide and samples were incubated for 16-18hrs in a dark humidifying chamber with parafilm coverslips. Slides were then washed 3x in 1xPBST for 10 minutes. 50μL of secondary antibody diluted 1:200 in PBST were then added to each sample and slides were incubated for 2hr in a dark humidifying chamber with parafilm coverslips. Slides were washed 3x in 1xPBST for 10 minutes, and then 50μL of 2μg/mL DAPI was applied to each slide. Samples were incubated in a dark humidifying chamber with parafilm coverslips for 5 minutes, then were washed 1x in PBST for 5 minutes. Slides were mounted with a No 1.5 coverslip (VWR) and sealed with nail polish. All slides were maintained at 4°C until imaging.

Immunofluorescence images were acquired at 512x512 or 1024x1024 pixel dimensions on an Applied Precision DeltaVision microscope with a 63x lens and a 1.5x optivar. All images were acquired in 3 dimensions with Z-stacks at 0.2μm intervals. In a minority of aged unirradiated

germlines, we noted that most nuclei in mid-late pachytene exhibited high levels of RAD-51 and condensed DNA morphology characteristic of apoptosis. These aberrant gonads were not included in our analyses. Images were deconvolved with Applied Precision softWoRx software and individual image tiles were stitched into a single image for analysis using the Grid/Collection Stitching module in Fiji with regression threshold 0.7 (Preibisch *et al.* 2009) or using Imaris Stitcher software (Bitplane).

Specific antibodies used and their dilution factors are: Rabbit αRAD-51 (1:500), Chicken αRAD-51 (1:1000), Rabbit αDSB-2 (1:5000) (Rosu *et al.* 2013), Alexa Fluor 488 Goat αChicken (1:200), Alexa Fluor 555 Goat αRabbit (1:200), and Alexa Fluor 488 Goat αRabbit (1:200).

Image analysis and quantification

Images were analyzed as described in (Toraason *et al.* 2021b). Image quantification was performed using Imaris software (Bitplane). Individual nuclei within stitched gonads were identified as Surface objects (Smooth 0.1-0.15, Background 3-4, Seed Point Diameter 3-4) based on DAPI staining intensity. Manual thresholding of specific values were used per gonad to generate surfaces which represented the nuclei observed. Defined surfaces were then split to designate individual nuclei using the Imaris Surfaces Split module. Nuclei which were partially imaged or overlapped with other nuclei were eliminated from the analysis. RAD-51 foci were defined as Spot objects (Estimated XY Diameter 0.1, Model PSF-elongation 1.37, Background Subtraction enabled). To determine the number of RAD-51 foci per nucleus, we either utilized the "Find Spots Close to Surface" MATLAB module (Threshold value 0.1) or utilized the "Closest Distance to Surface" statistic calculated by Imaris to find the number of Spots ≤0.1μm distant from nuclei. The length of each germline was defined using the Imaris Measurements tool. Measurement points were specifically placed at the beginning of the premeiotic tip and the end of pachytene. For germlines which had a defined transition zone by DAPI morphology, points were also placed at the start and end of the transition zone.

Nuclei positions were transformed from 3D coordinates to a linear order using the Gonad Linearization Algorithm implemented in R (Toraason *et al.* 2021b). Gonad length in germlines which lacked a defined transition zone (e.g. *fog-2* mutants, Figure S5.2) was normalized to the distance from the premeiotic tip to the end of pachytene, where the premeiotic tip begins at position 0 and the end of pachytene is at position 1. In all other germlines, the gonad length was

normalized to pachytene, where the beginning of pachytene is position 0 and the end of pachytene is position 1.

Germline DSB-2 staining was analyzed in Imaris using germlines stitched in Fiji as described above. The length of the germline was defined using the Imaris Measurements tool. Specific points were placed at the beginning of the transition zone, end of the transition zone, beginning of the DSB-2 zone (defined as the row of nuclei in which most nuclei had DSB-2 staining), the end of the DSB-2 zone, the final position of one or more nuclei which had DSB-2 staining, and the end of pachytene. The measured distances were then normalized to pachytene, where the beginning of pachytene is position 0 and the end of pachytene is position 1.

fog-2 Brood Viability Assay

C. elegans worms were maintained at 20°C during fertility assays. Feminized *fog-2* mutants were synchronized in age by placing gravid mated CB4108 females onto an NGM plate seeded with OP50 for one hour. Hatched female progeny were isolated as L4s from these plates and were kept in isolation from males to prevent mating. At adult day 1, 2, 3, 4, or 5, these isolated *fog-2* females were then placed on individual plates with n=2 young adult N2 males each. Mated *fog-2* females were then subsequently transferred to new NGM plates seeded with OP50 with young adult N2 males at either 6hr, 12hr, 18hr, 24hr, and 48hr after the first mating, or at 24hr and 48hr after the first mating. 72hr after the first mating, adult females were discarded. Plates were scored ~24hr after the parent female was removed for hatched progeny, dead eggs, and unfertilized oocytes. Brood viability was calculated as (hatched progeny) / (hatched progeny + dead eggs). Fertility assays were replicated twice with n=5 females of each age group assayed per replicate.

During the course of the brood viability assays, some mated *fog-2* females exhibited matricidal hatching. This phenotype was more pronounced in aged worms, consistent with previous work which showed that matricidal hatching is exacerbated with maternal age (Pickett and Kornfeld 2013). Only eggs which were successfully ovulated were scored in the assay.

Statistics

All statistics were calculated in R (v4.0.3). Data wrangling was performed using the Tidyverse package (v1.3.0) (Wickham *et al.* 2019). Specific statistical tests used are denoted in the figure legends and text. P values were adjusted for multiple comparisons when appropriate. If 3 pairwise comparisons were being performed, Bonferroni correction was applied. If >3 pairwise

comparisons were performed, Holm-Bonferroni correction was instead applied to reduce the risk of type II statistical errors.

Data and Code Availability

The gonad linearization algorithm is available on the Libuda Lab GitHub <github.com/libudalab/Gonad-Analysis-Pipeline> and on the Libuda Lab website <libudalab.org>

Results

Meiotic DNA damage levels are influenced by both aging and sperm depletion

To determine the relative contributions of reproductive aging and sperm depletion to DNA damage repair dynamics in the *C. elegans* germline, we examined DNA damage levels in the oocytes of aged hermaphrodites which were mated (to prevent sperm depletion) or unmated (to permit sperm depletion) (Figure 5.1A). DNA damage was quantified using immunofluorescence to visualize the recombinase RAD-51, which marks DSBs designated for repair by recombination (Gartner and Engebrecht 2022). "Young" germlines were isolated from N2 hermaphrodites on the first day of adulthood (1 day post-L4, Figure 5.1A), while "aged" germlines were isolated from N2 hermaphrodites on their fourth day of adulthood (4 days post-L4, Figure 5.1A). Aged hermaphrodites were maintained either unmated to males, or mated with males from their second to third day post-L4 larval stage (Figure 5.1A, see Methods).

To quantify the profile of DSB induction and repair across prophase I, we counted the number of RAD-51 foci per nucleus in oocytes from young and aged animals throughout the germline (see Methods). Under normal conditions, RAD-51 foci accumulate within nuclei following DSB induction by the conserved endonuclease SPO-11 in early pachytene (Dernburg *et al.* 1998; Colaiácovo *et al.* 2003). Then, as nuclei progress through mid and late pachytene, these RAD-51 foci decline in number as DSBs are repaired (Colaiácovo *et al.* 2003). During early pachytene, the amount of RAD-51 foci per nucleus was similar between aged mated germlines and young germlines (Figure 5.1B-C, Bin 2 Mann-Whitney U test $p=0.258$). Young germlines, however, accumulated a higher total number of RAD-51 foci per nucleus (Figure 5.1B-C, Bin 3 Mann-Whitney U test $p=0.005$), suggesting that DSB induction or RAD-51 loading is slightly compromised in aged mated germlines. We further noted that RAD-51 foci in aged unmated germlines were greatly decreased throughout early pachytene as compared to both

young and aged mated germlines (Figure 5.1B-C, Bins 2-3 Mann-Whitney U test $p<0.001$), indicating that sperm depletion in aged germlines may affect meiotic DSB induction and/or RAD-51 loading.

In contrast to early pachytene, nuclei throughout mid pachytene from aged mated germlines maintained higher levels of RAD-51 than young germlines (Figure 5.1B-C, Bins 4-5 Mann-Whitney U test $p<0.05$). We observed a similar effect in the aged unmated germlines, which also displayed elevated numbers of RAD-51 foci relative to young germlines throughout mid pachytene (Figure 5.1B-C, Bins 4-5 Mann-Whitney U test $p<0.001$). Thus, DSB repair at mid-pachytene may be delayed in aging germlines regardless of mating or sperm depletion. Notably, by late pachytene the number of RAD-51 foci per nucleus converged between young, aged mated, and aged unmated germlines (Figure 5.1B-C, Bin 6 Mann-Whitney U test $p>0.05$), indicating that ultimately all DSBs can be repaired or minimally offload RAD-51 in aged germlines. Taken together, our results suggest that parallel mechanisms may regulate DNA damage levels in aged *C. elegans* germlines: 1) depletion of sperm downregulates DSB induction and/or RAD-51 loading; and, 2) reproductive aging delays RAD-51 foci unloading at mid pachytene.

To determine if the persistent RAD-51 foci in aged mated and unmated germlines were derived from the programmed meiotic DSBs, we also examined RAD-51 foci in *spo-11(me44)* null mutants, which do not form meiotic DSBs (Figure S5.2) (Colaiácovo *et al.* 2003). We did not observe a notable increase in nuclei with RAD-51 foci in aged *spo-11* germlines, indicating that the persistent RAD-51 foci present at mid pachytene in aged wildtype gonads are derived from normal meiotic functions.

Nuclei which are competent for DSB induction in the *C. elegans* germline are marked with the protein DSB-2 (Rosu *et al.* 2013). To assess if the altered accumulation of DSBs which we observed in aged unmated germlines coincided with a change in competency for DSB induction, we quantified the extent of young and aged germlines in which ≥50% of nuclei exhibited DSB-2 staining (the "DSB-2 zone", Figures S5.2A-B). DSB-2 accumulates on meiotic chromatin beginning in the transition zone (leptotene/zygotene) and is offloaded from the majority of nuclei by mid pachytene (Rosu *et al.* 2013; Toraason *et al.* 2021b). Mutants which incur errors in crossover formation, however, maintain DSB-2 on meiotic chromatin later into pachytene (Rosu *et al.* 2013). While the length of the DSB-2 zone was only subtly altered in

aged mated germlines (Figure S5.2B-C, Mann-Whitney U test p=0.027), the DSB-2 zone persisted later into pachytene in aged unmated germlines relative to young germlines (Figure S5.2B-C, Mann-Whitney U test p=0.008). Thus, our data indicate that the extent of DSB-2 marked pachytene nuclei is influenced both by aging and by the absence of sperm.

Meiotic DNA damage is elevated in aging feminized germlines

To uncouple the relationship between sperm depletion and reproductive aging in regulating DSB induction and DNA repair, we examined RAD-51 levels in germlines which have never been impacted by sperm or mating. Hermaphrodites carrying the *fog-2(q71)* mutation do not produce sperm during larval development but proliferate a full adult complement of oocytes (Schedl and Kimble 1988), rendering them "obligate females." Due to the absence of signaling from sperm in *fog-2* mutants, both germline stem cell proliferation and meiotic progression are halted, such that meiotic oocytes are held within the gonad (Mccarter *et al.* 1999; Cinquin *et al.* 2016). Nonetheless, feminized mutants undergo reproductive senescence and exhibit reduced oocyte quality with age (Figure S5.3; (Andux and Ellis 2008; Luo *et al.* 2009))

We analyzed the levels of RAD-51 foci in oocyte nuclei from young (1 day post-L4), aged (4 days post-L4), and old (6 days post-L4) *fog-2* germlines (Figure S5.2A-B). During our experiments we noted that the cytologically distinctive transition zone, which demarcates meiotic entry and is composed of nuclei undergoing active chromosome motion to facilitate pairing, was dramatically reduced in aged *fog-2* germlines (Figure S5.4). Previous work has shown that mitotic germ cell proliferation is reduced in feminized and sperm-depleted germlines (Cinquin *et al.* 2016). Thus, the absence of a transition zone in aged *fog-2* germlines may be the product of two parallel effects: nuclei in the transition zone completing pairing and entering pachytene, and decreased proliferation also limiting the number of new nuclei which enter meiosis. This lack of the transition zone in aged *fog-2* germlines presented a challenge for staging meiotic nuclei to make comparisons between young and aged gonads. To quantify RAD-51 levels in *fog-2* germlines independent of meiotic stages, we normalized the germline length with position 0 at the premeiotic tip and position 1 at the end of pachytene and used a sliding window to assay RAD-51 foci within the germline (Figure S5.2D, see Methods) (Toraason *et al.* 2021b). To describe the RAD-51 profile of aging *fog-2* germlines, we calculated two metrics: 1) the "RAD-51 zone" indicating the extent of the germline which contained nuclei with RAD-51 foci; and, 2) the "peak RAD-51 window" indicating the maximum levels of RAD-51 within the germlines.

To assess whether the proportion of germline nuclei with RAD-51 foci was altered in aging *fog-2* germlines, we calculated the "RAD-51 zone" of each age group, which was defined as the germline distance extending from the most distal (near the premeiotic tip) to the most proximal (near the end of pachytene) windows in which at least 50% of nuclei had one or more RAD-51 foci (Figure 5.2B, 5.2D). We found that the RAD-51 zone extended more distally in the germline in aged and old *fog-2* animals as compared to young germlines (Figure 5.2B, 5.2D). This distal expansion of the RAD-51 zone can likely be explained by transition zone nuclei in young germlines completing the pairing process and entering pachytene as the germline ages. In contrast, the proximal end of the RAD-51 zone only subtly shifted distally in aged and old germlines (Figure 5.2B, 5.2D). This result indicates that later prophase I nuclei within aged *fog-2* germlines continue to either maintain or incur RAD-51 marked DSBs.

To determine if the number of RAD-51 marked DSBs in *fog-2* germline nuclei were altered with age, we identified the "peak RAD-51 windows" in each age group, defined as the window in which the mean RAD-51 foci per nucleus was highest (Figure 5.2C, 5.2D arrowheads). We noted that the position of the peak RAD-51 window moved distally in aged and old *fog-2* germlines (Figure 5.2D arrowheads), suggesting that the spatial regulation of DSB induction and repair may change as feminized germlines age. The number of RAD-51 foci per nucleus within the peak RAD-51 window was not significantly different in aged germlines as compared to young gonads (Figure 5.2C-D, Mann-Whitney U test p=1.000). Old germlines, however, exhibited a significant ~1.5 fold increase in RAD-51 foci per nucleus as compared to young and aged germlines within the peak RAD-51 window, indicating that *fog-2* mutant germ cells accumulate RAD-51 marked DNA damage foci during aging (Figure 5.2C-D, Mann-Whitney U test $p < 0.001$). This result notably differs from aged unmated wildtype germlines, which exhibit reduced DSBs with age (Figure 5.1B-C) (Achache *et al.* 2021; Raices *et al.* 2021). Our data therefore support a model in which sperm depletion, rather than absence of sperm, downregulates meiotic DSB induction.

DSB repair is altered in aged feminized germlines

The accumulation of RAD-51 foci observed in aging *fog-2* germlines may be the product of: 1) increased induction of DSBs; 2) defects in DSB repair; or, 3) a combination of these effects. To assess the efficiency of DSB repair during *fog-2* germline aging, we exposed young (1 day post-L4) and aged (4 days post-L4) *fog-2* mutant females to 5000 Rads of ionizing

radiation (Figure 5.3A, Supplemental Figure 5.5), inducing ~118 DSBs per nucleus throughout the germline (Yokoo *et al.* 2012). We then allowed the animals to age for 2 days to resolve this DNA damage before assessing germlines for persistent unrepaired DSBs as marked by RAD-51 foci (Figure 5.3A). As *fog-2* germlines accumulate DSBs during aging (Figure 5.2C-D), we established baseline levels of DNA damage based on comparing RAD-51 foci in animals of equivalent ages that were never exposed to radiation to the irradiated cohorts (Figure 5.3A). We noted considerable inter-nucleus variance in the RAD-51 foci, which persisted following irradiation in both young and aged germlines (Supplemental Figure 5.5). This effect was particularly prominent in the distal germlines of both groups (Supplemental Figure 5.5C-D), suggesting that a subpopulation of nuclei in the mitotic germline or early stages of meiosis are uniquely susceptible to exogenous DNA damage regardless of parental age.

To estimate the residual DSBs derived from irradiation which were not yet repaired two days post irradiation, we calculated the median number of RAD-51 foci in a sliding window across the germline (Figure 5.3B, see Methods) and subtracted the unirradiated median RAD-51 foci from the irradiated median RAD-51 foci in each window (Figure 5.3C). Both young and aged germlines maintain high levels of damage in the distal germline following irradiation (germline position 0.0-0.5, Figure 5.3C, Supplemental Figure 5.5C). Nuclei in the proximal region of young irradiated germlines did not consistently maintain median DNA damage levels higher than baseline; whereas aged irradiated germlines maintained a median elevation of ~6-10 RAD-51 foci per nucleus (germline position 0.5-1.0, Figure 5.3C). This result indicates that aged *fog-2* germlines exhibit DNA repair defects specifically in nuclei at later stages of meiotic prophase I. Taken together, our experiments in "feminized" germlines demonstrate that DNA repair efficiency is altered in aging germlines independent of any signals from sperm.

UEV-2 is required for 'youthful' germline DSB repair

To identify proteins which may regulate DNA damage repair in the aging *C. elegans* germline, we looked to candidate genes upregulated in long-reproductive *sma-2* mutant oocytes, which exhibit DNA damage resilience in addition to delayed reproductive senescence (Luo *et al.* 2010). The *sma-2* DNA damage resilience phenotype requires upregulation of the ubiquitin E2 ligase variant UEV-2, suggesting that this protein may promote efficient germline DNA repair (Luo *et al.* 2010). UEV proteins lack a catalytic cysteine residue conserved in E2 ubiquitin ligases (Sancho *et al.* 1998) but have been shown to form heterodimeric complexes with other E2

ubiquitin ligases to influence their function, implying regulatory roles for this protein class (Vandemark *et al.* 2001; Wijk and Timmers 2010).

To assess the influence of UEV-2 on DNA damage repair during germline aging, we utilized a strain carrying the putative null allele *uev-2(gk960600)*, which ablates the translation initiation site and second exon boundary of the gene (Supplemental Figure 5.6; see Methods). With the *uev-2* mutant strain, we examined the number of RAD-51 foci in germline nuclei derived from young (1 day post-L4) or aged (4 days post-L4) animals (Figure 5.4A). Aged *uev-2* mutants were also mated to avoid the DSB induction defects associated with sperm depletion (Figure 5.4A). If UEV-2 functions to promote efficient DSB repair in young gonads but becomes dysregulated or loses function during aging, then we would expect *uev-2* mutants to exhibit defects in DSB repair in young germlines but minimal additional defects in aged germlines. Indeed, when we compared the levels of RAD-51 observed in young and aged mated wildtype and *uev-2* germlines, we observed DSB repair defects that did not accumulate with age. In early pachytene, young and aged *uev-2* mutants exhibited similar levels of RAD-51 to young wildtype germlines (Figure 5.4B-C, Bins 2-3 Mann-Whitney U test $p>0.05$), indicating that UEV-2 is not required for meiotic DSB induction nor RAD-51 loading. In contrast, at mid pachytene, young *uev-2* mutant germlines maintained elevated RAD-51 foci relative to young wildtype germlines (Figure 5.4B-C, Bins 4-5 Mann-Whitney U test $p<0.05$). The specific levels of DSBs at mid pachytene in young *uev-2* mutants were also indistinguishable from aged wildtype germlines (Figure 5.4B-C, Bins 4-5 Mann-Whitney U test $p>0.05$). These results at mid pachytene indicate that DSB repair is delayed in young *uev-2* mutants to an extent which recapitulates the effect we observe during wildtype aging. Aged *uev-2* germline RAD-51 levels at mid pachytene were statistically indistinguishable from either young or aged mated wildtype germlines (Figure 5.4B-C, Bins 4-5 Mann-Whitney U test $p>0.05$), suggesting that the *uev-2* mutation does not grossly exacerbate DSB repair defects with age.

In late pachytene, the specific rates of DSB resolution diverged slightly between young and aged *uev-2* and wildtype germlines (Figure 5.4B-C, Bins 6-7 Mann-Whitney U test $p<0.05$), suggesting that UEV-2-independent and age-specific effects may contribute to DSB resolution at this meiotic stage. Taken together, our results indicate that loss of *uev-2* in young germlines is sufficient to phenocopy the mid pachytene patterns of DSB repair observed in an aged wildtype

context. This observation supports a model in which UEV-2 functions in young germlines specifically to promote efficient DSB repair.

Overexpression of *uev-2* alters RAD-51 foci levels in an age-dependent manner

As loss of *uev-2* in young germlines appeared to "prematurely age" RAD-51 foci patterns, we hypothesized that overexpression of *uev-2* in aged germlines could ameliorate persistent RAD-51 foci at mid pachytene. To test this hypothesis, we used CRISPR/Cas9 genome editing to generate a germline-specific overexpression construct of *uev-2* driven by the *pie-1* promoter (*pie-1p::uev-2*, see Methods). We then assessed for the presence of DSBs as marked by RAD-51 in the germlines of young (1 day post-L4) or aged (4 days post-L4) mated animals overexpressing UEV-2 and compared those levels to young and aged mated wildtype germlines (Figure 5.5A).

At the beginning of early pachytene, both young and aged mated *pie-1p::uev-2* mutants initially accumulated DSBs at levels similar to young and aged mated wildtype gonads (Figure 5.5B-C, Bin 2 Mann-Whitney U test $p>0.05$). However, aged mated *pie-1p::uev-2* mutants accumulated fewer total DSBs than young wildtype, aged mated wildtype, and young *pie-1p::uev-2* germlines (Figure 5.5B-C, Bin 3 Mann-Whitney U test $p<0.05$). At mid pachytene, young *pie-1p::uev-2* germlines maintained elevated RAD-51 foci over young wildtype germlines, suggesting that overexpression of *uev-2* deleteriously impacted recombination in this context (Figure 5.5B-C, Bin 4-5 Mann Whitney U test $p\leq0.001$). This effect was not preserved in aged mated *pie-1p::uev-2* germlines, which exhibited similar DSB levels as young wildtype germlines at the beginning of mid pachytene and slightly elevated foci at the end of mid pachytene (Figure 5.5B-C, Mann-Whitney U test Bin 4 $p=0.156$ Bin 5 $p=0.023$).

Throughout late pachytene, young *pie-1p::uev-2* germlines maintained subtle but significantly elevated DSBs relative to young and aged wildtype germlines (Figure 5.5B-C, Bin 6-7 Mann-Whitney U test $p<0.05$). Conversely, aged mated *pie-1p::uev-2* germlines maintained significantly fewer RAD-51 foci throughout late pachytene than young wildtype or young *pie-1p::uev-2* germlines (Figure 5.5B-C, Bin 6-7 Mann-Whitney U test $p<0.05$). Taken together, these data suggest that UEV-2 is not the sole regulator of DSB repair efficiency during *C. elegans* germline aging and appears to have age-dependent functions in regulating meiotic DSB accumulation and repair.

Discussion

C. elegans germline function is impacted both by reproductive aging and sperm signals. Our study demonstrates that aged *C. elegans* germlines exhibit delayed DSB repair in mid pachytene regardless of mated status, suggesting that deficiencies in germline DNA repair are a product of reproductive aging. We further find that sperm depletion, but not absence of sperm, reduces RAD-51 marked DSBs at early pachytene, suggesting that loss of signals from sperm downregulate DSB induction. Taken together, our study supports a model in which signals due to sperm depletion and reproductive aging operate in parallel to influence meiotic DSB induction and repair.

Sperm depletion and DSB induction

Our data indicate that aged unmated germlines exhibit dramatically reduced RAD-51 foci in early pachytene (Figure 5.6). Previous work has similarly reported that unmated hermaphrodites induce fewer DSBs with age (Achache *et al.* 2021; Raices *et al.* 2021). We find, however, that mating is sufficient to rescue RAD-51 foci accumulation at early pachytene in aged germlines. These results together implicate sperm as the primary regulator of DSB induction levels in aged germlines. We further show that aged feminized *fog-2* germlines which have never been exposed to sperm do not exhibit reduced RAD-51 marked DSBs during aging. Thus, we propose that DSB induction in aged germlines is repressed by signals caused specifically from sperm depletion rather than reproductive aging. Notably, we found that *spo-11(me44)* mutants do not exhibit increased DSBs with age, suggesting that the DSBs observed in aged gonads come from the endogenous meiotic machinery. This result contrasts with previous work done using *spo-11(ok79)* mutants, which incur notable numbers of SPO-11 independent DSBs with age (Raices *et al.* 2021). Thus, our data raises the possibility that the specific nature of *spo-11* mutation or background strain-specific effects influence the incursion of exogenous DSBs in aged germlines.

Why might sperm depleted hermaphrodites downregulate germline DSB induction? Recent evidence has unveiled a potential transition in hermaphrodite gonad function following sperm depletion (Kern *et al.* 2021). After all sperm have been utilized from the spermatheca, hermaphrodites continue to lay unfertilized oocytes and secrete a nutrient-rich yolk in what has been suggested to be a form of 'primitive lactation' (Kern *et al.* 2021). Thus, the reduction in DSBs induced in germ cells following sperm depletion may be a product of the hermaphrodite

germline functionally changing from a reproductive organ to a system which produces food for offspring. Reduced DSB formation, then, may be indicative of the hermaphrodite's metabolic resources being reallocated in favor of providing nutritional supplement for progeny.

Multiple mutants in *C. elegans* have been reported to exhibit age-dependent decline in meiotic DSB induction (Tang *et al.* 2010; Rosu *et al.* 2013). Our research raises the possibility that these proteins may mediate or respond to signals from sperm. Also, both reproductive aging and *C. elegans* yolk secretion are regulated by insulin/insulin-like growth factor signaling (Luo *et al.* 2010; Kern *et al.* 2021). How reproductive aging and sperm depletion signals are integrated through this pathway to enact distinct phenotypes that impact germline function remains unknown but opens an avenue for future investigation. In summary, we have illuminated a regulatory mechanism specifically associated with sperm depletion which downregulates DSB induction in the *C. elegans* germline.

DSB repair and *C. elegans* reproductive aging

Aged *C. elegans* germlines incur multiple DNA repair defects, including delays in recombination protein loading and increased engagement of error-prone repair mechanisms (Raices *et al.* 2021). Both RAD-51 loading and error prone pathway engagement are regulated by DSB end resection (Gartner and Engebrecht 2022), suggesting that differences in DSB repair during aging may be derived from defects at this DNA processing step. We demonstrated that the E2 ligase variant UEV-2 is required for 'youthful' patterns of RAD-51 foci resolution during mid pachytene, indicating that a loss of UEV-2 or an age-related change in its function may underly the DNA repair defects in aged germlines. However, overexpression of UEV-2 is not sufficient to rescue persistent RAD-51 foci at mid pachytene in aged germlines and instead introduces DSB repair defects in young germlines. These results suggest that the specific levels of *uev-2* expression or the co-expression of other proteins may be important for the function of UEV-2 in DNA repair processes.

While the specific molecular functions of UEV-2 remain unknown, previous yeast two-hybrid assays have evidenced that UEV-2 may interact with BRC-1, the *C. elegans* BRCA1 homolog (Gudgen *et al.* 2004). BRCA1 is an E3 ubiquitin ligase thought to regulate many DNA repair steps, including DSB resection (Cruz-García *et al.* 2014). Recent studies have demonstrated that BRC-1 is vital for preventing error prone repair in the *C. elegans* germline (Li *et al.* 2020; Kamp *et al.* 2020), in particular during mid pachytene (Chapter III). Given these

results, an appealing hypothesis is that UEV-2 may modulate BRC-1 activity in the germline to regulate resection of DSBs and promote efficient recombination. Under this model, overexpression of *uev-2* or loss of its function may cause hyper- or hypo-DSB resection respectively, and thus have a deleterious impact on the efficiency of recombination. Taken together, our work demonstrates that UEV-2 is involved in regulating efficient and 'youthful' meiotic DSB repair, thereby opening avenues to future work uncovering the specific roles this protein plays in meiosis.

Acknowledgements

We thank the CGC (funded by National Institutes of Health (NIH) P40 OD010440) for strains. We thank C. Cahoon, A. Naftaly, and N. Kurhanewicz for thoughtful comments on this manuscript. This work was supported by the National Institutes of Health T32GM007413 and Advancing Science in America (ARCS) Foundation Award to E.T. and R00HD076165 and R35GM128890 to D.E.L. D.E.L. is also a recipient of a March of Dimes Basil O'Connor Starter Scholar award and Searle Scholar Award.

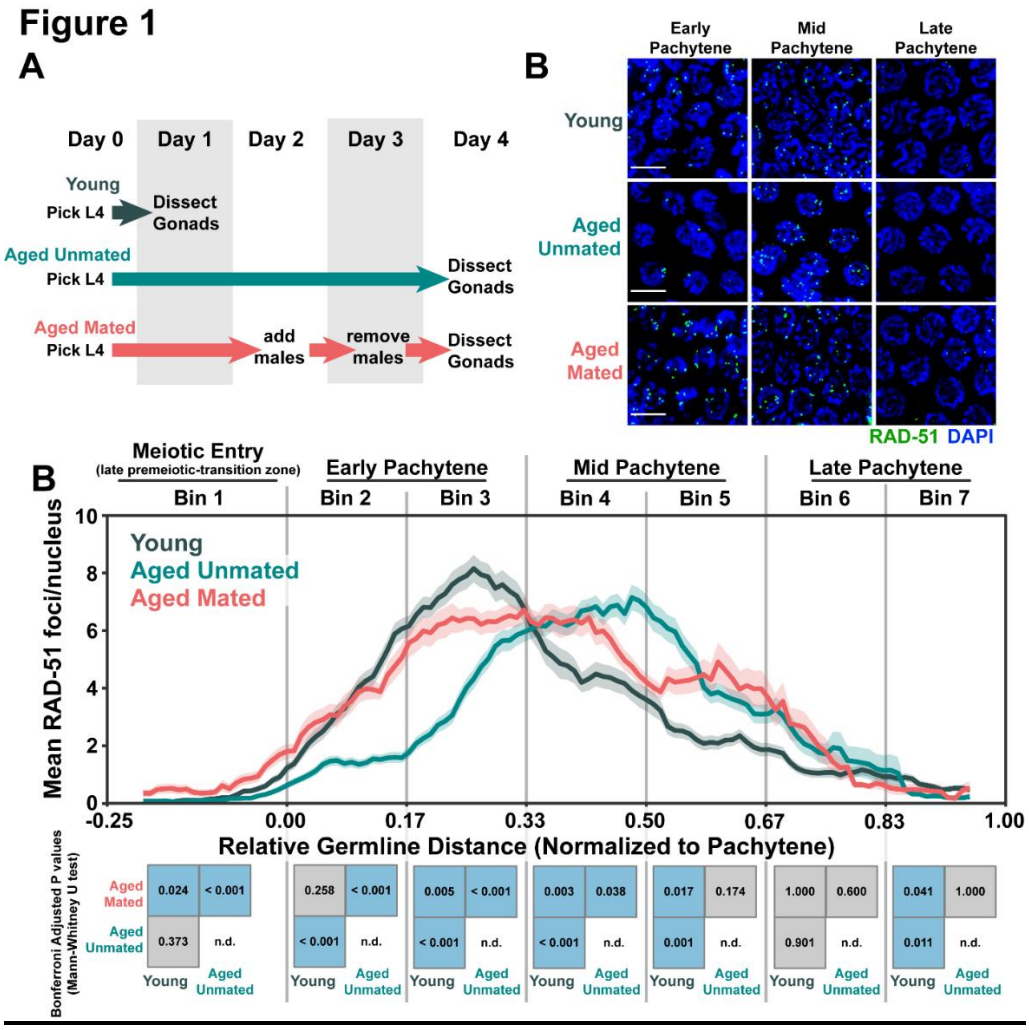

Figure 5.1. DNA damage levels are altered during *C. elegans* germline aging. A) Outline of maintenance schemes used to isolate young (1 day post-L4) and aged (4 days post L4) worms for experiments. Days count ~18-24 hour periods after hermaphrodites were isolated as L4 larvae and are separated by alternating grey shaded boxes. B) Representative images of RAD-51 foci meiotic nuclei in young and aged germlines. Scale bars represent 5µm. C) RAD-51 foci per nucleus in oocytes. Line plots represent the mean RAD-51 foci per nucleus along the length of the germline in a sliding window encompassing 0.1 units of normalized germline distance with a step size of 0.01 germline distance units. Mean RAD-51 foci were calculated from nuclei analyzed in n=9 total germlines derived from ≥3 experimental replicates within each age group. Shaded areas around each line represent ± SEM. Germlines distances were normalized to the start (0) and end (1) of pachytene based on DAPI morphology (see Methods). For analysis, the germline was divided into 7 bins encompassing the transition zone (Bin 1), early pachytene (Bins 2-3), mid pachytene (Bins 4-5), and late pachytene (Bins 6-7). The germline positions at which each bin start and end are marked on the X axis as vertical grey lines. Heat maps below each bin display the p values of pairwise comparisons of RAD-51 foci per nucleus counts within that bin. P values were calculated using Mann-Whitney U tests with Bonferroni correction for multiple comparisons. Blue tiles indicate significant differences (adjusted p value <0.05) and grey tiles indicate nonsignificant effects (adjusted p value >0.05).

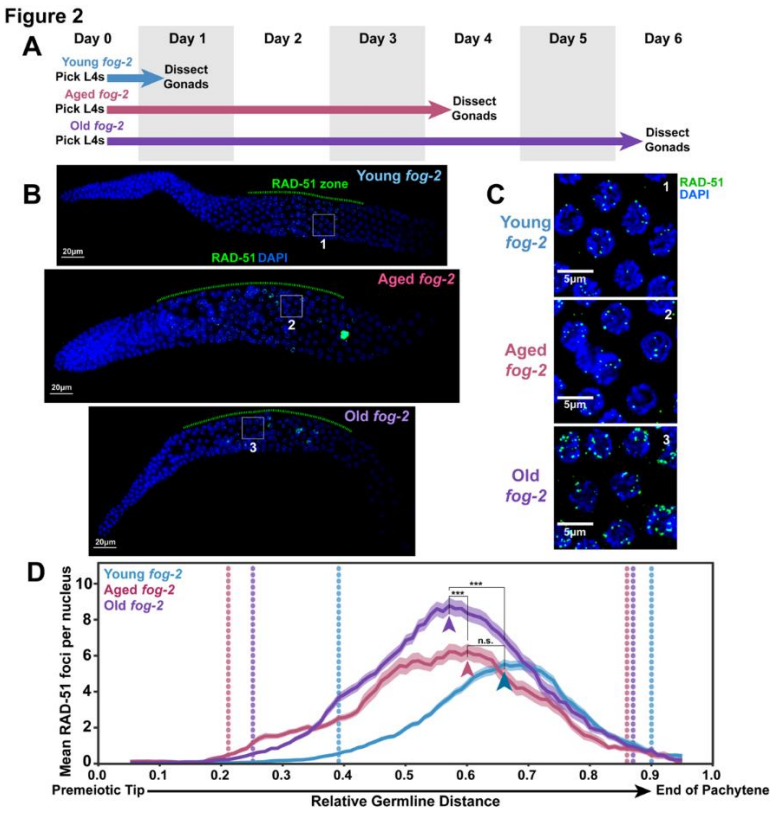

Figure 5.2. DNA damage levels increase with age in *fog-2* feminized germlines. A) Outline of maintenance schemes used to isolate young (1 day post-L4), aged (4 days post L4), and old (6 days post L4) *fog-2(q71)* worms for experiments. Days count ~18-24 hour periods after hermaphrodites were isolated as L4 larvae and are separated by alternating grey shaded boxes. B) Representative whole germline images of young, aged, and old *fog-2* germlines. The RAD-51 zone, defined as the region of the germline in which the majority of nuclei have one or more RAD-51 foci, is indicated with a green dashed line. All germlines are oriented with the distal mitotic tip on the left and the end of pachytene on the right. Scale bars represent 20µm. Grey numbered boxes indicate the positions of the images presented in panel C. C) Representative images of the peak levels of RAD-51 foci observed in meiotic nuclei of young, aged, and old *fog-2* germlines. Scale bars represent 5µm. Each panel is numbered to indicate the position in the germlines displayed in panel B that each inset was taken from. D) RAD-51 foci per nucleus in *fog-2(q71)* oocytes. Line plots represents the mean RAD-51 foci per nucleus along the length of the germline in a sliding window encompassing 0.1 units of normalized germline distance with a step size of 0.01 germline distance units. Mean RAD-51 foci were calculated from nuclei analyzed in n=9 total germlines derived from ≥3 experimental replicates within each age group. Shaded areas around each line represent ± SEM. Germline distance was normalized to the premeiotic tip (0) and end of pachytene (1) based on DAPI morphology (see Methods). Arrowheads indicate the "peak RAD-51" windows, defined as the windows along the length of the germline of each age group with the highest RAD-51 foci per nucleus. P values were calculated by Mann-Whitney U test comparisons of RAD-51 counts within these peak windows with Bonferroni correction for multiple comparisons (n.s. = $p>0.05$, *** = $p<0.001$). Vertical dotted lines indicate the distal and proximal bounds of the RAD-51 zone for each age group, defined as windows in which the median RAD-51 foci per nucleus count was ≥1.

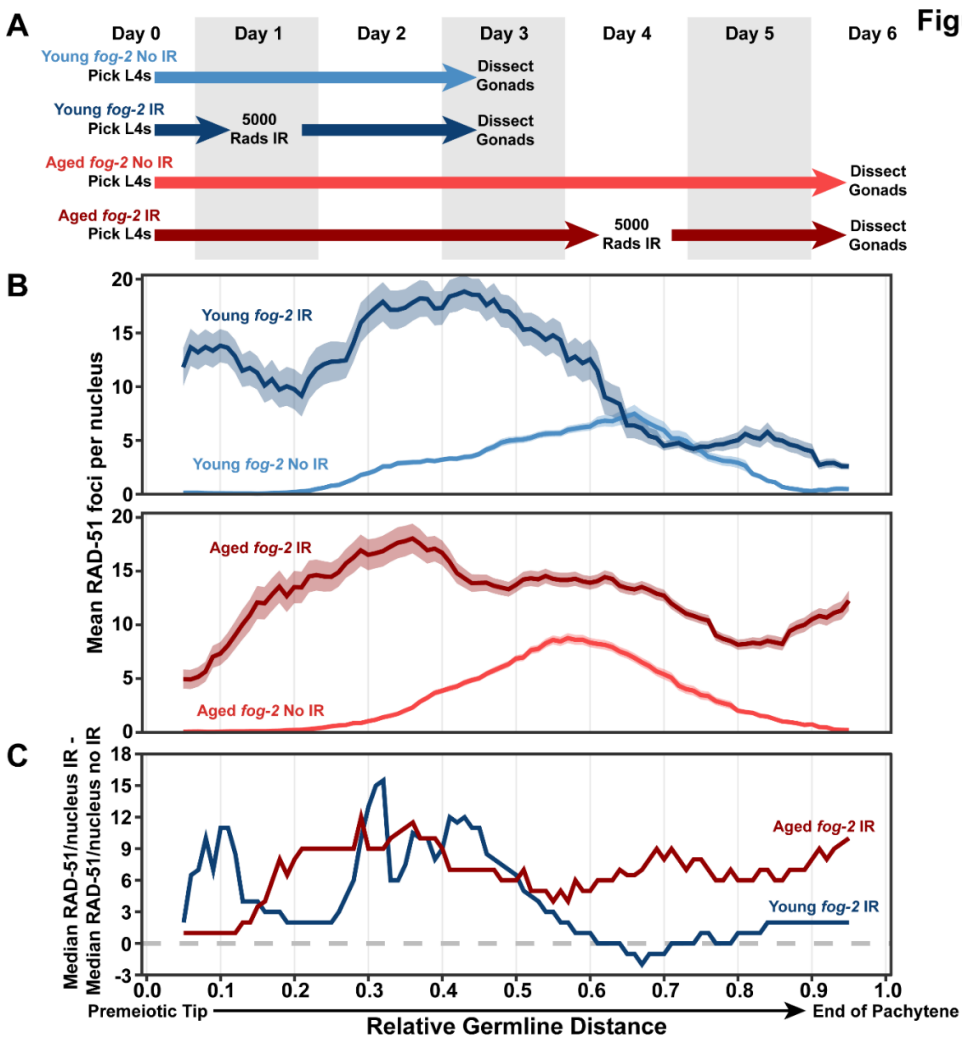

Figure 5.3. DNA damage repair is disrupted in aged *fog-2* feminized germlines. A) Outline of maintenance schemes used to isolate young and aged *fog-2(q71)* worms for experiments. Days count ~18-24 hour periods after hermaphrodites were isolated as L4 larvae and are separated by alternating grey shaded boxes. Irradiated (IR) germlines were exposed to ionizing radiation at the first or fourth day of adulthood and were allowed to recover for two days before analysis (see Methods). Unirradiated germlines (No IR) were never exposed to radiation. B) RAD-51 foci per nucleus in irradiated (IR) and unirradiated (no IR) oocytes. Line plots represents the mean RAD-51 foci per nucleus along the length of the germline in a sliding window encompassing 0.1 units of normalized germline distance with a step size of 0.01 germline distance units. Plots in panel B share an X axis with the plot in panel C. Mean RAD-51 foci were calculated from nuclei analyzed in n=9 total germlines derived from ≥3 experimental replicates within each age group. Shaded areas around each line represent ± SEM. Germline distance was normalized to the premeiotic tip (0) and end of pachytene (1) based on DAPI morphology (see Methods). Representative images of young and aged IR and No IR germlines are displayed in Supplemental Figure 5.5. C) Median RAD-51 foci per nucleus in irradiated germlines above median levels in unirradiated germlines of the same age (calculated as median RAD-51 foci in IR gonads – median RAD-51 foci in non-IR gonads within each window along the length of the germline).

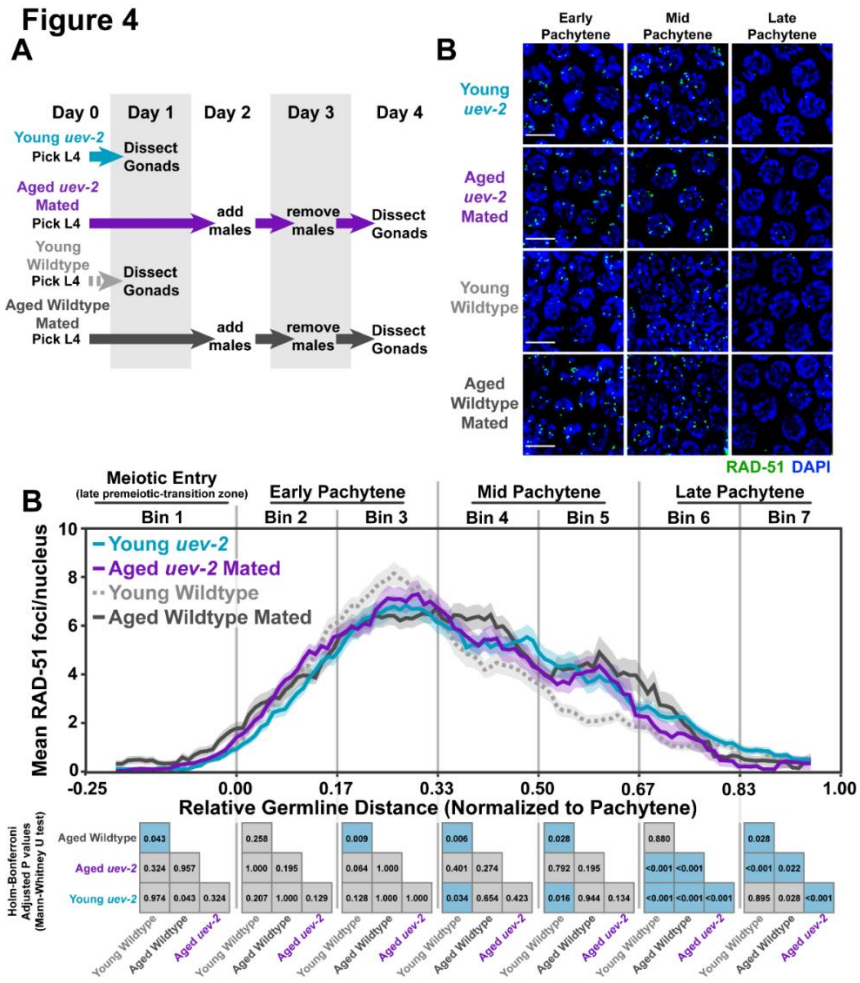

Figure 5.4. UEV-2 is required for 'youthful' DNA repair. A) Outline of maintenance schemes used to isolate young (1 day post-L4) and aged (4 days post L4) *uev-2* mutant worms for experiments. Days count ~18-24 hour periods after hermaphrodites were isolated as L4 larvae and are separated by alternating grey shaded boxes. B) Representative images of RAD-51 foci in meiotic nuclei of young *uev-2*, aged mated *uev-2*, young wildtype, and aged mated wildtype germlines. Scale bars represent 5μm. C) RAD-51 foci per nucleus in oocytes. Line plots represent the mean RAD-51 foci per nucleus along the length of the germline in a sliding window encompassing 0.1 units of normalized germline distance with a step size of 0.01 germline distance units. Mean RAD-51 foci were calculated from nuclei analyzed in n=9 total germlines derived from ≥3 experimental replicates within each age and genotype group. Shaded areas around each line represent ± SEM. Germlines distances were normalized to the start (0) and end (1) of pachytene based on DAPI morphology (see Methods). For analysis, the germline was divided into 7 bins encompassing the transition zone (Bin 1), early pachytene (Bins 2-3), mid pachytene (Bins 4-5), and late pachytene (Bins 6-7). The germline positions at which each bin start and end are marked on the X axis as vertical grey lines. Heat maps below each bin display the p values of pairwise comparisons of RAD-51 foci per nucleus counts within that bin. P values were calculated using Mann-Whitney U tests with Holm-Bonferroni correction for multiple comparisons. Blue tiles indicate significant differences (adjusted p value <0.05) and grey tiles indicate nonsignificant effects (adjusted p value >0.05).

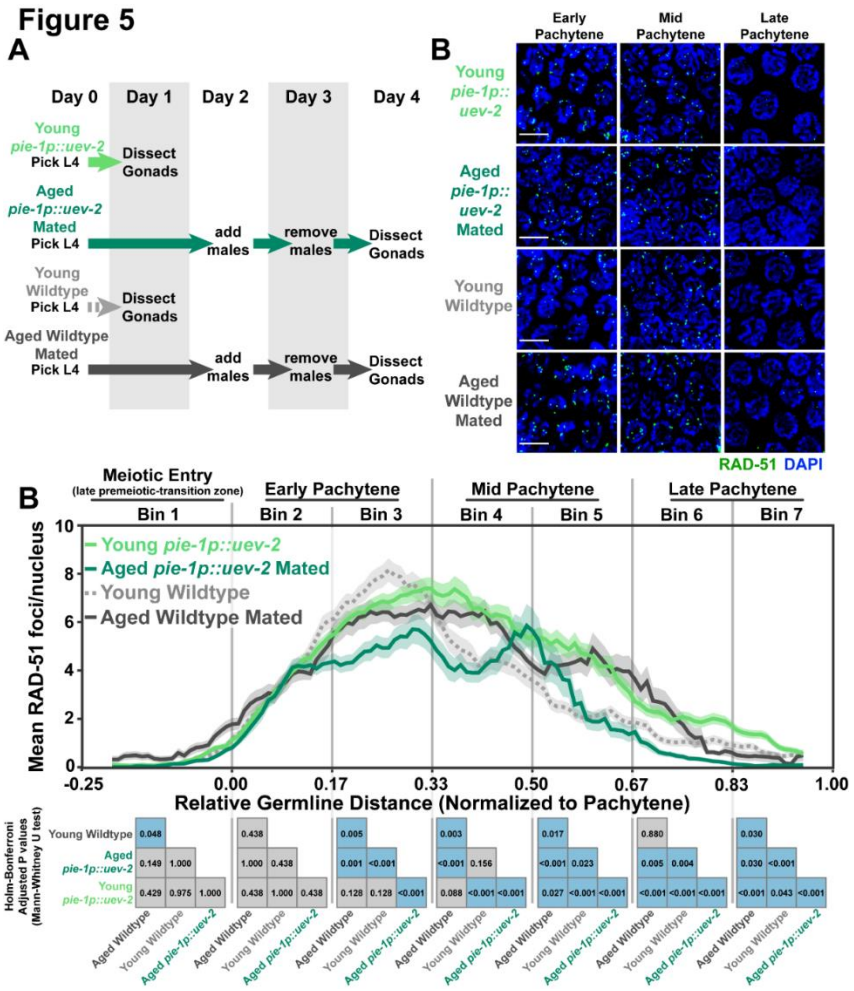

Figure 5.5. Germline *uev-2* overexpression differentially impacts DSB levels in young and aged germlines. A) Outline of maintenance schemes used to isolate young (1 day post-L4) and aged (4 days post L4) worms for experiments. Days count ~18-24 hour periods after hermaphrodites were isolated as L4 larvae and are separated by alternating grey shaded boxes. B) Representative images of RAD-51 foci in meiotic nuclei of young *pie-1p::uev-2*, aged *pie-1::uev-2*, and young wildtype germlines. Scale bars represent 5µm. C) RAD-51 foci per nucleus in oocytes. Line plots represent the mean RAD-51 foci per nucleus along the length of the germline in a sliding window encompassing 0.1 units of normalized germline distance with a step size of 0.01 germline distance units. Mean RAD-51 foci were calculated from nuclei analyzed in n=9 total germlines derived from ≥3 experimental replicates within each age group. Shaded areas around each line represent ± SEM. Germlines distances were normalized to the start (0) and end (1) of pachytene based on DAPI morphology (see Methods). For analysis, the germline was divided into 7 bins encompassing the transition zone (Bin 1), early pachytene (Bins 2-3), mid pachytene (Bins 4-5), and late pachytene (Bins 6-7). The germline positions at which each bin start and end are marked on the X axis as vertical grey lines. Heat maps below each bin display the p values of pairwise comparisons of RAD-51 foci per nucleus counts within that bin. P values were calculated using Mann-Whitney U tests with Holm-Bonferroni correction for multiple comparisons. Blue tiles indicate significant differences (adjusted p value <0.05) and grey tiles indicate nonsignificant effects (adjusted p value >0.05).

Figure 6

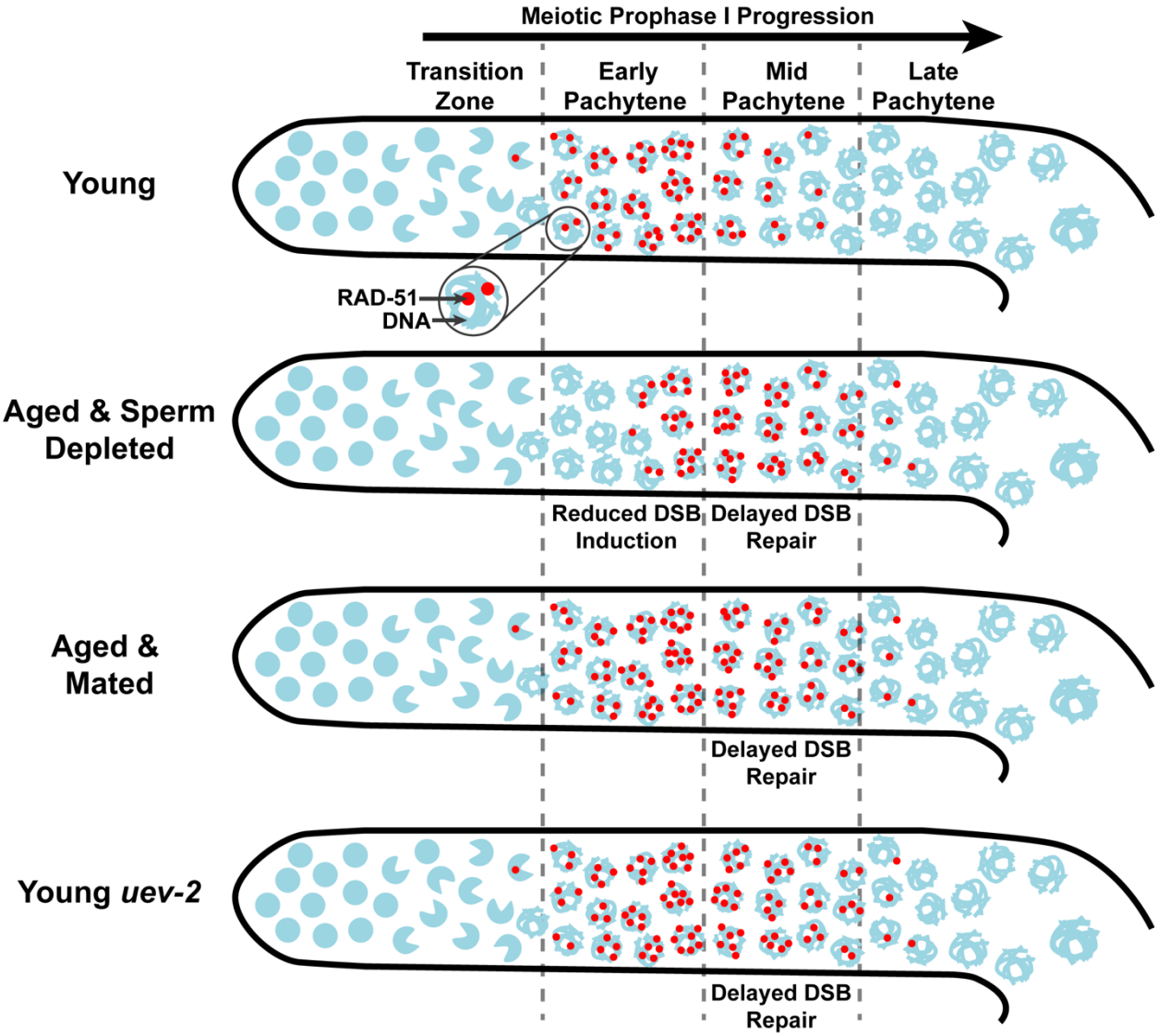

Figure 5.6. Model of aging and sperm effects on DSB levels during germline aging.

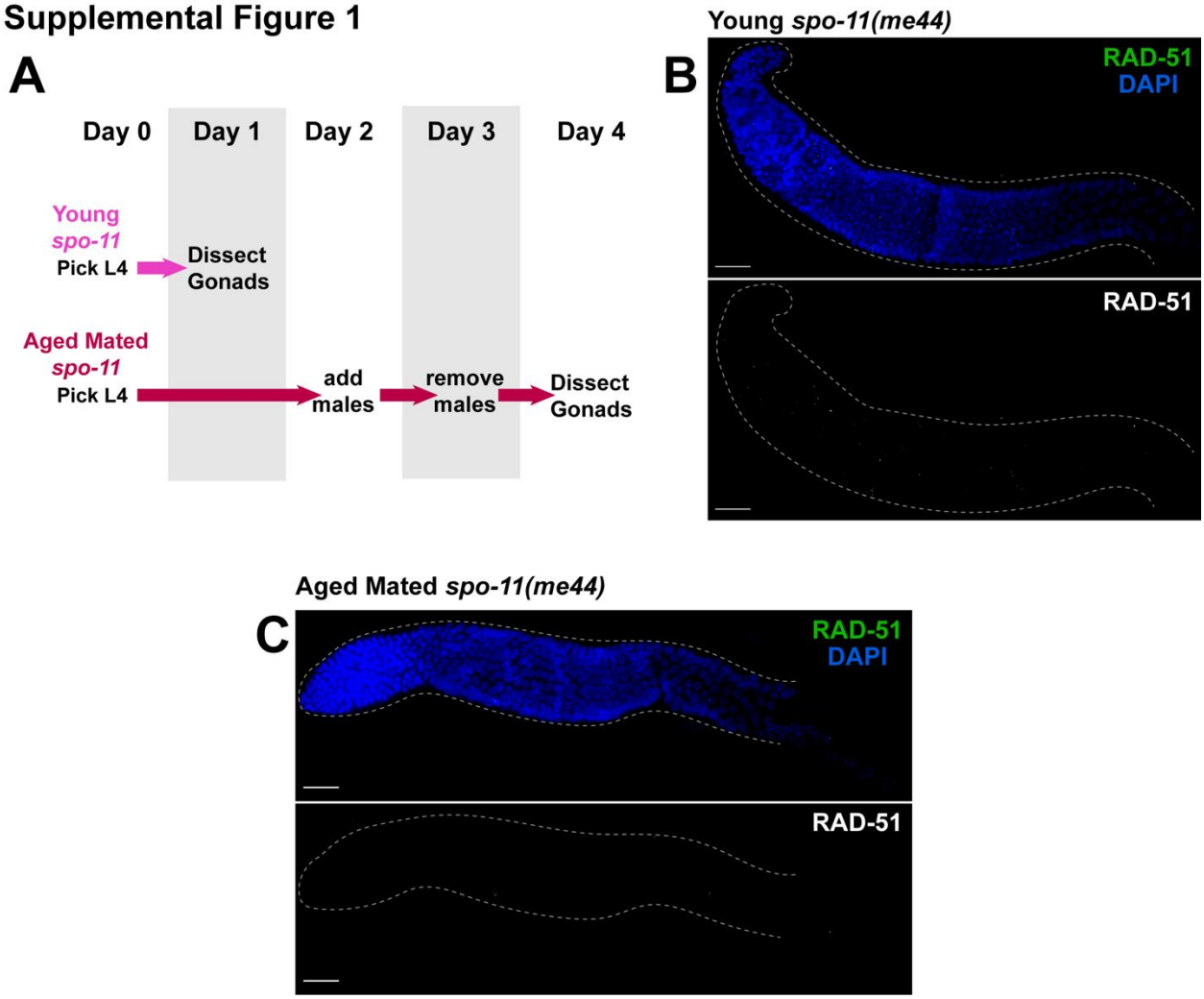

Figures S5.1. DSBs in aged germlines are SPO-11 dependent. A) Outline of maintenance schemes used to isolate young (1 day post-L4) and aged (4 days post L4) worms for experiments. B-D) Representative whole gonad images of RAD-51 stained germlines from young and aged mated *spo-11(me44)* mutants. Top panels show merged images of both RAD-51 and DAPI, while lower panels show only RAD-51 staining in greyscale. Gonads are oriented with the distal mitotic tip on the left and the end of pachytene on the right. Gonads are outlined with grey dashed lines and scale bars represent 20μm.

Supplemental Figure 2

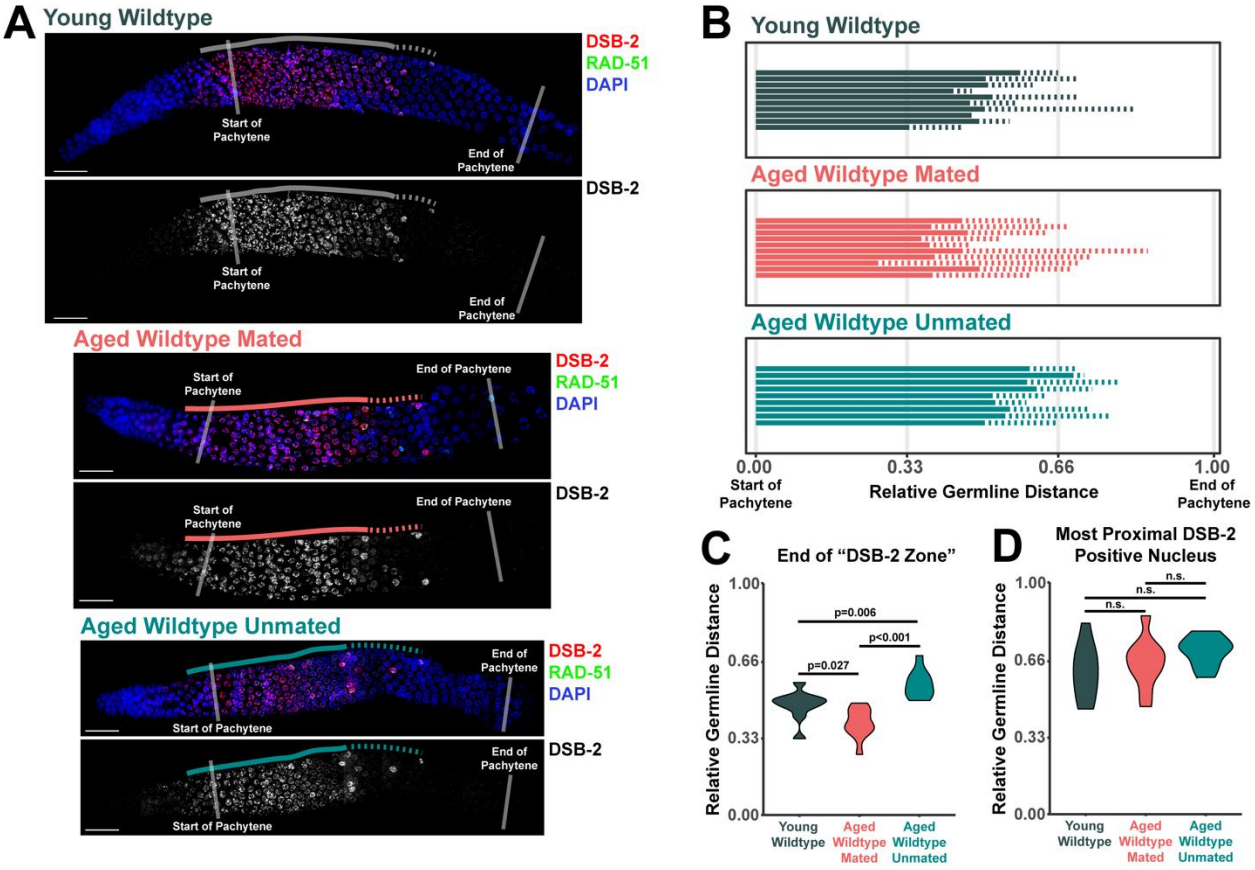

Figure S5.2. Aged mated and unmated germlines maintain DSB-2 localization in early pachytene. A) Representative images of germlines stained with DSB-2. Solid lines indicate the "DSB-2 zone", defined as the region of the germline in which >50% of nuclei are stained with DSB-2. Dashed lines extend from the end of the DSB-2 zone to the most proximal nucleus which has DSB-2 staining. Scale bars represent 20μm. B) Line plot representing the quantification of DSB-2 staining in young, aged mated, and aged unmated N2 hermaphrodite germlines. For specific maintenance schemes of these groups, see Figure 5.1A and Methods. Each horizontal line represents the portion of a single germline which contains DSB-2 positive nuclei. Solid lines represent the "DSB-2 zone", while dashed lines extend to the most proximal germline position at which 1 or more nuclei is marked with DSB-2. C-D) Violin plots comparing the end of the DSB-2 zone and the final position of DSB-2 positive nuclei in young, aged mated, and aged unmated germlines. P values were calculated by Mann-Whitney U test with Bonferroni correction for multiple comparisons.

Supplemental Figure 3

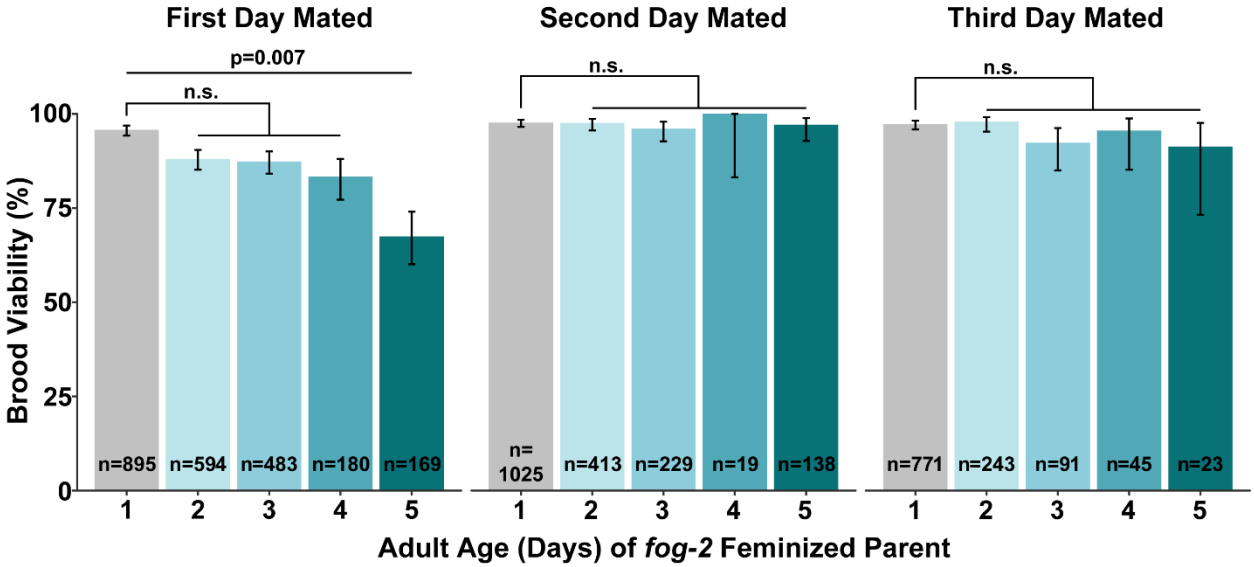

Figure S5.3. A population of *fog-2* mutant oocytes exhibit reduced viability with maternal age. Bar plots representing the population brood viability of mated *fog-2* mutant females. Error bars represent 95% Binomial confidence intervals. P values were calculated by Fisher's Exact Test. N values indicate the total number of live progeny and dead eggs scored. P values >0.05 are indicated as n.s. (not significant).

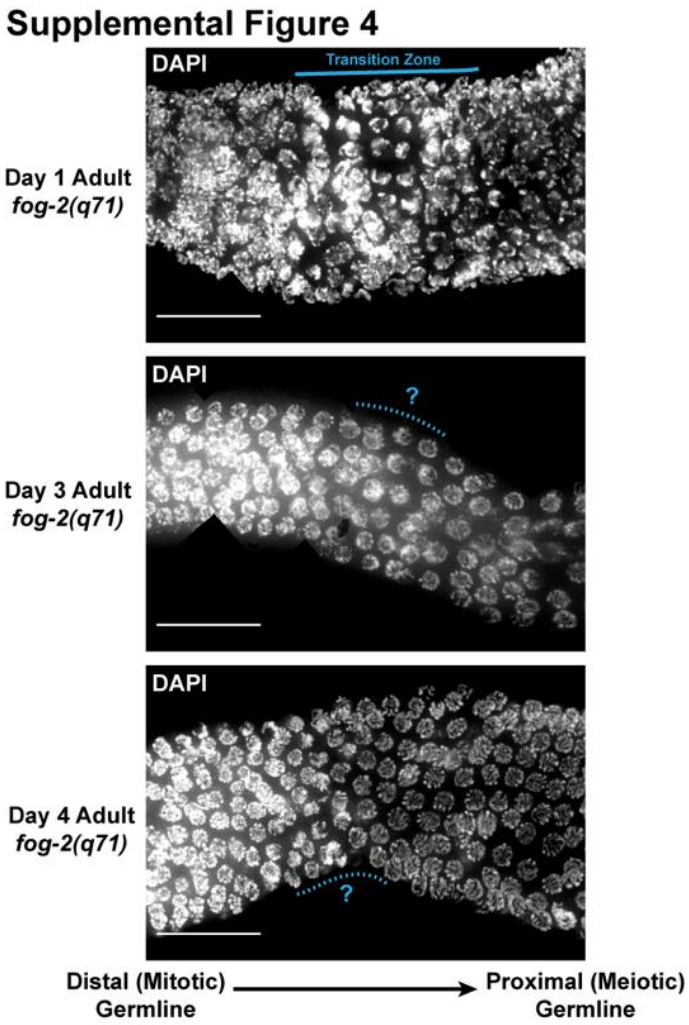

Figure S5.4. The transition zone is reduced/absent in aged feminized germlines. Representative images of *fog-2(q71)* feminized mutant germlines from animals 1, 3, or 4 days post-L4. The transition zone is marked with a solid blue line in germlines which have crescent shaped nuclei indicative of meiotic entry. Dashed lines indicate the regions of the germline presumably bridging the mitotic and meiotic germline in which crescent shaped 'transition zone' nuclei are absent. Gonads are oriented with the distal mitotic region on the left and the proximal meiotic region on the right. Scale bars represent 20μm.

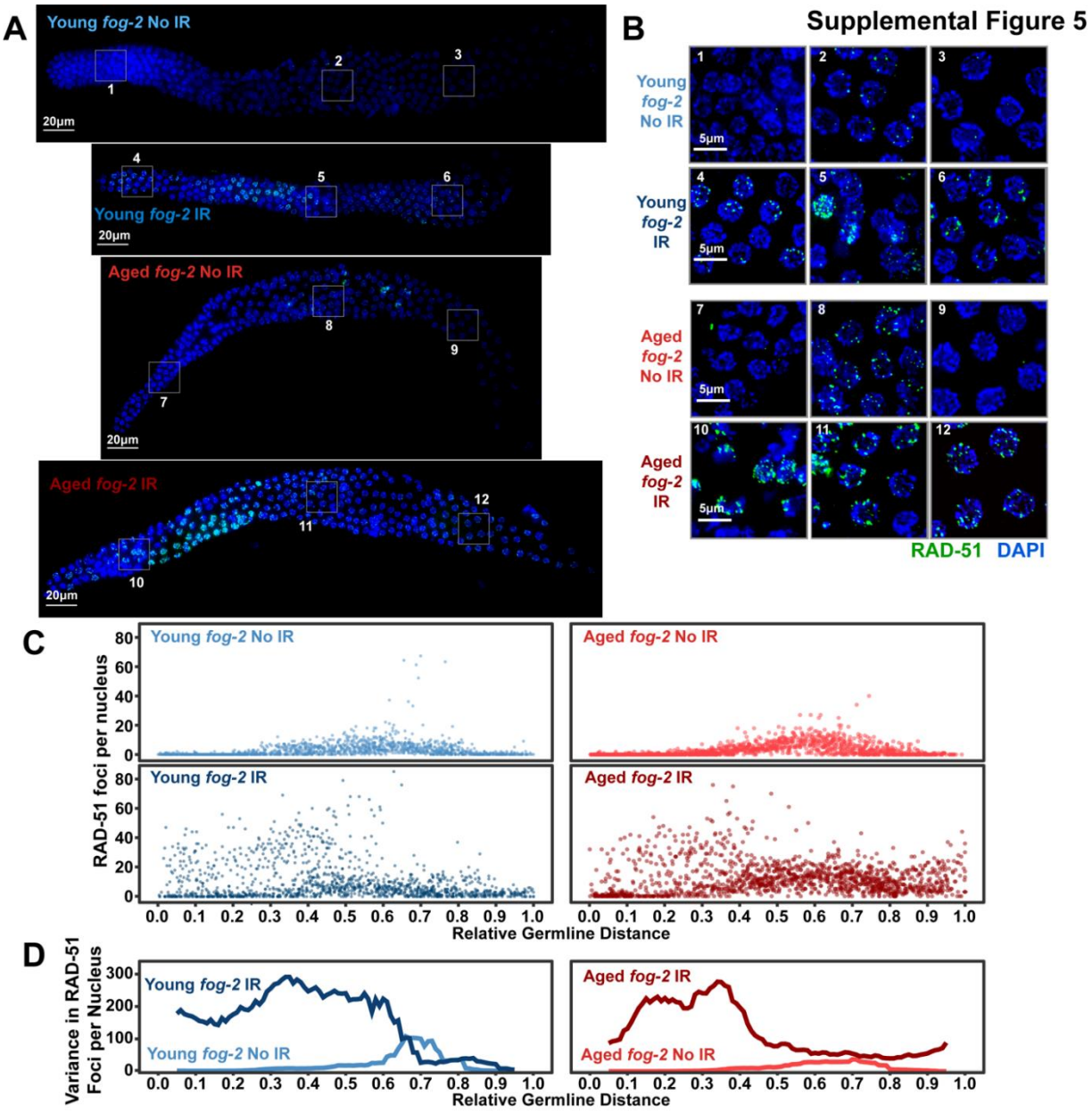

Figure S5.5. Irradiated *fog-2* germlines exhibit high internuclear variance in DSB repair following irradiation. A) Representative images of germlines from young and aged irradiated and unirradiated *fog-2(q71)* germlines. For specific maintenance schemes of each group, see Figure 5.3A. Scale bars represent 20μm. Grey numbered boxes indicate inset panels of nuclei displayed in panel B. B) Represented images of subsets of nuclei from germlines displayed in panel A. Numbers on images correspond to the grey boxes in panel A indicating the portion of the germline each image is derived from. Scale bars represent 5μm. C) Dot plots indicating the RAD-51 foci per nucleus in *fog-2(q71)* IR or No IR young and aged. Each point represents a single nucleus at a given germline position normalized by the premeiotic tip (0) to late pachytene (1) (see Methods). D) Variance in RAD-51 foci per nucleus calculated in a sliding window along the length of the germline where the width of the window is 0.1 germline distance units and the step size is 0.01 germline distance units.

Supplemental Figure 6

uev-2(gk960600gk429008gk429009)

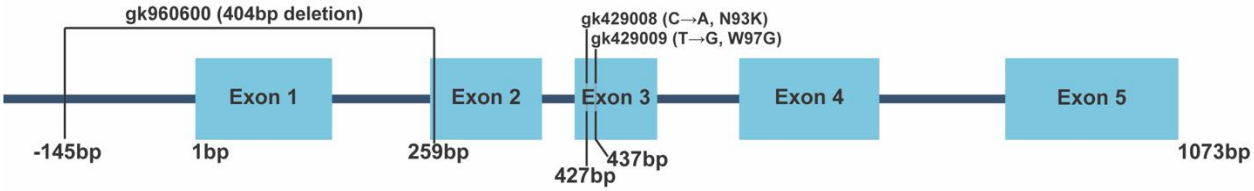

Figure S5.6. Diagram of *uev-2(gk960600gk429008gk429009)* sequence structure. Displayed is a scale cartoon of the *uev-2* locus where exons are displayed as boxes and intronic or noncoding upstream sequence is displayed as lines. The gk960600 allele deletes the translation start site and the 5' intron boundary of exon 2. This lesion generates a frameshift mutation and likely eliminates gene function. Additional point mutations gk429008 and 429009 cause single amino acid substitutions. Base pair distances are indicated relative to the translation start site of Exon 1 of the *uev-2* coding sequence.

CHAPTER VI
CONLUDING SUMMARY

Regulation of DNA repair during meiosis is fundamental to successful reproduction and ensuring germline "immortality" (Smelick and Ahmed 2005). Meiotic nuclei may resolve DSBs by many pathways, including crossover and noncrossover recombination with the homolog or sister chromatid, NHEJ, TMEJ, and SSA (Gartner and Engebrecht 2022). How these pathways are coordinated during meiosis is a fundamental question to the genome integrity field. The inaccessibility of intersister repair products for analysis, however, has posed a major hurdle to the study of metazoan meiotic DNA repair pathway choice. The work presented in this thesis overcomes this obstacle through the development of the ICR assay (Chapter II). Using the ICR assay, I demonstrate that crossover and noncrossover recombination occurs during metazoan meiosis, and also is the exclusive recombination repair pathway in late meiotic prophase I (Chapter II).

My data, in concert with previous studies, further show that the highly conserved protein complexes BRC-1, SMC-5/6, and HIM-6/BLM act to repress intersister crossovers during meiosis (Almanzar *et al.* 2021) (Chapter II, III). While HIM-6 is required for efficient interhomolog crossover formation (Schvarzstein *et al.* 2014), neither BRC-1 nor SMC-5/6 are required for this recombination outcome (Adamo *et al.* 2008; Bickel *et al.* 2010; Janisiw *et al.* 2018; Li *et al.* 2018). Thus, our data support the model that intersister and interhomolog crossovers are differentially regulated during meiosis. Further, the concerted suppression of intersister crossing over by multiple protein complexes implies that this DSB repair outcome is highly disfavored and may pose deleterious effects for gametes. In mitotic cells, crossover recombination with either the homologous chromosome or sister chromatid is repressed (Moynahan and Jasin 2010; Carvajal-Garcia *et al.* 2020). Mitotic interhomolog crossovers risk loss of heterozygosity in daughter cells, which can contribute to oncogenesis (Moynahan and Jasin 2010). Further, heterologous crossover recombination with either homolog or sister templates risks the formation of translocations (Moynahan and Jasin 2010). In contrast to mitosis, meiotic interhomolog crossover recombination is tightly regulated by meiosis-specific chromosome structure and recombination proteins to ensure accurate repair of DSBs (Libuda *et al.* 2013; Cahoon *et al.* 2019). Our research raises the possibility that regulation of meiotic

intersister recombination may be more 'mitotic-like' than meiotic interhomolog repair. Under this model, we would expect interhomolog-specific recombination proteins, such as the MutSγ homolog MSH-5/6 (Kelly *et al.* 2000), to be dispensable for intersister crossing over. Future work investigating the shared and distinct intersister/interhomolog repair functions of meiotic proteins will provide vital context for the regulation of meiotic DNA repair.

Both *brc-1* and *smc-5* mutants also exhibited highly elevated rates (~2.5-3 fold) of ICR assay recombinant progeny relative to wild type (Chapter III). This effect cannot be explained by increased excision of Mos1 alone, as we did not observe a similar global increase in non-Unc recombinants in the IH assay, which utilizes excision of Mos1 at the same locus as the ICR assay and employs an identical heat-shock inducible transposase construct. Thus, this result implies that ~70% of DSBs induced in the wild type ICR assay are repaired as GFP- events, and that these GFP- repair outcomes are promoted by SMC-5/6 and BRC-1. Delineating the mechanisms underpinning GFP- recombination events in the ICR assay is not only important for understanding the specific functions of SMC-5/6 and BRC-1, but may further provide key insight into the regulation of meiotic DSB repair more broadly. I propose that three different testable models for SMC-5/6 and BRC-1 function could account for this elevation in GFP+ progeny: 1) SMC-5/6 and BRC-1 restrict engagement of polymorphic repair templates during meiosis; 2) SMC-5/6 and BRC-1 promote error prone repair of ICR assay DSBs; or, 3) SMC-5/6 and BRC-1 promote ICR assay interhomolog repair.

The presence of polymorphisms in a repair template can reduce the recombination efficiency between loci (Chen and Jinks-Robertson 1999; Hum and Jinks-Robertson 2019). My finding of increased GFP+ ICR assay recombinant progeny could therefore indicate increased engagement of the polymorphic upstream ICR assay GFP repair template (Chapter III). The elevated frequency of recombinant ICR assay progeny in *smc-5* and *brc-1* mutants, then, raises the possibility that these proteins facilitate the detection and/or rejection of heteroduplex recombination intermediates. If this heteroduplex rejection model for SMC-5/6 and BRC-1 function is correct, then we would expect for ICR assay recombinants to be similarly increased in a *msh-2* mutant, which ablates both the MutSα and MutSβ complexes required for mismatch recognition (Gartner and Engebrecht 2022).

Conversely, it is hypothetically possible that BRC-1 and SMC-5/6 promote error prone repair of ICR assay DSBs under wild type conditions. Three major error-prone DNA repair

pathways are known to be active in the *C. elegans* germline: SSA, NHEJ, and TMEJ (Gartner and Engebrecht 2022). In Chapter II of this thesis, I demonstrate that SSA is not a major contributor to ICR assay repair events by performing the ICR assay in an *xpf-1* mutant. TMEJ is repressed by BRC-1 in the hermaphrodite *C. elegans* germline (Kamp *et al.* 2020). Thus, it is unlikely that TMEJ resolves the majority of ICR assay DSBs as GFP- events in a wild type context, as we would expect this effect to become exacerbated when *brc-1* is ablated. While NHEJ is largely dispensable in wild type *C. elegans* meiosis (Yin and Smolikove 2013; Kamp *et al.* 2020), it is nonetheless possible that ICR assay DSBs may be preferentially resolved via this pathway. If NHEJ is a primary mechanism of wild type ICR assay DSB repair, then we would expect c*ku-70/80* mutants, which cannot designate DSBs for NHEJ resolution (Lemmens *et al.* 2013), should also exhibit elevated GFP+ recombinants.

Finally, it is possible that DSBs in the wild type ICR assay are primarily resolved via interhomolog recombination. Across phyla, the homologous chromosome is the preferred repair template for meiotic DSB repair (Humphryes and Hochwagen 2014). While no GFP sequence is present on the homologous chromosome in the ICR assay parent hermaphrodites, DSB resection >2kb in length would expose *unc-5* sequence downstream of the ICR assay, which could then be utilized to engage the homolog for repair. Although the extent of DSB resection in *C. elegans* is unknown, evidence from other organisms suggests that 2kb of resection is not implausible. High resolution meiotic DSB resection profiling has been performed in both budding yeast and male mice, revealing that DSBs are resected 200-2000nt (mean 822nt) and ~300-2000nt (mean ~1100nt) in these species respectively (Mimitou *et al.* 2017; Yamada *et al.* 2020). The length of resection was further extended in both species when interhomolog recombination was perturbed through mutation of the meiosis-specific recombinase Dmc1 (Mimitou *et al.* 2017; Yamada *et al.* 2020). Thus, if *C. elegans* homolog partner bias limits intersister/intrachromatid DSB resolution in the ICR assay, then Mos1 excision-induced DSBs may similarly undergo longer resection, thereby exposing *unc-5* sequence and facilitating interhomolog repair.

To determine the contribution of interhomolog repair to DSB resolution in the ICR assay, two specific experiments are required. First, the ICR assay should be performed in a parent hermaphrodite which carries GFP- sequence on the homologous chromosome, facilitating interhomolog DSB repair but precluding the generation of GFP+ interhomolog recombinant progeny. If the interhomolog model of ICR assay DSB repair is correct, then we would expect

similar frequencies of intersister/intrachromatid GFP+ progeny regardless of the availability of GFP sequence on the homologous chromosome. Second, the ICR assay should be performed in a parent hermaphrodite heterozygous for the assay construct and either a chromosomal translocation or deletion which ablates the *unc-5* locus and surrounding sequence. Under this context, interhomolog recombination should be impeded and result in preferential DSB repair by intersister/intrachromatid repair, thereby increasing the observed GFP+ progeny.

In addition to defining mechanisms of intersister/intrachromatid recombination, the work in this thesis revealed that defects in DNA repair at mid pachytene are a feature of the aging *C. elegans* germline independent of sperm effects (Chapter V). The specific mechanisms which underpin these recombination defects, however, remain unknown. Combining the cytological analyses we performed with future ICR and IH assay experiments in aged hermaphrodites could delineate how interhomolog and intersister/intrachromatid repair are impacted by aging. Further, these tools would provide powerful insight into the function of UEV-2, as the role of this protein in promoting DSB repair in young germlines remains unclear.

Taken together, the work composing this thesis developed a novel cytological and genetic toolkit to assess DNA repair outcomes and, using those tools, defined mechanisms regulating homolog-independent DSB repair pathway engagement. This research lays the groundwork for future experiments decoding the mechanisms by which the immortal genome is passed from generation to generation.

APPENDIX A

THE *C. ELEGANS* MMS21/NSE2 HOMOLOG ZK1248.11 IS REQUIRED FOR MAINTENANCE OF MEIOTIC GENOME INTEGRITY

Erik Toraason, Alina Salagean, and Diana E. Libuda

Introduction

The highly conserved structural maintenance of chromosomes 5/6 (Smc5/6) complex regulates DNA repair in both meiotic and mitotic cells (Aragón 2018). Smc5/6 is vital for the preservation of genome integrity and is required for viability in most systems, but the specific roles this complex has in these processes remain largely unknown (Aragón 2018). The proteins which compose Smc5/6 are broadly classified into two groups: 1) structural maintenance of chromosomes (SMC) proteins defined by specific structural features; and, 2) non-SMC element (NSE) proteins which do not encode for SMC structural motifs. Most SMC and NSE elements are interdependent for complex assembly (Uhlmann 2016). A potential exception to this rule is the Smc5/6 subunit Nse2/Mms21, as this subunit is not structurally integral to the core complex, although its binding may stabilize the Smc5 protein (Stephan *et al.* 2011). Nse2 is an E3 SUMO ligase which functions through both ligase-dependent and -independent functions to regulate genome integrity (Potts and Yu 2005; Jacome *et al.* 2015). The specific functions Nse2 performs in regulating DNA repair and the extent to which it is required for Smc5/6 function remain unknown.

The *C. elegans* SMC-5/6 complex is not required for viability or fertility, enabling genetic analysis of null mutants for SMC-5/6 subunits in this species (Bickel *et al.* 2010). The *C. elegans* genome contains predicted homologs of many Smc5/6 complex NSE proteins, including Nse2 (ORF ZK1248.11, hereafter referred to as NSE-2). To determine the NSE-2 dependent and independent functions of *C. elegans* SMC-5/6, we employed both functional genome integrity assays and cytological analysis. We find that the SMC-5/6 core complex acts independently from NSE-2 in promoting transgenerational fertility. With regards to promoting meiotic genome integrity following irradiation, we find that NSE-2 exhibits overlapping functions with SMC-5/6. We further demonstrate that NSE-2 acts in parallel to the tumor suppressor BRCA1 (BRC-1 in *C. elegans*) to promote meiotic DSB repair. Our results also suggest that NSE-2 regulates early steps of recombination independently from SMC-5/6 and but in parallel with BRC-1. Finally, we

identify a single amino acid truncation in the NSE-2 peptide which is sufficient to repress DNA repair defects in an *smc-5* mutant, implying that this residue influences NSE-2 function in the absence of the SMC-5/6 complex. Taken together, we provide evidence that NSE-2 performs functions in regulating DSB repair independent of the SMC-5/6 complex to promote meiotic genome integrity.

Methods

C. elegans strain maintenance

C. elegans strains were maintained at 20°C on nematode growth medium (NGM) plates on a lawn of OP50 *Escherichia coli* bacteria. Strains used in this study include: N2 (wild type), DLW68 (*nse-2(lib8)*/tmC6[*dpy-2(tmIs1208)*] II), DLW70 (*nse-2(lib11)*/tmC6(*tmIs1208*) II), DLW80 (*nse-2(lib19[S8Δ]) smc-5(ok2421)*/mIn1[mIs14 *dpy-10(e128)*] II), DLW83 (*nse-2(lib18[S8A])*/ mIn1[mIs14 *dpy-10(e128)*] II), DLW84 (*nse-2(lib18[S8A]) smc-5(ok2421)*/mIn1[mIs14 *dpy-10(e128)*] II), DLW85 (*nse-2(lib20) smc-5(ok2421)*/mIn1 [mIs14 *dpy-10(e128)*] II), DLW136 (*nse-2(lib8)*/mIn1[mIs14 *dpy-10(e128)*] II), DLW137 (*smc-5(ok2421)*/mIn1[*dpy-10(e128)* mIs14] II; *brc-1(xoe4)* III), DLW138 (*nse-2(lib8)*/mIn1[*dpy-10(e128)* mIs14] II; *brc-1(xoe4)* III), DLW139 (*smc-5(ok2421) nse-2(lib20)*/mIn1[*dpy-10(e128)* mIs14] II; *brc-1(xoe4)* III), JEL730 (*brc-1(xoe4)* III), and YE57 (*smc-5(ok2421)* II).

CRISPR/Cas9 Genome Editing

Putative null alleles *nse-2(lib8)* and *nse-2(lib11)* were generated by injecting the germlines of N2 hermaphrodites with CRISPR/Cas9 ribonucleoprotein (RNP) mix using both *dpy-10* and *unc-58* co-conversion markers (0.3M KCl, 20µM HEPES pH 7.4, 20µM Cas9, 20µM tracrRNA, 20µM DLR002 *dpy-10* gRNA (5'- GCUACCAUAGGCACCACGAG-3'), 20µM DLR014 *nse-2* gRNA (5'- UACCCAGCUCGCCACUAGUA-3'), 20µM DLR021 *unc-58* gRNA (5'- UCCACGCACAUGGUCACUA-3'), and 50ng/µL ssDNA oligo *unc-58(e665)* repair template DLO845 (5'-CGAGTTAGGAAACAAATTTTTCTTTCAGGTTTCTCAGTAGTGACCATGTGCGTGGATCTT-3').

The in-frame deletion allele *nse-2(lib19(S8Δ))* was generated by injecting YE57 hermaphrodites with CRISPR/Cas9 RNP mix and the *rol-6(su1006)* co-injection marker

(0.25µg/µL Cas9 (IDT), 0.1µg/µL tracrRNA (IDT), 0.056µg/µL *nse-2* gRNA DLR014 (5'-UACCCAGCUCGCCACUAGUA -3'), pRF4::*rol-6(su1006)* 40ng/µL).

The putative null allele *nse-2(lib20)* and substitution mutants *nse-2(lib18[S8A])* were generated by injecting YE57 or N2 hermaphrodites with CRISPR/Cas9 RNP mix and the *rol-6(su1006)* co-injection marker (0.25µg/µL Cas9 (IDT), 0.1µg/µL tracrRNA (IDT), 0.056µg/µL *nse-2* gRNA DLR014 (5'- UACCCAGCUCGCCACUAGUA -3'), pRF4::*rol-6(su1006)* 40ng/µL, and 25ng/µL ssDNA oligo *nse-2* repair template DLO993 (5'-GCCTTTCTCAGACTTTTTCGAATAATTTCCATAGCAGTGGCGAGCTGGGTAGACATCTGGAAGG-3')).

All CRISPR edited isolates were backcrossed ≥3 times to N2 to remove any background mutations.

Brood viability and irradiation analysis

Brood viability experiments and Beta-binomial model fitting displayed in Figure 6.2 was done following an identical protocol as described in Methods of CHAPTER III in this thesis.

The brood viability experiment displayed in Figure 6.3 was performed using a different protocol. L4 hermaphrodites of each genotype were isolated ~24 hr before irradiation and were maintained at 20°C on NGM plates seeded with OP50. Plates of hermaphrodites were then exposed to 3176 Rads of ionizing radiation using a Cs^{137} source (University of Oregon). N=5 hermaphrodites of each genotype were then placed onto individual NGM plates seeded with OP50 and were maintained at 20°C. At ~24 and ~48 hours post irradiation, hermaphrodites were transferred to new NGM plates seeded with OP50 and both the progeny and irradiated parents were maintained at 20°C. At ~72 hours post irradiation, parent hermaphrodites were removed from the NGM plates and were discarded. Progeny were scored ~24 hours after removing the parent hermaphrodite for the number of living hatched worms (live), dead unhatched eggs (dead), and unfertilized oocytes. Brood viability was calculated as Live/(Live + Dead).

Germline mortal (Mrt) assay

Transgenerational fertility was assessed via a germline mortal (Mrt) phenotype assay adapted from the protocol described in (Ahmed and Hodgkin 2000). N=6 L1 progeny of each genotype were placed on NGM plates seeded with OP50 and were maintained for 1 week at 20°C, encompassing a period sufficient for 2 generations of *C. elegans* to be successively hatched. The plates were then scored qualitatively using the categories of wild-type, medium, few, and sterile

(Ahmed and Hodgkin 2000). N=6 L1 progeny from each plate were then transferred to new NGM plates seeded with OP50 and this process was repeated. 5 individual passaged isolates for each genotype were assayed in parallel.

Microscopy and image analysis

Immunofluorescence samples were prepared as described in (Libuda *et al.* 2013). For details, see Methods in CHAPTER V of this thesis. Antibodies used in this chapter and their dilution ratios include Rabbit αRAD-51 (1:5000) and Alexa Fluor 488 Goat αRabbit (1:200).

Images of germlines were captured in three dimensions as 1024x1024 pixels with 2μm Z stacks. a DeltaVision Ultra widefield microscope (GE) using a 60x lens. Images were deconvolved (softWoRx) and were unified using the Fiji Grid/Collection Stitching plugin (Preibisch *et al.* 2009). Images displayed in this chapter are maximum intensity projections of stitched germlines with intensities adjusted using Photoshop (Adobe).

Statistics

All statistics were calculated using R (v4.0.3). Data wrangling was performed using the Tidyverse package (v1.3.1) (Wickham *et al.* 2019). Bayesian model fitting was performed using RStan (Stan Development Team 2021). All specific statistical tests used are denoted in the text and figure legends.

Results

NSE-2 is not required for transgenerational fertility

To assess the functions of NSE-2 in *C. elegans* meiosis, we used CRISPR/Cas9 genome editing to generate null *nse-2* frameshift mutants (Figure 6.1A, see methods). Homozygous mutants for either of the core SMC-5/6 genes, *smc-5* and *smc-6*, become sterile over successive generations (Ahmed and Hodgkin 2000; Bickel *et al.* 2010). To determine whether NSE-2 is required for SMC-5/6 functions in promoting transgenerational fertility, we assayed the fecundity of wild type animals, *smc-5(ok2421)* null mutants, and two *nse-2* null mutants over 50 generations (Figure 6.1B). While all wild type replicates maintained robust fertility over the entire experiment, *smc-5* mutants became sterile within 14-32 generations (Figure 6.1B). Both *nse-2* mutants we assayed maintained fertility over the course of the experiment, although the fecundity of individual replicates varied slightly over successive generations (Figure 6.1B).

Taken together, this result demonstrates that NSE-2 is not required for SMC-5/6 functions in preserving transgenerational genome integrity.

Figure 1

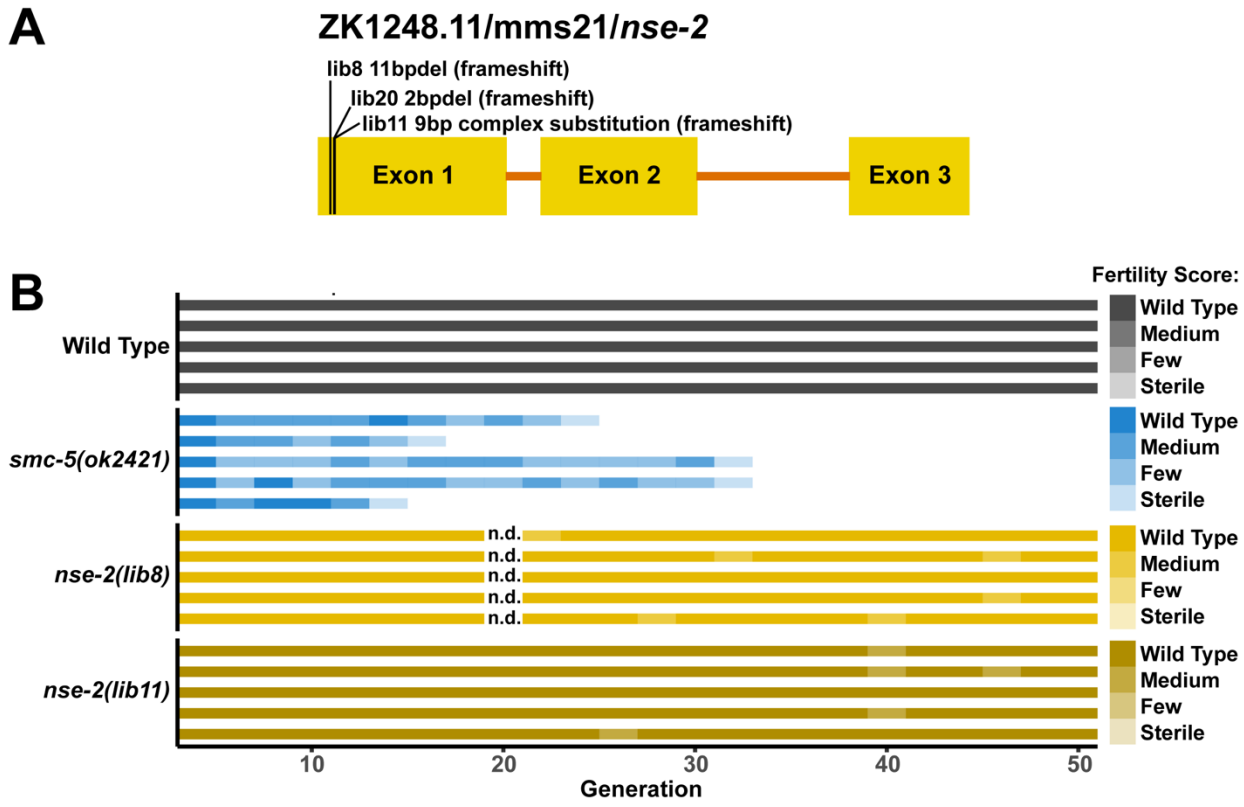

Figure 6.1. NSE-2 is not required for transgenerational fertility. A) Scale diagram of the ZK1248.11/*nse-2* locus with the location and nature of putative null mutations displayed. B) Germline mortal (Mrt) phenotype assay. Horizontal bars represent independent isolates passaged over the course of 50 generations. Every two generations, each isolate was scored qualitatively for the amount of progeny produced on a four-tiered scale based on (Ahmed and Hodgkin 2000): wild type, medium, few, or sterile. Generations which were not scored for fertility are indicated with 'n.d.'.

NSE-2 is required for effective DSB repair

To determine if NSE-2 functions to promote DNA repair in *C. elegans* meiosis, we assessed *nse-2* mutant germ cell capacity to resolve exogenous DSBs. We exposed *nse-2* mutants to 0, 2500, or 5000 Rads of ionizing radiation and assayed the viability of resultant progeny (see Methods). We further exploited the organization of the *C. elegans* germline to differentiate between meiotic nuclei which were at early stages of prophase, when both the homolog and

sister chromatid are available as repair templates ('interhomolog window', 22-58hr post IR), or at late stages of prophase when the homolog is not available as a repair template ('non-interhomolog window', 10-22hr) at the time of DSB induction. We found that *nse-2* mutants were sensitized to ionizing radiation relative to wild type germlines, although *nse-2* nuclei in the non-interhomolog window were less sensitized to exogenous DSBs than nuclei in earlier stages of prophase I (Figure 6.2A). Thus, our data indicate that NSE-2 is required for efficacious DSB repair in the *C. elegans* germline and is especially important to promote gamete viability in early meiotic prophase I.

To determine the genetic interactions of NSE-2 and the known DSB repair complexes SMC-5/6 and BRC-1 in regulating genome integrity, we constructed double and triple null mutants of *nse-2, smc-5,* and *brc-1* and exposed them to ionizing radiation (Figure 6.2A, see Methods). We noted that some of the double mutants exhibited reduced viability even when exposed to no ionizing radiation. Further, we observed high variance in the germline susceptibility of individual hermaphrodites of the same genotype to the ionizing radiation treatment (Figure 6.2A). To account for the different brood viability baselines of each genotype and the overdispersion of parental responses to irradiation in our analysis, we employed a Bayesian statistical modeling approach and fit a Beta-Binomial model to our data (see Methods). To infer the defects of radiation on brood viability independent of baseline fertility defects, we calculated a metric termed 'gamma', which estimates the sensitivity of each genotype to a given radiation dose normalized to its baseline viability (see Methods). A gamma estimate of 1 indicates that a genotype is not sensitized to a given radiation dose, while a gamma estimate of 0 indicates that a genotype was completely sterile due to the irradiation. We then compared the 95% credible intervals of the gamma estimate for each genotype to assess for differences in mutant sensitivity to exogenous DSBs.

To determine how loss of NSE-2 influenced DSB repair when the SMC-5/6 core complex is ablated, we compared the gamma estimates of *nse-2, smc-5,* and *nse-2;smc-5* double mutants. Mutants for *smc-5* were more sensitive to radiation than *nse-2* mutants at all timepoints and radiation doses (Figure 6.2B), indicating that loss of the SMC-5/6 core complex has greater consequences to DSB repair in meiotic cells than loss of its NSE-2 subunit. Double *smc-5;nse-2* mutants exhibited relatively similar levels of vulnerability to ionizing radiation as *smc-5* mutants alone (Figure 6.2B). At low doses of radiation (2500 Rads), however, loss of *nse-2* slightly

Figure 2

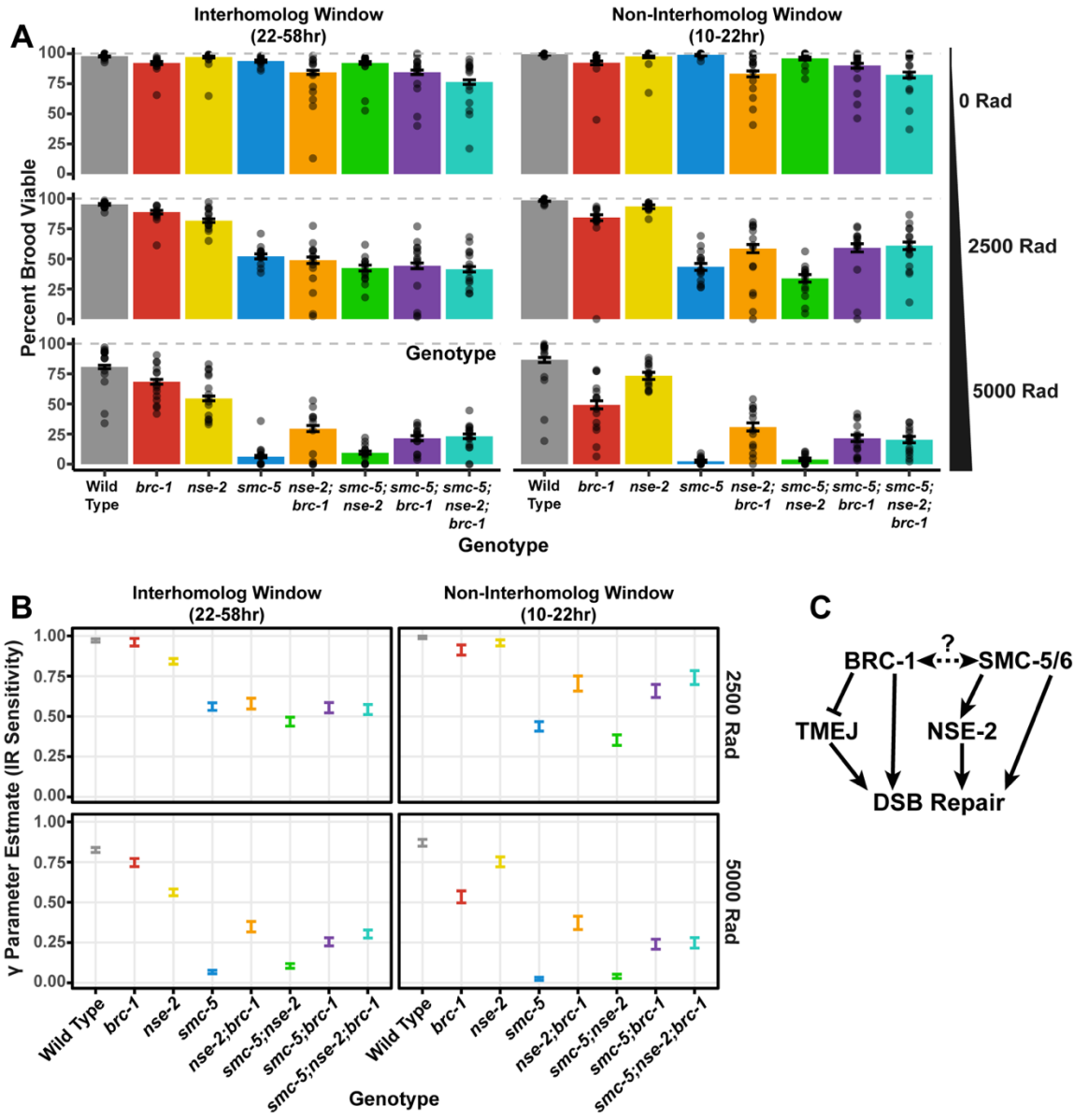

Figure 6.2. NSE-2, SMC-5/6, and BRC-1 genetically interact to regulate gamete viability. A) Brood viabilities of *nse-2*, *smc-5*, and *brc-1* single double and triple mutants following irradiation at doses of 0, 2500, or 5000 Rads. Bars represent the population brood viability, and error bars indicate the 95% Binomial confidence interval of the population brood viability. Dots represent the brood viabilities of individual parent hermaphrodites scored in the experiment. The dashed horizontal grey line indicates 100% brood viability for reference. B) Gamma parameter estimates derived from the Beta-binomial modeling analysis. Error bars represent 95% credible intervals of each estimate. C) Genetic diagram of SMC-5/6, NSE-2, and BRC-1 genetic interactions inferred from genotype susceptibilities to ionizing radiation. The interation from BRC-1 and TMEJ is demonstrated in Chapter III.

sensitized *smc-5* mutants to exogenous DSBs (Figure 6.2B). This sensitizing effect was reversed at high levels of radiation (5000 Rads), as *smc-5;nse-2* double mutants exhibited a slight resilience to exogenous DSBs over *smc-5* single mutants at this dose (Figure 6.2B). Taken together, these results imply that the majority of NSE-2's DSB repair functions overlap with the SMC-5/6 core complex, but also suggest that NSE-2 may exert SMC-5/6 independent functions which subtly impact oocyte viability depending on the amount of DSBs incurred (Figure 6.2C).

SMC-5/6 and BRC-1 genetically interact to regulate meiotic DSB repair (see Chapter III of this thesis). To determine if the SMC-5/6 subunit NSE-2 exhibits divergent or overlapping function with BRC-1 in promoting DNA repair, we compared the viability of *nse-2*, *brc-1*, and *nse-2;brc-1* mutants following irradiation (Figure 6.2A,B). Mutants for *nse-2* exhibited greater sensitivity to radiation than *brc-1* mutants within the interhomolog window (Figure 6.2B). In contrast, *brc-1* mutant sensitivity was greater than *nse-2* mutants in the non-interhomolog window (Figure 6.2B). Double *nse-2;brc-1* mutants, however, were more sensitized than either single mutant alone throughout prophase I and at all doses of radiation (Figure 6.2B). Taken together, these results imply that meiotic nuclei differentially require NSE-2 and BRC-1 within meiotic prophase I to ensure effective DSB repair and gamete viability. Further, our data support a model in which NSE-2 and BRC-1 act in parallel pathways to promote DSB repair (Figure 6.2C).

To test whether the parallel DNA repair functions of NSE-2 and BRC-1 were dependent upon SMC-5/6, we assessed *smc-5;nse-2;brc-1* triple mutant radiation sensitivity (Figure 6.2A,B). We previously demonstrated that loss of *brc-1* ameliorated DSB repair defects in *smc-5* mutants in part due to ectopic activity of theta-mediated end joining in this double mutant context (TMEJ) (Chapter III). At all meiotic stages and doses of radiation scored, we found that *smc-5;nse-2;brc-1* triple mutant gamma estimates were similar those of *smc-5;brc-1* double mutants (Figure 6.2B). This result implies that the activation of error-prone repair which occurs in *brc-1* mutants is also sufficient to counteract the defects of *nse-2* and *smc-5;nse-2* mutants (Figure 6.2C). Taken together, our experiments reveal genetic interactions between conserved DNA repair complexes in regulating meiotic DSB repair.

*nse-2(*S8Δ*)* truncation ameliorates DSB repair defects of *smc-5* mutants

In the course of generating *smc-5;nse-2* double mutants through CRISPR/Cas9 genome editing (see Methods), we incidentally created a double mutant for a null allele of *smc-5* and a 3bp in frame deletion of *nse-2* which specifically ablated the eighth serine of its coding sequence (*nse-2(*S8Δ*)*). This *nse-2(*S8Δ*)* mutation conveyed resilience to ionizing radiation relative to *smc-5* mutation alone (Figure 6.3). As serine residues may be the targets of posttranslational modifications, we hypothesized that mutation of this serine to a nonreactive alanine should phenocopy the effects of S8 deletion if NSE-2 is modified at this residue. We found that *smc-5;nse-2(S8A)* mutants did not exhibit resilience to ionizing radiation and were indistinguishable from *smc-5* mutants alone (Figure 6.3). Thus, our data supports a model in which specifically truncation of the eighth amino acid in the NSE-2 peptide is sufficient to alleviate DSB repair impairment in *smc-5* mutants.

NSE-2 influences DNA repair dynamics in the *C. elegans* germline

To determine whether simultaneous loss of SMC-5/6, NSE-2, and/or BRC-1 altered endogenous meiotic DSB repair dynamics, we used immunofluorescence to assess fixed germlines of *smc-5*, *nse-2*, and *brc-1* single and double mutants for RAD-51 foci, which mark DSBs at early steps of recombination. In a wild type context, RAD-51 marked DSBs are incurred at early pachytene and decline in number through mid and late pachytene as DSBs progress through successive steps of recombination (Figure 6.4). Persistent and elevated RAD-51 foci are therefore indicative of defects in DSB repair.

Similar to *smc-5* and *brc-1* mutants, *nse-2* mutants maintain persistent RAD-51 foci in mid and late pachytene, supporting a function for NSE-2 in promoting efficient recombination (Figure 6.4). Double *smc-5;nse-2* mutants exhibited elevated RAD-51 foci relative to either single mutant from early through late pachytene (Figure 6.4). This result suggests that NSE-2 performs some functions independent of SMC-5/6 to ensure efficient recombination. Double *nse-2;brc-1* mutants did not have notably elevated levels of DSBs in mid and late pachytene relative to *brc-1* or *nse-2* single mutants. However, the number of RAD-51 foci strikingly increased at the end of pachytene in this double mutant context. This result suggests that loading or maintenance of RAD-51 to DSBs is perturbed in *nse-2;brc-1* double mutants until the end of pachytene.

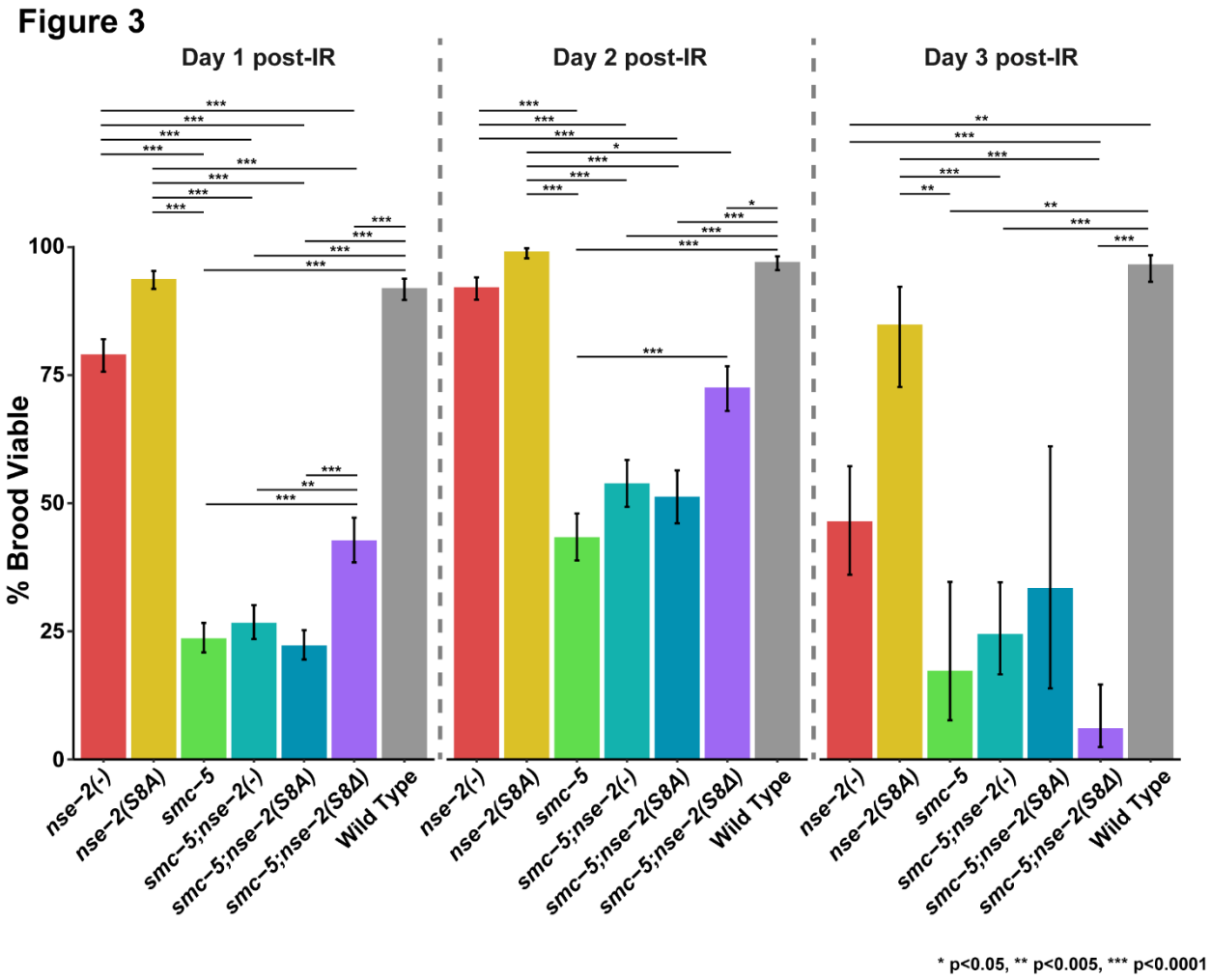

Figure 6.3. Truncation of S8 in NSE-2 ameliorates DSB repair defects in *smc-5* mutants. Brood viabilities of *smc-5* and/or *nse-2* mutants following exposure to 3176 Rads of ionizing radiation. Bars plots represent the population brood viabilities (broods of N=5 parent hermaphrodites scored for each genotype) and error bars represent the 95% confidence intervals of the population brood viability. The brood viabilities of each genotype were compared by Fisher's Exact Test with Bonferroni correction for multiple comparisons *** p<0.0001, **p<0.005, * p<0.05. For simplicity, only significant differences between genotypes are displayed in the figure.

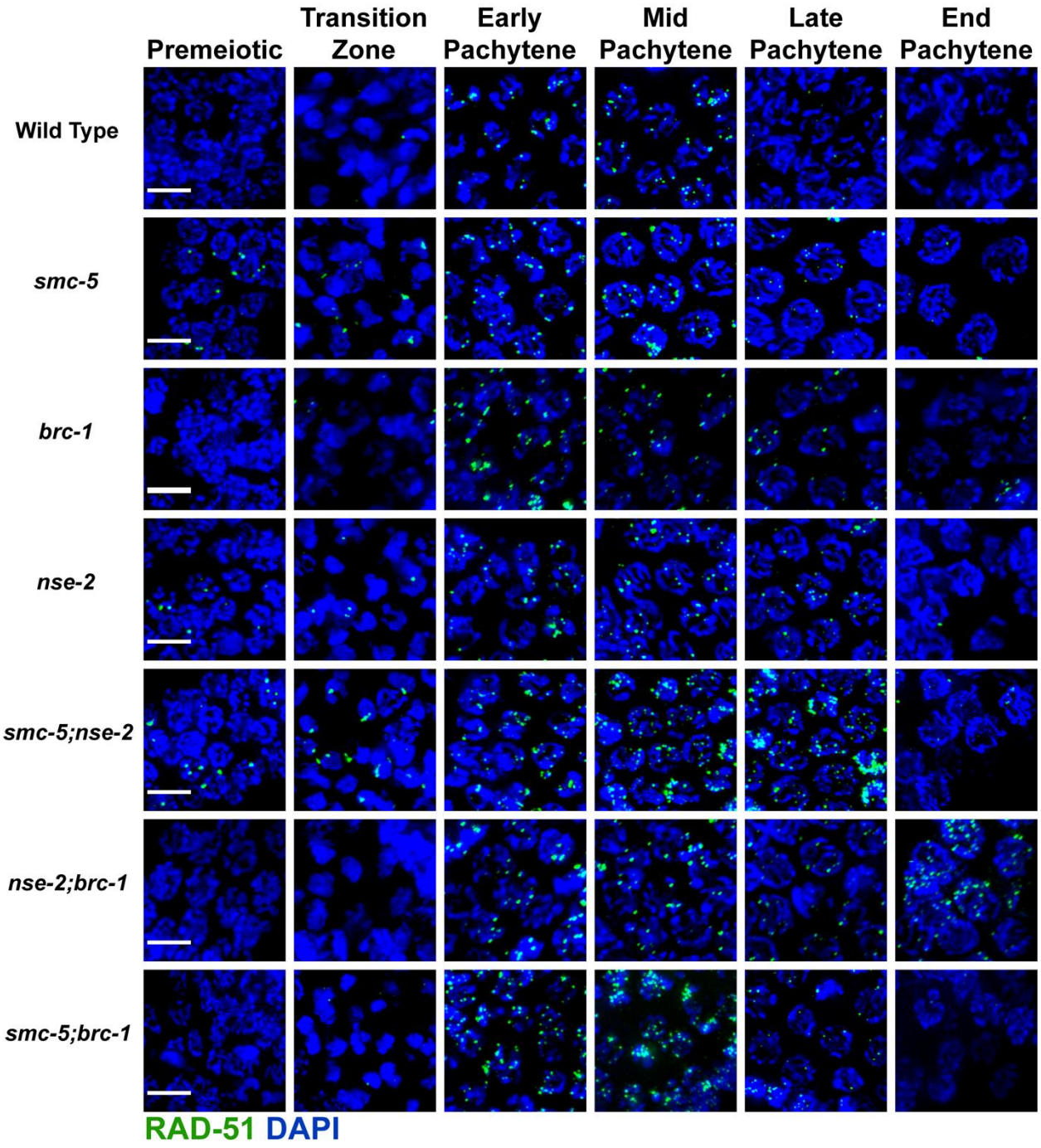

Figure 6.4. NSE-2 regulates early steps in meiotic DSB repair. Maximum intensity projections of nuclei in *C. elegans* hermaphrodite germlines. Scale bars represent 5µm.

Both *smc-5* and *nse-2* mutants also exhibited elevated RAD-51 foci in premeiotic nuclei, indicative of collapsed replication forks undergoing recombination repair (Wolters *et al.* 2014). These RAD-51 foci were not obviously increased in number in the *smc-5;nse-2* double mutant relative to the *smc-5* mutant alone, suggesting that the functions of NSE-2 in mitotic DNA repair largely overlap with those of the SMC-5/6 core complex. Premeiotic RAD-51 foci were suppressed in both *smc-5;brc-1* and *nse-2;brc-1* double mutant contexts, indicating that recombination defects associated with loss of NSE-2 or SMC-5/6 arise due to BRC-1 dependent functions. Taken together, our data reveal interactions of conserved protein complexes regulating DSB repair in the *C. elegans* germline.

Discussion

The functions of the SMC-5/6 complex and its non-SMC subunits in regulating genome integrity remain largely unknown. Our experiments provide evidence that the NSE-2 E3 SUMO ligase subunit of SMC-5/6 functions both in concert with and independent of the core SMC-5/6 complex to promote efficient recombination. Specifically, the SMC-5/6 core complex is vital for ensuring transgenerational fertility independent of NSE-2, but NSE-2 exhibits overlapping function with SMC-5/6 to promote gamete viability following induction of exogenous DNA damage. Our cytological examination of DSB repair dynamics over the course of meiotic prophase I further revealed that *smc-5;nse-2* double mutants exhibit a synthetic delay in early steps of DSB repair. These results may be explained by a model in which NSE-2 and SMC-5/6 act at successive steps of recombination. Under this framework, we propose that NSE-2 functions to ensure efficient progression of break repair past RAD-51 mediated steps while the SMC-5/6 core complex regulates resolution of these downstream recombination intermediates. Homolog-independent conversion tracts in *smc-5* mutants are not distinguishable from wild type tracts, consistent with SMC-5/6 regulatory functions late in recombination intermediate processing (see Chapter III of this thesis). Under this model, loss of *nse-2* in an *smc-5* mutant would be expected to elevate the early RAD-51 marked recombination intermediates but may not exacerbate brood viability defects over the *smc-5* single mutant if these downstream functions disproportionately affect gamete viability.

Our identification of *nse-2(*S8Δ*)* as a partial suppressor of *smc-5* mutant DNA damage sensitivity further supports a role for NSE-2 independent of the SMC-5/6 complex. As the DNA

damage resistance of *nse-2(*S8Δ*)* mutation was not phenocopied by *nse-2(*S8A*)* single amino acid substitution, we provide evidence that this effect is not related to posttranslational modification of S8 in NSE-2. We therefore hypothesize that truncation of S8 in the NSE-2 peptide may confer a structural change that influences the activity or specificity of NSE-2's function, potentially due to ectopic E3 SUMO ligase functions. Further experiments are required to determine how *nse-2(*S8Δ*)* may impact the localization or SUMOylation targets of NSE-2. Taken together, our results evidence that NSE-2 likely performs functions independent of SMC-5/6 to regulate DSB repair during *C. elegans* meiosis.

We further identified genetic interactions between NSE-2 and BRC-1 in regulating meiotic DSB repair. We demonstrate that NSE-2 and BRC-1 function in parallel to promote gamete viability following ionizing radiation exposure. Through these irradiation experiments, we additionally found that NSE-2 and BRC-1 are differentially required within prophase I to promote gamete viability. Together, these results support separate functions for BRC-1 and NSE-2 in promoting meiotic DSB repair. Simultaneous mutation of *nse-2* and *brc-1* revealed a particularly interesting cytological phenotype in DSB repair dynamics, as RAD-51 foci became grossly elevated in this double mutant only at the end of pachytene. This phenotype suggests that DSBs are present and unrepaired in the meiotic nuclei of *nse-2;brc-1* mutants but are not robustly loaded with RAD-51 until this late meiotic stage. Previous evidence has demonstrated that the requirements for RAD-51 loading change during the course of prophase I (Hayashi *et al.* 2007; Li *et al.* 2018). BRC-1 is required for maintenance and/or loading of RAD-51 specifically in mid/late pachytene (Li *et al.* 2018, Chapter III). Thus, our data are consistent with a role for NSE-2 in promoting the localization of RAD-51 to DSBs in early stages of pachytene. This data also raises the possibility that RAD-51 loading becomes differentially regulated at the end of pachytene independent of BRC-1 or NSE-2. In summary, our data uncovers genetic relationships between conserved DNA repair proteins in promoting DNA repair and meiotic genome integrity.

APPENDIX B

INTEGRATION OF THE *DROSOPHILA* MOS1 TRANSPOSON AT THE *C .ELEGANS UNC-5* LOCUS ALTERS PHARYNX MUSCLE-SPECIFIC TRANSGENE EXPRESSION ON THE mIn1 INVERSION CHROMOSOME

Erik Toraason and Diana E. Libuda

Cell type-specific gene expression is regulated both by *cis* and *trans* acting elements. Many *Drosophila* genes are regulated by 'transvection', which occurs when alleles on one chromosome act to suppress or enhance the expression of genes on different chromosomes (Fukaya and Levine 2017). In mammalian systems, enhancers from different chromosomes colocalize in nuclei to coordinate gene expression (Maass *et al.* 2019). While long-range *cis* interactions of enhancers on the same chromosome has been documented for the *myo-2* and *myo-3* locus in *C. elegans* (Okkema *et al.* 1993; Toraason *et al.* 2021a; c), long-range *trans* interactions of enhancers from different chromosomes has not been widely reported in *C. elegans*. Here we report that the incorporation of a Mos1 transposon at the *unc-5* locus of *C. elegans* Chromosome *IV* is sufficient to alter the expression pattern of a *pmyo-2::GFP* pharynx muscle specific transgene to also be expressed in the body wall muscle. Worms homozygous for the *mIn1* Chromosome *II* inversion marked with both a recessive null *dpy-10* body morphology allele and a *pmyo-2::GFP* transgene which expresses GFP specifically in the pharynx muscle (Figure 7.1). In strains which also carry Mos1 sequence at the *unc-5* locus on Chromosome *IV*, GFP fluorescence can also be detected in the body wall muscle (Figure 7.1). This effect cannot be explained by the presence of the *KrIs14* [*phsp-16.48::MosTransposase*; *lin-15B*; *punc-122::GFP*] transgene integrated on Chromosome *V* in this strain background (Bessereau *et al.* 2001; Robert and Bessereau 2007), as this ectopic body wall GFP expression is not observed in *mIn1* worms which are homozygous for *KrIs14* but do not carry a Mos1 transposon (Figure 7.1). Previous work has shown that the expression of transgenes driven by the *myo-2* promoter can be influenced by long-range *cis* interactions with the *myo-3* promoter sequence (Okkema *et al.* 1993). Our finding expands upon this observation and indicates that *trans* interchromosomal effects also influence the specificity of *pmyo-2* driven tissue-specific transgene expression in *C. elegans*.

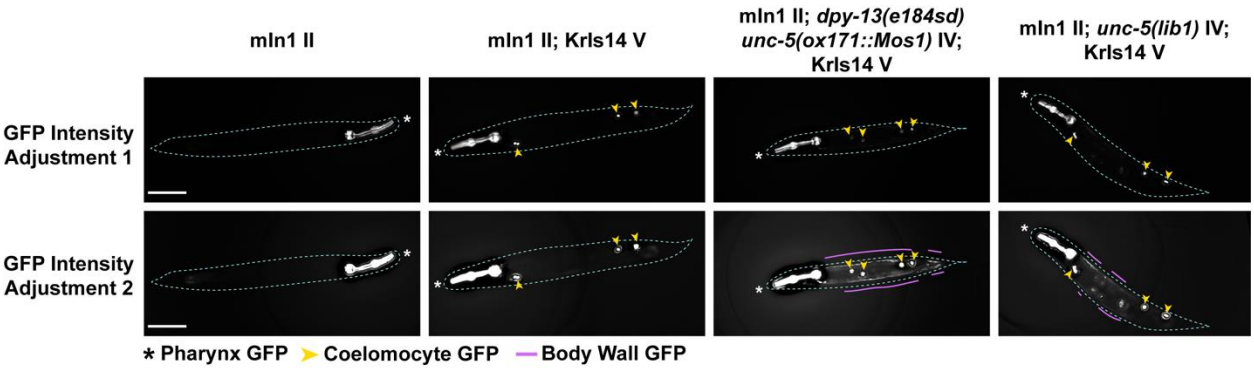

Figure 7.1. Presence of Mos1 at *unc-5* is sufficient to cause body wall misexpression of a *pmyo-2::GFP* transgene. Displayed are images of GFP fluorescence in young adult hermaphrodites carrying the mIn1 inversion chromosome. The outline of the worm is demarcated with a pale blue dotted line. Asterisks indicate the pharynx of the worm, yellow arrowheads indicate GFP expression in the coelomocytes due to the *punc-122::GFP* construct in the KrIs14 transgene, and purple lines indicate body wall GFP expression. As the pharynx GFP fluorescence is much brighter than in other tissues, images were adjusted in photoshop to best represent the pharynx GFP signal (GFP Intensity Adjustment 1) and the other tissues (GFP Intensity Adjustment 2).

Materials and Methods

C. elegans strain maintenance

C. elegans stocks were maintained at 20°C on NGM plates with a lawn of OP50 *Escherichia coli* bacteria. Strains used in this appendix include:

YE57 (*smc-5(ok2421)/*mIn1 [mIs14 *dpy-10(e128)*] II)

DLW215 (+/mIn1 [mIs14 *dpy-10(e128)*] II; KrIs14 [*phsp-16.48::MosTransposase*; *lin-15B*; *punc-122::GFP*] V)

DLW204 (ZK1248.11(*lib8*) / mIn1 [*dpy-10(e128)* mIs14] II; *unc-5(pmyo-3::GFP*; unc-119(+); pmyo-2::GFP(Mos1))* IV; KrIs14 (*phsp16.48::Mos1transposase; lin-15B; punc-122::GFP*) V)

DLW202 (*smc-5(ok2421)*/mIn1 [*dpy-10(e128)* mIs14] II; *dpy-13(e184sd) unc-5(ox171::Mos1)* IV; KrIs14 [*phsp-16.48::MosTransposase*; *lin-15B?*; *punc-122::GFP*] V)

Image Acquisition and Processing

C. elegans worms were immobilized in worm paralysis buffer (M9 with 10mM sodium azide and 0.1% Tween20) and were imaged on a GE IN Cell microscope with a 10X/NA 0.45 lens using a Z-step size of 25μm. Images were deconvolved using the IN Cell 3D deconvolution software. Individual Z-stack images were processed in Fiji and were stitched using the Stitcher plugin (Preibisch *et al.* 2009) if necessary to visualize whole worms.

REFERENCES CITED

Achache H., R. Falk, N. Lerner, T. Beatus, and Y. B. Tzur, 2021 Oocyte aging is controlled by mitogen-activated protein kinase signaling. Aging Cell 20.

Adamo A., P. Montemauri, N. Silva, J. D. Ward, S. J. Boulton, *et al.*, 2008 BRC-1 acts in the inter-sister pathway of meiotic double-strand break repair. EMBO Rep. 9: 287–292.

Agostinho A., B. Meier, R. Sonneville, M. Jagut, and A. Woglar, 2013 Combinatorial Regulation of Meiotic Holliday Junction Resolution in C. elegans by HIM-6 (BLM) Helicase, SLX-4, and the SLX-1, MUS-81 and XPF-1 Nucleases. PLoS Genet 9: 1–19.

Ahmed S., and J. Hodgkin, 2000 MRT-2 checkpoint protein is required for germline immortality and telomere replication in C. elegans. Nature 403: 159–164.

Ahuja J. S., C. S. Harvey, D. L. Wheeler, and M. Lichten, 2021 Repeated strand invasion and extensive branch migration are hallmarks of meiotic recombination. Mol. Cell 81: 4258–4270.

Albert Hubbard E. J., and D. Greenstein, 2000 The Caenorhabditis elegans gonad: A test tube for cell and developmental biology. Dev. Dyn. 218: 2–22.

Almanzar D. E., S. G. Gordon, and O. Rog, 2021 Meiotic sister chromatid exchanges are rare in C. elegans. Curr. Biol. 31: 1499–1507.

Almanzar D. E., A. Hamrick, and O. Rog, 2022 Single-sister labeling in the C. elegans germline using the nucleotide analog EdU. STAR Protoc. 3: 101344.

Alpi A., P. Pasierbek, A. Gartner, and J. Loidl, 2003 Genetic and cytological characterization of the recombination protein RAD-51 in Caenorhabditis elegans. Chromosoma 112: 6–16.

Andux S., and R. E. Ellis, 2008 Apoptosis maintains oocyte quality in aging Caenorhabditis elegans females. PLoS Genet. 4.

Angeles-Albores D., D. H. W. Leighton, T. Tsou, T. H. Khaw, I. Antoshechkin, *et al.*, 2017 The Caenorhabditis elegans female-like state: Decoupling the transcriptomic effects of aging and sperm status. G3 Genes, Genomes, Genet. 7: 2969–2977.

Ann Handel M., and J. C. Schimenti, 2010 Genetics of mammalian meiosis: regulation, dynamics and impact on fertility. Nat. Rev. Genet. 11: 124–138.

Aragón L., 2018 The Smc5/6 Complex: New and Old Functions of the Enigmatic Long-Distance Relative. Annu. Rev. Genet. 52: 89–107.

Bachrati C. Z., R. H. Borts, and I. D. Hickson, 2006 Mobile D-loops are a preferred substrate for the Bloom's syndrome helicase. Nucleic Acids Res. 34: 2269–2279.

Bae W., S. Hong, M. S. Park, H. K. Jeong, M. H. Lee, *et al.*, 2019 Single-strand annealing mediates the conservative repair of double-strand DNA breaks in homologous recombination-defective germ cells of Caenorhabditis elegans. DNA Repair (Amst). 75: 18–28.

Bessereau J. L., A. Wright, D. C. Williams, K. Schuske, M. W. Davis, *et al.*, 2001 Mobilization of a Drosophila transposon in the, Caenorhabditis elegans germ line. Nature 413: 70–74.

Bhalla N., D. J. Wynne, V. Jantsch, and A. F. Dernburg, 2008 ZHP-3 Acts at Crossovers to Couple Meiotic Recombination with Synaptonemal Complex Disassembly and Bivalent Formation in C. elegans. PLoS Genet 4: 1–15.

Bhargava R., D. O. Onyango, and J. M. Stark, 2016 Regulation of Single-Strand Annealing and its Role in Genome Maintenance. Trends Genet. 32: 566–575.

Bickel J. S., L. Chen, J. Hayward, S. L. Yeap, A. E. Alkers, *et al.*, 2010 Structural maintenance of chromosomes (SMC) proteins promote homolog-independent recombination repair in meiosis crucial for germ cell genomic stability. PLoS Genet. 6: 1–13.

Boulton S. J., J. S. Martin, J. Polanowska, D. E. Hill, A. Gartner, *et al.*, 2004 BRCA1/BARD1 Orthologs Required for DNA Repair in Caenorhabditis elegans. Curr. Biol. 14: 33–39.

Brabant A. J. Van, T. Ye, M. Sanz, J. L. German, N. A. Ellis, *et al.*, 2000 Binding and melting of D-loops by the Bloom syndrome helicase. Biochemistry 39: 14617–14625.

Broekmans F. J., E. A. H. Knauff, E. R. te Velde, N. S. Macklon, and B. C. Fauser, 2007 Female reproductive ageing: current knowledge and future trends. Trends Endocrinol. Metab. 18: 58–65.

Cahoon C. K., and D. E. Libuda, 2019 Leagues of their own: sexually dimorphic features of meiotic prophase I. Chromosoma 128: 199–214.

Cahoon C. K., J. M. Helm, and D. E. Libuda, 2019 Synaptonemal Complex Central Region Proteins Promote Localization of Pro-crossover Factors to Recombination Events During Caenorhabditis elegans Meiosis. Genetics 213: 395–409.

Cahoon C. K., and D. E. Libuda, 2021 Conditional immobilization for live imaging Caenorhabditis elegans using auxin-dependent protein depletion. G3 Genes, Genomes, Genet. 11.

Carvajal-Garcia J., K. N. Crown, D. A. Ramsden, and J. Sekelsky, 2020 DNA polymerase theta suppresses mitotic crossing over. Biorxiv 1–25.

Chandramouly G., A. Kwok, B. Huang, N. A. Willis, A. Xie, *et al.*, 2013 BRCA1 and CtIP suppress long-tract gene conversion between sister chromatids. Nat. Commun. 4.

Chatzidaki E. E., S. Powell, B. J. H. Dequeker, J. Gassler, M. C. C. Silva, *et al.*, 2021 Ovulation suppression protects against chromosomal abnormalities in mouse eggs at advanced maternal age. Curr. Biol. 31: 4038-4051.e7.

Chen W., and S. Jinks-Robertson, 1999 The Role of the Mismatch Repair Machinery in Regulating Mitotic and Meiotic Recombination Between Diverged Sequences in Yeast. Genetics 151: 1299–1313.

Chen L., C. J. Nievera, A. Y. L. Lee, and X. Wu, 2008 Cell cycle-dependent complex formation of BRCA1·CtIP·MRN is important for DNA double-strand break repair. J. Biol. Chem. 283: 7713–7720.

Chung W. H., Z. Zhu, A. Papusha, A. Malkova, and G. Ira, 2010 Defective resection at DNA double-strand breaks leads to de Novo telomere formation and enhances gene targeting. PLoS Genet. 6: 24.

Church D. L., Guan Kun-Liang, and E. J. Lambie, 1995 Three genes of the MAP kinase cascade, mek-2, mpk-1/sur-1 and let-60 ras, are required for meiotic cell cycle progression in Caenorhabditis elegans. Development 121: 2525–2535.

Cinquin A., M. Chiang, A. Paz, S. Hallman, O. Yuan, *et al.*, 2016 Intermittent Stem Cell Cycling Balances Self-Renewal and Senescence of the C. elegans Germ Line. PLoS Genet. 12.

Clejan I., J. Boerckel, and S. Ahmed, 2006 Developmental modulation of nonhomologous end joining in Caenorhabditis elegans. Genetics 173: 1301–1317.

Cloud V., Y. L. Chan, J. Grubb, B. Budke, and D. K. Bishop, 2012 Rad51 is an accessory factor for Dmc1-mediated joint molecule formation during meiosis. Science (80-.). 337: 1222–1225.

Colaiácovo M. P., A. J. MacQueen, E. Martinez-Perez, K. McDonald, A. Adamo, *et al.*, 2003 Synaptonemal complex assembly in C. elegans is dispensable for loading strand-exchange proteins but critical for proper completion of recombination. Dev. Cell 5: 463–474.

Copsey A., S. Tang, P. W. Jordan, H. G. Blitzblau, S. Newcombe, *et al.*, 2013 Smc5/6 Coordinates Formation and Resolution of Joint Molecules with Chromosome Morphology to Ensure Meiotic Divisions. PLoS Genet. 9: 1–24.

Crittenden S. L., C. H. Lee, I. Mohanty, S. Battula, K. Knobel, *et al.*, 2019 Sexual dimorphism of niche architecture and regulation of the Caenorhabditis elegans germline stem cell pool. Mol. Biol. Cell 30: 1757–1769.

Crown K. N., S. Mcmahan, and J. Sekelsky, 2014 Eliminating Both Canonical and Short-Patch Mismatch Repair in Drosophila melanogaster Suggests a New Meiotic Recombination Model. PLoS Genet 10: 1–11.

Cruz-García A., A. López-Saavedra, and P. Huertas, 2014 BRCA1 accelerates CtIP-ediated DNA-end resection. Cell Rep. 9: 451–459.

Davis M. W., M. Hammarlund, T. Harrach, P. Hullett, S. Olsen, *et al.*, 2005 Rapid single nucleotide polymorphism mapping in C. elegans. BMC Genomics 6: 1–11.

Dernburg A. F., K. McDonald, G. Moulder, R. Barstead, M. Dresser, *et al.*, 1998 Meiotic recombination in C. elegans initiates by a conserved mechanism and is dispensable for homologous chromosome synapsis. Cell.

Dokshin G. A., K. S. Ghanta, K. M. Piscopo, and C. C. Mello, 2018 Robust genome editing with short single-stranded and long, partially single-stranded DNA donors in caenorhabditis elegans. Genetics 210: 781–787.

Doniach T., and J. Hodgkin, 1984 A Sex-Determining Gene, fem-1, Required for Both Male and Hermaphrodite Development in Caenorhabditis elegans. Dev. Biol. 106: 223–235.

Engels W. R., D. M. Johnson-Schlitz, W. B. Eggleston, and J. Sved, 1990 High-Frequently P Element Loss in Drosophila Is Homolog Dependent. Cell 62: 515–525.

Ertl H. A., D. P. Russo, N. Srivastava, J. T. Brooks, T. N. Dao, *et al.*, 2017 The Role of Blm Helicase in Homologous Recombination, Gene Conversion Tract Length, and Recombination Between Diverged Sequences in Drosophila melanogaster. Genetics 207: 923–933.

Fasullo M. T., and R. W. Davis, 1987 Recombinational substrates designed to study recombination between unique and repetitive sequences in vivo. Proc. Natl. Acad. Sci. 84: 6215–6219.

Fleck O., E. Lehmann, P. Schär, and J. Kohli, 1999 Involvement of nucleotide-excision repair in msh2 pms1-independent mismatch repair. Nat. Genet. 21: 314–317.

Fukaya T., and M. Levine, 2017 Transvection. Curr. Biol. 27: R1047–R1049.

Garcia-Muse T., and S. J. Boulton, 2007 Meiotic recombination in Caenorhabditis elegans. Chromosom. Res. 15: 607–621.

Gartner A., and J. A. Engebrecht, 2022 DNA repair, recombination, and damage signaling. Genetics 220.

Goldfarb T., and M. Lichten, 2010 Frequent and efficient use of the sister chromatid for DNA double-strand break repair during budding yeast meiosis. PLoS Biol. 8: 1–12.

Gray S., and P. E. Cohen, 2016 Control of Meiotic Crossovers: From Double-Strand Break Formation to Designation. Annu. Rev. Genet. 50: 175–210.

Gudgen M., A. Chandrasekaran, T. Frazier, and L. Boyd, 2004 Interactions within the ubiquitin pathway of Caenorhabditis elegans. Biochem. Biophys. Res. Commun. 325: 479–486.

Guo X., Y. F. Hum, K. Lehner, and S. Jinks-Robertson, 2017 Regulation of hetDNA Length during Mitotic Double-Strand Break Repair in Yeast. Mol. Cell 67: 539-549.e4.

Hayashi M., G. M. Chin, and A. M. Villeneuve, 2007 C. elegans germ cells switch between distinct modes of double-strand break repair during meiotic prophase progression. PLoS Genet. 3: 2068–2084.

Hicks W. M., M. Kim, and J. E. Haber, 2010 Increased mutagenesis and unique mutation signature associated with mitotic gene conversion. Proc. Natl. Acad. Sci. U.S.A 329: 82–85.

Hillers K. J., V. Jantsch, E. Martinez-Perez, and J. L. Yanowitz, 2017 Meiosis. WormBook 146.

Holliday R., 1964 A mechanism for gene conversion in fungi. Genet. Res. 5: 282–304.

Hong Y., R. Sonneville, A. Agostinho, B. Meier, B. Wang, *et al.*, 2016 The SMC-5/6 Complex and the HIM-6 (BLM) Helicase Synergistically Promote Meiotic Recombination Intermediate Processing and Chromosome Maturation during Caenorhabditis elegans Meiosis. PLoS Genet 12: 1–24.

Howe M., K. L. Mcdonald, D. G. Albertson, and B. J. Meyer, 2001 HIM-10 Is Required for Kinetochore Structure and Function on Caenorhabditis elegans Holocentric Chromosomes. J. Cell Biol. 153: 1227–1238.

Hu Y., S. Raynard, M. G. Sehorn, X. Lu, W. Bussen, *et al.*, 2007 RECQL5/Recql5 helicase regulates homologous recombination and suppresses tumor formation via disruption of Rad51 presynaptic filaments. Genes Dev. 21: 3073–3084.

Hubbard E. J. A., and D. Greenstein, 2005 Introduction to the germ line. WormBook 1–4.

Hubbard J. E. A., and T. Schedl, 2019 Biology of the Caenorhabditis elegans Germline Stem Cell System. Genetics 213: 1145–1188.

Huen M. S. Y., S. M. H. Sy, and J. Chen, 2010 BRCA1 and its toolbox for the maintenance of genome integrity. Nat. Rev. Mol. Cell Biol. 11: 138–148.

Hum Y. F., and S. Jinks-Robertson, 2019 Mismatch recognition and subsequent processing have distinct effects on mitotic recombination intermediates and outcomes in yeast. Nucleic Acids Res. 47: 4554–4568.

Humphryes N., and A. Hochwagen, 2014 A non-sister act: Recombination template choice during meiosis. Exp. Cell Res. 329: 53–60.

Hunter N., 2015 Meiotic recombination: The essence of heredity. Cold Spring Harb. Perspect. Biol. 7.

Ishidate T., A. R. Ozturk, D. J. Durning, M. Seth, M. Shirayama, *et al.*, 2018 ZNFX-1 Functions within Perinuclear Nuage to Balance Epigenetic Signals Article ZNFX-1 Functions within Perinuclear Nuage to Balance Epigenetic Signals. Mol. Cell 70: 639–649.

Jacome A., P. Gutierrez-Martinez, F. Schiavoni, E. Tenaglia, P. Martinez, *et al.*, 2015 NSMCE2 suppresses cancer and aging in mice independently of its SUMO ligase activity. EMBO J. 34: 2604–2619.

Janisiw E., M. R. Dello Stritto, V. Jantsch, and N. Silva, 2018 BRCA1-BARD1 associate with the synaptonemal complex and pro-crossover factors and influence RAD-51 dynamics during Caenorhabditis elegans meiosis. PLoS Genet. 14.

Jantsch V., P. Pasierbek, M. M. Mueller, D. Schweizer, M. Jantsch, *et al.*, 2004 Targeted Gene Knockout Reveals a Role in Meiotic Recombination for ZHP-3, a Zip3-Related Protein in Caenorhabditis elegans. Mol. Cell. Biol. 24: 7998–8006.

Jaramillo-Lambert A., M. Ellefson, A. M. Villeneuve, and J. A. Engebrecht, 2007 Differential timing of S phases, X chromosome replication, and meiotic prophase in the C. elegans germ line. Dev. Biol. 308: 206–221.

Johnson R. D., N. Liu, and M. Jasin, 1999 Mammalian XRCC2 promotes the repair of DNA double-strand breaks by homologous recombination. Lett. to Nat. 401: 397–399.

Johnson R. D., and M. Jasin, 2000 Sister chromatid gene conversion is a prominent double-strand break repair pathway in mammalian cells. EMBO J. 19: 3398–3407.

Kadyk L. C., and L. H. Hartwell, 1992 Sister Chromatids are Preferred Over Homologs as Substrates for Recombinational Repair in Saccharomyces cerevisiae. Genetics 132: 387–402.

Kamp J. A., R. van Schendel, I. W. Dilweg, and M. Tijsterman, 2020 BRCA1-associated structural variations are a consequence of polymerase theta-mediated end-joining. Nat. Commun. 11: 1–10.

Kawasaki I., Y. H. Shim, J. Kirchner, J. Kaminker, W. B. Wood, *et al.*, 1998 PGL-1, a predicted RNA-binding component of germ granules, is essential for fertility in C. elegans. Cell 94: 635–645.

Keelagher R. E., V. E. Cotton, A. S. H. Goldman, and R. H. Borts, 2011 Separable roles for Exonuclease I in meiotic DNA double-strand break repair. DNA Repair (Amst). 10: 126–137.

Keeney S., C. N. Giroux, and N. Kleckner, 1997 Meiosis-Specific DNA Double-Strand Breaks Are Catalyzed by Spo11, a Member of a Widely Conserved Protein Family. Cell 88: 375–384.

Kelly K. O., A. F. Dernburg, G. M. Stanfield, and A. M. Villeneuve, 2000 Caenorhabditis elegans msh-5 Is Required for Both Normal and Radiation-Induced Meiotic Crossing Over but Not for Completion of Meiosis. 156: 617–630.

Kern C. C., S. J. Townsend, A. Salzmann, N. B. Rendell, G. W. Taylor, *et al.*, 2021 C. elegans feed yolk to their young in a form of primitive lactation. Nat. Commun. 12.

Kim K. P., B. M. Weiner, L. Zhang, A. Jordan, J. Dekker, *et al.*, 2010 Sister cohesion and structural axis components mediate homolog bias of meiotic recombination. Cell.

Kritikou E. A., S. Milstein, P. O. Vidalain, G. Lettre, E. Bogan, *et al.*, 2006 C. elegans GLA-3 is a novel component of the MAP kinase MPK-1 signaling pathway required for germ cell survival. Genes Dev. 20: 2279–2292.

Kurhanewicz N. A., D. Dinwiddie, Z. D. Bush, and D. E. Libuda, 2020 Elevated Temperatures Cause Transposon-Associated DNA Damage in C. elegans Spermatocytes. Curr. Biol. 30: 5007-5017.e4.

L'Hernault S. W., 2006 Spermatogenesis. WormBook 1–14.

Lao J. P., and N. Hunter, 2010 Trying to Avoid Your Sister. PLoS Biol. 8: 1–5.

Lee M. H., M. Ohmachi, S. Arur, S. Nayak, R. Francis, *et al.*, 2007 Multiple functions and dynamic activation of MPK-1 extracellular signal-regulated kinase signaling in Caenorhabditis elegans germline development. Genetics 177: 2039–2062.

Lee C., E. B. Sorensen, T. R. Lynch, and J. Kimble, 2016 C. elegans GLP-1/Notch activates transcription in a probability gradient across the germline stem cell pool. Elife 5: 1–23.

Lemmens B. B. L. G., and M. Tijsterman, 2011 DNA double-strand break repair in Caenorhabditis elegans. Chromosoma 120: 1–21.

Lemmens B. B. L. G., N. M. Johnson, and M. Tijsterman, 2013 COM-1 Promotes Homologous Recombination during Caenorhabditis elegans Meiosis by Antagonizing Ku-Mediated Non-Homologous End Joining. PLoS Genet. 9: 1–14.

Li Q., T. T. Saito, M. Martinez-Garcia Id, A. J. Deshong, S. Nadarajan Id, *et al.*, 2018 The tumor suppressor BRCA1-BARD1 complex localizes to the synaptonemal complex and regulates recombination under meiotic dysfunction in Caenorhabditis elegans. PLOS Genet. 14: 1–34.

Li Q., S. Hariri, and J. Engebrecht, 2020 Meiotic double-strand break processing and crossover patterning are regulated in a sex-specific manner by BRCA1-BARD1 in C. elegans. Genetics 216: 359–379.

Libuda D. E., S. Uzawa, B. J. Meyer, and A. M. Villeneuve, 2013 Meiotic chromosome structures constrain and respond to designation of crossover sites. Nature 502: 703–706.

Lilienthal I., T. Kanno, and C. Sjögren, 2013 Inhibition of the Smc5/6 Complex during Meiosis Perturbs Joint Molecule Formation and Resolution without Significantly Changing Crossover or Non-crossover Levels. PLoS Genet. 9.

Luo S., W. M. Shaw, J. Ashraf, and C. T. Murphy, 2009 TGF-ß Sma/Mab signaling mutations uncouple reproductive aging from somatic aging. PLoS Genet. 5.

Luo S., G. A. Kleemann, J. M. Ashraf, W. M. Shaw, and C. T. Murphy, 2010 TGF-β and Insulin Signaling Regulate Reproductive Aging via Oocyte and Germline Quality Maintenance. Cell 143: 299–312.

Maass P. G., A. R. Barutcu, and J. L. Rinn, 2019 Interchromosomal interactions: A genomic love story of kissing chromosomes. J. Cell Biol. 218: 27–38.

Macaisne N., Z. Kessler, and J. L. Yanowitz, 2018 Meiotic double-strand break proteins influence repair pathway utilization. Genetics 210: 843–856.

Mack H. I. D., T. Heimbucher, and C. T. Murphy, 2018 The nematode Caenorhabditis elegans as a model for aging research. Drug Discov. Today Dis. Model. 27: 3–13.

Macqueen A. J., and A. M. Villeneuve, 2001 Nuclear reorganization and homologous chromosome pairing during meiotic prophase require C. elegans chk-2. Genes Dev. 15: 1674–1687.

MacQueen A. J., M. P. Colaiácovo, K. McDonald, and A. M. Villeneuve, 2002 Synapsis-dependent and -independent mechanisms stabilize homolog pairing during meiotic prophase in C. elegans. Genes Dev. 16: 2428–2442.

MacQueen A. J., C. M. Phillips, N. Bhalla, P. Weiser, A. M. Villeneuve, *et al.*, 2005 Chromosome sites play dual roles to establish homologous synapsis during meiosis in C. elegans. Cell 123: 1037–1050.

Manandhar M., K. S. Boulware, and R. D. Wood, 2015 The ERCC1 and ERCC4 (XPF) genes and gene products. Gene 569: 153–161.

Mao Z., M. Bozzella, A. Seluanov, and V. Gorbunova, 2008 Comparison of nonhomologous end joining and homologous recombination in human cells. DNA Repair (Amst). 7: 1765–1771.

Marsolier-Kergoat M. C., M. M. Khan, J. Schott, X. Zhu, and B. Llorente, 2018 Mechanistic View and Genetic Control of DNA Recombination during Meiosis. Mol. Cell 70: 9-20.e6.

Martinez-Perez E., M. Schvarzstein, C. Barroso, J. Lightfoot, A. F. Dernburg, *et al.*, 2008 Crossovers trigger a remodeling of meiotic chromosome axis composition that is linked to two-step loss of sister chromatid cohesion. Genes Dev. 22: 2886–2901.

Maures T. J., L. N. Booth, B. A. Benayoun, Y. Izrayelit, F. C. Schroeder, *et al.*, 2014 Males shorten the life span of C. elegans hermaphrodites via secreted compounds. Science (80-.). 343: 541–544.

Mccarter J., B. Bartlett, T. Dang, and T. Schedl, 1999 On the Control of Oocyte Meiotic Maturation and Ovulation in Caenorhabditis elegans. Dev. Biol. 205: 111–128.

McVey M., J. R. LaRocque, M. D. Adams, and J. J. Sekelsky, 2004 Formation of deletions during double-strand break repair in Drosophila DmBlm mutants occurs after strand invasion. PNAS 101: 15694–15699.

Mets D. G., and B. J. Meyer, 2009 Condensins Regulate Meiotic DNA Break Distribution, thus Crossover Frequency, by Controlling Chromosome Structure. Cell 139: 73–86.

Mimitou E. P., S. Yamada, and S. Keeney, 2017 A global view of meiotic double-strand break end resection. Science (80-.). 355.

Moghadam A. R. E., M. T. Moghadam, M. Hemadi, and G. Saki, 2022 Oocyte quality and aging. J. Bras. Reprod. Assist. 26: 105–122.

Moynahan M. E., and M. Jasin, 2010 Mitotic homologous recombination maintains genomic stability and suppresses tumorigenesis. Nat. Rev. Mol. Cell Biol. 11: 196–207.

Nadarajan S., F. Mohideen, Y. B. Tzur, N. Ferrandiz, O. Crawley, *et al.*, 2016 The MAP kinase pathway coordinates crossover designation with disassembly of synaptonemal complex proteins during meiosis. Elife 5.

Nasmyth K., and C. H. Haering, 2009 Cohesin: Its roles and mechanisms. Annu. Rev. Genet. 43: 525–558.

Niu H., L. Wan, B. Baumgartner, D. Schaefer, J. Loidl, *et al.*, 2005 Partner choice during meiosis is regulated by Hop1-promoted dimerization of Mek1. Mol. Biol. Cell 16: 5804–5818.

Nottke A. C., S. E. Beese-Sims, L. F. Pantalena, V. Reinke, Y. Shi, *et al.*, 2011 SPR-5 is a histone H3K4 demethylase with a role in meiotic double-strand break repair. Proc. Natl. Acad. Sci. U. S. A. 108: 12805–12810.

O'Neil N. J., J. S. Martin, J. L. Youds, J. D. Ward, M. I. R Petalcorin, *et al.*, 2013 Joint Molecule Resolution Requires the Redundant Activities of MUS-81 and XPF-1 during Caenorhabditis elegans Meiosis. PLoS Genet 9: 1–14.

Okkema P. G., S. W. Harrison, V. Plunger, A. Aryana', and A. Fire, 1993 Sequence Requirements for Myosin Gene Expression and Regulation in Caenorhabditis elegans. Genetics 135: 385–404.

Ouyang J. P. T., A. Folkmann, L. Bernard, C. Y. Lee, U. Seroussi, *et al.*, 2019 P Granules Protect RNA Interference Genes from Silencing by piRNAs. Dev. Cell 50: 728.

Pâques F., and J. E. Haber, 1999 Multiple Pathways of Recombination Induced by Double-Strand Breaks in Saccharomyces cerevisiae. Microbiol. Mol. Biol. Rev. 63: 349–404.

Peterson S. E., S. Keeney, and M. Jasin, 2020 Mechanistic Insight into Crossing over during Mouse Meiosis. Mol. Cell 78: 1–12.

Pickett C. L., and K. Kornfeld, 2013 Age-related degeneration of the egg-laying system promotes matricidal hatching in Caenorhabditis elegans. Aging Cell 12: 544–553.

Pierce A. J., R. D. Johnson, L. H. Thompson, and M. Jasin, 1999 XRCC3 promotes homology-directed repair of DNA damage in mammalian cells. Genes Dev. 13: 2633–2638.

Potts P. R., and H. Yu, 2005 Human MMS21/NSE2 Is a SUMO Ligase Required for DNA Repair. Mol. Cell. Biol. 25: 7021–7032.

Preibisch S., S. Saalfeld, and P. Tomancak, 2009 Globally optimal stitching of tiled 3D microscopic image acquisitions. Bioinforma. Appl. 25: 1463–1465.

Putnam A., M. Cassani, J. Smith, and G. Seydoux, 2019 A gel phase promotes condensation of liquid P granules in C. elegans embryos. Nat Struct Mol Biol 26: 220–226.

Raices M., R. Bowman, S. Smolikove, and J. L. Yanowitz, 2021 Aging Negatively Impacts DNA Repair and Bivalent Formation in the C. elegans Germ Line. Front. Cell Dev. Biol. 9.

Ramsden D. A., J. Carvajal-Garcia, and G. P. Gupta, 2022 Mechanism, cellular functions and cancer roles of polymerase-theta-mediated DNA end joining. Nat. Rev. Mol. Cell Biol. 23: 125–140.

Rinaldo C., S. Ederle, V. Rocco, and A. La Volpe, 1998 The Caenorhabditis elegans RAD51 homolog is transcribed into two alternative mRNAs potentially encoding proteins of different sizes. Mol. Genet. Genomics 260: 289–294.

Robert V., and J.-L. Bessereau, 2007 Targeted engineering of the Caenorhabditis elegans genome following Mos1-triggered chromosomal breaks. EMBO J. 26: 170–183.

Robert V. J., M. W. Davis, E. M. Jorgensen, and J.-L. Bessereau, 2008 Gene Conversion and End-Joining-Repair Double-Strand Breaks in the Caenorhabditis elegans Germline. Genetics 180: 673–679.

Rosu S., D. E. Libuda, and A. M. Villeneuve, 2011 Robust crossover assurance and regulated interhomolog access maintain meiotic crossover number. Science (80-.). 334: 1286–1289.

Rosu S., K. A. Zawadzki, E. L. Stamper, D. E. Libuda, and A. L. Reese, 2013 The C. elegans DSB-2 Protein Reveals a Regulatory Network that Controls Competence for Meiotic DSB Formation and Promotes Crossover Assurance. PLoS Genet 9: 1–23.

Ruth K. S., F. R. Day, J. Hussain, A. Martínez-Marchal, C. E. Aiken, *et al.*, 2021 Genetic insights into biological mechanisms governing human ovarian ageing. Nature 596: 393–397.

Saito T. T., J. L. Youds, S. J. Boulton, and M. P. Colaiácovo, 2009 Caenorhabditis elegans HIM-18/SLX-4 interacts with SLX-1 and XPF-1 and maintains genomic integrity in the germline by processing recombination intermediates. PLoS Genet. 5: 1–19.

Saito T. T., D. Y. Lui, H. M. Kim, K. Meyer, and M. P. Colaiácovo, 2013 Interplay between Structure-Specific Endonucleases for Crossover Control during Caenorhabditis elegans Meiosis. PLoS Genet. 9: 1–13.

Sancho E., M. R. Vila, L. Sanchez-Pulido, J. J. Lozano, R. Paciucci, *et al.*, 1998 Role of UEV-1, an Inactive Variant of the E2 Ubiquitin-Conjugating Enzymes, in In Vitro Differentiation and Cell Cycle Behavior of HT-29-M6 Intestinal Mucosecretory Cells. Mol. Cell. Biol. 18: 576–589.

Schedl T., and J. Kimble, 1988 fog-2, a Germ-Line-Specific Sex Determination Gene Required for Hermaphrodite Spermatogenesis in Caenorhabditis elegans. Genetics 119: 46–61.

Schendel R. Van, S. F. Roerink, V. Portegijs, S. Van Den Heuvel, and M. Tijsterman, 2015 Polymerase θ is a key driver of genome evolution and of CRISPR/Cas9-mediated mutagenesis. Nat. Commun. 6: 1–8.

Schvarzstein M., D. Pattabiraman, D. E. Libuda, A. Ramadugu, A. Tam, *et al.*, 2014 DNA Helicase HIM-6/BLM Both Promotes MutSg-Dependent Crossovers and Antagonizes MutSg-Independent Interhomolog Associations During Caenorhabditis elegans Meiosis. Genetics 198: 193–207.

Seol J. H., E. Y. Shim, and S. E. Lee, 2018 Microhomology-mediated end joining: Good, bad and ugly. Mutat. Res. 809: 81–87.

Severson A. F., L. Ling, V. Van Zuylen, and B. J. Meyer, 2009 The axial element protein HTP-3 promotes cohesin loading and meiotic axis assembly in C. elegans to implement the meiotic program of chromosome segregation. Genes Dev. 23: 1763–1768.

Seydoux G., 2018 The P Granules of C. elegans: A Genetic Model for the Study of RNA–Protein Condensates. J. Mol. Biol. 430: 4702–4710.

Shakes D. C., J.-C. Wu, P. L. Sadler, K. Laprade, and L. L. Moore, 2009 Spermatogenesis-Specific Features of the Meiotic Program in Caenorhabditis elegans. PLoS Genet 5: 1–17.

Shi C., and C. T. Murphy, 2014 Mating Induces Shrinking and Death in *Caenorhabditis* Mothers. Science (80-.). 343: 536–540.

Shim E. Y., A. K. Walker, and T. Keith Blackwell, 2002 Broad requirement for the mediator subunit RGR-1 for transcription in the Caenorhabditis elegans embryo. J. Biol. Chem. 277: 30413–30416.

Silva-García C. G., A. Lanjuin, C. Heintz, S. Dutta, N. M. Clark, *et al.*, 2019 Single-copy knock-in loci for defined gene expression in caenorhabditis elegans. G3 Genes, Genomes, Genet. 9: 2195–2198.

Smelick C., and S. Ahmed, 2005 Achieving immortality in the C. elegans germline. Ageing Res. Rev. 4: 67–82.

So A., E. Dardillac, A. Muhammad, C. Chailleux, L. Sesma-Sanz, *et al.*, 2022 RAD51 protects against nonconservative DNA double-strand break repair through a nonenzymatic function. Nucleic Acids Res. 50: 2651–2666.

Stamper E. L., S. E. Rodenbusch, S. Rosu, J. Ahringer, and A. M. Villeneuve, 2013 Identification of DSB-1, a Protein Required for Initiation of Meiotic Recombination in Caenorhabditis elegans, Illuminates a Crossover Assurance Checkpoint. PLoS Genet 9: 1–18.

Stan Development Team, 2021 "RStan: the R interface to Stan."

Stephan A. K., M. Kliszczak, and C. G. Morrison, 2011 The Nse2/Mms21 SUMO ligase of the Smc5/6 complex in the maintenance of genome stability. FEBS Lett. 585: 2907–2913.

Strome S., and W. B. Wood, 1982 Immunofluorescence visualization of germ-line-specific cytoplasmic granules in embryos, larvae, and adults of Caenorhabditis elegans. Proc. Natl Acad. Sci. USA 79: 1558–1562.

Szostak J. W., T. L. Orr-Weaver, R. J. Rothstein, and F. W. Stahl, 1983 The Double-Strand-Break Repair Model for Recombination. Cell 33: 25–35.

Tang L., T. Machacek, Y. M. Mamnun, A. Penkner, J. Gloggnitzer, *et al.*, 2010 Mutations in Caenorhabditis elegans him-19 Show Meiotic Defects That Worsen with Age. Mol. Biol. Cell 21: 885–896.

Terentyev Y., R. Johnson, M. J. Neale, M. Khisroon, A. Bishop-Bailey, *et al.*, 2010 Evidence that MEK1 positively promotes interhomologue double-strand break repair. Nucleic Acids Res. 38: 4349–4360.

Thompson O., M. Edgley, P. Strasbourger, S. Flibotte, B. Ewing, *et al.*, 2013 The million mutation project: A new approach to genetics in Caenorhabditis elegans. Genome Res. 23: 1749–1762.

Toraason E., A. Horacek, C. Clark, M. L. Glover, V. L. Adler, *et al.*, 2021a Meiotic DNA break repair can utilize homolog-independent chromatid templates in C. elegans. Curr. Biol. 31: 1508-1514.e5.

Toraason E., V. L. Adler, N. A. Kurhanewicz, A. DiNardo, A. M. Saunders, *et al.*, 2021b Automated and customizable quantitative image analysis of whole Caenorhabditis elegans germlines. Genetics 217.

Toraason E., M. Glover, A. Horacek, and D. E. Libuda, 2021c Detection of homolog-independent meiotic DNA repair events in C. elegans with the intersister/intrachromatid repair assay. STAR Protoc. 2: 100801.

Tzur Y. B., C. Egydio De Carvalho, S. Nadarajan, I. Van Bostelen, Y. Gu, *et al.*, 2012 LAB-1 Targets PP1 and Restricts Aurora B Kinase upon Entrance into Meiosis to Promote Sister Chromatid Cohesion. PLOS Biol. 10: 1–14.

Tzur Y. B., E. Winter, J. Gao, T. Hashimshony, I. Yanai, *et al.*, 2018 Spatiotemporal Gene Expression Analysis of the Caenorhabditis elegans Germline Uncovers a Syncytial Expression Switch. Genetics 210: 587–605.

Uebel C. J., D. Agbede, D. C. Wallis, and C. M. Phillips, 2020 Mutator foci are regulated by developmental stage, RNA, and the germline cell cycle in Caenorhabditis elegans. G3 10: 3719–3728.

Uhlmann F., 2016 SMC complexes: From DNA to chromosomes. Nat. Rev. Mol. Cell Biol. 17: 399–412.

Van M. V, B. J. Larson, and J. A. Engebrecht, 2016 To break or not to break: Sex chromosome hemizygosity during meiosis in Caenorhabditis. Genetics 204: 999–1013.

Vandemark A. P., R. M. Hofmann, C. Tsui, C. M. Pickart, and C. Wolberger, 2001 Molecular Insights into Polyubiquitin Chain Assembly: Crystal Structure of the Mms2/Ubc13 Heterodimer. Cell 105: 711–720.

Volkova N. V, B. Meier, V. González-Huici, S. Bertolini, S. Gonzalez, *et al.*, 2020 Mutational signatures are jointly shaped by DNA damage and repair. Nat. Commun. 11: 1–15.

Wan G., B. D. Fields, G. Spracklin, A. Shukla, C. M. Phillips, *et al.*, 2018 Spatiotemporal regulation of liquid-like condensates in epigenetic inheritance. Nature 557: 679–683.

Wasserzug-Pash P., R. Rothman, E. Reich, L. Zecharyahu, O. Schonberger, *et al.*, 2022 Loss of heterochromatin and retrotransposon silencing as determinants in oocyte aging. Aging Cell 21.

Weinert B. T., and D. C. Rio, 2007 DNA strand displacement, strand annealing and strand swapping by the Drosophila Bloom's syndrome helicase. Nucleic Acids Res. 35: 1367–1376.

Wickham H., M. Averick, J. Bryan, W. Chang, L. McGowan, *et al.*, 2019 Welcome to the Tidyverse. J. Open Source Softw. 4: 1686.

Wijk S. J. L., and H. T. M. Timmers, 2010 The family of ubiquitin-conjugating enzymes (E2s): deciding between life and death of proteins. FASEB J. 24: 981–993.

Woglar A., and A. M. Villeneuve, 2018 Dynamic Architecture of DNA Repair Complexes and the Synaptonemal Complex at Sites of Meiotic Recombination. Cell 173: 1678–1691.

Woglar A., K. Yamaya, B. Roelens, A. Boettiger, S. Köhler, *et al.*, 2020 Quantitative cytogenetics reveals molecular stoichiometry and longitudinal organization of meiotic chromosome axes and loops. PLoS Biol. 18.

Wolters S., M. A. Ermolaeva, J. S. Bickel, J. M. Fingerhut, J. Khanikar, *et al.*, 2014 Loss of caenorhabditis elegans BRCA1 promotes genome stability during replication in smc-5 mutants. Genetics 196: 985–999.

Xaver M., L. Huang, D. Chen, and F. Klein, 2013 Smc5/6-Mms21 Prevents and Eliminates Inappropriate Recombination Intermediates in Meiosis. PLoS Genet. 9.

Yamada S., A. G. Hinch, H. Kamido, Y. Zhang, W. Edelmann, *et al.*, 2020 Molecular structures and mechanisms of DNA break processing in mouse meiosis. Genes Dev. 34: 806–818.

Yin Y., and S. Smolikove, 2013 Impaired Resection of Meiotic Double-Strand Breaks Channels Repair to Nonhomologous End Joining in Caenorhabditis elegans. Mol. Cell. Biol. 33: 2732–2747.

Yin Y., and T. D. Petes, 2014 The Role of Exo1p Exonuclease in DNA End Resection to Generate Gene Conversion Tracts in Saccharomyces cerevisiae. Genetics 197: 1097–1109.

Yokoo R., K. A. Zawadzki, K. Nabeshima, M. Drake, S. Arur, *et al.*, 2012 COSA-1 Reveals Robust Homeostasis and Separable Licensing and Reinforcement Steps Governing Meiotic Crossovers. Cell 149: 75–87.

Zakharyevich K., Y. Ma, S. Tang, P. Y. H. Hwang, S. Boiteux, *et al.*, 2010 Temporally and Biochemically Distinct Activities of Exo1 during Meiosis: Double-Strand Break Resection and Resolution of Double Holliday Junctions. Mol. Cell 40: 1001–1015.

Zhang W., N. Miley, M. S. Zastrow, A. J. MacQueen, A. Sato, *et al.*, 2012 HAL-2 Promotes Homologous Pairing during Caenorhabditis elegans Meiosis by Antagonizing Inhibitory Effects of Synaptonemal Complex Precursors. PLoS Genet. 8.

Zhao W., J. B. Steinfeld, F. Liang, X. Chen, D. G. Maranon, *et al.*, 2017 BRCA1-BARD1 promotes RAD51-mediated homologous DNA pairing. Nature 550: 360–364.